UNIVERSITY OF CALIFORNIA
SANTA CRUZ

# TOWARDS THE EMISSION MECHANISM OF PULSARS

A dissertation submitted in partial satisfaction of the
requirements for the degree of

DOCTOR OF PHILOSOPHY

in

PHYSICS

by

**Brent Williams Limyansky**

September 2022

The Dissertation of Brent W. Limyansky
is approved:

Professor Robert Johnson, Chair

Dr. Pablo Saz Parkinson

Professor David Smith

Professor Tesla Jeltema

Peter Biehl
Vice Provost and Dean of Graduate Studies

This work is licensed under a Creative Commons Attribution 4.0
International License 🅭 🅯 by
Brent W. Limyansky
2022

# Contents

# List of Figures

# List of Tables

# Towards the Emission Mechanism of Pulsars

## Abstract

**Brent W. Limyansky**

Pulsars are small, dense, rotating stars that appear to flash as they sweep the sky with beams of radiation. This light originates from high energy particles following curved paths as they flow into interstellar space. Where these particles originate, and how they are accelerated to the necessary energies, is still an open question. The answer may change as the pulsar goes through its evolutionary process.

Theorists have focused on four accelerating regions: the polar cap, slot gap, outer gap, and current sheet. Testing these models requires detecting pulsars and measuring their spectra and spin characteristics. It is to this task that I devote myself in this thesis, focusing in particular on the millisecond and soft $\gamma$-ray pulsar populations.

Millisecond pulsars are the oldest known pulsars, and are defined by their millisecond periods. I characterized the *Fermi*-LAT spectrum of PSR J0218+4232 as part of a larger work on searching for very high energy emission with MAGIC. While MAGIC was not able to detect the source, the *Fermi*-LAT spectrum was useful in providing insight as to why this was the case.

Soft $\gamma$-ray pulsars are brightest at MeV energies, and are challenging to study due to the lack of an instrument sensitive in this energy region. I characterize the spin characteristics of the soft pulsars PSR J1813-1749 and PSR J1846-0258 with NICER, and attempt to detect them with the *Fermi*-LAT to characterize a portion of their MeV spectra. While the spin characterization will aid in detecting these sources with future MeV telescopes, there was not a strong enough LAT detection to extract spectral information. Examining PSR J2022+3842 with NICER did lead to a detection of pulsations with *Fermi*-LAT, which improved upon the prior detection, as well as provided spectral information for emission modeling.

*I would like to thank...*

My family - the only people without whom I can say with 100% certainty this would not have been possible. ∗ Pablo Saz Parkinson, who may well fall within the error bars of my previous statement. ∗ Robert Johnson, for his guidance through every day of this 6+ year endeavor. I will fondly remember his home pizza parties. ∗ Bill Atwood and Steve Ritz, members of the local LAT Collaboration, for their advice throughout the process. ∗ David Williams and David Smith, for helping me become a more rounded scientist through our journal club. ∗ Tesla Jeltema, along with the rest of my committee, for their invaluable roll in making my degree something I can be proud of. ∗ David Smith, one of the friendliest scientists I've encountered, and who greatly contributed to my work on PSR J1846-0258 and PSR J2022+3842. ∗ Senior graduate students Brendan Wells, Christian Johnson, Caitlin Johnson, and Mike Testa for their mentorship early in my graduate student career. ∗ Continuing graduate student Megan Splettstoesser for giving me the opportunity to pay a small fraction of this forward. ∗ Roy Sfadia and Carolyn Gee, who are fully deserving of their place at the start of the "fun" section of the acknowledgments. ∗ Austin Bush, Richard Stauffer, Maddi Frank, Joseph Newman, Lyndsey Walsh, Elizabeth Gwinn, Zach Justice, Cameron Low, and Jenn Sittler, for over a decade of friendship, and hopefully more to come. ∗ Smith [214] and Ginn [105] for helping me avoid burnout, and teaching me to live a less toxic life. ∗ Et al., for the remarkable feat of making me feel that acknowledging over 25 people is far too few.

# Chapter 1

# Introduction

Pulsars are a truly unique astrophysical source. Forged in the crucible of a supernova [62], the most energetic explosions in the universe [185], pulsars are also one of the densest objects in the universe, second only to the singularity of a black hole [106]. Observationally, pulsars are known for their unique pulsating nature. Often compared to a lighthouse, their powerful emissions sweep the sky, making them appear to be flashing [107].

It is the origin of this pulsating emission that I investigate in my thesis. This emission is known to originate from highly energetic charged particles moving in pulsars' super-strong magnetic fields [69]. The charged particles require strong electric fields in order to be accelerated to these energies. However, this is at odds with that of the plasma-filled pulsar magnetosphere. Much like how there are no electric fields inside a conductor, this plasma will cancel out accelerating electric fields around the pulsar [109]. The study of a pulsars emission can thus be reduced to a simple question: Where does particle acceleration occur around a pulsar?

I attempt to make headway into this problem for two classes of pulsar: the MeV pulsar, with peak emissions in the MeV range, and the millisecond pulsar, with periods on the order of milliseconds. Study of MeV pulsars is challenging due to the lack of a sufficiently sensitive instrument in this energy range [118]. I examine three potential MeV pulsars: PSR J1813-1749, PSR J1846-0258, and PSR J2022+3842. Of these, only PSR J2022+3842 was detected by *Fermi*-LAT with sufficient strength to be used for emission mechanism modeling.

I also examine the millisecond pulsar PSR J0218+4232. Due to the properties of this source, we had hoped it would be the first MSP detected imaging atmospheric Cherenkov telescopes (IACTs). While no such emission was detected, we had sufficient *Fermi*-LAT data to model the emission mechanism of this source up to 10's of GeV.

Chapter 2 provides a broad overview of pulsars, with an emphasis on common back-of-the-envelope values used to describe pulsars in the literature. This is followed by an overview of pulsar emission physics, and descriptions of the theoretical modeling software used to study the emission mechanism.

Chapter 3 describes the two primary instruments I use in my thesis: the *Fermi* Large Area Telescope (LAT) to study $\gamma$-ray emission and the Neutron Star Interior Composition ExploreR (NICER) to study X-ray emission. Chapter 4 provides a low-level overview of the analysis techniques used examine data from these telescopes. While important for a researcher to understand, much of what is described in this chapter is implemented in publicly available software.

Chapter 5 covers techniques used to study pulsars in photon-by-photon datasets. The H-Test is perhaps the most important topic covered in this chapter, as it is the current standard used to asses the significance with which pulsations from a $\gamma$-ray pulsar are detected. Techniques for initially detecting pulsars' characteristic drifting periodic signals are also covered. However, while a useful skill, the search techniques make only a small appearance in my thesis, specifically when examining PSR J1813-1749.

The remaining chapters cover the particular pulsars I look at in my thesis. Chapters 6 and 7 cover two *soft* $\gamma$-ray pulsars, PSR J1813-1749 and PSR J1846-0258, which I characterized but which had insufficient significance to perform emission mechanism modeling. Chapter 8 covers PSR J2022+3842, a *soft* $\gamma$-ray pulsar which was used for emission mechanism modeling. Chapter 9 covers PSR J0218+4232, a millisecond pulsar we observed with the *Fermi*-LAT and MAGIC, and which we used to examine the millisecond pulsar emission mechanism. Chapter 10 presents the overall conclusions of my thesis, as well as prospects for further research.

# Chapter 2

# About Pulsars

A pulsar is, for some stars, one of the final stages of their stellar evolution. When a star in the mass range 9-25 $M_\odot$[1] exits the main sequence via a supernova explosion, the core will be compressed into a neutron star [134]. While many exact quantities regarding neutron stars are still unknown, they are expected to contain roughly 80% neutrons, and 5-10% each of protons and electrons [82].

This unique composition limits the mass and radii ranges of neutron stars, with the canonical neutron star having a radius of 10 km and a mass of 1.4 $M_\odot$[2] [123]. This mass and radius is intimately related to the fundamental physics of dense matter — being essentially a large clump of nuclear material, repulsive nuclear forces are in equilibrium with attractive gravitational forces. Above a theoretical limit, the Tolman-Oppenheimer-Volkoff limit, the neutron star will collapse into a black hole [198]. Historically, this limit was placed at about 2.9 $M_\odot$ [152], but is still an area of active research, with recent gravitational wave events placing an upper limit closer to 2.3 $M_\odot$ [212]. More broadly, the relation between neutron star mass and radius is described by the neutron star equation of state, which is a key research focus of NASA's NICER telescope [54].

While most pulsars are neutron stars[3], not every neutron star is a pulsar. As

---

[1] This range can vary considerably due to factors such as metal content of the star, and whether or not it exists in a binary system [134, 94].

[2] At a rather impressive $6.7 \times 10^{11}$ kg/cm$^3$, the world's largest cargo aircraft, the late An-225, could carry the equivalent of about 3 sand-sized grains of neutron star matter, and a Boeing 747 about one grain.

[3] There is at least one known white dwarf pulsar [61].

the name suggests, pulsars are distinguished by their "pulsating" nature. Often compared to a lighthouse beacon [107], they can be seen turning on and off several times per second. Continuing the lighthouse analogy, the reason for this periodic behavior is the rapidly rotating nature of the neutron star, which is a result of inheriting the angular momentum of its progenitor star as the core contracts into the smaller, denser neutron star[4] [123]. As the radiation is tightly focused, the pulsar can only be seen when the beam is pointed at earth. The "pulsar emission mechanism" describes how this radiation is generated.

As with angular momentum, the contracting core also conserves magnetic flux, producing very strong field lines in the vicinity of the neutron star [246]. This strong magnetic field is the final component in what makes up one of the most basic pictures of pulsars: a small, dense object that is rapidly rotating and has a strong magnetic field. From this picture, several useful approximations follow[5] [69].

## 2.1 Canonical Approximations

There are a handful of values used for back-of-the-envelope calculations regarding pulsars. These values, and subsequent derived quantities, are termed "canonical". Common canonical quantities for pulsars include a 10 km radius and 1.4 $M_\odot$ mass, as previously mentioned. Derived quantities include the spin-down luminosity, magnetic field strength, and characteristic age. The latter two of these quantities also include the assumption that a pulsar behaves as a magnetic dipole.

Spin-down luminosity, calculated as the rate of change of the pulsar's rotational kinetic energy due to its measured period derivative, is

$$\dot{E} = -\frac{d}{dt}\left(\frac{1}{2}I\Omega^2\right) = -\frac{4\pi^2 I\dot{P}}{P^3} \tag{2.1}$$

---

[4] In the discovery paper of the first pulsar, it was thought the most likely source of the pulsed signal was from radial oscillations of either white dwarfs or neutron stars [139]. Gold [107] suggested later that year that the emission was due to rotation. They also mention the still used lighthouse analogy, dipolar magnetic field configuration, and co-rotating magnetosphere, as well as correctly predict a slight slow down in period and the existence of shorter period pulsars.

[5] Chapter 6 of Condon and Ransom [69] presents a nice derivation of these properties, and is available freely online. The process is also described in chapter 1 of Ghosh [104], and some illustrative exercises are included in chapter 11 of Griffiths [114].

where $I$ is the neutron star moment of inertia[6], $\Omega$ is the angular frequency, $P$ is the period, and $\dot{P}$ is the rate of change of the period. A test of spin-down luminosity, and for that matter other canonical pulsar values, is the Crab Nebula (Figure 2.1) and associated pulsar. The luminosity across all wavelengths of the Crab Nebula agrees well with the spin-down luminosity of the pulsar, suggesting that the pulsar is powering the nebula [108].

The surface magnetic field strength can be approximated by equating the loss of rotational kinetic energy described above to the energy radiated by a uniformly charged sphere with a magnetic dipole moment. This yields:

$$B > \left(\frac{3c^3 I}{8\pi^2 R^6}\right)^{\frac{1}{2}} (P\dot{P})^{\frac{1}{2}} \tag{2.2}$$

The calculated strength of $B$ will be related to the angle between the dipole moment and the axis of rotation, with a stronger magnetic field needed to radiate the same amount of energy as the dipole moment becomes more aligned with the axis of rotation. The inequality in the above equation comes from assuming a maximally misaligned (90°) dipole moment and axis of rotation. If $R$ is taken to be the canonical radius of a neutron star, the resulting quantity is referred to as the surface magnetic field strength. While dipole radiation does cause the star's rotation to slow, the radiation itself cannot be directly observed [69]. Being of the same frequency as the pulsar, radio signals in this range are absorbed by the interstellar medium and any surrounding nebula.

The radius of the "light cylinder" is also important in the study of neutron stars. The boundary of the light cylinder occurs at the radius where an object co-rotating with the neutron would need to be traveling at the speed of light to maintain co-rotation. Setting the velocity equal to the speed of light:

$$\frac{2\pi R}{P} = c \tag{2.3}$$

---

[6] $I = 10^{45}$ g cm$^2$, as derived from a uniform sphere of canonical mass and radius.

Figure 2.1: The Crab Nebula, as seen in the infrared, visible, and X-ray wavelengths. The Crab pulsar, PSR B0531+21, can be seen in the center of the composite image as a bright white dot.
Image Credits: NASA, ESA, CXC, JPL-Caltech, J. Hester and A. Loll, R. Gehrz, STScI

yields

$$R_{LC} = c\frac{P}{2\pi} \tag{2.4}$$

where $R_{LC}$ is the radius at the light cylinder. Using $R_{LC}$ instead of the canonical pulsar radius yields $B_{LC}$, the magnetic field at the light cylinder. Notably, the magnetic field at the surface and light cylinder have different dependencies on $P$. It may be possible to discern if a magnetically sensitive process occurs near the surface of the pulsar or near the light cylinder by studying the process in a range of pulsars covering a varying range of $P$ values [8].

Characteristic age approximates the age of a pulsar under the assumptions that its rotation has significantly slowed since birth and that the magnetic field can be accurately modeled as a rotating dipole. The characteristic age $\tau$ is:

$$\tau = \frac{P}{2\dot{P}} \tag{2.5}$$

A derivation of this is presented in Appendix B, as the underlying setup is less intuitive than for the other derived quantities.

There are a few ways that the characteristic age can be tested. In the case of the Crab, this task is quite easy. Knowing that pulsars are formed in supernovae, and knowing the exact date of SN 1054 from historical documents[7], such as in Figure 2.2, one can directly compare the theoretical and observed values. The characteristic age of the Crab pulsar is approximately 1300 years, and the true age is approximately 1000 years.

The characteristic age is not always so close to the true age. In the case of PSR B1951+32 [186] and PSR J0538+2817 [158], the true ages of the pulsars were measured by looking at their proper motion, and extrapolating backwards towards the center of their associated supernova remnant. For PSR B1951+32, this produces an age of 64,000 years vs a characteristic age of 107,000 years. For PSR J0538+2817 the discrepancy is larger, with an estimated age of 30,000 years vs a characteristic age of 620,000 years. Noutsos et al. [195], in studying the correlation between a pulsar's spin axis and velocity, look at both a pulsar's characteristic age, and its "kinematic age", measured by looking at its displacement from the Galactic plane (and assuming that it was born in the plane). While a relation between spin axis and velocity is not established when pulsars are grouped by characteristic age, one does exist when kinematic age is used. All this is to say that, while the above relations are commonly used in the study of pulsars, it is important to remember that they come from assumptions that may be over simplified.

The $P - \dot{P}$ diagram (Figure 2.3) summarizes the above canonical quantities, and shows how they relate to the pulsar's measured spin. On the X-axis of this diagram is period, and on the Y-axis is period derivative, giving rise to the name. Lines on the diagram representing surface magnetic field strength, characteristic age, and spin-down luminosity emphasize the relations of these canonical relationships with

---

[7] There are quite a few claims of historical recordings of SN 1054, some of which have generated significant debate. Eastern records, such as that presented in Figure 2.2, are generally considered to be the most reliable, with considerable debate surrounding references from the West [68, 221]. Cave drawings from Native Americans have also been suggested to depict SN 1054 [187], but the vague nature of these drawings (do they even depict stars?), combined with astrophysical constraints, make these claims the hardest to substantiate [159].

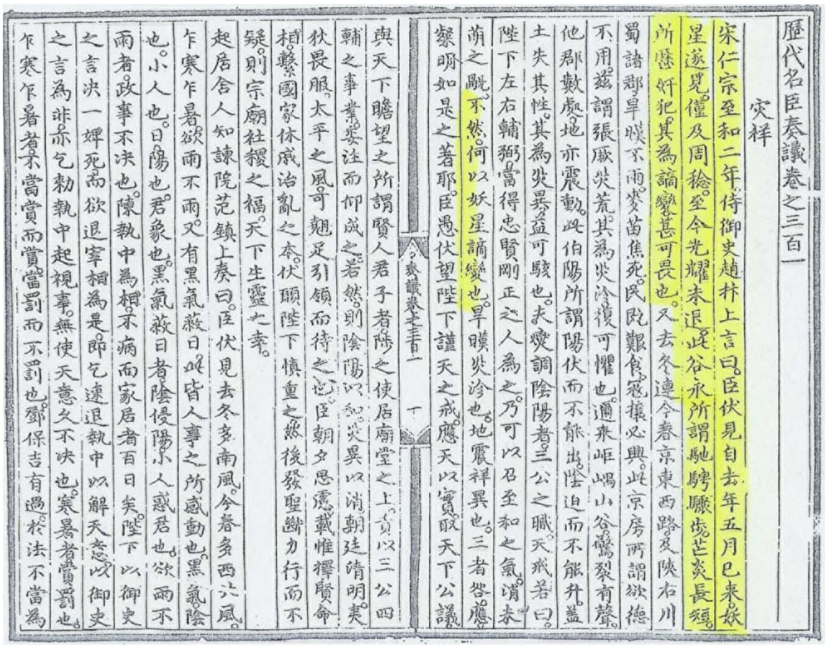

歷代名臣奏議卷之三百一

災祥

宋仁宗至和二年侍御史趙抃上言曰臣伏見自去年五月已來妖星遂見僅及周稔至今光耀未退此谷永所謂馳騁驟歩芒炎長短所歷奸犯其為謫變甚可畏也又去冬連今春京東西路及陝右川蜀諸郡旱暵不雨麥苗焦死民既艱食寇攘必興此京房所謂欲德不用茲謂張厥災荒其為災沴複可懼也邇來岠嵎山谷驚裂有聲他郡數處地亦震動此伯陽所謂陽伏而不能出陰迫而不能升蓋土失其性其為災異益可驗也夫燮調陰陽者三公之職天戒若曰陛下左右輔弼當得忠賢剛正之人為之乃可以召至和之氣消未萌之亂不然何以妖星謫變也旱暵災沴也地震祥異也三者咎應粲昞如是之著耶臣愚伏望陛下謹天之戒應天以實取天下公議與天下瞻望之所謂賢人君子者陟之使居廟堂之上責以三公四輔之事業委注而仰成之若然則陰陽以和災異以消朝廷清明夷狄畏服太平之風可翹足引領而待之也臣朝夕思慮載惟擇賢命相繫國家休戚治亂之本伏願陛下慎重之然後發聖斷力行而不疑則宗廟社稷之福天下生靈之幸

起居舍人知諫院范鎮上奏曰臣伏見去冬多南風今春多西北風乍寒乍暑欲雨不雨又有黑氣蔽日此皆人事之所感動也黑氣陰也小人也日陽也君象也黑氣蔽日者陰侵陽小人惑君也欲雨不雨者政事不決也陳執中為相不病而家居者百日矣陛下以御史之言決一婢死而欲退宰相為是耶乞速退執中以解天意以御史之言為非耶乞勅執中起視事無使天意久不決也寒暑者賞罰也乍寒乍暑者未當賞而賞當罰而不罰也鄧保吉有過於法不當為

奏議卷之三百一　十

Figure 2.2: A record from the Chinese Song dynasty referencing supernova SN 1054 with sufficient detail to date the event as occurring on July 4th, 1054 CE. The highlighted text translates to:

> 2nd year of the Zhihe reign period of Emperor Renzong of Song [1055]; Attendant Censor Zhao Bian submitted a letter saying: “Your servant considers that, since the 5th month of last year [when] the baleful star appeared, a full year has passed and until now its brilliance has not faded [lit. ‘retreated’]. This is what Gu Yong meant by ‘its rapid movement, the variations in the length of its flaming rays, and the [asterisms] on which it has trespassed successively,’ as a censorious anomaly it is greatly to be feared.”

Image (public domain) and Translation from Pankenier [200]

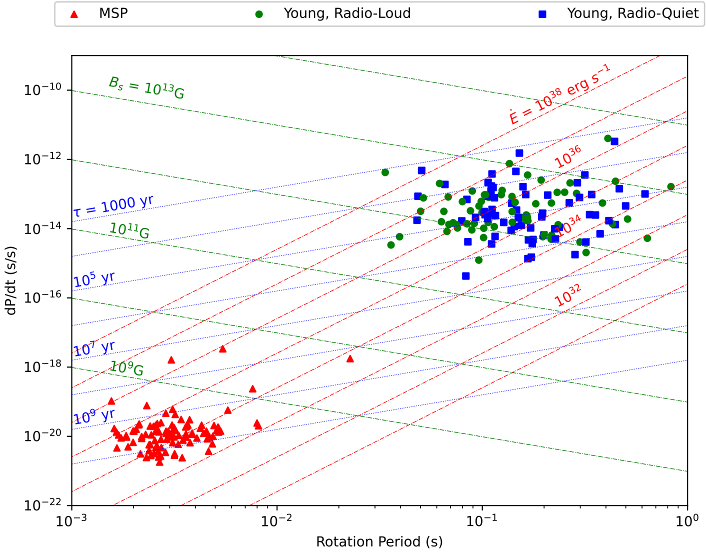

Figure 2.3: The $P - \dot{P}$ diagram, taken from Limyansky [170], showing the set of pulsars to be included in the *Fermi* LAT Third Catalog of Gamma-Ray Pulsars (3PC). On the axes are period and period derivative. Green, blue, and red lines show how the canonical surface magnetic field strength, characteristic age, and spin-down luminosity depend on period and period derivative. Young pulsars are shown as green circles and blue squares, depending on whether they are visible in radio. Millisecond pulsars are shown as red triangles.

period and period derivative. Notably, this figure only includes ∼ 300 pulsars that were set for inclusion in the The Third *Fermi* Large Area Telescope Catalog of Gamma-ray Pulsars (3PC) at the time of Limyansky [170]. However, there are over 3000 known pulsars[8]. Radio telescopes are the most prominent detectors of pulsars, so much so that the fact that a pulsar is not visible to radio telescopes is of notable distinction.

In addition to the derived properties displayed in Figure 2.3, several other aspects of the pulsar population are also apparent in the figure. As seen in the legend, there are two main classification of pulsars: young pulsars, and millisecond pulsars (MSPs). Young pulsars are what have been described in this chapter so far. MSPs, so named because they have periods on the scale of milliseconds, are a further evolution of the young pulsar[29]. In a binary system, there are some instances where one star will transition into a pulsar while remaining in a stable orbit with

---

[8] See the ATNF pulsar catalog for an updated list: `https://www.atnf.csiro.au/research/pulsar/psrcat/`

its main sequence companion. As the companion star ages into a red or blue giant, it will significantly increase in radius. In certain configurations, this leads to an overflowing of the Roche lobe, where matter is transferred from the companion star to the surface of the neutron star. Along with this mass transfer comes a transfer of angular momentum, which causes the neutron star to spin faster and faster, eventually reaching these millisecond periods after billions of years. This also explains why MSPs are sometimes referred to as "recycled pulsars" — if the pulsar has slowed down to the point of where its emission mechanism turns off, it can be recycled by this mass transfer process into an MSP.

MSPs have extremely predictable periods. Once the period (and higher derivatives of the period) is measured, the precision rivals that of some atomic clocks [144]. Proof of concept experiments, such as SEXTANT[9], have already demonstrated that these pulsars can be used in place of GPS satellites for navigation [244]. The NANOGrav collaboration has used these millisecond pulsars much like LIGO and VIRGO use laser interferometers to search for gravitational waves [37]. Recently, *Fermi*-LAT has also demonstrated its ability to perform similar searches using millisecond pulsars [22]. Despite sounding like a rare process, the long time scales involved give these sources time to accumulate. As can be seen in Figure 2.3, a substantial fraction of pulsars seen with *Fermi*-LAT are millisecond pulsars.

As shown in Figure 2.4, there are further classifications of pulsar than apparent in Figure 2.3. Magnetars are a type of pulsar defined by their extremely strong magnetic fields [83]. Compact Core Objects (CCOs) are neutron stars without a binary companion and located at the center of supernova remnants [123]. They are seen to emit only black body radiation. Isolated Neutron Stars (INSs) are similar, but are not associated with a supernova remnant. High-mass X-ray binaries (HMXBs) and low-mass X-ray binaries (LMXBs) are both types of neutron star undergoing accretion from a companion star. The accretion produces a system primarily bright in the X-ray band. "High-mass" or "low-mass" refers to the mass of the companion star. A more detailed overview of these sources can be found in

---

[9] a component of the NICER mission

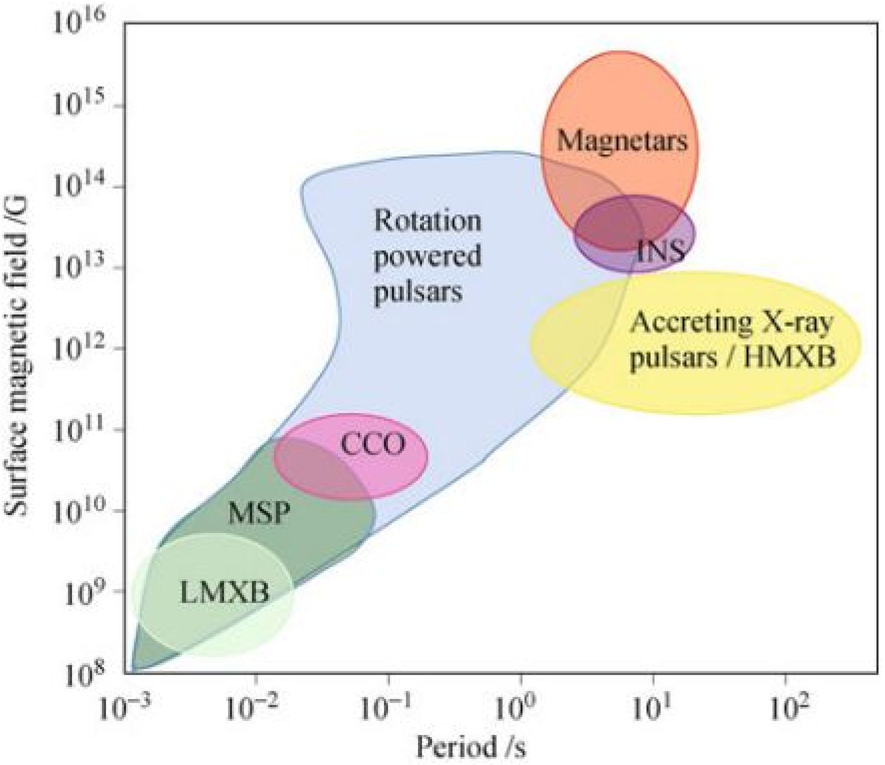

Figure 2.4: A qualitative representation of the $P - \dot{P}$ diagram. Note that period derivative has been replaced by surface magnetic field strength. Other types of neutron star not mentioned in this thesis are present, including low mass X-ray binaries (LMXB), central compact objects (CCO), isolated neutron stars (INS), and high mass X-ray binaries (HMXB). Image reproduced from Harding [123].

Harding [123].

This thesis pays particular attention to MeV pulsars. MeV pulsars are a sub-type of young pulsars, distinguished by the fact that their spectra peak in the MeV range. MeV pulsars tend to lie towards the top right of the $P - \dot{P}$ diagram, indicating that they are among the newer young pulsars[162]. They are an area ripe for discovery, as a lack of instrumental coverage in the MeV range means that few are known. Of particular interest is their relation to magnetars. Magnetars are believed to be an even younger type of pulsar, with their energy coming from the decay of their very strong magnetic fields.

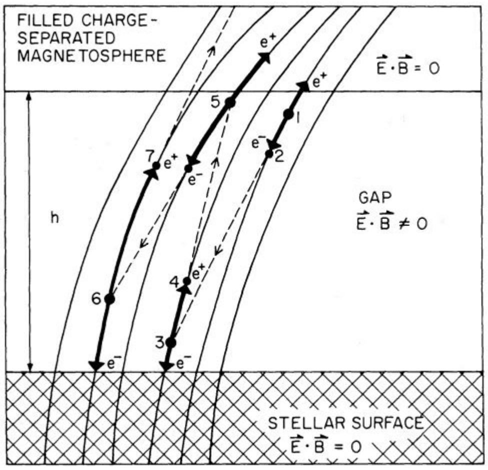

Figure 2.5: A schematic of a pair cascade in the polar cap, responsible for limiting the size of the accelerating region. The first electron/positron pair is generated at location 1. The electron is accelerated towards the neutron star, eventually gaining enough energy to radiate a $\gamma$-ray at point 2. The $\gamma$-ray pair produces at point 3. This time, the positron gains enough energy to produce a $\gamma$-ray, and the process repeats. Image reproduced from Ruderman and Sutherland [206].

## 2.2 The Pulsar Emission Mechanism

As has been previously mentioned, dipole radiation cannot explain the observed emission from pulsars. The observed radio flux is much too low, and the dipole radiation would not at all account for being able to see pulsations up to TeV energies [69].

The pulsar emission mechanism is thought to be accelerating highly energetic charged particles. The big question, and that which this thesis attempts to answer, is *how* these particles are accelerated to high energies in the first place. In particular, this is in contrast to the idea of the force-free magnetosphere, where charged particles in a plasma surrounding the pulsar screen any accelerating electric field (similar to the statement that conducting objects will be equipotential). The problem of pulsar radiation thus consists of two main questions: how are the particles accelerated to high energies, and once at the high energies, how do they radiate?

### 2.2.1 Accelerating Regions

As pulsars are surrounded by a plasma [109], the majority of their magnetosphere is thought to be in the ideal magnetohydrodynamic (MHD) state. One aspect of an ideal plasma is that it has infinite conductivity. Recall the general form of Ohm's law:

$$\frac{1}{\sigma}\vec{J} = \vec{E} + \vec{v} \times \vec{B} \tag{2.6}$$

where $\vec{J}$ is the current density and $\sigma$ is the conductivity[10]. Letting $\sigma \to \infty$ produces the ideal Ohm's law for a plasma:

$$0 = \vec{E} + \vec{v} \times \vec{B} \tag{2.7}$$

Because of their strong magnetic fields, particles in a pulsar magnetosphere are generally thought of as being bound to the pulsar's magnetic field lines. To get particles moving at high speeds along a magnetic field line, we want some accelerating electric field parallel to $\vec{B}$, which we will call $E_{\|}$. But, $\vec{v} \times \vec{B}$ produces a vector perpendicular to both $\vec{v}$ and $\vec{B}$, meaning that $E_{\|} = 0$. In the literature, it is thus common to see the problem of finding an accelerating region stated as finding a place where $E_{\|} \neq 0$.

In pulsars, there are four often looked at sites where the ideal MHD conditions break down. Three of these, the polar cap (PC), slot gap (SG), and outer gap (OG), are *vacuum gaps*, where an absence of plasma allows $E_{\|} \neq 0$. The final location is the current sheet, where magnetic reconnection accelerates particles to high energies.

The framework for much of what is to follow was first described by Goldreich and Julian [109], who studied the case of the *aligned rotator*, or a neutron star with its magnetic dipole moment aligned with its axis of rotation[11]. A diagram of their work is shown in Figure 2.6a.

Earlier in this chapter, I introduced the idea of the light cylinder as the boundary where co-rotation with the neutron star surface would require a speed equal to the speed of light. The pulsar's dipolar magnetic field lines, despite being somewhat of a

---

[10] Derivation of Ohm's law in a plasma is non-trivial, and can be found in chapters 11 and 12 of Somov [218]

[11] Ruderman and Sutherland [206] describe the case of the aligned rotator as being an *antipulsar*, and consider a *pulsar* to be the case where the magnetic dipole moment is anti-aligned with the spin axis.

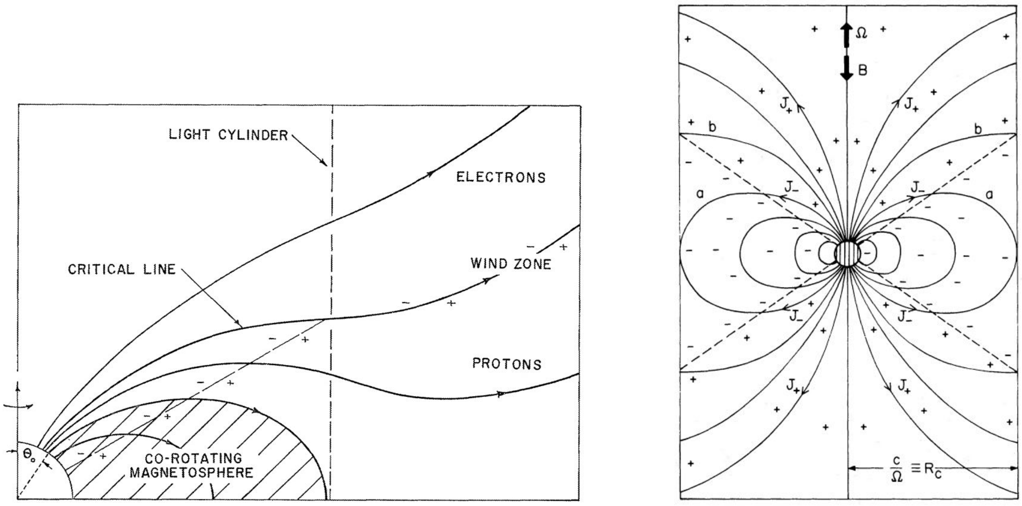

(a) Sketch of the magnetosphere in an a pulsar with nearly aligned dipole moment. Image reproduced from Goldreich and Julian [109].

(b) Sketch of the magnetosphere for a pulsar with anti-aligned dipole moment. Image reproduced from Ruderman and Sutherland [206].

Figure 2.6: Sketches of various aspects of the pulsar magnetosphere. Image (a) has the neutron star in the lower left corner. The co-rotating magnetosphere is shaded, and extends from the star surface to the light cylinder. Above this region, field lines can be seen opening and extending past the light cylinder. Also extending from the neutron star surface is a cone denoting regions of the magnetosphere at higher and lower electric potential than the surrounding interstellar medium. This intersects the critical field line at the light cylinder. Protons and electrons are shown streaming from the neutron star on either side of the critical line. Image (b) shows much the same picture, but with magnetic moment anti-aligned to the axis of rotation. The full cone separating positive and negative charge densities is shown. Note how these regions are flipped in potential when compared to (a).

theoretical abstraction, are nonetheless subject to this condition. Field lines existing entirely withing the light cylinder form the closed loops commonly associated with magnetic dipoles. These are *closed* field lines. Field lines crossing the light cylinder cannot form these orderly loops, and are called *open* field lines. As particles are considered bound to their field lines, particles existing on the closed field lines are neatly bound to the region of space within the light cylinder, making up the region called the co-rotating magnetosphere.

Figure 2.6 illustrates properties of magnetospheres for aligned and anti-aligned rotators. Each magnetic field line has a different (but, abiding by $E_{\parallel} \neq 0$, equal along the path of the field line) electric potential relative to the interstellar medium surrounding the neutron star. This potential is tied to the latitude from which the field line originates. In an aligned rotator, field lines originating closer to the equator are at a higher potential than the surrounding interstellar medium. If the field line is open, positive particles will tend to stream outward from the pulsar along these field lines. Similarly, high latitude open field lines will tend to be at a lower potential than the region surrounding the neutron star, causing negatively particles to stream outward along them. The field line which is at equal potential to the interstellar medium is called the critical line, and divides these two streaming regions.

Calculating the charge density of the magnetosphere, one finds it is composed of conical regions of positive and negative charge. In the case of an aligned rotator, there are some open field lines along which positive charges may flow outside the light cylinder, yet originate in an area where they are bathed in negatively charged magnetosphere. It is along this region that the first of the accelerating regions, now referred to as the *outer gap*, was theorized [146]. Holloway [146] noted that the zero-charge lines between the conical charge densities could block certain evacuated regions of the magnetosphere from being refilled. This would lead to a long-lived vacuum gap. This idea was further refined by Cheng, Ho, and Ruderman [64]. The gap can be shaped by the process of pair production. High energy photons pair produce in the large magnetic fields of vacuum gaps, generating electrons and positrons that replenish lost plasma and re-fill the gaps. A schematic of the outer gap is shown in Figure 2.7.

The polar cap followed, and was proposed by Ruderman and Sutherland [206]. This work builds on that carried out by Goldreich and Julian [109], but considers the case of the anti-aligned rotator, where the magnetic dipole vector is directly opposite to the spin vector. As mentioned in the discussion on the outer gap, the magnetosphere has conical regions separating areas of positively and negatively charged plasma. In the case of the aligned rotator, negative charges have a tendency to flow from the polls (that is to say, the *polar caps*) to regions outside the light cylinder. As pointed out by Ruderman and Sutherland [206], this plasma can be replenished by pulling electrons from the neutron star surface.

In the case of the anti-aligned rotator, the charge densities and field line po-

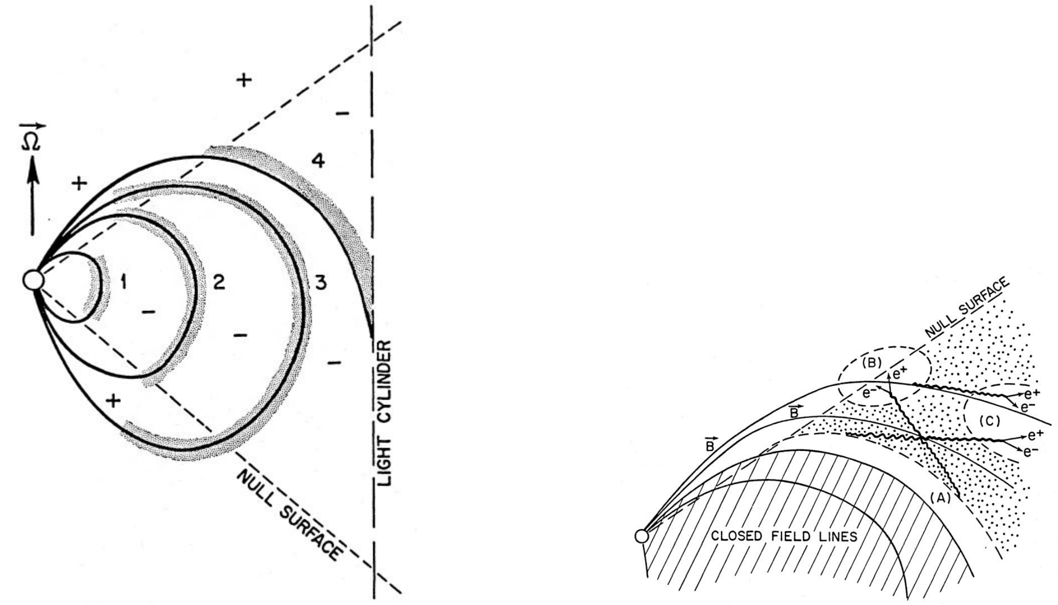

(a) Various “test” gaps in the pulsar magnetosphere. Of these, only gap 4 will persist. Image reproduced from Cheng, Ho, and Ruderman [64].

(b) Gaps forming significantly above the co-rotating region can be replenished from high energy photons generated by the outer gap. Image reproduced from Cheng, Ho, and Ruderman [64].

Figure 2.7: Schematics explaining the presence of the outer gap. Figure (a) shows four artificially constructed “test” gaps. Gap 1 can be replenished through its ends, which are within the area of negative charge density. Gap 2 has its ends “blocked” by the zero charge region between positive and negative ares of charge density. However, the plasma can be refilled gradually through pair production. Gap 3 extends well past the zero charge region. It will reduce to the case of gap 2 as positive charges flow into the extended ends. Gap 4 is persistent. The ends are blocked by the zero charge region and the light cylinder, and plasma generated via pair production within it will continually flow outward through the light cylinder. Figure (b) shows why gap 4 is located on top of the co-rotating region. Geometrically, it is easier for high energy photons generated at low altitudes to enter gaps at higher altitudes. As the co-rotating magnetosphere does not produce high-energy photons, the lowest altitude gap will persist, with its photons adequately filling higher altitude gaps.

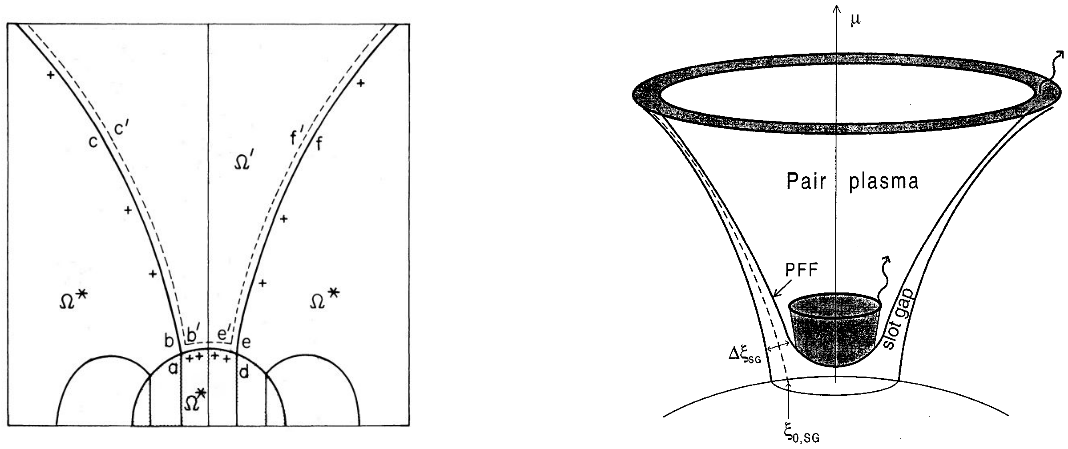

(a) Schematic of the polar cap region. Image reproduced from Ruderman and Sutherland [206].

(b) Schematic of the slot gap region. Imaged reproduced from Muslimov and Harding [189].

Figure 2.8: Schematic pictures of the polar cap and slot gap regions. While Ruderman and Sutherland [206] emphasized the region directly above the pulsar, Muslimov and Harding [189] examine the region along the open field line.

tentials are flipped, causing *positive* charges to flow outward along open field lines. While it is relatively easy to pull electrons from the neutron star surface, it is much more difficult to pull positive charges [12]. This produces a vacuum gap, with an accelerating $E_{||}$ inside it. As in the case with the outer gap, the vacuum gap above the polar cap is held in equilibrium via pair production of high energy photons (see Figure 2.5. As the gap grows, so does the electric field strength, making it easier for gamma rays to produce electrons and positrons, which in turn generate a plasma filling the gap.

The final vacuum gap is the slot gap, which is theorized to lie somewhere between the polar cap and outer gap [34]. The slot gap is, in admittedly oversimplified terms, a correction to the polar cap region [189]. Looking at the polar cap as described by Ruderman and Sutherland [206], one can see that the accelerating region is somewhat "U" shaped, and bounded on the edges by magnetic field lines (see Figure 2.8a). This boundary, below which particle acceleration is allowed to occur, came to be

---

[12] In strong magnetic fields, the electron energy levels become much more closely spaced than in standard atoms, with the electron clouds taking the form of concentric cylinders along the magnetic field lines [205]. In this configuration, covalent bonds between atoms are able to form with *all* the electrons belonging to each atom, as opposed to just those in valence bands. The result is super-strong molecular chains that cannot be ripped apart by the pulsar to supply positive charges to the magnetosphere.

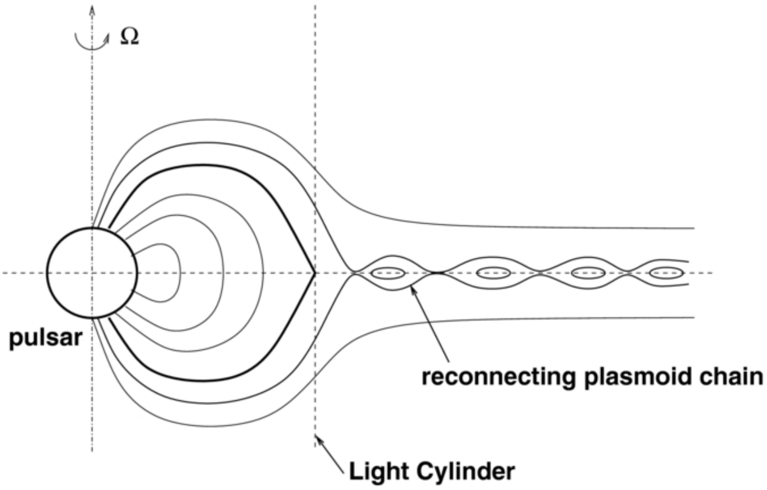

Figure 2.9: A schematic picture of the current sheet (reconnecting plasmoid chain). Additionally, note how the field lines are no longer shown as perfectly dipolar near the light cylinder, reflecting a more detailed knowledge of the magnetic field. Image reproduced from Uzdensky and Spitkovsky [231].

known as the particle formation front (PFF). Arons and Scharlemann [34] looked at this in more detail, finding that the relatively thin region extends all the way to the light cylinder, along the boundary between the open and closed field lines (see Figure 2.8b). Subsequent works [127, 189] further fleshed out this idea.

The last accelerating region is the current sheet [231], which operates on a different principle than the vacuum gap models. Within the light cylinder, we have repeatedly referred to magnetic field lines as being open or closed, where closed field lines remain inside the light cylinder and open field lines pass through it. These lines are able to undergo a process called "magnetic reconnection", where the magnetic field lines rearrange themselves into more stable configurations, and in the process release large amounts of energy that can be used to drive particle acceleration [13].

### 2.2.2 Radiative Processes

Having some idea of how particles are accelerated to high energies, let us now examine the different ways that they will radiate. The two main categories of emission are synchro-curvature (SC) and inverse Compton (IC). Synchro-curvature is composed

---

[13] Magnetic reconnection is thought to be at least partially responsible for the Earth aurora. Magnetic reconnection events are also quite common on the surface of the sun. Solar magnetic reconnection has been recorded, with the resulting videos making nice real-world examples of the process.

of synchrotron radiation and curvature radiation, while inverse Compton is largely composed of synchrotron self-Compton (SSC) radiation.

Particles traveling in magnetic fields will follow helical paths, with the axis of the helix itself also curving [154]. Curvature radiation occurs when the dominant effect is the curving of the axis, and plays an important role in radio and $\gamma$-ray emissions[14], although as we will see it is still important to the higher energy emission. Synchrotron radiation occurs when the helical cork-screwing motion dominates. In pulsars, synchrotron radiation is particularly strong if the particle has a large initial velocity component tangential to the magnetic field (that will rapidly decrease as radiation is emitted), or if it acquires a large tangential component through the absorption of radio photons [175]. Synchro-curvature (SC) radiation, as the name suggests, exists where the full curving and corkscrewing motion must be accounted for [65].

The last, basic, interaction involved in pulsar emission is inverse Compton (IC) scattering. Compton scattering describes the scenario where a photon hits a charged particle and imparts it with some kinetic energy. Inverse Compton scattering is the opposite process[15] — a charged particle hits a photon, upscattering the photon to higher energies.

The above radiative processes have a tendency to intermix, producing Synchrotron self-Compton (SSC) radiation. In this process, a group of particles first emit synchrotron photons, which then undergo inverse Compton scattering by the same group of particles from which they originated, boosting them to higher energies [103].

---

[14] The problem of a pulsar's radio spectrum is interesting in and of itself. Using a pulsar's radio emission to calculate the temperature at which a black body would reproduce the observed spectrum produces a value much too large to be considered physical. However, this can be explained by the pulsar's radio emission being *coherent*, which is an important constraint that must be accounted for by the radio emission mechanism [50].

[15] Physically speaking, the processes differ only by a choice of reference frame.

## 2.3 Connecting Theory to Experiment

With so many theories of pulsar emission available, how is one to determine which are ultimately responsible for what we observe? In some cases, the differences are stark enough to make direct comparisons between the emission model and observations.

One historical example of such predictions, particularly in relation to the energy range covered by *Fermi*-LAT, was presented by Harding [120]. Of interest in this paper were the differing predictions of the polar cap and outer gap models in regards to the pulsar spectral shape and the Geminga-fraction, or the number of pulsars seen in *gamma*-rays but not radio [124]. The polar cap models predicted a sharper, super-exponential energy cutoff in the GeV range than the outer gap models, which predicted a shallower exponential cutoff [250, 64]. When assessing the Geminga-fraction, emission mechanism geometry begins to play an important role. As the radio emission is believed to originate primarily from the polar cap, $\gamma$-ray emission, which also originates from the polar cap, would predict a large overlap in the populations of $\gamma$-ray and radio pulsars [110]. In contrast, outer gap emission would originate from a different region of the pulsar, introducing both a phase offset in the pulse profile of each band, and predicting less overlap in the number of $\gamma$-ray and radio pulsars [250].

The claims presented in Harding [120] were reviewed 13 years later by Harding [119], after *Fermi*-LAT had collected a significant amount of data. In the case of particularly bright pulsars, some aspects of the emission mechanism were able to be answered quite satisfactorily. Vela [7], the Crab [9], and Geminga [9] all had their spectral indices measured (i.e. to determine whether their high energy cutoff was exponential or super exponential) with enough precision to exclude the polar cap as a region of high energy emission. Vela and the Crab were later studied with imaging atmospheric Cerenkov telescopes, and shown to emit pulsed radiation up to TeV energies [80, 31]. This result was somewhat unexpected, with attempts to adequately explain the observations lending support to the current-sheet model of emission[16][130].

---

[16] The discussion in Harding et al. [130] is an interesting example of how models of pulsar emission

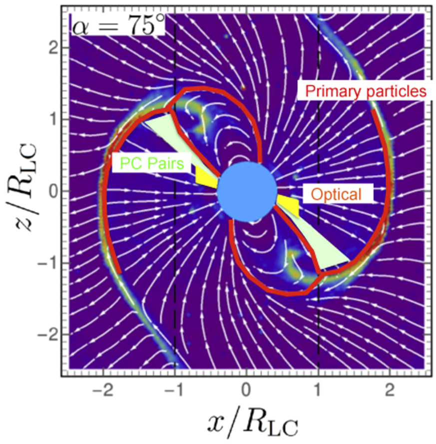

Figure 2.10: A schematic of a pulsar simulation by Harding et al. [130]. Image reproduced from Harding et al. [130].

Millisecond pulsars deserve a brief mention at this point. Their high energy emission can be constrained not by looking at a particular spectral feature, but by examining the shape of the pulsar light curve [240, 232]. This led to the conclusion that the polar cap was not the accelerating region for millisecond pulsars [119]. I do not perform any such light curve modeling in this thesis. However, this result is convenient in that it suggests the same code used to model young pulsars can also be used to model recycled pulsars, as the polar cap can be largely omitted for both.

### 2.3.1 Pulsar Modeling

In this thesis, we collaborated with Alice Harding and Diego Torres to use the computational models presented in their respective works. The Harding model is described in depth in Harding and Kalapotharakos [125] and Harding et al. [130]. The pulsar magnetosphere is simulated assuming a force free magnetosphere, with field distributions informed by prior work[17], and from the perspective of a non-rotating outside observer. Particles are injected by the simulation at the polar cap (both originating from the surface of the pulsar, and through the pair creation process which we previ-

---

evolve with time. Prior to the TeV detection of these pulsars, existing gap models of emission mechanisms offered a sufficient explanation. Even after the discovery, the gap models still technically *worked* [204]. However, they required particles to be accelerated to 10 TeV within the magnetosphere to emit the required curvature radiation, which is on the edge of what is thought to be possible [121]. The current sheet model, emitting synchrotron radiation, is able to produce the same results with electrons accelerated to only 0.1 TeV, which makes the current sheet a more plausible explanation.

[17] See Chapter 2 of Harding and Kalapotharakos [125] for an extensive list of papers.

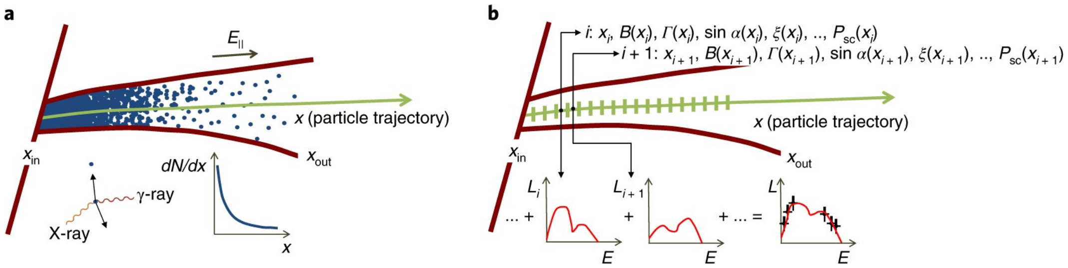

Figure 2.11: An illustrative example of the synchrocurvature model used by Torres [226]. a) shows particles as blue dots being accelerated by $E_{||}$. b) demonstrates how the simulation software tracks the particles at discrete points along their path. The final spectrum is the sum of the individual spectra. Image reproduced from Torres [226].

ously discussed as limiting the height of the polar cap accelerating region), with the computer numerically tracing their path through the magnetosphere. The number of particles to inject, where to inject them, that they only accelerate in the slot gap and current sheet, and their pitch angle (the angle between the particle and magnetic field line, related to synchrotron radiation) are assumed, and informed by prior theoretical work. The magnetic inclination angle, viewing angle, period, and period derivative are also hard-coded into the simulation, although on a pulsar-by-pulsar basis. As particles travel, their synchro-curvature and inverse Compton (including synchrotron self Compton) radiation is also calculated. This simulation extends from the neutron star surface to a distance of twice the light cylinder radius, which includes a current sheet. Although the observational data points and theoretical predictions appear on the same plot, it isn't fair to say that the models are fit to the data points (although in Harding and Kalapotharakos [125], two different values for the multiplicity of particle pairs are used). Rather, the model is compared to the data points by the reader, who can then infer if the model appears to well represent the data, and if so which components (the type of radiation released, and where the particles originated from) contribute to which energy regions of the observed spectrum.

The Torres model is described in Torres [226] and Torres et al. [227]. In essence, some accelerating region is assumed to exist between 0.5 $R_{lc}$ and $1.5R_{lc}$ (a slot gap or outer gap, without drawing distinction between the two). This region is populated with particles, which have their synchrocurvature radiation tracked as they leave the system. The description of the broadband X-ray and $\gamma$-ray emission can ultimately be distilled to just four parameters: the accelerating electric field ($E_{\parallel}$), contrast ($R_{lc}/x_0$), magnetic gradient ($b$) and normalization ($N_0$). $E_{\parallel}$ is the same as elsewhere in this section — the accelerating electric field that gets the charged particles to high energies. $R_{lc}/x_0$ describes the distribution of particles in the line of sight of the observer. $b$ models the changing strength of the magnetic field as a function of radius. Finally, $N_0$ doesn't impact the shape of the resulting spectrum at all, but just shifts it up or down in flux (i.e. normalizes the spectrum). This does involve a fit of the model to data.

## 2.4 This Thesis and Physics

Having reviewed the relevant theory, it is worth examining where the work of this thesis fits into the theoretical framework of pulsars. Looking at the state of emission mechanism physics before and after the advent of *Fermi*-LAT, one thing should be clear: in order to make progress towards the understanding of the pulsar emission mechanism, one needs to see pulsars emitting in the relevant wavelengths. When new samples have been found, they can be analyzed through these theoretical frameworks.

This thesis examines two classes of pulsar: the MeV pulsar and the millisecond pulsar. As has been previously discussed, MeV pulsars are likely under represented in the known pulsar population, as we lack instruments sufficiently sensitive in the energy range where the emission is expected to peak. By synergizing with X-ray telescopes and taking advantage of recent (relative to 2016) advantages in *Fermi*-LAT data processing, we hoped to narrow the “MeV” gap in which these pulsars reside.

One millisecond pulsar, PSR J0218+4232, is also presented in this thesis. Observationally, there were aspects of this pulsar which suggested it may be visible with high energy Imaging Atmospheric Cherenkov Telescopes (IACTs). It would be very scientifically interesting if this turned out to be the case, as it would be the first MSP detected at these energies, possibly spurring discoveries similar to those which occurred when Vela was detected with H.E.S.S. [130]. Although this turned out not to be the case, the data we did obtain were still of sufficient quality to examine other features of the underlying emission mechanism.

# Chapter 3

# Instrumentation

The primary instruments used in my analysis are the *Fermi* Large Area Telescope (LAT), and the Neutron Star Interior Composition ExploreR (NICER). The LAT is a survey instrument, providing continual monitoring of the entire sky at $\gamma$-ray energies [41]. NICER is a pointed X-ray telescope purpose-made for studying pulsars [101]. Using these two instruments together is particularly helpful when looking at soft $\gamma$-ray pulsars. Using NICER to characterize the pulsar's spin, this can then be applied to data taken from the LAT to study the source at MeV and GeV energies.

## 3.1 The Large Area Telescope

The concept that would eventually come to realization as the *Fermi* Large Area Telescope (LAT) was first published in 1994 [42]. Then known as the Gamma Large Area Silicon Telescope, GLAST[1], *Fermi*-LAT was envisioned to be a successor to the Energetic Gamma Ray Experiment Telescope (EGRET) instrument on the Compton Gamma Ray Space Observatory (CGRO). As hinted at in the original naming scheme, the utilization of silicon strip particle detectors, instead of a spark chamber, was the key piece of technological innovation responsible for improving upon EGRET. On June 11, 2008, fourteen years after its conception, the completed Fermi telescope was launched into low earth orbit [190, 2].

---

[1] By the time the satellite was completed, it had been renamed to the Gamma-ray Large Area Space Telescope, retaining the "GLAST" acronym. While in orbit, it was renamed once again to the *Fermi* Gamma-ray Space Telescope [191]

Figure 3.1: Engineers inspect the *Fermi* spacecraft. GBM detectors are visible in white on the front facing portion. The LAT is the silver portion on the top of the satellite. The white frame surrounding the satellite is a crane, and not part of the *Fermi* telescope.
Image Credit: NASA/Kim Shiflett

There are two instruments onboard the *Fermi* spacecraft - the Large Area Telescope (LAT) [41] and the Gamma-ray Burst Monitor (GBM) [183]. The instruments are complimentary, with the LAT covering the energy range of 30 MeV to $> 300$ GeV and the GBM covering the energy range of $\sim 8$ keV to $\sim 40$ MeV. The LAT is typically referred to as the primary instrument[2], with the GBM aiding in pointing the LAT towards Gamma Ray Bursts (GRB's), and extending the lower energy limit at which they can be analyzed. This thesis uses only data from the LAT.

The basic operational principles of the LAT are as follows[3]:

1. A $\gamma$-ray converts to an electron-positron pair in a layer of high-$Z$ material
2. The path of the electron-positron pair is tracked, giving directional information about the progenitor $\gamma$-ray
3. The electron-positron pair deposits its energy in the calorimeter, which is used to determine the energy of the progenitor $\gamma$-ray

---

[2] Due to the GBM detection of GW170817, three of the top five most cited *Fermi* papers are from the GBM (with 8716 citations for the GBM vs 3476 citations for the LAT as of July 2022). Updated records can be found at: `fermi.gsfc.nasa.gov/cgi-bin/bibliography_fermi`

[3] Operational principles in regards to $\gamma$-rays. The LAT can detect charged particles, too[10].

(a) The ACD (black), with micrometeorite shield (gold) suspended above. Image Credit: Diane Schuster / NASA

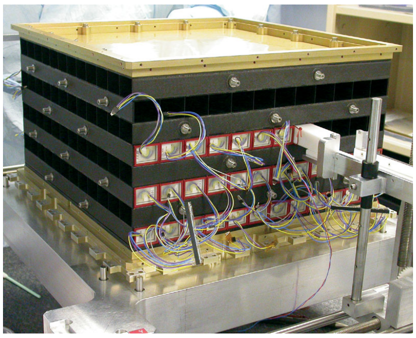

(b) A single calorimeter module under assembly. The perpendicular arrangement of the scintillating crystals is visible. Image Credit: NASA

This operational sequence requires three main components: an anticoincidence detector (ACD) to help distinguish incoming $\gamma$-rays from charged particle backgrounds, a particle tracker containing the high-$Z$ material and the means to discern the path of subsequent charged particles, and a calorimeter to measure the energy of the charged particles after they have been tracked. I describe these individual components in more detail below. Further information can be found in Atwood et al. [41], Ajello et al. [23], and subsequent references within.

### 3.1.1 Anti-coincidence Detector

The ACD is composed of 89 plastic scintillating tiles covering the tracker portion of the LAT. Light from charged particles passing through the tiles is read out by photomultipliers, two per tile. Tiles overlap to ensure full coverage of the tracker. Any remaining gaps are instrumented with scintillating ribbons, which function in much the same way as the tiles.

The segmented nature of the ACD is an important improvement over that of previous $\gamma$-ray instruments. When electron-positron pairs from particularly high energy $\gamma$-rays enter the calorimeter, they can produce showers of particles that scatter *backwards* through the tracker, hitting the ACD. Such a backsplash event causing the data from the incoming $\gamma$-ray to be erroneously discarded is called a self-veto.

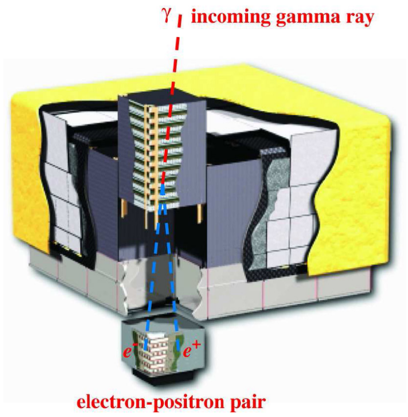

(a) A schematic view of *Fermi*-LAT, including the ACD, tracker modules, and calorimeter. A $\gamma$-ray can be seen converting into an electron-positron pair, which then has its energy measured by the calorimeter. Image reproduced from Atwood et al. [41].

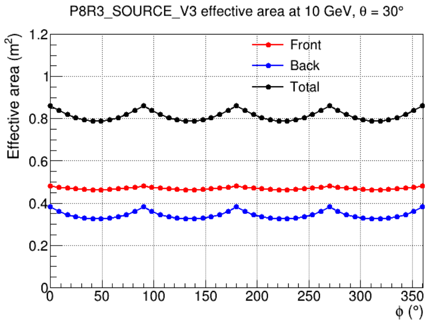

(b) The effective area of *Fermi*-LAT as a function of azimuth angle at 30° off axis incidence. The square shape of the tracker is apparent. Image reproduced from the LAT performance web page [1].

The design goal of the segmented ACD is to limit self-vetos of 300 GeV $\gamma$-rays to 20% by being better able to discriminate backsplash from background (versus 50% at 10 GeV for EGRET[224]).

### 3.1.2 Tracker

The tracking portion of the LAT consists of 16 towers arranged in a $4 \times 4$ grid [43]. Each tower has layers of tungsten interleaved with layers of silicon strip trackers. Tungsten serves as the aforementioned high-$Z$ material that facilitates conversion from $\gamma$-rays to electron positron pairs. The thickness of the tungsten offers a trade-off between effective area and the size of the point spread function (PSF), which characterizes the precision which the direction of an incoming photon can be determined. Thicker layers of tungsten will increase the number of photons converting in the detector, leading to a larger effective area. However, particularly at low energies, the tendency of electrons and positrons to undergo multiple scattering (ricochets within the tungsten) means their path through the detector can't be as precisely reconstructed, leading to the increased point spread function[4]. In this regard, the LAT trackers make a compromise. The first twelve layers of tungsten are thin, with

---

[4] Proposed telescopes focusing on the MeV range remove the tungsten entirely, using multiple layers of silicon strip trackers as converting material instead [74, 182].

a thickness of 0.1 mm (0.03 radiation lengths). The next four layers are 0.72 mm (0.18 radiation lengths) thick. The final two layers of the detector incorporate no tungsten at all.

Accordingly, there are 18 tracking planes per tower - one after each tungsten foil, and an additional two at the bottom. Each tracking plane has two layers of perpendicular silicon strip detectors. Taken together with the vertical position of the silicon, this provides the position of a particle in 3 dimensions.

The geometry of the tracker means that the LAT's field of view is quite large - 2.4 sr, or $\sim 20\%$ of the sky simultaneously. Combined with the LAT's 96.5 minute orbit, this leads to approximately 30 minutes of exposure to any given point on the sky in a 3 hour (two orbit) time period[5].

### 3.1.3 Calorimeter

The final detector component of the *Fermi* telescope is the calorimeter. Each calorimeter module (one per tower) is composed of 96 CsI scintillating crystals. The crystals have two photodiodes on each end (of different sizes and sensitivities), and the relative signal amplitude between each end allows for determination of where along the length of the crystal the energy was deposited. In turn, this allows for 3D imaging of the particle shower. This imaging capability aids in discriminating between $\gamma$-ray photons and charged particles. It is also particularly important in determining the energy of high energy photons, for which the particle shower cannot be fully contained in the calorimeter.

The calorimeter is 8.6 radiation lengths thick, compared to only about 1.1 radiation lengths of tungsten converter foils. There will be photons which bypass the tracker completely, and only interact with the calorimeter. Such events are called "cal only" events, and may be used for analysis if one is willing to sacrifice the benefits to angular resolution and background rejection when an event is recorded in both the tracker and calorimeter [223, 222].

---

[5] `fermi.gsfc.nasa.gov/ssc/data/analysis/documentation/Cicerone/Cicerone_Introduction/mission_overview.html`

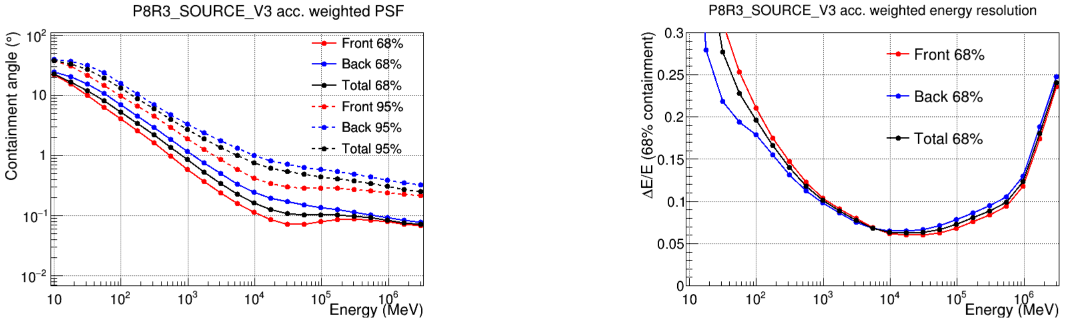

(a) The point spread function of the LAT. At low energies, the PSF is limited by multiple scattering. At high energies, it is limited by the spacing of the tracker's silicon strips.

(b) The energy resolution of the LAT as a function of energy. Low energy photons will deposit much of their energy in the tracker, while high energy photons will produce showers that leak out of the back of the calorimeter.

Figure 3.4: Various measures of the LAT's performance. These plots were reproduced from [1].

### 3.1.4 Performance Metrics

With a basic understanding of the LAT, it is useful to look at some of the telescope's key performance metrics[6]. Figure 3.4a shows the PSF of the LAT. If a point source emits photons with a particular energy, the PSF measures how much the photons will appear to disperse when viewed by the telescope. For example, the plot indicates that 95% of photons emitted by a 100 MeV source will lie within about 10° of that source's true location. At lower energies, the PSF of the LAT is dominated by multiple scattering within the detector [43]. At higher energies, the limiting factor is the spacing of the silicon strips which track the particles.

Figure 3.4b shows the energy resolution of the LAT. As can be seen, this is highly dependent on the energy of the incident photon. At low energies (particularly below 100 MeV), a substantial fraction of the photon's energy may be deposited into the tracker, instead of the calorimeter [39]. At higher energies, portions of the electromagnetic shower will leak out the back of the calorimeter.

As *Fermi* spends more time in space, the understanding of its instruments has improved, particularly in the realms of background rejection and event reconstruc-

---

[6] Updated performance metrics are maintained at: `www.slac.stanford.edu/exp/glast/groups/canda/lat_Performance.htm`

tion. Data processed through a particular reconstruction pipeline is called a *pass*. Enough information is downloaded from that LAT such the new pipelines can be applied retroactively, making it possible to use data from a single pass for all data in an analysis.

The most recent version is Pass 8, Release 3, Version 3, which is reflected in the naming schema in the titles of Figures 3.4 and 3.3b [39]. The LAT also provides users with a number of photon classifications, which may be relevant to different analysis goals[7]. "SOURCE" is one such class, which is optimized for point source analysis. Other common event classes are "ULTRACLEANVETO" and "TRANSIENT". These classes have differing background rates, which is a measure of how well charged particle events can be distinguished from photon events. GRBs are both incredibly bright and short (versus, say, a constant point source), so letting in more false positives in exchange for more photons works out favorably. This is the trade-off made in the "TRANSIENT" class. In contrast, modeling an extended source that has been visible for the entirety of the LAT mission is a task that is more sensitive to the cosmic ray background. For this, the "ULTRACLEANVETO" class may be used, which provides the best background rejection of all photon classes.

Also present in the performance plots are the "Front" and "Back" event types. In this case, "Front" describes photons which pair convert in the top, thinner layers of tungsten, while "Back" refers to photons converting in the thicker layers. All photons are also ranked relative to each other in regards to how well their position and energy can be reconstructed. These rankings make up the PSF and EDISP event types, with subcategories of each type containing 25% of the photons.

### 3.1.5 Time Resolution

Of particular interest to pulsar science with the LAT is the time resolution of the instrument, 10 $\mu$s or better. To achieve this, the LAT uses a combination of GPS satellites and a 20 MHz internal clock. From the GPS satellites, the LAT generates a one pulse per second (PPS) signal which informs the integer portion of event

---

[7] `fermi.gsfc.nasa.gov/ssc/data/analysis/documentation/Cicerone/Cicerone_Data/LAT_DP.html`

timestamps. The 20 MHz internal clock is used to determine the fractional portion of the timestamps. This internal clock was extensively characterized on the ground, and is also continually calibrated via comparison to the PPS signals. In the event that *Fermi* does not detect enough GPS satellites to take advantage of their signal, the internal clock is used for the duration of the outage. When a GPS connection is reestablished, the internal clock is checked to ensure drift was not large enough affect scientific operations.

Pulsars, being highly periodic sources, can be used as an independent check on the accuracy of LAT timestamps. Such tests have been done, using millisecond pulsars to check the clock's stability and the Crab pulsar to check its absolute accuracy [216, 23].

To check stability, six millisecond pulsars having narrow, bright $\gamma$-ray pulse profiles and good radio timing were selected. The 10 year dataset was broken down into 1 and 0.25 year chunks, with the timing of the incoming photons compared to that which was predicted by the radio timing solution. As a well timed millisecond pulsar behaves as regularly as an atomic clock, measuring these residuals can provide a measure of clock drift. Directly comparing the $\gamma$-ray and radio pulse profiles can also give some idea about the absolute accuracy of the clock. However, underpinning this assumption is the notion that these two emission components originate from the same location on the star. Better determining the emission mechanism of millisecond pulsars would thus aid this type of measurement.

To test the absolute timing of the LAT, the Crab pulsar is used. Like with the millisecond pulsars, radio telescopes are used to generate a timing solution. The absolute phase shift between the radio and $\gamma$-ray pulse profiles is unknown, for reasons mentioned in the prior paragraph. However, regardless of emission mechanism, it is believed that this phase shift should remain constant in time. When higher derivatives of a pulsar's frequency are taken into account, an absolute timing offset between the LAT and radio telescopes would present as a drift in phase offset over time. Succinctly, the phase of a photon can be assigned as:

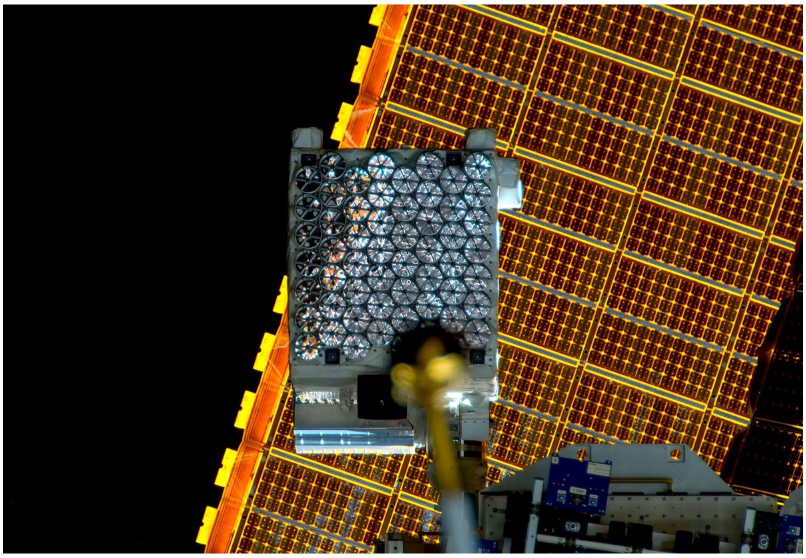

Figure 3.5: The NICER telescope pictured on the ISS, with solar panel in the background. The arrangement of the 56 X-ray concentrators is clearly visible.

$$\phi = fT + \frac{1}{2}\dot{f}T^2 \tag{3.1}$$

Where $f$ and $\dot{f}$ are the pulsar frequency and frequency derivative, and $T$ is the measured photon time. If there is some error in $T$ between the two instruments, say $T \to T + \epsilon$, then there will be a portion of the phase difference which grows as $\dot{f}T\epsilon$. This test, and the millisecond pulsar test, confirmed the LAT's stated $< 10\,\mu$s precision.

## 3.2 The Neutron Star Interior Composition Explorer

The Neutron Star Interior Composition ExploreR (NICER) was launched to the international space station (ISS) on June 3, 2017 [99]. It is not a stand-alone satellite, and is instead mounted on a robotic arm attached to the station [101]. NICER's main science goals include improving measurements pertaining to the neutron star equation of state, demonstrating that pulsars can be used for navigational purposes, and testing X-ray communication devices.

NICER is an X-ray telescope covering the energy range of 0.25-12 KeV. Grazing-incidence optics concentrate X-rays onto silicon drift detectors, which determine the time and energy of the incident photon. There are 56 such detectors on the telescope, each with 24 nested conical shells to focus X-rays onto them. With grazing incidence optics, two reflections (sometimes called "bounces") are needed to form an image [213, 245]. However, NICER is a single bounce, and thus non-imaging, telescope. By looking at "on" and "off" phases of pulsars, NICER can extract background subtracted spectra without needing to image the source. Efficiency also decreases with each bounce, as a fraction of X-rays will not be properly reflected. Compared to XMM-Newton, which is a double-bounce imaging X-ray telescope with a similar energy range, NICER is able to achive an over 2x improvement in maximum effective area [101]. Finally, double-bounce optics require either two mirrors, or one mirror with a complex geometry (when compared to NICER's simple conic shape). Choosing single-bounce optics helped to keep the cost of NICER down.

The X-ray detectors themselves are silicon drift detectors (SDD's) [102]. When an X-ray hits an SDD, it produces a cloud of electrons proportional to the incident X-ray's energy [147]. This cloud travels to the detector's anode for measurement.

NICER's SDDs are off-the-shelf Amptek FastSDDs[8] [102]. While this is a 25 mm$^2$ detector, NICER's optics use a collimator such that only a 2 mm diameter is exposed to the mirrors. As the distance the electron cloud travels is more predictable, timing can be guaranteed to better than 300 ns [9]. Similarly to the LAT, NICER achieves this timing resolution with a combination of GPS and an internal oscillator[10]. Background events, such as stray $\gamma$-rays and charged particles, penetrating the collimator and striking areas outside the central region can be identified and rejected in the analysis stage.

---

[8] Amptek even includes a picture of NICER on their product page!

[9] `heasarc.gsfc.nasa.gov/docs/nicer/mission_guide/`

[10] There was an interesting timing error which occurred for a couple of weeks in July 2019, and was directly related to this fact. When recording data, the GPS and oscillator time stamps are stored separately. During these two weeks, time stamps from the oscillator were scrambled, while the GPS portion remained unaffected. This led to data which was only accurate to about 1.3 seconds, the rate of the GPS time stamping. `heasarc.gsfc.nasa.gov/docs/nicer/data_analysis/nicer_analysis_tips.html`

# Chapter 4

# Analysis Techniques

## 4.1 *Fermi*-LAT Analysis

### 4.1.1 Binned Likelihood Analysis - Statistics

*Fermi*-LAT data are analyzed via maximum likelihood techniques, where a hypothetical model populated with astrophysical sources and backgrounds is compared to observational data collected by the instrument. By use of a maximum likelihood estimator, the model is refined until it matches (to a sufficient degree) the observational data. Parameters from the model are then taken to be representative of the underlying sources, and used for further study. The *log-likelihood function* is the goodness-of-fit test used to quantify how well a model matches the data.

Maximum likelihood techniques are a necessity for *Fermi*-LAT, which in most circumstances[1] lacks sufficient angular resolution to make use of aperture photometry . In aperture photometry the user selects a source region containing the target of interest and a background region which ideally contains only diffuse background emission. Subtracting the background region flux from the source region flux leaves the spectrum of the target of interest. This technique is typically used to analyze data from X-ray telescopes, which have angular resolutions of several arcseconds

---

[1] Aperture photometry is occasionally used to generate *Fermi*-LAT light curves.The benefits of doing this are reduced computational complexity and model independence.

(e.g. NuSTAR[2], XMM-Newton[3]) or better (e.g. Chandra[4]). In contrast, the point spread function (PSF) of *Fermi*-LAT is on the order of degrees (see Ch. 3.1 for a more detailed discussion of PSF). This comparatively low angular resolution makes it exceedingly difficult, if not impossible, to select source and background regions which are not contaminated by photons from other astrophysical sources. Such an analysis may only be possible for GeV sources (an energy band where the *Fermi*-LAT's PSF is smaller) far from the galactic plane, where sources are comparably spread out.

The likelihood maximization may be performed photon-by-photon in an *unbinned* analysis, or the photons may first be grouped into spatial and energy bins in a *binned* analysis. An unbinned analysis is more precise, but requires prohibitively large computational resources when looking at large Regions of Interest (RoI's), long time periods, or a combination of both. The studies comprising this work utilize only binned analyses, which are expounded upon below. Unbinned analyses follow similar procedures, but are not covered in my thesis. In a broad sense, an unbinned analysis is a binned analysis where the bin size is the native digitization of the instrument.

Within each bin of the analysis, the data are represented as a single number: the number of detected photons. The number of photons expected in each bin is described by a Poisson Distribution:

$$P(k) = \frac{\lambda^k e^{-\lambda}}{k!} \tag{4.1}$$

where $\lambda$ is the number of photons predicted by a model of the region and $P(k)$ is the Poisson probability that $k$ photons are detected given $\lambda$. Maximizing the likelihood is thus the task of varying the model such that the product of all $P(k)$ is maximized when $k$ is set to the number of detected photons in each bin:

---

[2] `https://heasarc.gsfc.nasa.gov/docs/nustar/nustar_obsguide.pdf`

[3] `https://www.cosmos.esa.int/web/xmm-newton/technical-details-epic`

[4] `https://cxc.harvard.edu/proposer/POG/html/chap4.html#tth_chAp4`

$$L = \prod_i P_i(k_i) = \prod_i \frac{\lambda_i^{k_i} e^{-\lambda_i}}{k_i!} \tag{4.2}$$

Noting

$$\prod_i e^{-\lambda_i} = e^{-\sum_i \lambda_i} \tag{4.3}$$

and that $\sum_i \lambda_i \equiv \lambda_{tot}$ is simply the overall number photons predicted in the entire RoI, Eqn. 4.2 becomes

$$L = e^{-\lambda_{tot}} \prod_i \frac{\lambda_i^{k_i}}{k_i!} \tag{4.4}$$

This is *Fermi*-LAT's "binned Likelihood function", and is the figure of merit maximized when the model is fit to data.

During the analysis of an RoI, a common task is to determine the significance with which a source is detected. An application of Wilks' Theorem to the likelihood function provides a ready answer to this question in the form of the "Test Statistic", or TS. Wilks' Theorem [242] states that the TS, as defined in Eq. 4.5, approaches a $\chi^2$ distribution as the number of data points (in this case, detected photons) tends to infinity[5]. Letting $L_0$ be the likelihood of a model without the source of interest (the null hypothesis, as required by Wilks's Theorem), and $L_1$ be the likelihood of a model with the source of interest, the TS is defined as:

$$TS = -2 \ln \left( L_0 / L_1 \right) \tag{4.5}$$

with the useful *approximation*

$$\sigma \approx \sqrt{\mathrm{TS}} \tag{4.6}$$

Here $\sigma$ represents the number of standard deviations above the mean background noise at which a signal lies, assuming that the background follows a normal distribu-

---

[5] See Appendix A.1 for important discussion and caveats surrounding this application of Wilks' Theorem.

tion. $\sigma$ is a standardized method of quantifying how likely an event is to be "real" as opposed to being caused by chance fluctuations. Further discussion on Wilks' Theorem, TS, and $\sigma$ (and an analysis of Eqn. 4.6)is presented in Appendix A.1.

### 4.1.2 LAT Data Selection

By nature of its large field of view (nearly 20% of the sky) and state of near continuous operation, *Fermi*-LAT acquires more data than is needed for most analyses. Relevant photons are intermixed with those of no interest due to, for example, originating from the Earth's limb or an area of sky away from our source of interest. From a list of all photons observed by the LAT, the first task is selecting only those relevant to our analysis.

At a basic level, photons are selected which lie within a particular radius of a point of the sky, and which fall within a particular time and energy range. A maximum Earth zenith angle must be specified to exclude background radiation from the Earth's limb, which, due to its proximity, is the brightest source in $\gamma$-rays[6] that *Fermi*-LAT observes [17].

A particular *event class* of photons must be selected for inclusion in the analysis. As described in Sec. 3.1, each photon has unique uncertainties in position and energy. When studying a transient event, such as a GRB, greater uncertainties are an acceptable trade-off for an increased number of photons. Conversely, the study of large diffuse sources is particularly sensitive to background events, and thus precisely characterized photons are preferable. The recommended event class for use in different analysis scenarios can be found on the Fermi Science Support Center (FSSC) web page[7]. This work uses "SOURCE" class photons, which are recommended for analyzing point sources (e.g. pulsars).

Each event class is further subdivided into *event type*: PSF quartile, EDISP quartile, and FRONT/BACK. PSF and EDISP event types divide the photons into quartiles based on the uncertainty of position and energy reconstruction, respec-

---

[6] Originating from cosmic-rays interacting with the atmosphere.

[7] `https://fermi.gsfc.nasa.gov/ssc/data/analysis/documentation/Cicerone/Cicerone_Data/LAT_DP.html`

| Energies | Energy Bins | Width | Zmax | Pixel Size (deg) | | | | |
|---|---|---|---|---|---|---|---|---|
| (GeV) | | (deg) | (deg) | PSF0 | PSF1 | PSF2 | PSF3 | All |
| 0.05 - 0.1 | 3 | 7 | 80 | ... | ... | ... | 0.6 | ... |
| 0.1 - 0.3 | 5 | 7 | 90 | ... | ... | 0.6 | 0.6 | ... |
| 0.3 - 1 | 6 | 5 | 100 | ... | 0.4 | 0.3 | 0.2 | ... |
| 1 - 3 | 5 | 4 | 105 | 0.4 | 0.15 | 0.1 | 0.1 | ... |
| 3 - 10 | 6 | 3 | 105 | 0.25 | 0.1 | 0.05 | 0.04 | ... |
| 10 - 1000 | 10 | 2 | 105 | ... | ... | ... | ... | 0.04 |

Table 4.1: Specifics of the data selection used in the creation of the the Fermi Large Area Telescope Fourth Source Catalog (4FGL) [13]. “Width” refers to “ring width” which is added to a “core width” of varying size to form the overall RoI components.

tively. FRONT and BACK event types classify photons based on whether pair-conversion occurred in the thin conversion foils at the FRONT of the tracker, or the thicker foils at the BACK. For further discussion of this aspect of *Fermi*-LAT, see Sec. 3.1. Whereas an event class must always be specified, an event type selection is not necessary.

Particular recommendations for event class and zenith angle can be found on the FSSC web site[8]. Energy range should be chosen on an analysis-by-analysis basis. RoI size will also vary, but can be informed by the size of the PSF at the energies which the analysis covers.

A more systematic option for point source analysis is to use the selections of the Fermi Large Area Telescope Fourth Source Catalog (4FGL) (note that there are multiple versions of this catalog, and I have listed the selections of the first version) [13]. Each source in the 4FGL is associated with a “core” of a unique width surrounded by a “ring” of standardized width. The total associated RoI is made up of 15 components, each entailing a particular selection of PSF class, energy range, and zenith angle. These selection criteria are described in Table 4.1, and are grounded in the behavior of *Fermi*-LAT’s PSF. As higher energies correspond to a more accurate determination of photon position, it is acceptable to use a smaller RoI and less stringent zenith angle cut at high energies.

Different *passes* of *Fermi*-LAT data also exist, although this grouping is of a wholly different variety than the others mentioned in this section. Event reconstruc-

---

[8] `https://fermi.gsfc.nasa.gov/ssc/data/analysis/documentation/Cicerone/Cicerone_Data/LAT_DP.html`

tion, described with greater detail in Chapter 3.1, is the process by which electrical signals in *Fermi*-LAT are converted into a list of photons. Occasionally, such as when a better characterization of *Fermi*-LAT becomes available, changes are made to the event reconstruction pipeline which broadly improve the quality of data [18, 39, 58]. The "pass" of *Fermi*-LAT data thus refers to the particular event reconstruction pipeline which was used to create it. Old events are "reprocessed" for inclusion in the latest data pass, which is also appended to as *Fermi*-LAT acquires more data. The user should default to the most recent data version, which at the time of writing is Pass 8, Version 3 (i.e. `P8_SOURCE_V3`, for Pass 8, Version 3, SOURCE class photons). Likewise, the work presented in this thesis use Pass 8, Version 3 data.

After photons are selected, they should be filtered to remove times when *Fermi*-LAT is either not in normal science configuration, or not taking good data. The status of *Fermi*-LAT is recorded in the "spacecraft file", which should be downloaded alongside the photon data files.

In my analyses, I use the most recent version of SOURCE class photons currently available. If I am interested in the low energy spectrum of a source, I will use a lower energy limit of 50 MeV. Otherwise, beginning an analysis at 100 MeV is preferable, as I do not have to account for energy dispersion (see Section 4.1.6).

### 4.1.3 Binning

The defining characteristic of a *binned* analysis is that photons are placed into discrete spatial and energy bins, which considerably decreases the computational resources needed to perform an analysis. The FSSC generally recommends using 10 logarithmically spaced energy bins per decade of energy and spatial bins of $0.2^\circ \times 0.2^\circ$[9]. Alternatively, the 4FGL is a good reference for binning, as described in Table 4.1.

---

[9] `https://fermi.gsfc.nasa.gov/ssc/data/analysis/scitools/binned_likelihood_tutorial.html`

### 4.1.4 Livetime and Exposure

Due to the geometry of *Fermi*-LAT, its field of view is not exposed uniformly. Information regarding *Fermi*-LAT's sensitivity across its field of view and energy range is stored in the Instrument Response Functions (IRFs). The first step towards the calculation of exposure is to generate a "livetime cube", which contains information regarding how long each region of the sky spends at a particular inclination relative to *Fermi*-LAT. With this information, it is possible to integrate the instrument response function over the RoI, producing an exposure map. This exposure map, when combined with information regarding the intensity of a particular source, can be used to predict the number of counts that said source would produce.

### 4.1.5 Generation of a Model

A model must now be initialized for the purpose of being fit to the data. This is typically done by querying a catalog of sources produced by the *Fermi*-LAT collaboration, with the most recent version of such a catalog being the fourth *Fermi*-LAT catalog of $\gamma$-ray sources, data release three (4FGL-DR3) [13, 67], which covers 12 years of *Fermi*-LAT data. Prior to the 4FGL, catalogs were released covering four years (3FGL, [16]), two years (2FGL, [194]), eleven months (1FGL, [8]), and three months (0FGL, [12]) of data. In contrast, the 4FGL has had incremental releases every two years [45, 67], with the first version covering eight years of data [13]. Incremental releases may include improvements beyond covering additional *Fermi*-LAT data. For example, changes were made to the way pulsar spectra were modeled, which decreased the covariance between spectral parameters. This change greatly benefited the work presented in this thesis by increasing the ease at which convergence could be achieved when fitting a model to *Fermi*-LAT data.

When creating a model, care should be taken to include sources outside the RoI, as due to the PSF of *Fermi*-LAT, they may still contribute significantly to the photons within the RoI. Adding sources from an additional 10 degrees outside the RoI is a typical starting point[10]. After a model is initialized, an intermediate data

---

[10] `https://fermi.gsfc.nasa.gov/ssc/data/analysis/scitools/binned_likelihood_`

product called the "source map" may be computed. A source map is the combination of spectral (and possibly spatial, if the source is not modeled as a delta function) information from the model, the exposure map, and the PSF of *Fermi*-LAT. This step *is* necessary for a binned analysis, but will be performed on the fly by the tools handling the likelihood analysis if not pre-computed. However, pre-calculating and storing these quantities will decrease the time needed to perform subsequent likelihood analyses.

### 4.1.6 Energy Dispersion

*Fermi*-LAT has finite energy resolution, of ≈ 20% at 100 MeV and ≈ 5% at 10 GeV[11] (see Sec. 3.1 for further discussion on the performance of *Fermi*-LAT)[18]. This effect is termed "energy dispersion", and is a source of systematic errors if left unaccounted for. These errors are particularly important to consider when working at energies below 100 MeV[12]. Energy dispersion can be accounted for via the "Detector Response Matrix", or "DRM". For example, if $P^{E_i}$ is the number of photons in energy bin $E_i$, the DRM may indicate:

$$P^{E_i}_{actual} = 0.1 \times P^{E_{i-1}}_{measured} + 0.8 \times P^{E_i}_{measured} + 0.1 \times P^{E_{i+1}}_{measured} \tag{4.7}$$

The energy dispersion correction is applied to the model described in Sec. 4.1.5 before it is used in the likelihood function. To do so, spatial information is discarded from the model, leaving only a vector, $V_{true}$, which contains the number of photons in each energy bin. $V_{true}$ is then extrapolated to cover energy bins above and below those included in the analysis. Multiplying the DRM with $V_{true}$ produces the vector $V_{measured}$, which is the of number photons *Fermi*-LAT would observe in each energy bin with energy dispersion accounted for. For each energy bin, the ratio $V^{E_i}_{measured}/V^{E_i}_{true}$ is calculated and applied to the model (with spatial bins included) as a simple scaling factor. An illustrative example of an energy dispersion calculation

---

`tutorial.html`

[11] `https://www.slac.stanford.edu/exp/glast/groups/canda/lat_Performance.htm`

[12] `https://fermi.gsfc.nasa.gov/ssc/data/analysis/documentation/Pass8_edisp_usage.html`

is included in Appendix A.2.

### 4.1.7 Performing the Likelihood Analysis - Software

Armed with the above data products, the user has all the information necessary to perform a likelihood analysis. The *Fermi*-LAT collaboration provides tools necessary to perform all of the above calculations. The calculations themselves are performed by the `fermitools`[13]. A Python package called `pyLikelihood`[14] provides a Python based interface to the `fermitools`. An additional Python package called `Fermipy`[15] [247] is in turn built on top of `pyLikelihood`, and provides higher level functionality. The vast majority of *Fermi*-LAT analyses carried out in this work were performed using `Fermipy`. Both the `fermitools` and `Fermipy` are being actively developed, and the work presented in this thesis does not exclusively use a particular version of this software.

### 4.1.8 Evaluating the Likelihood Analysis

Successfully fitting a model to data does not ensure that the model is a good representation of the RoI. There are two main ways that the representation can be evaluated: by looking at the difference between the binned data and model map, and by creation of a TS map. The differencing method is most straightforward. For each pixel of the RoI, the difference between the number of counts in the binned data and the number predicted by the model is found. If desired, additional complications may be incorporated into this method. For example, `Fermipy` will attempt to convert the ratio of model counts to actual counts into a $\sigma$ value and smooth the result[16].

To generate a TS map, a new source (generally a power-law with index 2) is added to, and its normalization fit at, the center of each spatial bin. Its TS at each position is recorded, with the collection of these values composing the TS map. A

---

[13] `https://github.com/fermi-lat/Fermitools-conda/`

[14] `https://github.com/fermi-lat/pyLikelihood`

[15] `https://github.com/fermiPy/fermipy`

[16] There has been debate regarding how this $\sigma$ value should be interpreted. The user should thoroughly familiarize themselves with the latest `Fermipy` documentation and source code if these plots are used.

high TS value may indicate that there are unmodeled sources in that area.

The above methods are presented graphically in Fig. 4.1. The data and model were taken from the analysis presented in Ch. 9. Both techniques were performed with the true model, as well one where the target of interest was removed. The model was not re-fit after the target of interest was removed, so the effect is more exaggerated than what would occur if the target was missing at the beginning of the analysis.

### 4.1.9 Source Spectra

A standard analysis goal is the extraction of a source spectrum, or Spectral Energy Distribution (SED). This is a more involved process than simply stating the best fit spectral parameters garnered from a likelihood analysis.

The *Fermi*-LAT spectrum shown Fig. 4.2 has two main components: an overall spectrum shown as a solid line, and individual spectral points shown as crosses or upper limits. There is one spectral point per energy bin in the analysis. The points are calculated by replacing the spectrum of the source of interest with a simple power law, and then examining only data within a particular energy bin. The standard power-law index for this point source is 2, but it could in principle be any value, such as one which approximates the overall source spectrum in that energy bin. A "miniature" binned analysis is then performed, and the resultant flux of the power law source plotted as a spectral point. The horizontal bars show the energy range over which each flux point was represents. The vertical bars correspond to symmetric $1\sigma$ errors on the flux. Depending on the significance with which the point source is detected in each bin, the user may choose to plot an upper limit instead of a flux point. In `fermipy`, the default significance below which an upper limit is plotted is TS = 4. Upper limits typically represent 95% confidence, as determined by a profile likelihood method[17][203].

The process of examining energy bins independently serves as an important consistency check of the global fit. For example, I frequently found that poorly fit low

---

[17] `https://fermi.gsfc.nasa.gov/ssc/data/analysis/scitools/upper_limits.html`

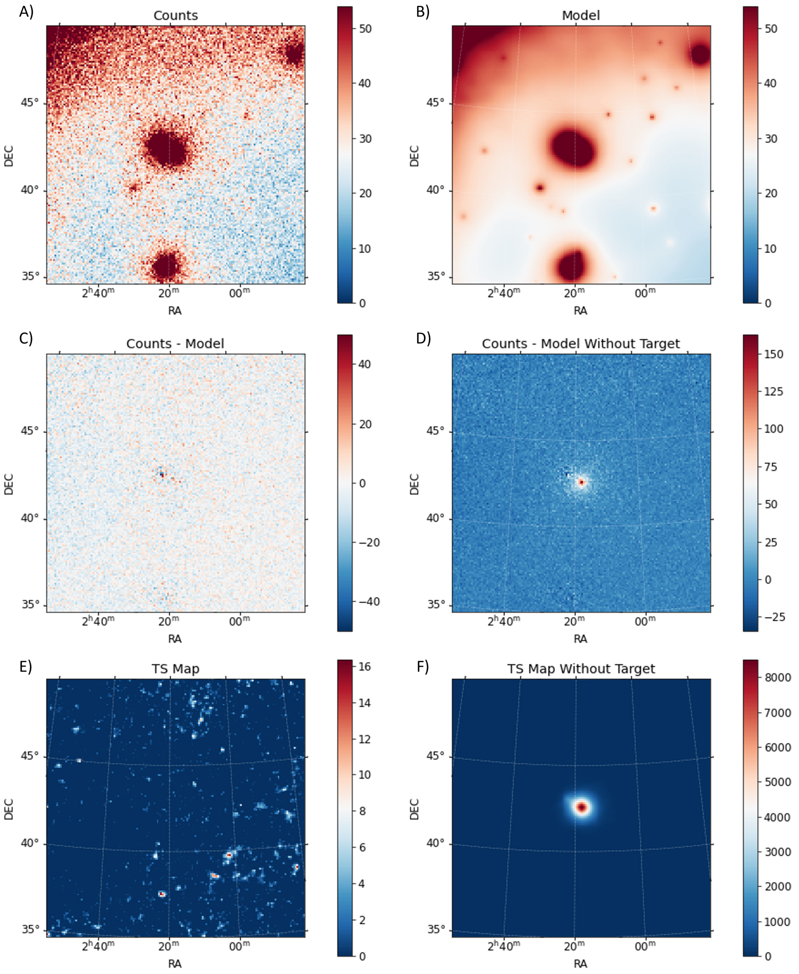

Figure 4.1: Different methods of evaluating the model's fit to data. The data and model used in the creation of this figure are the same as presented in Ch. 9. The model was not re-fit when the target of interest was moved.

- Image A) shows the binned data.
- Image B) shows the model after fitting to the data.
- Image C) shows the difference between the model and data (i.e. the difference between Images A) and B)).
- Image D) shows the difference between the model and data if the target of interest were removed from the model.
- Image E) shows the TS map produced by adding a power-law source at different positions to the model presented in image B), and computing its TS value.
- Image F) shows the TS map produced by adding a power-law source at different positions to the model presented in image B), but without the target of interest, and computing its TS.

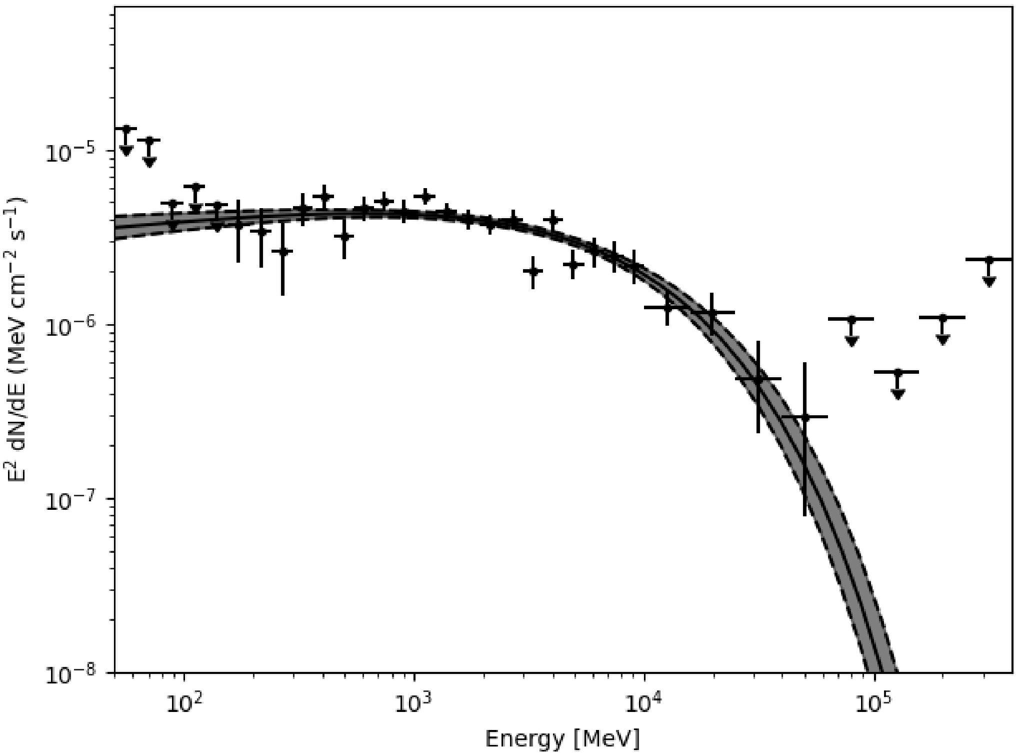

Figure 4.2: A source spectrum extracted from a *Fermi*-LAT analysis.

energy bins would adversely affect my global spectrum. The spectral points may also visually imply a particular choice of model spectrum.

During the creation of this data product, the collection of parameters allowed to vary is often different from those used in the overall likelihood analysis. This is to ensure convergence of the minimizer. As there may typically be 40 energy bins in the analysis, spectral shape parameters for all but the strongest sources (such as the Galactic diffuse emission) often remain fixed, with only the normalizations allowed to vary. Sources with low significance in the global fit lack sufficient statistics to be properly parameterize in this constrained regime, and thus have their normalizations set to remain constant. It is common to allow normalizations to vary based on the distance of the source to the target of interest. While fewer sources may be allowed to vary during the spectral analysis, beginning from a completed likelihood analysis ensures background sources are fixed to reasonable values. For consistency, the spectrum of the target source is re-fit over the entire energy range with the same subset of background sources allowed to vary as is used to produce the spectral points. The result of this fit is presented in the spectral plot as the solid line in Fig. 4.2. The $1\sigma$ uncertainty of the spectral parameters is represented by a shaded region surrounding the solid line, and bounded with dashed lines.

### 4.1.10 Light Curves

Light curves show how the brightness of a source varies over time. To generate a light curve, the overall data set is broken into discrete time bins. Within each time bin, a unique instance of a binned analysis is performed, as described in Sec. 4.1.1. The flux of the target source within each time period is then plotted to form the light curve.

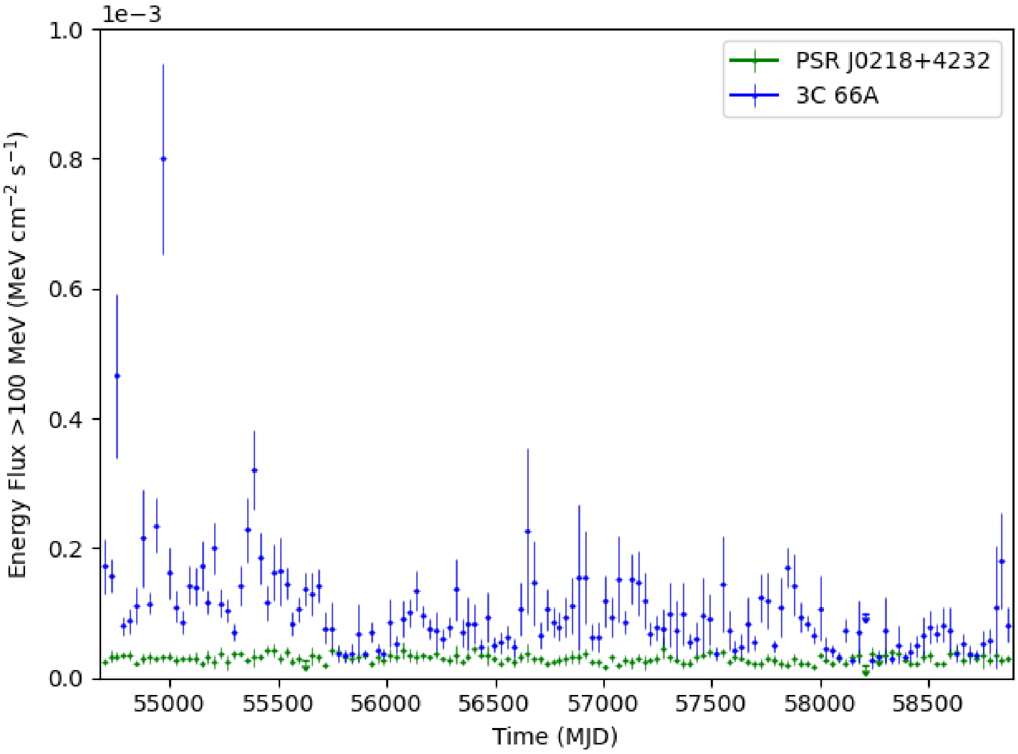

Figure 4.3: A light curve showing flux variability in the pulsar PSR J0218+4232 (green) and the blazar 3C 66A (blue). This is the same data shown in Fig. 9.2 and described in Ch. 9.

As in the creation of source spectra, described in Sec. 4.1.9, the underlying background model is seeded from the overall RoI analysis. Similarly, for purposes of convergence, fewer parameters are allowed to vary as compared to the overall likelihood analysis. If `fermipy` is used, a maximum of five attempts will be made to get the likelihood analysis in each bin to converge. Each subsequent attempt allows progressively fewer sources to vary, as described below:

1. All user specified parameters are allowed to vary.
2. Only user specified normalizaitons are allowed to vary.
3. Sources with TS $< 4$ have their parameters fixed.
4. Sources with TS $< 9$ have their parameters fixed.
5. Sources lying further than 1 deg from the target source have their parameters fixed.

If all of the above attempts fail, a failure is reported for that time bin.

### 4.1.11 Photon Weighting

Kerr [155] showed that, by assigning each photon a weight corresponding to the probability of having originated from a particular source, *Fermi*-LAT's sensitivity to pulsar signals could be improved by $> 50\%$. The underlying mathematics necessary to include photon weights in pulsation tests (such as the H-Test, see Chapter 5.3) were first deduced by Bickel, Kleijn, and Rice [52]. This technique could in principle benefit any instrument with significantly contaminated source photons. With the relatively large PSF of *Fermi*-LAT (particularly at low energies), this method is frequently implemented in *Fermi*-LAT analyses. Once a likelihood analysis has been performed, calculating the probability that a photon originates from a particular source is straightforward.

Let $r_j(E, \vec{\Omega}, \vec{\lambda}_j)$ be the differential photon flux at position $\vec{\Omega}$ from source $j$ with spectral parameters $\vec{\lambda}_j$ (which may be taken from a likelihood analysis) at energy $E$. $r_j$ is a function of the photon flux density of source $j$, *Fermi*-LAT's exposure to that source, and the PSF of *Fermi*-LAT. The flux density is denoted $\mathcal{F}_j(E, \vec{\lambda}_j)$. The exposure of *Fermi*-LAT to a point at $\vec{\Omega_j}$ is denoted by $\epsilon(E, \vec{\Omega_j})$. The point spread function is denoted $f(\vec{\Omega}; \vec{\Omega_j}, E)$. Together, these form the relation:

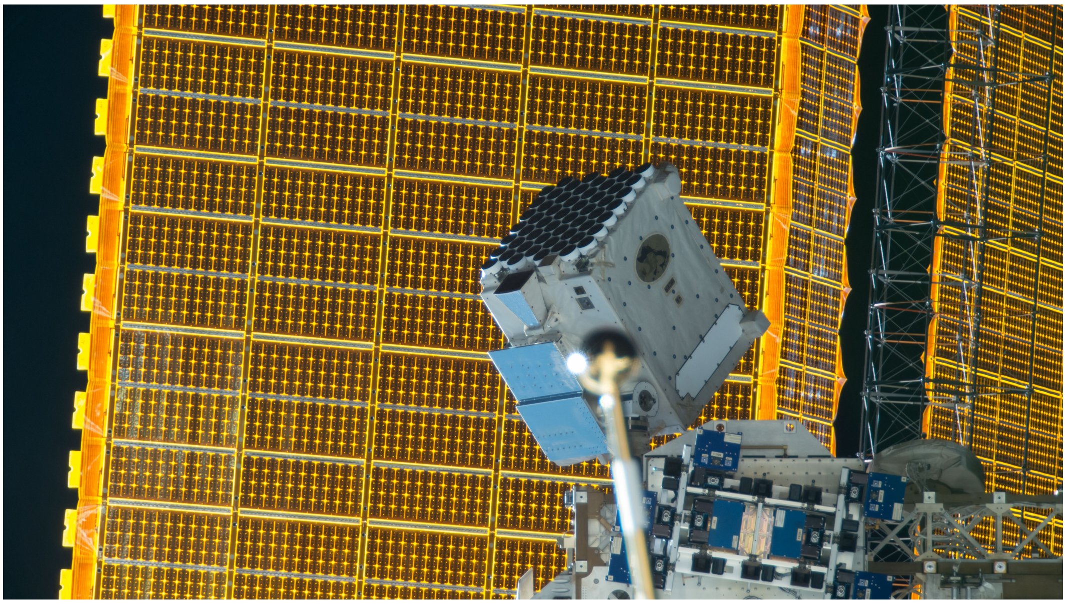

Figure 4.4: NICER aboard the ISS, with a solar panel array in the background [193].

$$r_j(E, \vec{\Omega}, \vec{\lambda}_j) = \mathcal{F}_j(E, \vec{\lambda}_j) \times \epsilon(E, \vec{\Omega}_j) \times f(\vec{\Omega}; \vec{\Omega}_j, E) \tag{4.8}$$

The probability that a photon originates from source $j$, $w_j$, is the fraction of the total photon flux at position $\Omega$ and energy $E$ which comes from source $j$.

$$w_j(E, \vec{\Omega}|\vec{\lambda}_j) \equiv \frac{r_j(E, \vec{\Omega}, \vec{\lambda}_j)}{\sum_i r_i(E, \vec{\Omega}, \vec{\lambda}_i)} \tag{4.9}$$

This calculation is implemented in the `fermitool` ‘gtsrcprob’, which takes list of photons, a spacecraft file, and a RoI model as inputs and returns the resultant photon weights.

## 4.2 NICER Analysis

The process of analyzing data from the Neutron Star Interior Explorer (NICER) bears little similarity to that of analyzing *Fermi*-LAT data. As opposed to being survey instrument, NICER is pointed at a target of interest by the mechanical arm anchoring it to the International Space Station (ISS) [41, 101]. With a field of view of only 30 arcmin$^2$ (about 0.008 deg$^2$), at any given time NICER is viewing an area of the sky about a million times smaller than *Fermi*-LAT’s field of view (about

7880 deg$^2$). Additionally, NICER is composed of X-ray concentrators that focus to a single point and do not produce an image. With an energy range of less than two decades (0.2 - 12 KeV), NICER covers a relatively smaller energy range than *Fermi*-LAT's five-plus decades (20 MeV - >300 GeV)[18].

Consequently, preparing NICER data for analysis is less complex than preparing *Fermi*-LAT data. NICER observations are scheduled[19], and can be downloaded on a source-by-source basis [20]. NICER data files are processed into a usable "Level 2" format by the "nicerl2" tool included in the `HEASoft`[21] software package, managed by NASA. This process is fully automated, and includes:

1. Calibrating the data file.
2. Filtering the data for bad time intervals (such as passage into the South Atlantic Anomaly).
3. Combining data from NICER's 7 detector modules into a single file.

Once the level 2 data are created, a few additional selection criteria are recommended[22]. The minimum energy to include in an analysis is 0.2-0.5 KeV, as below this range data may be contaminated by detector noise. Eight detectors (DET_ID 10 to 17) experienced a timing anomaly from about July 8-23 of 2019, and should be excluded if an analysis is covering this time range. Finally, two detectors (14 and 34) are known to be excessively noisy, and may be excluded.

---

[18] See Chapter 3 for more thorough technical specifications of *Fermi*-LAT and NICER

[19] `https://heasarc.gsfc.nasa.gov/docs/nicer/schedule/nicer_sts_current.html`

[20] `https://heasarc.gsfc.nasa.gov/docs/nicer/nicer_archive.html`

[21] `https://heasarc.gsfc.nasa.gov/docs/software/heasoft/`

[22] `https://heasarc.gsfc.nasa.gov/docs/nicer/data_analysis/nicer_analysis_tips.html`

# Chapter 5

# Periodic Data

This chapter provides an overview of the techniques used to detect and analyze a pulsar's periodic signal, particularly as applies to data sets composed of individual photons. If a pulsar's spin characteristics are not already known (perhaps the source may not yet be identified as a pulsar), a search for prominent frequencies can be carried out through use of the Fourier transform. This technique is used, albeit briefly, in Chapter 6.

I also discuss different significance tests used to determine if such a signal came from a truly time-variable source, or arose due to chance. Of these tests, the H-Test occurs most often in this thesis, and is mentioned in all of the chapters analyzing specific pulsars. Differences between the H-Test and the $\mathrm{Z}_1^2$-Test are particularly important in regards to Chapter 7, where the choice of test makes a notable impact on the interpretation of the pulsar's significance.

## 5.1 Necessary Corrections

When studying pulsars, one of the most basic tasks for the user is to convert the arrival time of a photon to a corresponding pulsar phase. This process requires two steps: a time correction, and a conversion of the corrected times into phases[172]. The software suites typically used to perform these corrections are `Tempo2`[145] and `PINT`[173, 172]. The file containing information about the pulsar needed to perform these calculations is colloquially referred to as a "par-file" (with ".par" file extension) and the data itself a “timing solution”.

### 5.1.1 Time Corrections

Pulsar timing is typically carried out in Barycentric Dynamical Time (TDB). TDB is the time as measured in a theoretical general-relativistic frame located at our solar system’s barycenter in the absence of solar and planetary gravity wells[1]. When pulsar scientists refer to “barycentered data” there is an additional implication that they are referring to the time at which a *photon emitted by the pulsar* would have arrived at the solar system barycenter. This is an important distinction, as it requires knowledge of the position of the pulsar, whereas simply converting a spacecraft timestamp to TDB would not. For example, Roemer Delay accounts for the difference in an arrival time of a photon based on where the earth is in its orbit relative to the position of the pulsar, something barycentering a spacecraft time stamp would not require[86]. Practically, preparing barycentered data in this manner greatly simplifies the work of analysis tools. A data file containing the position of one satellite mission may be substantially different from those containing the position of a different satellite mission. This way, each team may make their own tools for barycentering data, and then this barycenterd data may be fed into common analysis tools to examine the pulsar characteristics.

Overall, the simplest way to think of these time corrections is that scientists seek the time at which a photon was emitted from the position of the pulsar/pulsar system’s barycenter in the absence of any gravity wells from said system. Practically, this involves a plethora of general relativistic corrections requiring information regarding both our own solar system and the system in which the pulsar resides. Practical implementations of these corrections strive for an accuracy of 1 ns, with this precision motivated by the desire to use pulsars as clocks to search for certain types of gravitational waves [150, 86]. Two independent realizations of this goal are the `Tempo2` and `PINT` software packages. The respective papers for these packages more fully detail the individual corrections included in pulsar analysis [145,

---

[1] IAU 1996 Recommendation 3, IAU 2006 Resolution 3

173, 172]. I primarily use `PINT` in this thesis, with further details provided in the applicable chapters.

### 5.1.2 Phase Calculation

Once the data have been time corrected, photon times may be assigned to a particular rotational phase of the pulsar. The most common way of doing this is by a Taylor series expansion:

$$\theta_i(t_i) = \theta_0 + f t_i + \frac{1}{2}\dot{f} t_i^2 + \frac{1}{6}\ddot{f} t_i^3 + \cdots \tag{5.1}$$

where $t$ represents the corrected times, and $f$, $\dot{f}$, and $\ddot{f}$ represent the pulsar frequency and its derivatives. Typically, the fractional portion of the photon phase is of most interest. This also has the benefit of allowing for additional features to be easily included. For example, timing solutions include an "epoch" $t_e$, which is the non-zero time at which the frequency and its derivative are measured. This can be included as:

$$\theta_i(t_i) = \theta_0 + f(t_i - t_e) + \frac{1}{2}\dot{f}(t_i - t_e)^2 + \frac{1}{6}\ddot{f}(t_i - t_e)^3 + \cdots$$

Pulsars also experience different types of "timing noise", or irregularities in their spin features. One such phenomena is the "glitch", or a sudden change in the frequency and its derivatives. One can imagine modifying Eqn. 5.1 to be piecewise, where at some glitch epoch ("`GLEPH`" in `Tempo2` format) the values of $f$ and its derivatives suddenly change. Full lists of available parameters are available in Hobbs, Edwards, and Manchester [145] and Luo et al. [172].

## 5.2 Fourier Techniques

The study of pulsars with instruments such as *Fermi*-LAT is a challenging task. For example, as presented in Chapter 8, *Fermi*-LAT detected an estimated 7200 photons PSR J2022+3842 over the course of 13 years of observation. With a period of 48.2 ms, this is a rate of about 1 photon per million rotations (or per 15.6 hours).

Further, these 7200 photons make up less than half a percent of all photons included in the analysis. Yet, with a proper timing solution, PSR J2022+3842 can be detected with $13\sigma$ significance in 5.7 years of data.

One of the most widely studied methods of analyzing periodic data, and searching for such a signal, is the Fourier transform. Generally, this can be used to transform a time series (such as a list of photon detection times) into a frequency series, with more present frequencies (such as that of a pulsar generating said photons) having a greater spectral "power". The way of computing a frequency's power from a finite list of photons is through the discrete Fourier transform (DFT), often implemented via the fast Fourier transform (FFT) algorithm.

The computational hurdles related to using Fourier techniques with $\gamma$-ray photons are well documented (e.g. Buccheri, Sacco, and Ozel [59] and Atwood et al. [40]), but I will review some of the points below.

### 5.2.1 Pulsar Searches

DFT's are the preferred method of searching for new pulsars in $\gamma$-ray data. Because DFT's are so important to a variety of fields, they are well understood and routines have been made to perform them quite efficiently. Unfortunately, when it comes to finding a new pulsar, if a particular quantity can not be directly measured, it must be determined via some method typically involving a large number of trials. If the value being determined is well constrained, this may be carried out through MCMC procedures, with the process being termed "refinement". For example, if a pulsar is initially detected in one month of *Fermi*-LAT data, and the dataset is then extended to two months, the timing solution could be refined through MCMC techniques. If the value is not well determined, a search may be carried out through use of a DFT, and termed a "blind search". If *Fermi*-LAT sees an unidentified source, and one believes the spectral properties to be consistent with a pulsar, they may carry out a blind search in frequency (and higher order derivatives), position, and even orbital parameters. It is also possible for a pulsar to fall somewhat in between these two scenarios, which may be examined through a "semi-blind search". If a pulsar was detected some years ago, but follow-up observations have not been made, one may have a fairly good idea of its parameters, but with errors too large to actually see pulsations. In such a scenario, a semi-blind search could be carried out using DFT's (for speed), or other methods (for ease, lower memory requirements, etc.).

Briefly, let a signal be sampled at some rate $f_s$ over some time $t_s$. The resulting input (in an FFT, the input data is overwritten as the output is calculated) data will have $N = f_s * t_s$ bins and be sensitive to signals with frequency $\frac{1}{2}f_s$ (by Nyquist's theorem). The fastest spinning pulsar has a frequency of 716 Hz[138]. Using a sample rate of 1432 Hz over *Fermi*-LAT's 14 years of operation, and assuming each bin takes eight bytes (i.e. double precision) of memory, this would require about 5 TB of memory (not to mention the sheer computational time involved to perform such a calculation). At the time of writing, a high-end desktop computer may include a 2 TB hard drive and 32 GB of memory.

Additionally, there is the issue of frequency drift. In DFTs, where frequencies are grouped into bins, a frequency drift will have the effect of smearing a signal across several bins, thus eroding its detectability. Some forms of frequency drift, such as higher order frequency derivatives, can be accounted for by modifying the underlying time series as described below.

At this point, aspects of $\gamma$-ray astronomy prohibitive to a straightforward application of the DFT begin to become clear.

### First Frequency Derivative

Consider a pulsar with frequency $f(t) = f_0 + \dot{f}t$, where $f_0$ is the frequency at time $t = 0$ and $\dot{f}$ is the frequency rate of change (a constant across time) [40]. For long observational periods, the total change in frequency $f(t_{max}) - f(t)$ will almost certainly be larger than the binning of the DFT being used to search for the pulsar. This results in what would ideally be a single significant bin in the power spectrum diffusing across neighboring bins. Uncorrected, the pulsar may be impossible to find using the blind search technique. It is thus necessary to remove the effect of frequency drift from a data set before searching it for a pulsar.

Consider searching a list of photons with times $t_i$ for a pulsar with frequency $f$ and frequency derivative $\dot{f}$.

The phase of an individual photon, $\phi_i$ can be calculated as

$$\phi_i(t_i) = \phi_0 + ft_i + \frac{1}{2}\dot{f}t_i^2 \tag{5.2}$$

To remove an assumed frequency drift $\dot{f}$, we require a transformation $t_i \rightarrow T_i$ such that

$$\phi_i(T_i) = \phi_0 + fT_i \tag{5.3}$$

The transformation can be calculated by solving $\phi_i(T_i) = \phi_i(t_i)$.

$$\phi_0 + fT_i = \phi_0 + ft_i + \frac{1}{2}\dot{f}t_i^2 \tag{5.4}$$

$$fT_i = ft_i + \frac{1}{2}\dot{f}t_i^2 \tag{5.5}$$

$$\boxed{T_i = t_i + \frac{1}{2}\frac{\dot{f}}{f}t_i^2} \tag{5.6}$$

As is now apparent, removing the impact of frequency drift from a time series involves the ratio of $\dot{f}$ to $f$. Rather scanning over a decoupled $f$ and $\dot{f}$, it is more pertinent to think in terms "steps of $\dot{f}/f$". The process of scanning over a range of frequencies and frequency derivatives thus proceeds over the following three steps:

1. Correct the set of photon times for a given $\dot{f}/f$ ratio
2. Perform a Fourier transform over the corrected times
3. Note the peak $f$ from this particular step, and back-calculate the corresponding $\dot{f}$

The distance between successive $\dot{f}/f$ steps is an important value to consider when performing a blind search. Steps that are too large will not allow the pulsar to be detected, while steps that are too small will waste computational resources. Recall that the resolution of a DFT is:

$$\Delta_{DFT}f = 1/T_w \tag{5.7}$$

where $T_w$ is the size of the time window over which the DFT is performed. As discussed further in Sec. 5.2.2, the total observation of length $T_v$ bay be broken down into several smaller segments of length $T_w$. The goal of the $\dot{f}/f$ correction is to ensure that the frequency drift $\Delta_{tot}f = \dot{f} * T_v$ is less than $\Delta_{DFT}f$.

Equating these two equations yields an $\dot{f}$ tolerance of:

$$\dot{f}_{tol} <= \frac{1}{T_v T_w} \tag{5.8}$$

In determining $\dot{f}/f$, taking the maximum value of $\dot{f}_{tol}$ suggests the most efficient way to search for the true $\dot{f}$ without wasting computational resources.

As the total viewing period is broken up into $M$ shorter viewing windows according to $T_w = T_v/M$, this gives:

$$\dot{f}_{tol} <= \frac{M}{T_v^2} \tag{5.9}$$

Comparing the $M = 1$ case of the standard FFT, we can see that we will need a factor of $M$ fewer trials to scan $\dot{f}$.

$f$ must be taken as the worst-case scenario: the largest frequency to be searched. The result is the following formula:

$$\text{step}\frac{\dot{f}}{f} <= \frac{1}{T_v * T_w * f_{max}} \tag{5.10}$$

### Second Frequency Derivative

The process of correcting for a second frequency derivative is similar to that shown above, but is presented here for completeness. The phase of a photon arriving at time $t_i$ given a pulsar with frequencies and frequency derivatives $f$, $\dot{f}$, and $\ddot{f}$ is

$$\phi_i(t_i) = \phi_0 + f t_i + \frac{1}{2}\dot{f} t_i^2 + \frac{1}{6}\ddot{f} t_i^3 \tag{5.11}$$

We desire a transformation $t_i \rightarrow T_i$ such that

$$\phi_i(T_i) = \phi_0 + f T_i \tag{5.12}$$

Equating these relations

$$T_i = t_i + \frac{1}{2}\frac{\dot{f}}{f} t_i^2 + \frac{1}{6}\frac{\ddot{f}}{f} t^3 \tag{5.13}$$

### 5.2.2 Time Differencing

There are two primary techniques for turning the blind search into a realizable computation. The first, suggested by Buccheri, Sacco, and Ozel [59], is to break the underlying data set into multiple shorter windows, and then add the individual FFT power spectra. However, the gains provided by this are only marginal. The computational complexity of a FFT is $\mathcal{O} = N log_2(N)$, where $N$ is the number of FFT points in the transform. Dividing $N$ into $M$ bins thus has complexity $\mathcal{O} = N log_2(N/M)$, where the prefactor remains $N$ because the calculation will need to be carried out $M$ times, once per bin. Nevertheless, this is realizable, and has been used successfully in the past.

Even better is the time differencing technique, first described by Atwood et al. [40]. Instead of performing a FFT on the photons directly, it is performed on a binned list of the differences between photon arrival times. The creation of this binned list is as follows:

- Select a maximum time difference, $T_w = T_v/M$
- Calculate the difference in arrival time for the first photon and all subsequent photons, up to the maximum difference $T_w$, binning the result.
- Repeat for the remaining photons.

Using this procedure, one keeps the $log_2(N/M)$ benefit from before, but the prefactor also sees a reduction of $1/M$, as the FFT need be carried out only once. This produces $\mathcal{O} = (N/M)log_2(N/M)$. Further, as shown by Eqn. 5.9, the number of steps in $\dot{f}$ also decreases by a factor of $M$, making the overall process $1/M^2$ more efficient than a simple stacking method. Monte Carlo simulations were performed by Atwood et al. [40], showing this method to perform approximately as well as simple stacking, but requiring 1/15 the processing time.

## 5.3 Photon-by-Photon Statistics

After detecting a candidate pulsar signal, the next step is to determine that it is, in fact, a pulsar. In practical terms, this equates to proving the detection of a pulsed signal. This problem is mathematically equivalent to many others across a broad range of fields, and the path to the H-Test (the current standard in pulsar science) I present is one of many. I will start with the Rayleigh Test, which originally sought to characterize random walks in two dimensions [89]. However, the Rayleigh Test is explained extraordinary well in a textbook on biostatistics [249], where it is used to characterize circular distributions (such as compass directions or times of day). Whilst powerful for unimodal distributions, the Rayleigh Test is not ideal for detecting arbitrary distributions. Therefore, mathematicians have studied Fourier series density estimators [131], of which one example is the $Z^2_m$-Test [75]. This test can be thought of as an extension of the Rayleigh Test to higher harmonics, allowing for a larger variety of distribution shapes (or, the $\mathrm{Z}^2_m$-Test can be derived independently, and shown to reduce to the Rayleigh Test!). However, as we will see, this $m$ term introduces a level of subjectivity to the $\mathrm{Z}^2_m$-Test. This is the problem addressed by the H-Test, which allows an (in principle) infinite number of $m$ values to be tested without significant degregation of the significance by trial factors[75, 155].

### 5.3.1 Rayleigh Test

The Rayleigh Test is named after Lord Rayleigh, who first studied its properties while studying the random walks in several dimensions[89]. In two dimensions, this scenario lends itself well to the polar coordinate system; each step is of unit length and in direction $\theta$. The Rayleigh Test may be used to determine if the final collection of $\theta$ values are uniformly distributed, or follow some unimodal distribution[249].

To reach the Rayleigh Test, it is necessary to define the mean angle ($\bar{\theta}$) and a measure of dispersion ($R^2$). To do this, we place each angle measurement on a unit circle at coordinate ($r = 1$, $\theta_i$). This can be broken into Cartesian coordinates in the standard manner:

$$X_i = \cos(\theta_i)$$

$$Y_i = \sin(\theta_i)$$

and the means $\bar{X}$ and $\bar{Y}$ computed, again in a standard manner:

$$\bar{X} = \frac{1}{n}\sum_{i=1}^{n}\cos(\theta_i)$$

$$\bar{Y} = \frac{1}{n}\sum_{i=1}^{n}\sin(\theta_i)$$

The collection of circular data points can now be characterized by a vector of length $R$ and direction $\bar{\theta}$:

$$R = \sqrt{\bar{X}^2 + \bar{Y}^2} \tag{5.14}$$

$$\bar{\theta} = \arcsin(\bar{Y}/R) = \arccos(\bar{X}/R) \tag{5.15}$$

The intermediate conversion to Cartesian coordinates accounts for the cyclic nature of these data sets. For example, if you have the data $\theta_i = \{1^\circ, 359^\circ\}$, then it is desired that $\bar{\theta} = 0^\circ$, whereas $(1^\circ + 359^\circ)/2 = 180^\circ$.

$R$ can be thought of as (and indeed, with slight modification, can be rigorously transformed into) a measure of unimodal uniformity. For example, consider a dataset consisting of $N$ identical phases $\theta_1 = \theta_2 = ... = \theta_N = \theta$.

$$\bar{X} = \frac{1}{n}\sum_{i=1}^{n}\cos(\theta_i) = \frac{1}{N} \times N\cos\theta = \cos\theta$$
$$\bar{Y} = \frac{1}{n}\sum_{i=1}^{n}\sin(\theta_i) = \frac{1}{N} \times N\sin\theta = \sin\theta$$

From which it follows

$$R = \sqrt{\bar{X}^2 + \bar{Y}^2} = \sqrt{\cos^2(\theta) + \sin^2(\theta)} = 1$$

If there is a dataset consisting of $N$ phases uniformly distributed, one may convince themselves that each individual element in the $\bar{X}$ or $\bar{Y}$ sums will either be 0, or have conjugate terms which cancel. As such,

$$\bar{X} = 0, \bar{Y} = 0, R = 0$$

The $R = 0$ case does deserve special mention in regards to Eqn. 5.15, as this equation indicates division by $R$. What *should* the mean angle be in the case of a uniformly distributed set of angles? Because no particular direction is preferable, the mean angle should not exist. The fact that $R = 0$ quantitatively indicates this, and as such the inability to calculate $\bar{\theta}$ is not alarming. Thus, $R = 1$ indicates perfectly aligned data while $R = 0$ indicates perfectly uniform data.

It is now also possible to demonstrate why $R$ is only an indicator of *unimodal* clustering. For example, consider a collection of $N$ data points with $N/2$ each lying at $\theta = 0°$ and $\theta = 180°$. For reasonably large $N$, one can say with confidence that this data is in fact (bimodally) clustered. Yet, it is clustered in such a manner that $R = 0$, meaning that it is undetectable with Rayleigh Test. It is this problem that is addressed by the $Z_m^2$-Test.

The final objective when working with the Rayleigh Test is to describe the distribution of $R$ values (or a related quantity) when $\theta$ is randomly sampled from a uniform distribution on the unit circle.

Working with Eqn. 5.14, it can be shown:

$$R^2 = \frac{1}{n^2}\left[\sum_{i=1}^{n}\cos(\theta_i)\right]^2 + \frac{1}{n^2}\left[\sum_{i=1}^{n}\sin(\theta_i)\right]^2$$

More conveniently

$$nR^2 = \frac{1}{n}\left[\sum_{i=1}^{n}\cos(\theta_i)\right]^2 + \frac{1}{n}\left[\sum_{i=1}^{n}\sin(\theta_i)\right]^2 \tag{5.16}$$

is typically what is meant when a pulsar scientist refers to the Rayleigh-Test.

Let $E[Z]$ represent the expected value of $Z$. If we expand the first term as a quadratic and use the linearity of the expectation value:

$$\begin{aligned}
E\left[\left(\sum_{i=1}^{n}\cos(\theta_i)\right)^2\right] &= E\left[\sum_{i=1}^{n}\cos^2(\theta_i) + \sum_{i\neq j}\cos(\theta_i)\cos(\theta_j)\right] \\
&= E\left[\sum_{i=1}^{n}\cos^2(\theta_i)\right] + E\left[\sum_{i\neq j}\cos(\theta_i)\cos(\theta_j)\right] \\
&= \sum_{i=1}^{n}E\big[\cos^2(\theta_i)\big] + \sum_{i\neq j}E\big[\cos(\theta_i)\cos(\theta_j)\big] \\
&= \sum_{i=1}^{n}E\big[\cos^2(\theta_i)\big] + \sum_{i\neq j}E\big[\cos(\theta_i)\big]E\big[\cos(\theta_j)\big]
\end{aligned}$$

where in the last line we have made use of the property $E[W \cdot Z] = E[W] \cdot E[Z]$, which holds so long as $W$ and $Z$ are independent. $\theta_i$ and $\theta_j$ are indeed independent, as we are examining the case where $\theta$ is randomly sampled from a uniform distribution on the unit circle.

From symmetry arguments, $E\big[\cos(\theta)\big] = 0$ and the second term disappears. It thus remains to find $E\big[\cos^2(\theta_i)\big]$. The "law of the unconscious statistician"[2] states:

$$E[g(X)] = \int_{-\infty}^{\infty} g(x) f_X(x) dx$$

where $X$ is a random variable with probability density function $f_X$. As in this case $\theta$ is drawn from a uniform distribution, we have

---

[2] The law of the unconscious statistician (LOTUS) is so-named because it is often assumed axiomatic, yet requires rigorous proof[77].

$$g(x) \to \cos^2(\theta)$$

$$f_X(x) \to H(\theta) - H(\theta - 2\pi)$$

where $H$ is the Heaviside step function. This gives

$$\begin{aligned}
E\big[\cos^2(\theta)\big] &= \frac{1}{2\pi}\int_0^{2\pi} \cos^2(\theta)d\theta \\
&= \frac{1}{2\pi}\frac{1}{4}\int_0^{2\pi} \big(e^{i\theta} + e^{-i\theta}\big)^2 d\theta \\
&= \frac{1}{2\pi}\frac{1}{4}\int_0^{2\pi} \big(e^{2i\theta} + e^{-2i\theta} + 2\big) d\theta \\
&= \frac{1}{2\pi}\frac{1}{2}\int_0^{2\pi} \big(\cos(2\theta) + 1\big) d\theta \\
&= \frac{1}{2\pi}\frac{1}{2}(0 + 2\pi) \\
&= \frac{1}{2}
\end{aligned}$$

and as such

$$E\Bigg[\bigg(\sum_{i=1}^{n} \cos(\theta_i)\bigg)^2\Bigg] = \frac{n}{2} \tag{5.17}$$

Recall that $\chi_k^2$ represents the distribution of the sum of $k$ normally distributed random variables squared, and has mean $k$. Due to the central limit theorem, it can be said that $\sum_{i=1}^{n} \cos(\theta_i)$ is distributed in a Gaussian manner for sufficiently large $n$. Thus,

$$\Bigg[\sum_{i=1}^{n} \cos(\theta_i)\Bigg]^2$$

behaves as a single Gaussian distributed value squared, and has an expected value of $n/2$.

Taken together, this means that the first term of Eqn. 5.16, multiplied by a factor of 2,

$$\frac{2}{n}\left[\sum_{i=1}^{n}\cos(\theta_i)\right]^2$$

behaves as a single normally distributed value square, with the $2/n$ prefactor serving to rescale the Gaussian distribution into a standard normal distribution. Thus, it is $\chi_1^2$ distributed.

A similar procedure can be followed for the second term in Eqn. 5.16, showing that $2nR^2$ is distributed as $\chi_2^2$ for sufficiently large $n$ if $\theta$ is pulled from a uniform distribution over one period[55]. As such, if trying to determine if an astrophysical source shows periodic behavior, $2nR^2$ can be used as a well defined way of testing the null hypothesis.

### 5.3.2 $\mathrm{Z}_m^2$-Test

As mentioned in the previous section, one of the shortcomings of the Rayleigh test is that it does not perform well when studying non-unimodal distributions. In particular, a diametrically opposed clustering of phases will tend to cancel each other out.

For example, consider Fig. 5.1, the pulse profile for PSR J2022+3842 from NICER (further described in Chapter 8). This pulse profile contains two narrow peaks separated by very nearly half a phase. Examining the significance of this pulse profile with the Rayleigh test gives a significance of $9.49\sigma$, far below the $73.81\sigma$ detection claimed in Chapter 8.

A useful step towards addressing this problem is the $\mathrm{Z}_m^2$-Test [60]:

$$\mathrm{Z}_m^2 = \frac{2}{n}\sum_{j=1}^{m}\left(\left[\sum_{i=1}^{n}\cos(j\theta_i)\right]^2 + \left[\sum_{i=1}^{n}\sin(j\theta_i)\right]^2\right) \tag{5.18}$$

By comparison to the Rayleigh test (Eqn. 5.16), we can note two primary changes. The change is that an additional factor of 2 has been included, so that $\mathrm{Z}_m^2$ can be directly compared to a $\chi^2$ distribution, instead of needing to use $2\mathrm{Z}_m^2$. The more consequential change is that $\mathrm{Z}_m^2$ represents a sum over several harmonics ($j$, in Eqn. 5.18). This change allows the $\mathrm{Z}_m^2$-Test to better detect a variety of pulse

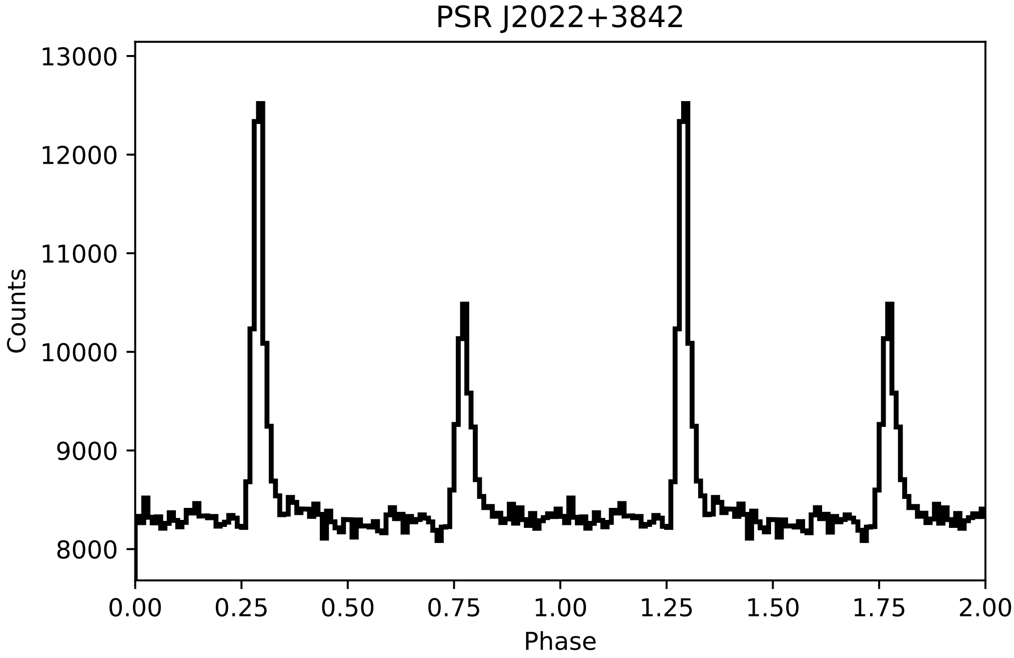

Figure 5.1: The pulse profile of PSR J2022+3842 using data from the NICER telescope, as described in Chapter 8. The data are doubled to cover two periods for illustrative purposes. Note how the two pulses bear similar shape, and are located roughly half a phase apart.

shapes. It also keeps the $\chi^2$ distributed aspect of the Rayleigh test. Specifically, under the null hypothesis, $Z_m^2$ is distributed as $\chi^2_{2m}$[49]. $Z_1^2$ is equivalent to using the Rayleigh test.

The natural next question when using the $Z_m^2$ test is the appropriate choice of $m$. $m = 2$ was used by Buccheri et al. [60], the first to apply this test to astrophysical data. This choice was studied in greater detail by de Jager, Raubenheimer, and Swanepoel [75], who showed its use as an omnibus test able to detect a variety of pulse shapes was somewhat optimistic (and proposed the H-Test, described in 5.3.3). If some existing knowledge suggests a broad pulse shape, $m = 1$ may be a more powerful test. Such a case occurred in Kuiper, Hermsen, and Dekker [160], and as discussed in Chapter 7.

### 5.3.3 H-Test

The H-Test is, at the time of writing, the standard by which $\gamma$-ray pulsation significance is measured. It takes the form [75]:

$$H \equiv \max_{1 \leq m \leq 20} (Z_m^2 - 4(m-1)) \tag{5.19}$$

where $m$ is limited to 20 for practical reasons, but could in principle be infinitely large [155]. The inclusion of the second term, $4(m-1)$, is motivated by the study of Fourier series density estimators [131]. When seeking to approximate a signal as a truncated Fourier series, Hart [131] provided a function which suggests the highest harmonic at which to truncate the series. If small terms are ignored, this function takes the form of the H-Test [75].

The $c(m-1)$ component with arbitrary $c$ have been considered. In particular, de Jager, Raubenheimer, and Swanepoel [75] presents a comparison of the $c = 0$ and $c = 4$ cases, including $\mathrm{Z}_1^2$ (the Rayleigh test), $\mathrm{Z}_2^2$, $\mathrm{Z}_{10}^2$, and others which I have not addressed. Of most interest in this comparison are pulse profiles of one and two peaks and varying widths, as these most closely resemble known $\gamma$-ray pulse profiles. While no single significance test dominated in all conditions, the H-Test was shown to perform best as an omnibus test for pulsar-like light curves of unknown prior pulse shape. In contrast, the Rayleigh test performed best for broad single peaks, and $\mathrm{Z}_{10}^2$ for double peaks or narrow single peaks (although the closely related $c = 0$ was not examined in these latter two instances). Overall, de Jager, Raubenheimer, and Swanepoel [75] and Kerr [155] report the results of comparing various significance tests via MCMC techniques.

Unfortunately, the H-Test can no longer be simply compared to a $\chi^2$ distribution when calculating a significance in $\sigma$. The cumulative density function of the H-Test can be approximated as:

$$\mathrm{CDF(H)} \approx \exp(-0.4H) \tag{5.20}$$

which has been verified via MCMC techniques in de Jager, Raubenheimer, and

Swanepoel [75], de Jager, O. C. and Büsching, I. [76], and Kerr [155]. Further, Kerr [155] provides an analytical derivation of the H-Test's CDF under the null hypothesis for arbitrary choices of $m$ and $c$.

### Extension to Weighted Photons

As discussed in Chapter 4.1.11, photons may be assigned a *weight* by various methods, including one aimed at determining the likelihood that a photon originated from a particular source. The extension of the Z (and thus H) tests to weighted photons is straightforward: each term in the summation gains a weight $w_i$, and the overall score is re-normalized.

$$\mathrm{Z}_m^2 = \frac{2}{n}\left(\frac{1}{n}\sum_{i=1}^{n} w_i^2\right)^{-1} \sum_{j=1}^{m}\left(\left[\sum_{i=1}^{n} w_i \cos(j\theta_i)\right]^2 + \left[\sum_{i=1}^{n} w_i \sin(j\theta_i)\right]^2\right) \tag{5.21}$$

This procedure is introduced by Kerr [155], and does not change distributions of these tests under the null hypothesis.

## 5.4 Temporal Analysis Caveats

It is important to be mindful of spurious signals that enter periodic datasets through other means, as the above analysis techniques cannot distinguish between source fluctuations and instrumental effects. For example, *Fermi*-LAT has an orbital period of approximately 96 minutes. Any temporal analysis sensitive to 96 minute periods will detect this orbital period in the data. A list of this temporal effect, and others, is provided by the FSSC[3]. In regards to *Fermi*-LAT, the known temporal effects are on time scales too large to affect most pulsar observations, but may become more visible if one looks at other possible variable sources, such as AGN.

However, there are a couple of avenues for NICER observations to generate spurious temporal signals which may mimic a pulsar[4]. Telemetry saturation, where NICER must stop taking data while it reads out events stored to its internal buffer,

---

[3] `https://fermi.gsfc.nasa.gov/ssc/data/analysis/LAT_caveats_temporal.html`

[4] `https://heasarc.gsfc.nasa.gov/docs/nicer/data_analysis/nicer_analysis_tips.html`

can occur when observing a very bright source. These gaps in data taking tend to occur at 1/10 and 1/100 second intervals, which produce peaks in the power spectrum at these respective frequencies.

Additionally, NICER's field of view begins to drop off further than 1 arcminute away from the boresight. If a source position is not precisely known, and the final pointing position is greater than 1 arcminute away from the true source position, the source will appear to fluctuate in brightness as NICER attempts to track the false position. The NICER team recommends skepticism with regards to frequencies below 0.5 Hz when the precise position of the source is not yet known.

# Chapter 6

# PSR J1813-1749: The Shooting Star

The following chapter has been modified from Ho et al. [141] "Proper motion, spectra, and timing of PSR J1813-1749 using *Chandra* and *NICER*", where I contributed to the *NICER* analysis detailed in Sec. 6.3. I also performed the *Fermi*-LAT analysis detailed in Sec. 6.5, although this does not appear in the published paper.

PSR J1813-1749 is one of the most energetic rotation-powered pulsars known, producing a pulsar wind nebula (PWN), $\gamma$-ray emission, and TeV emission, but its spin period is only measurable in X-rays. We present an analysis of two *Chandra* datasets that are separated by more than ten years and recent *NICER* data. The long baseline of the *Chandra* data allows us to derive a pulsar proper motion $\mu_{\mathrm{R.A.}} = -(0.''067 \pm 0.''010)\ \mathrm{yr}^{-1}$ and $\mu_{\mathrm{decl.}} = -(0.''014 \pm 0.''007)\ \mathrm{yr}^{-1}$ and velocity $v_{\perp} \approx 900 - 1600\ \mathrm{km\ s}^{-1}$ (assuming a distance $d = 3 - 5$ kpc), although we cannot exclude a contribution to the change in measured pulsar position originating from an alteration in brightness structure of the PWN very near the pulsar. We model the PWN and pulsar spectra using an absorbed power law and obtain best-fit absorption $N_{\mathrm{H}} = (13.1 \pm 0.9) \times 10^{22}\ \mathrm{cm}^{-2}$, photon index $\Gamma = 1.5 \pm 0.1$, and 0.3–10 keV luminosity $L_{\mathrm{X}} \approx 5.4 \times 10^{34}\ \mathrm{erg\ s}^{-1}(d/\ 5\ \mathrm{kpc})^{2}$ for the PWN and $\Gamma = 1.2 \pm 0.1$ and $L_{\mathrm{X}} \approx 9.3 \times 10^{33}\ \mathrm{erg\ s}^{-1}(d/\ 5\ \mathrm{kpc})^{2}$ for PSR J1813-1749. These values do not change between the 2006 and 2016 observations. We use *NICER* observations from 2019 to obtain a timing model of PSR J1813-1749, with spin frequency $\nu = 22.35$ Hz (truncated, with error on the order of $10^{-10}$ Hz) and spin frequency time derivative $\dot{\nu} = (-6.428 \pm 0.003) \times 10^{-11}$ Hz s$^{-1}$. We also fit $\nu$ measurements from 2009–2012 and our 2019 value to find a long-term spin-down rate $\dot{\nu} = (-6.3445 \pm 0.0004) \times 10^{-11}$ Hz s$^{-1}$. We speculate that the difference in spin-down rates is due to glitch activity or emission mode switching.

## 6.1 Introduction

PSR J1813-1749 (also known as CXOU J181335.16−174957.4) has a previously measured spin frequency $\nu = 22.37$ Hz and spin-rate change $\dot{\nu} = -6.333 \times 10^{-11}$ Hz s$^{-1}$ [111, 117], which make this pulsar's spin-down energy loss rate $\dot{E} = 5.6 \times 10^{37}$ erg s$^{-1}$ the fourth largest among the ∼2800 known pulsars, behind only PSR J0537-6910, the Crab pulsar, and PSR B0540-69 [177]. This large rate probably explains the pulsar's association with the TeV source HESS J1813-178 [230] and $\gamma$-ray source IGR J18135-1751 [20] and makes the pulsar an interesting target for LIGO/Virgo searches of continuous gravitational waves [3, 5]. The spin frequency is only measurable at X-ray energies, as it seems to be a variable, but unpulsed, radio source [84, 85]. PSR J1813-1749 is located in the young ($<$ 3 kyr) supernova remnant G12.82−0.02 [56] at a distance $d \approx 3 - 5$ kpc [184].

Observations at X-ray energies are crucial to the study of PSR J1813-1749. For example, the exceptional spatial resolving power of *Chandra* allows an accurate measurement of the position of PSR J1813-1749 and separation of the X-ray spectra of the pulsar and pulsar wind nebula (PWN) in which the pulsar is embedded. Using a 30 ks ACIS-I observation taken in 2006, Helfand et al. [135] measure the pulsar position to be R.A.= $18^{\mathrm{h}}13^{\mathrm{m}}35\overset{\mathrm{s}}{.}166$, decl.= $-17^{\circ}49'57\overset{''}{.}48$ (J2000). They perform a spectral analysis on three spatial components, i.e., the PWN, an inner nebula, and the pulsar, and find each is well fit by an absorbed power law. More recently, Townsley et al. [228] analyze a number of *Chandra* observations, including those considered here, to compile a catalog of X-ray sources and their spectral properties, such as those of PSR J1813-1749. Meanwhile, Halpern, Gotthelf, and Camilo [117] use *Chandra* ACIS-S3 (in continuous clocking mode[1]) and *XMM-Newton* EPIC-pn observations to measure the pulsar spin frequency at three epochs, in 2009, 2011, and 2012. While a simple linear fit of these measurements results in a value of $\dot{\nu}$, this is insufficient to obtain a rotation phase-connected timing model of PSR J1813-1749.

Here we re-analyze the 2006 *Chandra* observation and compare it to a set of 2016 observations. This comparison allows us to investigate any long-term variability and pulsar proper motion over the ten-year timespan. We present measurements of the spin frequency of PSR J1813-1749 using recent *NICER* data, which enables us to update the timing model that is vital for the most sensitive searches of continuous gravitational waves from this pulsar.

## 6.2 Analysis of *Chandra* data

*Chandra* observed PSR J1813-1749 with ACIS-I for 30 ks on 2006 September 15 (ObsID 6685), for 13 ks on 2016 May 29 (ObsID 17695), and for 17 ks on 2016 June 5 (ObsID 17440); see Table 6.1. We reprocess data with `chandra_repro` and Chandra Interactive Analysis of Observations (CIAO) 4.11 and Calibration Database (CALDB) 4.8.5 [93]. As in Helfand et al. [135], we do not account for photon pile-up since, as they note, the maximum count rate centered on PSR J1813-1749 is $< 0.004$ c s$^{-1}$ for ObsID 6685 and $< 0.002$ c s$^{-1}$ for ObsIDs 17440 and 17695. We note that Townsley et al. [228] include a pile-up correction in their analysis of ObsID 6685 but not of 17440 and 17695.

### 6.2.1 Proper motion and velocity

We follow the recommended procedure[2] to improve *Chandra*'s astrometry. In particular, we use `wavdetect` to detect sources in each observation and `wcs_match` and `wcs_update` to match detected sources in each 2016 observation with those detected

---

[1] The alternative to continuous clocking (CC) mode is timed exposure (TE) mode. In TE mode, a 2D X-ray image is taken every 0.2-10 sec., with 3.2 sec. being generally recommended to minimize deadtime (the time needed to read out each image is a constant 3.241 sec.) and pile-up. CC mode allows for a 3 ms time resolution, at the expense of one image dimension (which is summed over). See: `https://cxc.cfa.harvard.edu/proposer/POG/html/ACIS.html#sec:acis_ccmode`

[2] https://cxc.harvard.edu/ciao/threads/reproject_aspect/

| Telescope | ObsID | Date | Exposure (ks) |
|---|---|---|---|
| *Chandra* | 6685 | 2006 September 15 | 30 |
| *Chandra* | 17695 | 2016 May 29 | 13 |
| *Chandra* | 17440 | 2016 June 5 | 17 |
| *NICER* | 1020440101 | 2018 August 25 | 6 |
| *NICER* | 2579030101 | 2019 June 28 | 17 |
| *NICER* | 2579030102 | 2019 June 29 | 22 |
| *NICER* | 2579030103 | 2019 June 30 | 13 |
| *NICER* | 2579030201 | 2019 July 10 | 3 |
| *NICER* | 2579030202 | 2019 July 11 | 7 |
| *NICER* | 2579030203 | 2019 July 12 | 17 |
| *NICER* | 2579030204 | 2019 July 13 | 23 |
| *NICER* | 2579030301 | 2019 July 30 | 5 |
| *NICER* | 2579030302 | 2019 July 31 | 18 |
| *NICER* | 2579030303 | 2019 August 1 | 13 |
| *NICER* | 2579030304 | 2019 August 2 | 6 |
| *NICER* | 2579030305 | 2019 August 3 | 1 |
| *NICER* | 2579030306 | 2019 August 4 | 6 |

Table 6.1: *Chandra* and *NICER* observations of PSR J1813-1749.

in the 2006 observation; ObsID 6685 is used as the reference dataset given its longer exposure time. We then run `wavdetect` on the updated datasets of ObsID 17695 and 17440 to obtain new pulsar positions, given with $1\sigma$ uncertainties in Table 6.2.

Note that the position uncertainties determined by `wavdetect` suggest there could be a small increase ($<$ 15 percent) in R.A. asymmetry in between 2006 and 2016, perhaps due to a brightness change in the PWN, although the PWN flux contribution near the pulsar is likely to be small. We also note that the position in ObsID 6685 is $0\farcs43$ from the position found by Helfand et al. [135] (see Section 6.1) but is still consistent, given their $1\sigma$ uncertainty of $0\farcs3$. While we consider the absolute position (calibrated to optical sources in the USNO-B catalog) from Helfand et al. [135] to be reliable, we use our measured position from ObsID 6685 for consistency in order to determine relative displacements and extract the pulsar spectrum.

From Table 6.2, we see that the position of PSR J1813-1749 after astrometric correction appears have moved southwest by $\approx 0\farcs7$ between 2006 and 2016. To refine this displacement, we select four of the nearest (to the pulsar) and brightest sources, and use their position and $1\sigma$ uncertainty in each dataset as deter-

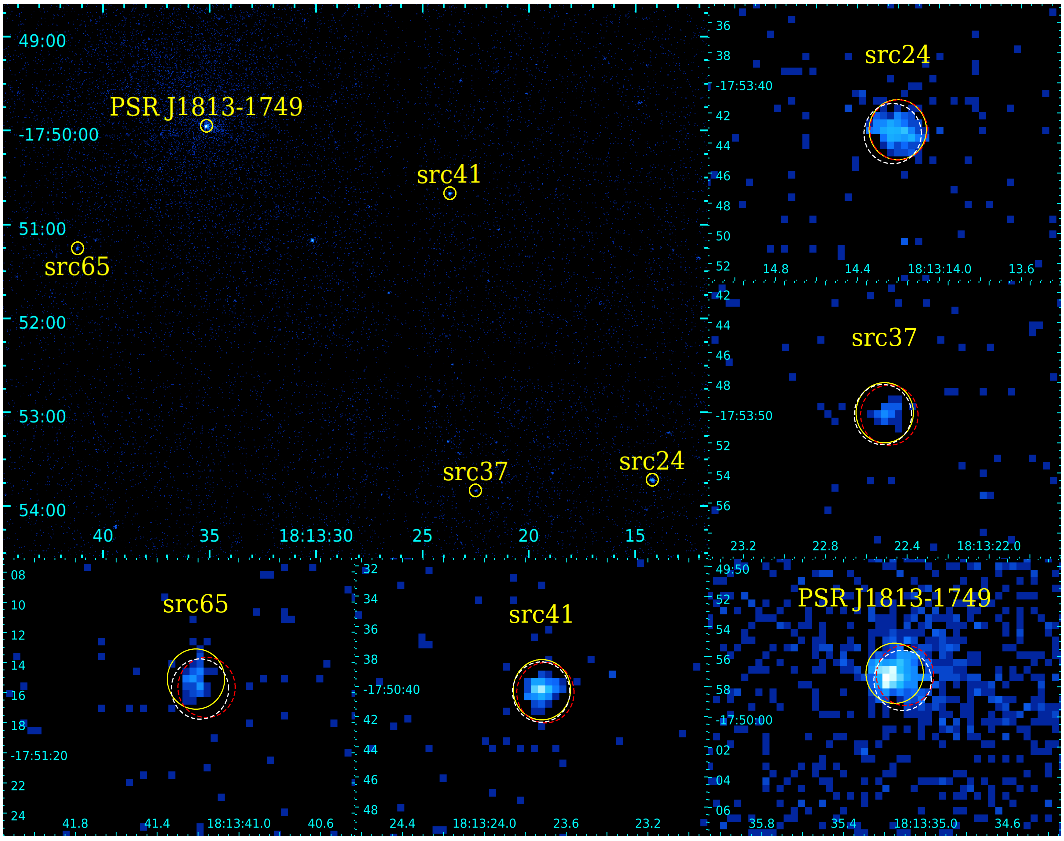

Figure 6.1: *Chandra* 2006 image (ObsID 6685) of PSR J1813-1749 and four nearby and bright sources that are used to refine the astrometry between 2006 and 2016. The latter four sources are labeled by their source number from Table 1 of Helfand et al. [135] (see also Table 6.2). Solid yellow, dashed red, and dashed white circles (with radius of $2''$ in all zoomed-in panels) indicate positions of each source in 2006, 2016 (ObsID 17695), and 2016 (ObsID 17440), respectively.

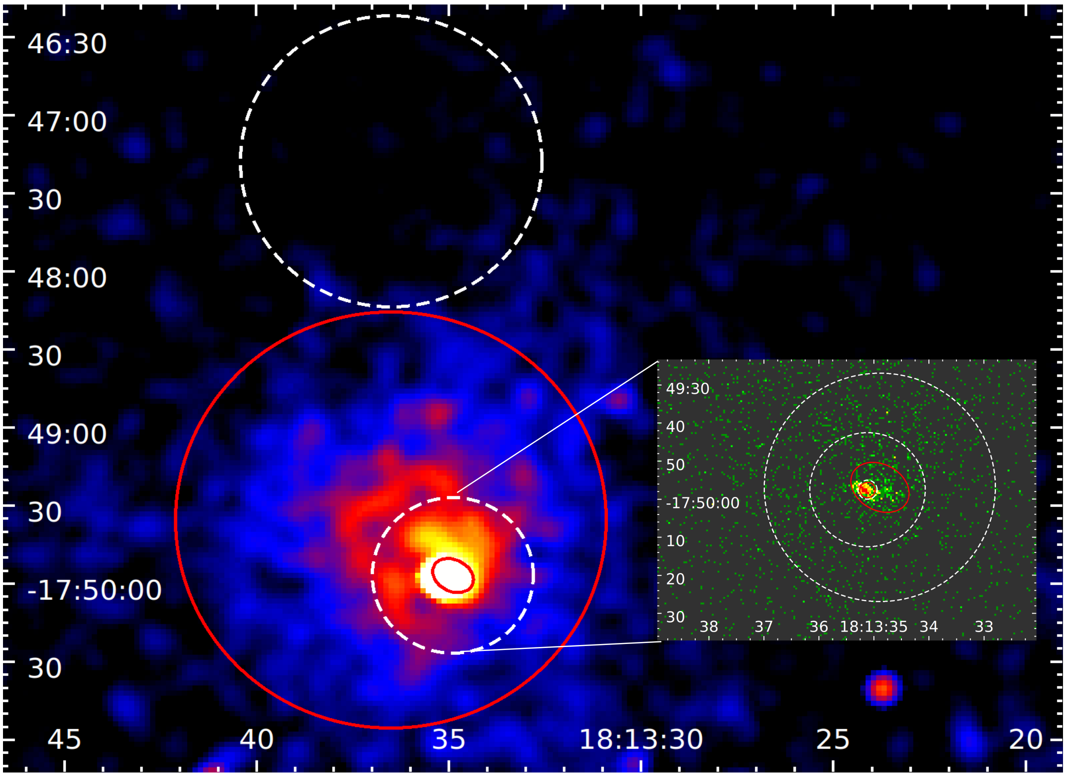

Figure 6.2: *Chandra* image (ObsID 17440) of the PWN, inner nebula, and PSR J1813-1749; 0.5–7 keV image is smoothed to make the PWN more visible. Inset: Zoomed-in unsmoothed view of inner nebula and PSR J1813-1749. Solid curves indicate extraction regions for the PWN (80″ radius), inner nebula (6″ × 8″ radii ellipse), and pulsar (2″ radius) spectra. Dotted curves indicate background extraction regions for the PWN (56″ radius), inner nebula (30″ radius), and pulsar (2.″5–15″ radii annulus). Embedded regions are excluded from each source's spectral extraction (see text for details)

mined by `wavdetect`. These sources are shown in Figure 6.1 and their positions are given in Table 6.2; source names and labels are from Helfand et al. [135] and Townsley et al. [228]. There are a few other sources in ObsID 6685 that are brighter, but which become dimmer than the four chosen here in ObsID 17695 and/or 17440. We calculate a weighted (by square of uncertainty) mean shift of these four sources: (ΔR.A.,Δdecl.) $= (-0\farcs22 \pm 0\farcs07, -0\farcs16 \pm 0\farcs07)$ for ObsID 17695 and $(+0\farcs19 \pm 0\farcs08, -0\farcs20 \pm 0\farcs06)$ for ObsID 17440. Accounting for this shift, we obtain a weighted mean displacement (ΔR.A.,Δdecl.) $= (-0\farcs62 \pm 0\farcs09, -0\farcs15 \pm 0\farcs08)$ for PSR J1813-1749. Considering the 9.7 year time difference between 2006 and 2016 observations, we determine that PSR J1813-1749 appears to be moving with a proper motion of $\mu_{\rm R.A.} = -(0\farcs067 \pm 0\farcs010)$ yr$^{-1}$ and $\mu_{\rm decl.} = -(0\farcs014 \pm 0\farcs007)$ yr$^{-1}$, after accounting for cos(decl.) in the apparent R.A. motion of $-(0\farcs064 \pm 0\farcs009)$ yr$^{-1}$. For an uncertain distance of $\approx 3 - 5$ kpc [184, 117], the proper motion implies a transverse velocity $v_\perp \approx 900 - 1600$ km s$^{-1}$, with an uncertainty of $\sim 300$ km s$^{-1}$. This velocity is high, but not extraordinary compared to that measured for other neutron stars [153, 78, 72]. Finally, the pulsar is $\sim 20''$ from the center of the supernova remnant G12.82$-$0.02 (see, e.g., Dzib et al. [85]), and therefore this velocity would indicate a pulsar age of $\sim 300$ yr, which is at the lower end of the age range of 200–3000 yr for the remnant [56].

### 6.2.2 Spectra

Spectra are extracted using `specextract` from regions shown in Figure 6.2 (from ObsID 17440; see also Figure 13 of [161] for an image from ObsID 6685) for the PWN, inner nebula, and pulsar. These regions are chosen to be the same as those used by Helfand et al. [135], which are notably different from those used by Townsley et al. [228]. Specifically, source counts for the PWN are from a $80''$ radius circle centered on R.A.= $18^{\rm h}13^{\rm m}36\fs50$, decl.= $-17^\circ49'35\farcs6$ and excluding the inner nebula source region, while background for the PWN is from a $56''$ radius circle centered on R.A.= $18^{\rm h}13^{\rm m}36\fs50$, decl.= $-17^\circ47'17\farcs6$, i.e., $2\farcm3$ north of source region. Source counts for the inner nebula are from a $6'' \times 8''$ radii ellipse centered on R.A.= $18^{\rm h}13^{\rm m}34\fs89$,

| ObsID | R.A. | decl. | ΔR.A. | Δdecl. |
|---|---|---|---|---|
| CXOU J181335.16−174957.4 (PSR J1813-1749) | | | | |
| 6685 | 18:13:35.151(2) | −17:49:57.10(3) | | |
| 17695 | 18:13:35.100(6) | −17:49:57.24(8) | −0.″73(10) | −0.″14(9) |
| 17440 | 18:13:35.112(6) | −17:49:57.57(7) | −0.″55(10) | −0.″47(8) |
| CXOU J181314.20−175343.4 (src24) | | | | |
| 6685 | 18:13:14.204(4) | −17:53:43.12(5) | | |
| 17695 | 18:13:14.200(6) | −17:53:43.13(12) | −0.″05(11) | −0.″01(13) |
| 17440 | 18:13:14.229(6) | −17:53:43.37(8) | +0.″36(11) | −0.″25(9) |
| CXOU J181322.48−175350.2 (src37) | | | | |
| 6685 | 18:13:22.510(13) | −17:53:50.00(7) | | |
| 17695 | 18:13:22.487(5) | −17:53:50.16(11) | −0.″33(20) | −0.″16(13) |
| 17440 | 18:13:22.518(5) | −17:53:50.13(6) | +0.″11(20) | −0.″13(9) |
| CXOU J181323.71−175040.5 (src41) | | | | |
| 6685 | 18:13:23.719(3) | −17:50:40.21(3) | | |
| 17695 | 18:13:23.701(6) | −17:50:40.41(15) | −0.″26(10) | −0.″20(15) |
| 17440 | 18:13:23.722(9) | −17:50:40.36(13) | +0.″04(13) | −0.″15(13) |
| CXOU J181341.20−175115.4 (src65) | | | | |
| 6685 | 18:13:41.210(8) | −17:51:15.11(17) | | |
| 17695 | 18:13:41.158(16) | −17:51:15.66(19) | −0.″74(25) | −0.″55(25) |
| 17440 | 18:13:41.190(26) | −17:51:15.77(30) | −0.″28(38) | −0.″66(34) |

Table 6.2: Positions of X-ray sources. Source names are those from Townsley et al. [228], while src# refers to the source number in Table 1 of Helfand et al. [135]. Number in parentheses is $1\sigma$ error in last digit (e.g. $0.1(23) = 0.1 \pm 0.023$).

decl.= $-17^\circ 49' 56''.9$ and excluding the pulsar source region, while background for the inner nebula is from a $30''$ radius circle centered on it and excluding the inner nebula region. Source counts for the pulsar are from a $2''$ radius circle (a 90 percent containment radius at 4.5 keV) centered on its position as given in Table 6.2, while background for the pulsar is from a $2''.5 - 15''$ radius circular annulus around the pulsar. Since ObsIDs 17440 and 17695 are taken only one week apart, we merge spectra extracted from these two observations using `combine_spectra` and `dmgroup`. PWN, inner nebula, and pulsar spectra are binned with a minimum of 30, 15, and 20 counts per energy bin, respectively. Fit results for the PWN and pulsar are the same within uncertainties when using a minimum of 15 counts per bin, as done in Helfand et al. [135].

We perform spectral fitting using Xspec 12.10.1 [33]. We use an absorbed power law (PL) model composed of `tbabs` and `powerlaw`. The former is to model photoelectric absorption in the interstellar medium, with abundances from Wilms, Allen,

| Year | $N_{\rm H}$ | $\Gamma$ | PL norm. | $f^{\rm abs}_{2-10}$ | $\chi^2$/dof |
|---|---|---|---|---|---|
| | | | PWN | | |
| 2006 | $13.11^{+0.89}_{-0.86}$ | $1.46 \pm 0.12$ | $20.3^{+4.9}_{-3.9}$ | $7.5^{+0.1}_{-0.3}$ | 330/308 |
| 2016 | | | $20.7^{+5.0}_{-3.9}$ | $7.7^{+0.1}_{-0.3}$ | |
| | | | | | |
| 2006 | $12.6^{+1.3}_{-1.2}$ | $1.32^{+0.17}_{-0.16}$ | $16.0^{+5.6}_{-4.0}$ | $7.8^{+0.1}_{-0.6}$ | 173/160 |
| 2016 | $13.8^{+1.3}_{-1.2}$ | $1.63^{+0.18}_{-0.17}$ | $27.1^{+10.0}_{-7.1}$ | $7.4^{+0.1}_{-0.9}$ | 153/146 |
| | | | inner nebula | | |
| 2006 | 13.1 | $0.77 \pm 0.17$ | $0.40^{+0.12}_{-0.10}$ | $0.54^{+0.04}_{-0.07}$ | 56.0/54 |
| 2016 | | | $0.93^{+0.29}_{-0.22}$ | $1.2 \pm 0.1$ | |
| | | | | | |
| 2006 | $14.9^{+9.2}_{-8.1}$ | $0.47^{+0.84}_{-0.76}$ | $0.27^{+1.1}_{-0.27}$ | $\lesssim 0.6$ | 19.4/18 |
| 2016 | $13.8^{+4.8}_{-4.4}$ | $1.03^{+0.49}_{-0.46}$ | $1.4^{+2.1}_{-0.8}$ | $1.2^{+0.1}_{-1.0}$ | 33.5/33 |
| | | | PSR J1813-1749 | | |
| 2006 | 13.1 | $1.24 \pm 0.11$ | $2.79^{+0.49}_{-0.42}$ | $1.6 \pm 0.1$ | 55.8/66 |
| 2016 | | | $2.77^{+0.50}_{-0.43}$ | $1.5 \pm 0.1$ | |
| | | | | | |
| 2006 | $16.5^{+3.9}_{-3.6}$ | $1.44^{+0.44}_{-0.42}$ | $4.3^{+5.4}_{-2.3}$ | $1.6^{+0.1}_{-0.7}$ | 34.7/37 |
| 2016 | $14.7^{+4.1}_{-3.8}$ | $1.67^{+0.50}_{-0.46}$ | $5.6^{+9.2}_{-3.6}$ | $1.4^{+0.1}_{-0.9}$ | 16.1/26 |

Table 6.3: Spectral fits with absorbed power law. Absorption $N_{\rm H}$ is in $10^{22}$ cm$^{-2}$, power law normalization is in $10^{-4}$ photon cm$^{-2}$ s$^{-1}$ keV$^{-1}$, and absorbed 2–10 keV flux $f^{\rm abs}_{2-10}$ is in $10^{-12}$ erg cm$^{-2}$ s$^{-1}$. Errors are $1\sigma$, and parameter values without errors are fixed.

and McCray [243] and cross-sections from Verner et al. [236]; note that use of `phabs`, instead of `tbabs`, leads to very similar results except for a slightly higher best-fit $N_{\rm H}$ ($= 13.4 \times 10^{22}$ cm$^{-2}$ for the PWN). The power law is to model the intrinsic spectrum of the pulsar or pulsar wind. For each set of spectra (PWN, inner nebula, and pulsar), we conduct two different fits. For the PWN, we first allow varying but linked values of absorption and photon index between the 2006 and 2016 data, so that only the power law normalization varies between these two epochs. For the inner nebula and pulsar, our first fit fixes the absorption to the best-fit value of the PWN spectral model, i.e., $N_{\rm H} = 13.1 \times 10^{22}$ cm$^{-2}$ (see Table 6.3), but allows a varying but linked value of the photon index. The second fits have all model parameters free to vary and untied between observations.

The results of our different spectral fits are given in Table 6.3. A comparison between the fit where all PWN parameters are free to vary and the fit where some PWN parameters are tied between observations yields a $F$-test probability of 22 percent for the fit improvement of the former to be produced by chance. $F$-test comparisons for fits to the inner nebula and pulsar spectra yield probabilities of 41 percent and 11 percent, respectively. These probabilities indicate that tied values of $N_{\rm H}$ and photon index $\Gamma$ are sufficient to describe the combined spectra, and we also see that all model parameter values for both sets of fits are within each other's uncertainties. Thus, $N_{\rm H}$ and $\Gamma$ do not change between 2006 and 2016 observations. While the PWN and pulsar fluxes are also the same, the inner nebula flux may be different, although uncertainties in the precise spectral extraction and inferred values allow for consistency between 2006 and 2016.

Figure 6.3 shows the PWN, inner nebula, and pulsar spectra best-fit models, with model parameters tied between observations. For the PWN, $N_{\rm H} = (13.1 \pm 0.9) \times 10^{22}$ cm$^{-2}$, $\Gamma = 1.5 \pm 0.1$, and absorbed 2–10 keV flux $f^{\rm abs}_{2-10} \approx 7.6 \times 10^{-12}$ erg cm$^{-2}$ s$^{-1}$. The flux is constant across the 10 years between observations and equates to an unabsorbed 0.3–10 keV flux $f_{\rm X} = 1.8 \times 10^{-11}$ erg cm$^{-2}$ s$^{-1}$ and luminosity $L_{\rm X} = 5.4 \times 10^{34}$ erg s$^{-1}$ $(d/\ 5\ {\rm kpc})^2$. For PSR J1813-1749, $\Gamma = 1.2 \pm 0.1$ and $f^{\rm abs}_{2-10} \approx 1.5 \times 10^{-12}$ erg cm$^{-2}$ s$^{-1}$, which results in $f_{\rm X} = 3.1 \times 10^{-12}$ erg cm$^{-2}$ s$^{-1}$ and $L_{\rm X} = 9.3 \times 10^{33}$ erg s$^{-1}$ $(d/\ 5\ {\rm kpc})^2$. The X-ray luminosity relative to spin-down power of PSR J1813-1749 is $L_{\rm X}/\dot{E} = 1.7 \times 10^{-4}$ (assuming a distance of 5 kpc), and it is $L_{\rm X}({\rm PWN})/\dot{E} = 9.6 \times 10^{-4}$ for the PWN; these are typical for rotation-powered pulsars [47, 48, 87].

We briefly compare our spectral fitting results to those of previous works. Helfand et al. [135] fit the PWN spectra (ObsID 6685) with absorption $N_{\rm H} = 9.8^{+1.2}_{-0.9} \times 10^{22}$ cm$^{-2}$, $\Gamma = 1.3 \pm 0.3$ (errors are at 90 percent confidence), and $f^{\rm abs}_{2-10} = 5.6 \times 10^{-12}$ erg cm$^{-2}$ s$^{-1}$. Spectra of the inner nebula and pulsar are each fit with a PL and fixing $N_{\rm H}$ to that of the PWN. The inner nebula spectral fit yields $\Gamma = 0.4^{+0.4}_{-0.7}$ and $f^{\rm abs}_{2-10} = 4 \times 10^{-13}$ erg cm$^{-2}$ s$^{-1}$, while the pulsar spectral fit yields $\Gamma = 1.3 \pm 0.3$ and $f^{\rm abs}_{2-10} = 1.3 \times 10^{-12}$ erg cm$^{-2}$ s$^{-1}$. Kuiper and Hermsen [161] analyze a 98 ks *XMM-Newton* EPIC-pn spectrum taken on 2009 March 27 (ObsID 0552790101) and, with an extraction radius of $15''$ which includes some contribution from the PWN,

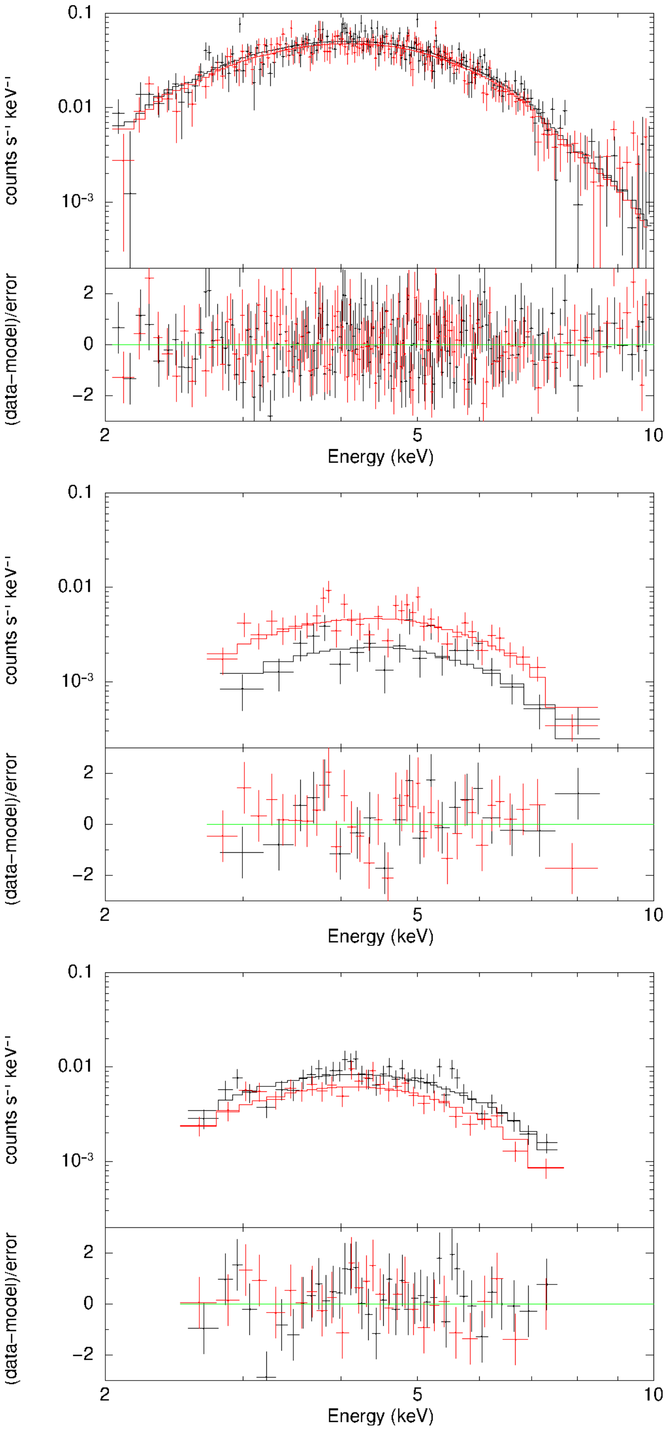

Figure 6.3: Upper panels show *Chandra* spectra (black for ObsID 6685 and red for merged 17695/17440) of the PWN (top), inner nebula (middle), and PSR J1813-1749 (bottom) and best-fit absorbed power law model. The model is from the analysis with $N_{\mathrm{H}}$ and $\Gamma$ tied between observations and $N_{\mathrm{H}}$ for the inner nebula and pulsar fixed to the best-fit value ($N_{\mathrm{H}} = 13.1 \times 10^{22}$ cm$^{-2}$) for the PWN. Lower panels show fit residuals.

find a consistent photon index $\Gamma = 1.31 \pm 0.01$ and flux $f^{\rm abs}_{2-10} = (1.94 \pm 0.11) \times 10^{-12}$ erg cm$^{-2}$ s$^{-1}$ but somewhat higher absorption $N_{\rm H} = (11.7 \pm 0.35) \times 10^{22}$ cm$^{-2}$. Townsley et al. [228] fit the 2006 and 2016 *Chandra* spectral data used here and find $N_{\rm H} = (17 \pm 2) \times 10^{22}$ cm$^{-2}$, $\Gamma = 1.6 \pm 0.3$, and absorbed 2–8 keV flux $f^{\rm abs}_{2-8} = (0.8 - 0.9) \times 10^{-12}$ erg cm$^{-2}$ s$^{-1}$.

Other than absorption $N_{\rm H}$, our best-fit model parameter values for the PWN, inner nebula, and pulsar agree with those of Helfand et al. [135] in their analysis of just the 2006 *Chandra* data, except for a ≈ 20 percent difference in inferred flux of the PWN, and with the parameter values of Kuiper and Hermsen [161] and Townsley et al. [228]. For $N_{\rm H}$, our fit to the PWN spectrum using either the 2006, 2016, or combined data yields $N_{\rm H} \sim (12 - 15) \times 10^{22}$ cm$^{-2}$, which is significantly higher than Helfand et al. [135] find from their fit to the 2006 observation, i.e., $\approx (9 - 11) \times 10^{22}$ cm$^{-2}$ [see also [178], who find $\approx (5 - 13) \times 10^{22}$ cm$^{-2}$]. Note that the Galactic HI column density in the direction of PSR J1813-1749 implies only $N_{\rm H} = 1.7 \times 10^{22}$ cm$^{-2}$ [140]. A similarly high absorption, albeit with large uncertainties, is obtained in our fit to the pulsar (or inner nebula) 2006 or 2016 spectrum, which is in agreement with $\sim 17 \times 10^{22}$ cm$^{-2}$ from the pulsar spectral fits of Townsley et al. [228]. In addition, fits of *XMM-Newton* data, which cannot fully separate PWN and pulsar emission components, yield a high absorption of $N_{\rm H} \approx (10 - 13) \times 10^{22}$ cm$^{-2}$ [97] and $(11 - 12) \times 10^{22}$ cm$^{-2}$ [161]. Therefore, a higher value of $N_{\rm H}$ than that found by Helfand et al. [135] is likely more indicative of the X-ray absorption of the PWN and pulsar (see also discussion of $N_{\rm H}$ and its implication on the distance to PSR J1813-1749 in [117]).

## 6.3 Timing analysis of *NICER* data

We process and filter *NICER* data of PSR J1813-1749 (see Table 6.1) using HEASoft 6.26.1, NICERDAS 2019-06-19_V006a, and the `psrpipe.py` script from the NICERsoft package[3]. We exclude all events from "hot" detector 34, which gives elevated count rates in some circumstances, and portions of exposure accumulated

---

[3] `https://github.com/paulray/NICERsoft`

during passages through the South Atlantic Anomaly. *NICER* experienced a time stamp anomaly which resulted in incorrect time stamps for data taken with MPU1[4] between 2019 July 8 and 23; we follow the recommended procedure for excluding MPU1 data (for only ObsIDs 2579030201–4) from our analysis[5]. Using these filtering criteria, we obtain a total of 301,084 events with individual exposure times shown in Table 6.1 and a total exposure time of 159 ks. We run `barycorr` to transform between Terrestrial Time, used for event time stamps, and Barycentric Dynamical Time (TDB). We adopt the JPL-DE405 solar system ephemeris and absolute sky position measured using the most recent *Chandra* observation (ObsID 17440 from 2016 June 5), i.e., R.A.= $18^{\rm h}13^{\rm m}35\overset{\rm s}{.}112$, decl.= $-17°49'57\overset{''}{.}57$ (J2000).

*NICER* is sensitive to 0.25–12 keV photons. Previous measurements of the 44.7 ms spin period of PSR J1813-1749 are made at 2–10 keV using *Chandra* and *XMM-Newton* with a pulsed fraction $\approx 50$ percent [111, 117, 161] and at ∼2–27 keV using *RXTE*, with pulsations being stronger at lower energies [161]. As we show in Section 6.2.2 and in agreement with previous works, the pulsar spectrum suffers from strong interstellar absorption ($N_{\rm H} \sim 10^{23}$ cm$^{-2}$). Therefore we initially select data in the 1–10 keV range, resulting in 218,624 events. We do not conduct spectral analyses using *NICER* data since the large non-imaging field of view implies an extracted spectrum will primarily be due to that of the PWN and supernova remnant, and spectra from *Chandra* and *XMM-Newton* of these extended sources are presented in other studies [97, 135].

We perform a blind pulsation search[6] on the merged dataset of all 14 *NICER* observations, using the time differencing technique applied to $\gamma$-ray data in previous works [38, 6, 208]. We use a time window of 524,288 seconds (Fast Fourier Transform size = 67108864, with resolution of $1.90735 \times 10^{-6}$ Hz) and scan $\dot{\nu}/\nu$ between 0 and $1.300 \times 10^{-11}$ Hz in 6494 steps of $2.002 \times 10^{-15}$ Hz. The best pulsation candidate has a frequency $\nu = 22.35194397$ Hz and $\dot{\nu} = -6.480 \times 10^{-11}$ Hz s$^{-1}$ at

---

[4] MPU's are collections of 8 detectors.

[5] `https://heasarc.gsfc.nasa.gov/docs/nicer/data_analysis/nicer_analysis_tips.html\#July2019-MPU1_Timing_Errors`

[6] Although the spin characteristics for this pulsar were already known, more standard search techniques had failed to yield a *NICER* detection.

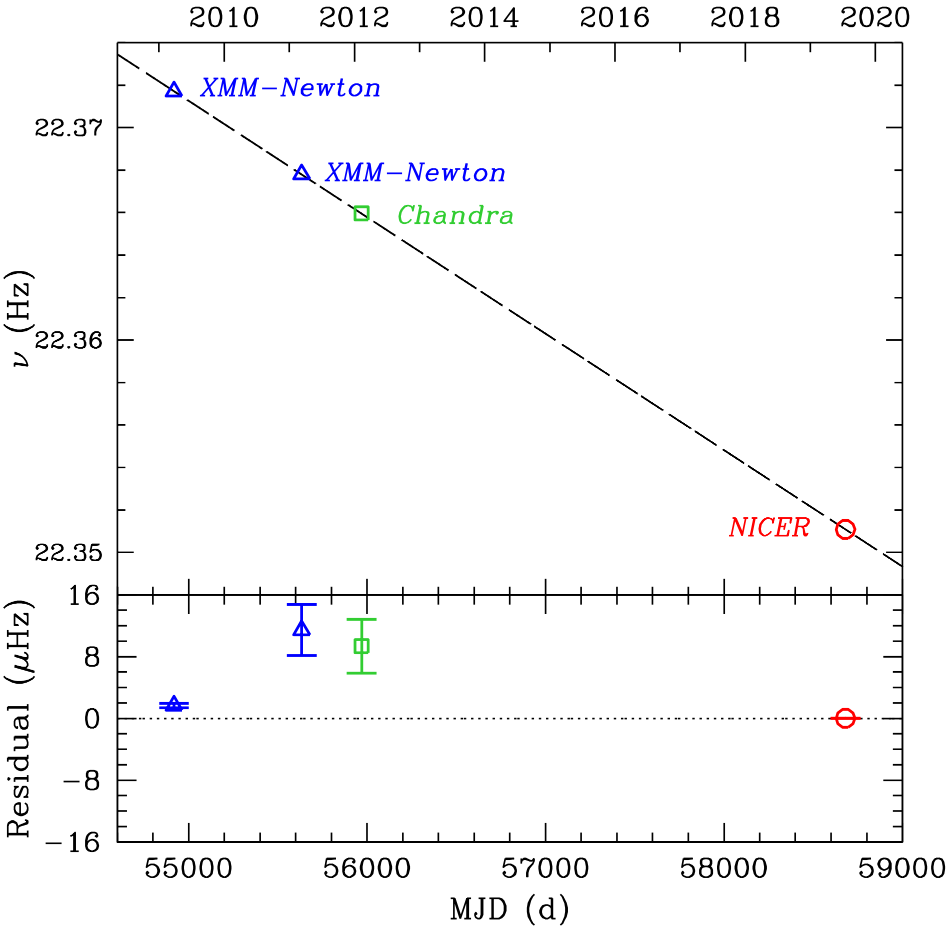

Figure 6.4: Top: Spin frequency of PSR J1813-1749 as measured using *XMM-Newton* in 2009 and 2011, *Chandra* in 2012, and *NICER* in 2019. Dashed line shows a linear model fit to the spin frequencies, with best-fit slope $\dot{\nu} = -6.3445 \times 10^{-11}$ Hz s$^{-1}$. Bottom: Spin frequency residual after subtracting off the best-fit linear model. Error bars are $1\sigma$ uncertainty in measured $\nu$.

MJD 58527.51318287 (mid-point of observations), with a p-value of $8.9 \times 10^{-7}$. Recall that Halpern, Gotthelf, and Camilo [117] determine an incoherent timing model with $\nu = 22.3717124$ Hz and $\dot{\nu} = -6.333 \times 10^{-11}$ Hz s$^{-1}$ at MJD 54918.14; this $\dot{\nu}$ leads to a frequency change $\Delta\nu = -0.01975$ Hz by the time of the *NICER* observations and an expected $\nu = 22.35196$ Hz, which closely matches our detection, while a $\ddot{\nu}$ contribution, assuming a braking index $n \equiv \nu\ddot{\nu}/\dot{\nu}^2 = 3$, would only change the $\dot{\nu}$ from Halpern, Gotthelf, and Camilo [117] by 0.3 percent to $\dot{\nu} \approx -6.317 \times 10^{-11}$ Hz s$^{-1}$.

We improve detection significance and refine the timing model using a Markov

Chain Monte Carlo (MCMC) refiner in combination with the PINT package[7] and the $H$-statistic as a measure of significance [75, 148]. Here we ignore the first observation (ObsID 1020440101) because of its short exposure time and because it is too far removed in time (ten months) from the other observations to smoothly connect with the timing model obtained from these later observations. We add an increasing number of terms in frequency derivative and stop at $\ddot{\nu}$ (see below) since the addition of $\dddot{\nu}$ only yields a marginal $H$-test improvement. We use TEMPO2 [143] with the `photons` plugin[8] to assign pulse phases to each event. Then using the `ni_Htest_sortgti.py` script from the NICERsoft package, we determine the optimum energy range to be 3.0–9.2 keV (124,656 events), which yields a maximum significance of $10.1\sigma$; we note that the choice of lowest energy to include has a large impact on detection significance while the choice of highest energy produces very similar significance levels. The resulting timing model has $\nu = 22.351086 \pm 0.000002$ Hz, $\dot{\nu} = (-6.07 \pm 0.01) \times 10^{-11}$ Hz s$^{-1}$, and $\ddot{\nu} = (-1.0221 \pm 0.0001) \times 10^{-17}$ Hz s$^{-2}$. The large negative value of $\ddot{\nu}$ implies that, not only is $\dot{\nu}$ becoming more negative, but $\dot{\nu}$ changes significantly over the short timespan covered by the timing model, i.e., $|\Delta\dot{\nu}/\dot{\nu}| = 0.55$ in 37.5 days. Such a $\ddot{\nu}$ cannot be the pulsar's long-term value since it would produce a different $\dot{\nu}$ from that determined about a decade ago, and instead likely reflects timing noise present in the pulsar. Figure 6.4 shows the spin frequency of PSR J1813-1749 over the last ten years, i.e., those from 2009–2012 measured by Halpern, Gotthelf, and Camilo [117] and our 2019 narrow windows search result (see below). A simple linear model fit to these $\nu$ yields a best-fit spin-down rate of $\dot{\nu} = (-6.3445 \pm 0.0004) \times 10^{-11}$ Hz s$^{-1}$, which is within $3\sigma$ of that determined by Halpern, Gotthelf, and Camilo [117], i.e., $\dot{\nu} = (-6.3335 \pm 0.0032) \times 10^{-11}$ Hz s$^{-1}$, and is clearly the long-term spin-down rate of the pulsar. In addition to the blind searches described above, we perform a search in narrow windows around the expected $\nu$ and $\dot{\nu}$ (i.e., $\nu = [22.35108\text{ Hz}, 22.35108995\text{ Hz}]$ with steps of $5 \times 10^{-8}$ Hz and $\dot{\nu} = [-7 \times 10^{-11}\text{ Hz s}^{-1}, -6 \times 10^{-11}\text{ Hz s}^{-1}]$ in steps of $1 \times 10^{-13}$ Hz s$^{-1}$) and assuming $\ddot{\nu} = 0$. Search results (with $H$-test value of 72) are presented in Table 6.4,

---

[7] `https://github.com/nanograv/PINT`

[8] `http://www.physics.mcgill.ca/~aarchiba/photons_plug.html`

| Parameter | Value |
|---|---|
| R.A. (J2000) | $18^{\mathrm{h}}13^{\mathrm{m}}35\overset{\mathrm{s}}{.}112$ |
| Decl. (J2000) | $-17^{\circ}49'57\overset{''}{.}57$ |
| Position epoch (MJD) | 57544 |
| Timing reference epoch (MJD) | 58681.04405092593 |
| Spin frequency $\nu$ (Hz) | 22.351083818(17) |
| 2019 June–2019 August | |
| Timespan of model (MJD) | 58662.3–58699.8 |
| Frequency derivative $\dot{\nu}$ (Hz s$^{-1}$) | $-6.4283(33) \times 10^{-11}$ |
| 2009 March–2019 August | |
| Timespan of model (MJD) | 54918.14–58699.8 |
| Frequency derivative $\dot{\nu}$ (Hz s$^{-1}$) | $-6.34450(44) \times 10^{-11}$ |

Table 6.4: Timing parameters of PSR J1813-1749. Two sets of parameters are provided: The first is from a narrow windows search of only the 2019 *NICER* data (see text); the second is from a linear fit of $\nu$ from 2009–2012 and $\nu$ from the first set. Number in parentheses is $1\sigma$ error in last digit.

including a $\dot{\nu} = (-6.428 \pm 0.003) \times 10^{-11}$ Hz s$^{-1}$, which differs but is much closer to the long-term value.

To investigate possible changes in the timing parameters within the *NICER* dataset, we break the dataset into three segments, i.e., ObsIDs 2579030101–3 (2019 June 28–30) for 52 ks of total exposure, ObsIDs 2579030201–4 (July 10–13) for 50 ks, and ObsIDs 2579030301–6 (July 30–August 4) for 49 ks. The first *NICER* observation of 6 ks exposure time (ObsID 1020440101) is dropped since it is not long enough to yield an independent detection on its own. A blind search is run on each segment independently, with the same search parameters as given above. A clear detection is made only in the third segment, and the best pulsation candidate has $\nu =$ 22.35099411 Hz and $\dot{\nu} = -6.217 \times 10^{-11}$ Hz s$^{-1}$, which are consistent with results from the merged dataset search, with a p-value of $5.62 \times 10^{-5}$. Meanwhile, performing a search of each segment in a narrow window, with steps in $\nu$ of $1 \times 10^{-7}$ Hz but using a fixed $\dot{\nu} = -6.428 \times 10^{-11}$ Hz s$^{-1}$, yields a detection in all three segments ($H$-test values $> 30$). There is also evidence from the structure of the significance peaks in $\nu$ in the third segment that a glitch of magnitude $\Delta\nu \approx 3$ $\mu$Hz occurred on MJD 58698, but data limitations prevent a more definitive conclusion.

In summary, Table 6.4 presents the final parameters of two timing models we derived above. The first is based on only the narrow windows search of the 37 d

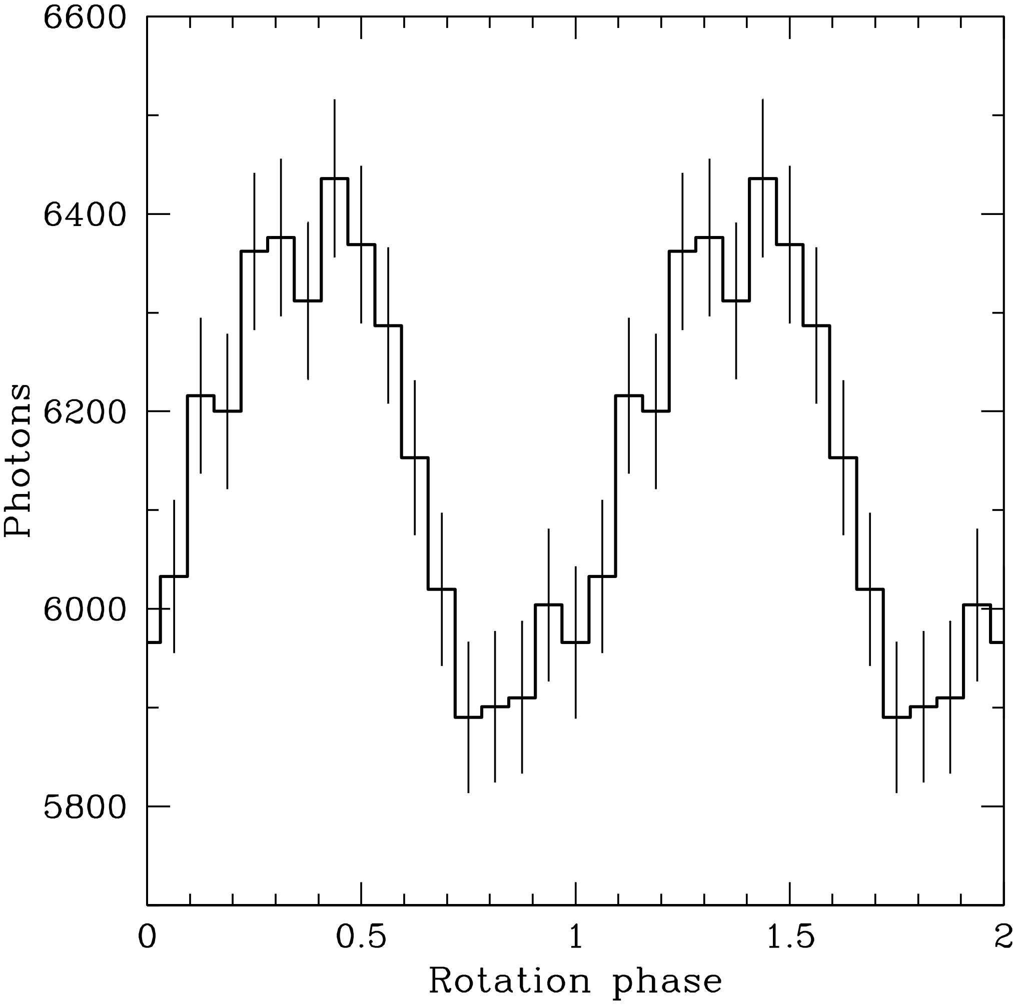

Figure 6.5: Pulse profile (3–9.2 keV) of PSR J1813-1749 using the 2019-only timing model given in Table 6.4. Two rotation cycles are shown, with 16 bins per cycle. Error bars are $1\sigma$.

span in 2019 of *NICER* data. The second is based on the linear fit to the long-term ten-year spin frequency evolution starting from 2009 to our 2019 measurement using *NICER* and shown in Figure 6.4. The main distinction between the two is $\dot{\nu} = -6.428 \times 10^{-11}$ Hz s$^{-1}$ in the former and $\dot{\nu} = -6.3445 \times 10^{-11}$ Hz s$^{-1}$ in the latter. We also show in Figure 6.5 the 3–9.2 keV pulse profile using *NICER* data and the *NICER*-only timing model; because *NICER* cannot spatially resolve PWN and supernova remnant contributions to the unpulsed component of the pulse profile, an estimate of the pulsed fraction would be unreliable.

There are several possible explanations for the differing spin-down values, such as the pulsar's timing behavior is affected by timing noise, glitches, and/or mode switching. First, young pulsars, such as PSR J1813-1749, tend to exhibit timing noise [142, 211, 88]. For example, PSR J1124-5916 in the supernova remnant G292.0+1.8 has comparable spin properties but is noisy; it also has a low negative braking index and glitched at least once [201]. As for glitches, PSR J1813-1749 could glitch at a rate as high as once every $\approx 200$ d, based on its spin-down rate $\dot{\nu}$ [133].

In this case, there is a $\approx 15$ percent probability one glitch occurred during the *NICER* observations if glitch occurrence follows Poisson statistics, and we indeed have tentative evidence for the occurrence of such a glitch. However, Fuentes et al. [96] and Fuentes, Espinoza, and Reisenegger [95] find that, while glitch activity correlates with spin-down rate for $|\dot{\nu}| < 10^{-10.5}$ Hz s$^{-1}$ and is highest at the top of this range, some pulsars with even greater $|\dot{\nu}|$ show lower glitch activity. Thus PSR J1813-1749 could have a relatively low rate of glitches since it has a $|\dot{\nu}| = 10^{-10.2}$ Hz s$^{-1}$, but this is far from certain.

Lastly, some pulsars switch between radio emission states, such that their spin-down rate can be up to 50 percent higher when in an active state [157, 174, 137]. In the case of PSR J1813-1749, the best-fit long-term spin-down rate differs from that of the timing model by only 1 percent. Dzib et al. [85] indicate pulsed radio emission may have been detected but only at high frequencies due to extreme scattering. An interesting comparison could potentially be made between PSR J1813-1749 and the third highest $\dot{E}$ pulsar, PSR B0540-69, which glitches and has a similar age ($\sim 1000$ yr) and spin rate ($= 19.7$ Hz) and $\dot{\nu}$ and $\ddot{\nu}$ that changed from $-1.87 \times 10^{-10}$ Hz s$^{-1}$ to $-2.53 \times 10^{-10}$ Hz s$^{-1}$ and $3.7 \times 10^{-21}$ Hz s$^{-2}$ to $0.1 \times 10^{-21}$ Hz s$^{-2}$, respectively, due possibly to a switch between radio emission states [90, 180, 179]. More extensive X-ray monitoring and continued searches in radio may be able to answer this issue.

## 6.4 Conclusions

In this work, we analyze *Chandra* and *NICER* observations of the highly energetic rotation-powered pulsar PSR J1813-1749. The ten years between *Chandra* observations allow us to measure a pulsar proper motion $\mu_{\mathrm{R.A.}} = -0.\!\!''067\ \mathrm{yr}^{-1}$ and $\mu_{\mathrm{decl.}} = -0.\!\!''014\ \mathrm{yr}^{-1}$, which implies a transverse velocity $v_{\perp} = 1600\ \mathrm{km\ s}^{-1}\ (d/\ 5\ \mathrm{kpc})$; note the distance is uncertain, with a range of 3–5 kpc [184, 117]. *Chandra* spectra of the pulsar and its PWN can each be well-fit by an absorbed power law model and reveal no evidence of significant changes in flux and model parameters between observations. However, we find that the X-ray absorption ($N_{\mathrm{H}} = 13.1 \times 10^{22}\ \mathrm{cm}^{-2}$) is higher than that found in early studies but in agreement with more recent works. We detect pulsations at the 44.7 ms spin period of PSR J1813-1749 using recent *NICER* data. We find that the spin-down rate determined over the past decade differs from that measured over a month with the timing model.

The spin period of PSR J1813-1749 has only been previously measured using *XMM-Newton* in 2009 and 2011 and *Chandra* in 2012 and not found in radio or using *Fermi* [117, 161]. The pulsar is a target of interest for direct gravitational wave (GW) searches. These searches are beginning to achieve meaningful constraints on possible energy loss due to GW emission in the case of PSR J1813-1749 [3, 5]. The most sensitive searches that can be conducted are those that have contemporaneous electromagnetic timing models [4]. If such a timing model had been available for PSR J1813-1749, an improvement of ~5 on upper limits to GW strain and ~25 to GW energy would have been possible over those obtained in the less sensitive search by Abbott et al. [5]. Efforts are underway to search the latest, most sensitive GW data from the third observing run (O3), which collected data from 2019 April 1 to 2020 March 27. The contemporaneous timing model provided here using *NICER* data will enable improved limits on GW emission from this highly energetic pulsar.

## 6.5 Soft Pulsar Investigations

Independently of the work detailed above, we (Principal Investigator P.M. Saz Parkinson, with A. Belfiore, P.Caraveo, M.Marelli, R.P. Johnson, A. Harding, J. Rodriguez Garcia, and myself) identified PSR J1813-1749 as a possible "soft" $\gamma$-ray pulsar, which would have peak emissions in the MeV range. PSR J1813-1749 was identified as a candidate primarily because of its large spindown flux. Additionally, high resolution X-ray observations provide a precise position that greatly aids pulsation searches in *Fermi*-LAT data. Finally, there is a 4FGL source coincident with the position of PSR J1813-1749 (although, this source is extended, meaning there is likely a large contribution from the PWN)[13]. The above factors make a search for PSR J1813-1749 with *Fermi*-LAT both promising and practical.

In support of this project, we applied for and received NuSTAR observations of PSR J1813-1749. When combined with a theoretical *Fermi*-LAT detection, NuSTAR's high-energy X-ray data and *Fermi*-LAT's MeV $\gamma$-ray data provide the kind of broad-band spectral information necessary for well constrained tests of the pulsar emission mechanism[9].

### 6.5.1 Preliminary *Fermi*-LAT Analysis

The *Fermi*-LAT analysis utilizes `Fermipy`[247] 1.0.1 and `FermiTools` 2.0.8, spans the time range of August 4, 2008 (MJD 54682.7) to September 13, 2021 (MJD 59470.7), and covers an energy range of 50 MeV to 1 TeV. Pass 8 reprocessed [39, 58] data is used, specifically the P8R3_SOURCE_V3 instrument response function. The region of interest (RoI) is centered at the position of 4FGL J1813.1-1737e (RA=262.5°, DEC=$-24.1°$).

A binned analysis is performed using a similar binning schema to that of the 8-year *Fermi*-LAT Fourth Source Catalog [13] (further detailed in Sec. 4.1.2), and as shown in Table 6.5. A correction for energy dispersion is applied by setting `edisp_bins`=-2 in the `FermiTools`[10].

---

[9] Such a test was carried out for PSR J0218+4232 (although, not a soft $\gamma$-ray pulsar), as detailed in Chapter 9.

[10] See Chapter 4.1.6 for further details on energy dispersion.

| Energy Interval (GeV) | NBins | Width (deg) | Zmax (deg) | Pixel Size (deg) | | | | |
|---|---|---|---|---|---|---|---|---|
| | | | | PSF0 | PSF1 | PSF2 | PSF3 | All |
| 0.05 - 0.1 | 3 | 7.9 | 80 | ... | ... | ... | 0.6 | ... |
| 0.1 - 0.3 | 5 | 7.9 | 90 | ... | ... | 0.6 | 0.6 | ... |
| 0.3 - 1 | 6 | 5.9 | 100 | ... | 0.4 | 0.3 | 0.2 | ... |
| 1 - 3 | 5 | 4.9 | 105 | 0.4 | 0.15 | 0.1 | 0.1 | ... |
| 3 - 10 | 6 | 3.9 | 105 | 0.25 | 0.1 | 0.05 | 0.04 | ... |
| 10 - 1000 | 10 | 2.9 | 105 | ... | ... | ... | ... | 0.04 |

Table 6.5: Specifics of the 15 component model used when analyzing the RoI, with each PSF selection corresponding to a single component. Nbins refers to the number of energy bins, and Zmax refers to the maximum zenith angle. Width is the size of the total extracted region, which is composed of a 0.9° core surrounded by a ring of various widths.

After the data has been binned, an initial RoI model is created by querying the 4FGL for sources which lie within a square 20° × 20° region centered on 4FGL J1813.1-1737e. The RoI model is iteratively fit to the data, with sources being removed if they have a test statistic (TS) that falls below 9, which is approximately equivalent to $3\sigma$[11]. 4FGL J1813.1-1737e is modeled with a LogParabola spectral shape[12]:

$$\frac{dN}{dE} = N_0 \left( \frac{E}{E_b} \right)^{-(\alpha + \beta \log{(E/E_b)})} \tag{6.1}$$

where $E_b$ is a scale parameter which remains fixed[181]. J1813 is an extended source, as opposed to a point source, with the extension modeled as a disk with radius 0.6°.

The final fit is performed with Minuit [149]. The normalization ($N_0$), $\alpha$, and $\beta$ of 4FGL J1813.1-1737e is allowed to vary, along with the index and normalization of the galactic diffuse background, and the normalization of background sources with TS > 100. This produces the photon and energy flux presented in Table 6.6. Utilizing the "`gtsrcprob`" `FermiTool` this model is also used to assign photons a probability (weight) that they originate from 4FGL J1813.1-1737e, as opposed to other sources in the model[13].

The spectrum of 4FGL J1813.1-1737e is generated via the techniques described in Sec. 4.1.9. To find the total spectrum, $N_0$, $\alpha$ and $\beta$ of 4FGL J1813.1-1737e and

---

[11] See Appendix 4.1.1 for further information on the test statistic, and Appendix A.1 for a derivation of this approximation.

[12] `https://fermi.gsfc.nasa.gov/ssc/data/analysis/scitools/source_models.html`

[13] See Sec. 4.1.11 for further discussion on photon probability weighting

| Parameter | Value |
|---|---|
| $N_0$ (ph cm$^{-2}$ s$^{-1}$ MeV$^{-1}$)....... | $(4.4 \pm 0.1) \times 10^{-12}$ |
| $E_b$ (MeV) ...................... | 2053 (fixed) |
| $\alpha$............................. | $(2.43 \pm 0.04)$ |
| $\beta$ ............................. | $0.23 \pm 0.02$ |
| Photon flux (photons cm$^{-2}$ s$^{-1}$) | $(7.67 \pm 0.15) \times 10^{-8}$ |
| Energy flux (MeV cm$^{-2}$ s$^{-1}$) ... | $(3.05 \pm 0.04) \times 10^{-5}$ |

Table 6.6: $\gamma$-ray spectral parameters for the total emission from 4FGL J1813.1-1737e. Photon and energy flux cover the entire 50 MeV - 1 TeV energy range.

the index and normalization of the galactic diffuse background is again allowed to vary. However, the normalization of background sources is only allowed to vary if the source has a TS $>$ 1000. This produces the spectrum shown in Fig. 6.6. Notably, the high-energy spectral points do not appear to be in good agreement with the global-fit spectrum. As previously mentioned, we know that, as an extended source, 4FGL J1813.1-1737e cannot *actually* be PSR J1813-1749. We have speculated that including a point source in the model as PSR J1813-1749 while keeping 4FGL J1813.1-1737e as the PWN may improve the agreement. However, this has not yet been attempted.

Nevertheless, we applied the *NICER* timing solution presented in Table. 6.4 to the weighted *Fermi*-LAT data. While this did not produce significant pulsations, we remain optimistic that PSR J1813-1749 may yet be detectable in $\gamma$-rays. For example, the *NICER* timing solution may be too short for the pulsar's signal to overcome background noise from the PWN. If this is the case, blind search techniques performed over longer spans of data may be a fruitful path forward.

## 6.6 Acknowledgements

The authors thank the anonymous referee for comments which led to improvements in the manuscript. WCGH thanks D.L. Kaplan and G.G. Pavlov for helpful comments on astrometry analysis, P.S. Ray for advice on timing analysis, and W.A. Majid for comments on an early draft. WCGH appreciates use of computer facilities at the Kavli Institute for Particle Astrophysics and Cosmology. WCGH acknowledges support through grant 80NSSC19K1444 from NASA. SG acknowledges support of

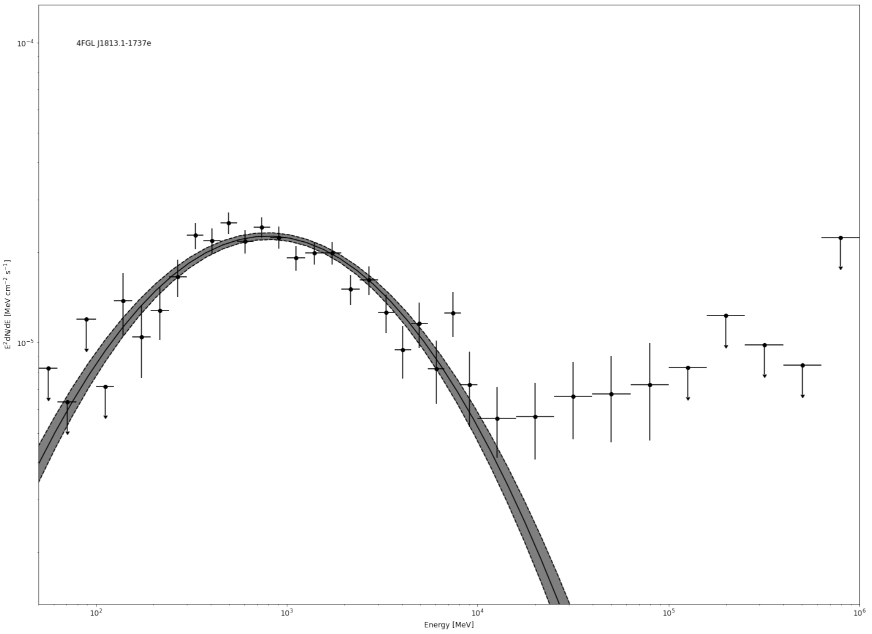

Figure 6.6: The spectrum of 4FGL J1813.1-1737e.

CNES. MB is partially supported by Polish NCN grant no. 2017/26/M/ST9/00978. CME acknowledges funding from ANID grant FONDECYT/Regular 1171421. CM is supported by an appointment to the NASA Postdoctoral Program at Marshall Space Flight Center, which is administered by Universities Space Research Association under contract with NASA.

# Chapter 7

# PSR J1846-0258: Gone from 3PC, but not Forgotten

The following chapter is a modified excerpt from the Third Fermi Pulsar Catalog (3PC, in preparation), detailing my work to reproduce the published detection of PSR J1846-0258 [163], and attempting to detect the pulsar in a second time period with the aid of NICER. While the former was successful, applying a NICER timing solution to *Fermi*-LAT data did not yield a significant detection.

PSR J1846-0258 (hereafter J1846) is a young ($\tau \approx 723$ yr, the third youngest known), high magnetic field ($5 \times 10^{13}$G) pulsar located in the Kes 75 supernovae remnant [113]. Although radio quiet [32], it has been timed regularly in X-rays by RXTE, Swift, INTEGRAL, and, recently, NICER. J1846 behaves largely as a rotation powered pulsar, but has twice exhibited magnetar-like outbursts [100, 53]. These outbursts have garnered interest in this source as a "transitioning" pulsar, possibly able to shed light on the evolutionary relationship between rotation powered pulsars and magnetars. It is the only *Fermi*-LAT pulsar with a published $\gamma$-ray detection which did not meet the significance criteria to appear in the 3PC [163]. Additionally, this source is believed to be a "soft" $\gamma$-ray pulsar, with peak emissions in the MeV range [161]. The X-ray spectrum suggests that *Fermi*-LAT may well be able to detect (at the 5 $\sigma$ level or greater) the the high energy tail of these pulsations, with such a detection aiding research into the soft pulsar emission mechanism [226].

| Start<br>(MJD) | Finish<br>(MJD) | Epoch<br>(MJD) | $\nu$<br>(Hz) | $\dot{\nu}$<br>(Hz s$^{-1}$) | $\ddot{\nu}$<br>(Hz s$^{-2}$) |
|---|---|---|---|---|---|
| 58261 | 58675 | 58468 | 3.04130522(56) | $-6.5675(90) \times 10^{-11}$ | $1.24(64) \times 10^{-20}$ |
| 58675 | 58900 | 58788 | 3.0394921(80) | $-6.59(12) \times 10^{-11}$ | $1.5(35) \times 10^{-20}$ |
| 58900 | 59026 | 58963 | 3.0384935(70) | $-6.58(14) \times 10^{-11}$ | $9.6(76) \times 10^{-21\dagger}$ |

Table 7.1: The spin parameters of PSR J1846-0258 determined during the NICER analysis. The full timing solutions and parameter fit outputs are given in Appendix C.
†: Due to the short time span of this observation, $\ddot{\nu}$ may be unreliable.

## 7.1 Replicating the Prior Detection

Kuiper, Hermsen, and Dekker [163] present a 4.2 $\sigma$ (via unweighted $Z^2_{m=1}$, described in Chapter 5.3.2) detection of J1846 *Fermi*-LAT in the 30 - 100 MeV energy range. This result is achieved by using the *RXTE* PCA and *Swift* XRT to form a phase-aligned timing solution, verifying this solution with *INTEGRAL* ISGRI and the *Fermi* GBM, and, finally, applying it to *Fermi*-LAT data.

To replicate this detection, albeit with Pass 8 Data not available at the time of initial publication[1] , we follow the prescription laid out by the original authors. *Fermi*-LAT Pass 8 data within 11° of J1846 and covering an energy range of 30-100 MeV are selected. The data are filtered to include only times when *Fermi*-LAT is operating nominally.

An additional selection criterion is imposed to include only photons lying within $\theta_{68}$ of J1846, calculated as $\theta_{68}^2(E) = (5\overset{\circ}{.}1)^2(100\,\mathrm{MeV}/E)^{1.56} + (0\overset{\circ}{.}1)^2$ [217][2]. A zenith angle cut is implemented according to $\zeta^{max}_{Earth}(E) = 105° - 2 \times \theta_{68\%}(E)$ to reduce contamination from the Earth's limb while accounting for increasing spatial precision at higher energies. The data is barycentered to $18^{\mathrm{h}}46^{\mathrm{m}}24\overset{\mathrm{s}}{.}94$, $-02°58'30\overset{''}{.}1$ [136] using the JPL DE200 Solar system ephemeris.

The pulsar ephemeris presented in Kuiper, Hermsen, and Dekker [163] is applied to the remaining photons, producing a 4.3$\sigma$ detection consistent with the currently

---

[1] Pass 8 improved sensitivity below 100 MeV, which should increase the detection significance [39]

[2] While this bears a striking similarity to *Fermi*-LAT's PSF as described in Chapter 3.1, the constants used here are determined by an independent process, as described in Bruel [57]. The values are periodically updated with new releases of *Fermi*-LAT data.

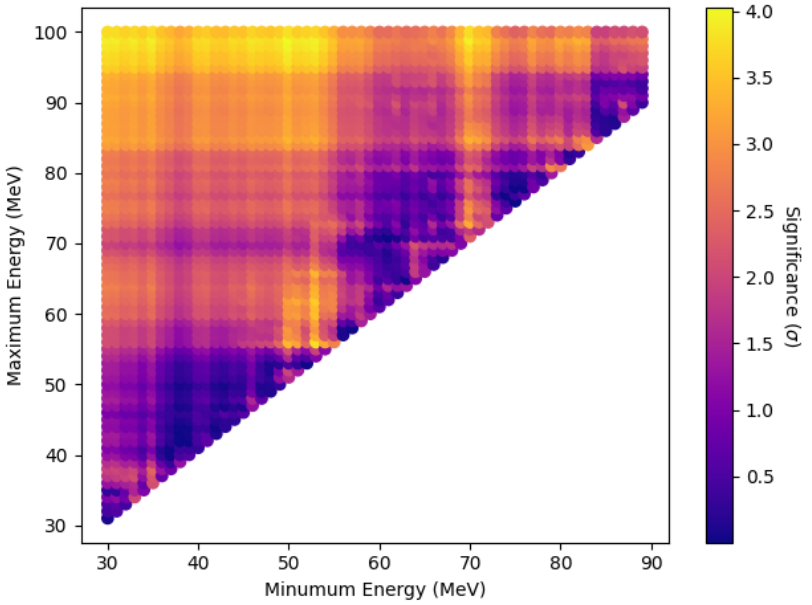

Figure 7.1: The significance of J1846 as a function of minimum and maximum energy. Significance is calculated using the H-Test, and converted to $\sigma$(see Chapter 5.3.3).

published result. If, instead of the $Z^2_{m=1}$ test, the H-Test is used[3], this significance becomes $3.8\sigma$. The majority of detected signal strength appears to come from the higher energy bands(see Fig. 7.1), with, for example, the 83 - 100 MeV range still producing a $2.8\sigma$ result (as measured with the H-Test).

The Kuiper, Hermsen, and Dekker [163] ephemeris is a phase-aligned combination of 10 shorter timing solutions, each modeling J1846 with up to and including two spin derivatives. The average span of an individual timing solution is $\sim$ 370 days, with the overall ephemeris covering $\sim$ 3100 days. There is some overlap in timing solutions, and $\sim$ 150 days over which the X-ray instruments could not accurately time the pulsar are excluded. It is possible that such timing solutions may produce significance vs time curves which peak outside the ephemeris validity range. This is indeed the case with J1846, with a maximum H-Test ($Z^2_{m=1}$) of $4.39\sigma$ ($4.99\sigma$) occurring at $\sim$ 58119 MJD[4] as shown in Fig. 7.2.

---

[3] See Chapter 5.3 for an overview of the $Z^2_m$ and H-tests.

[4] Significances given without accounting for the additional trial factors.

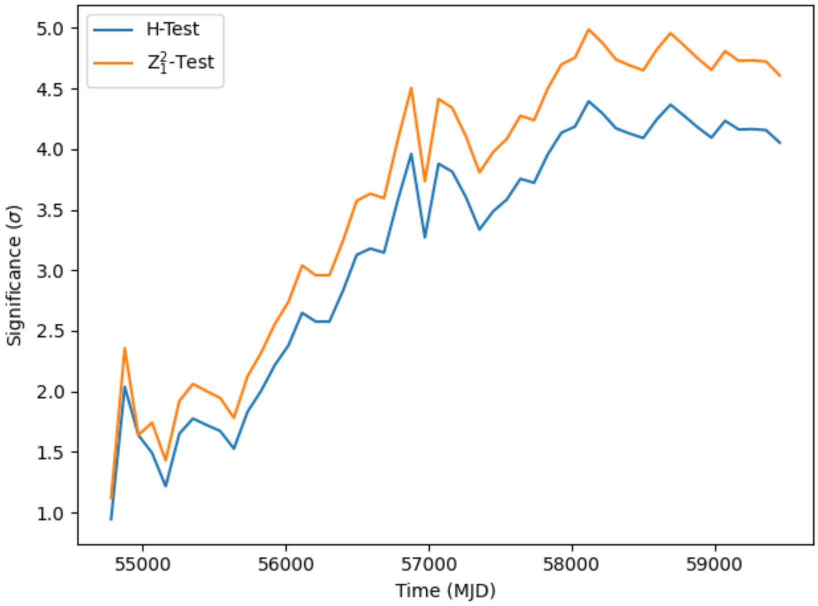

Figure 7.2: The significance of J1846 as a function of time, as calculated with the timing solution presented in Kuiper, Hermsen, and Dekker [163]. Significance is determined by applying the indicated test and converting to $\sigma$(See Chapter 5.3). Although the timing solution ends at MJD 57635, the significance continues to climb until about MJD 58119.

## 7.2 NICER Assisted Analysis

NICER data spanning 58261 - 59026 MJD with a total exposure of 171 ks were processed using NICERDAS[5] 2019-06-19_V006a and the NICERsoft[6] script `psrpipe.py`. The data are again barycentered to the position given in Helfand, Collins, and Gotthelf [136], but the JPL DE405 Solar system ephemeris is used. Three timing solutions were generated covering 415, 226, and 127 days, each consisting of spin parameters up to and including two derivatives (although there is large uncertainty on the second derivative term of the 127 day timing solution), and are presented in Table 7.1 and Appendix C.

Stacking these timing solutions produces a 16.5$\sigma$ signal over the 0.25-12 KeV energy range of NICER. The pulse profile after stacking is shown in Fig. 7.3. When the energy range is optimized to 2.53 - 9.73 KeV via the `ni_Htest_sortgti.py` NICERsoft script, this significance increases to 20.5$\sigma$.

---

[5] `https://heasarc.gsfc.nasa.gov/docs/software/heasoft/`
[6] `https://github.com/paulray/NICERsoft`

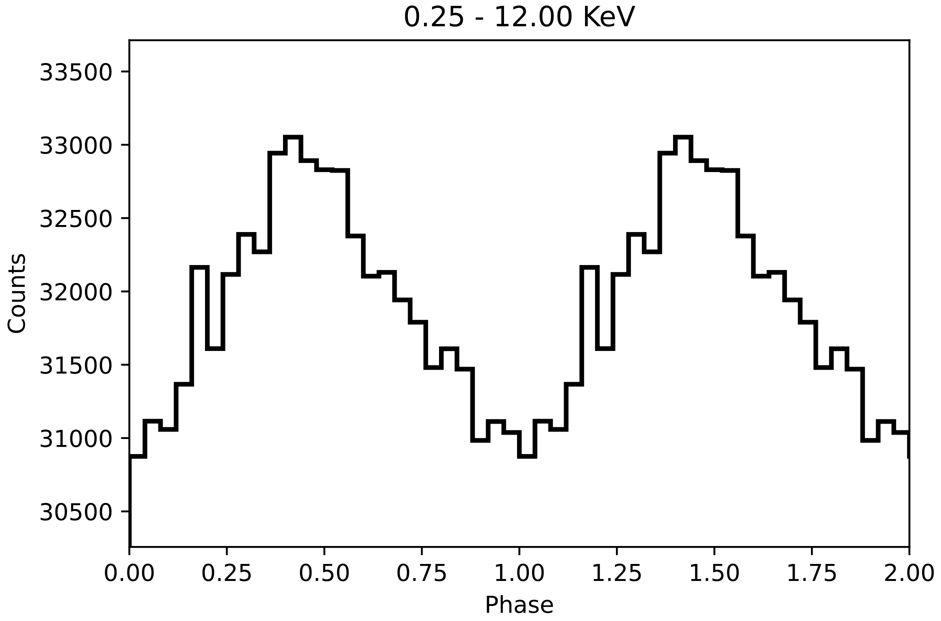

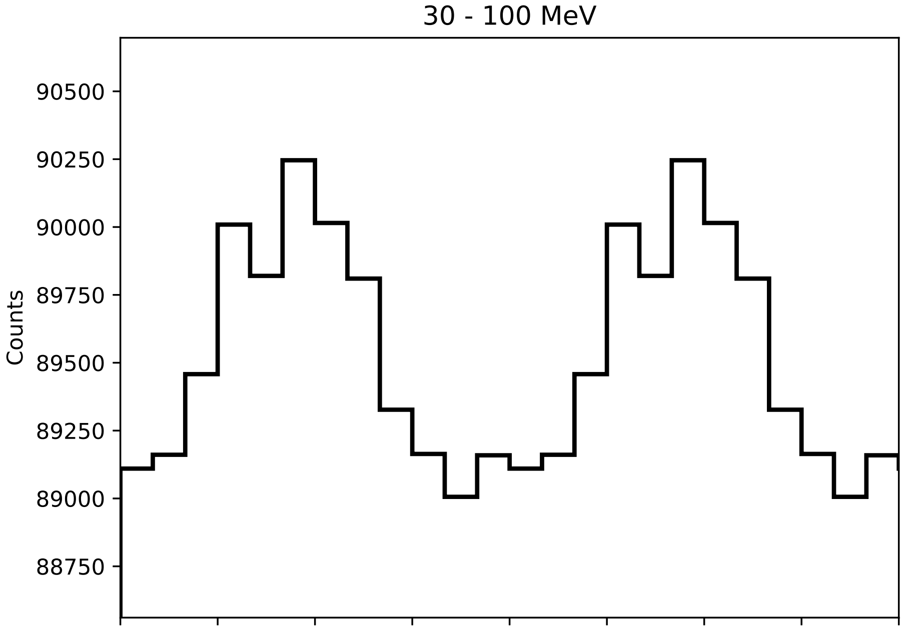

Figure 7.3: The pulse profile of PSR J1846-0258. The data have been duplicated to show two phases.  
**Top**: Using NICER, as described in Sec. 7.2.  
**Bottom**: Using *Fermi*-LAT, as described in Sec. 7.1  
**Note**: These pulse profiles use two different time periods and two different timing solutions. The absolute phase of each pulse should not be compared.

Applying this timing solution to *Fermi*-LAT data prepared using the variable width and zenith angle cuts described in Sec. 7.1 did not produce a pulsed signal. This non-detection is consistent with the previously published results, as the pulsar would only reach a significance of $\sim 2\sigma$ in $\sim$ 770 days if the signal is the same strength as in Kuiper, Hermsen, and Dekker [163].

We also used the NICER timing solution in combination with the "Model Weights" technique described in Bruel [57] in an attempt to detect J1846 with *Fermi*-LAT. This technique uses 6 trials, informed by a study of 144 *Fermi*-LAT pulsars, to scan a range of probable spectral parameters. Once the optimal values are determined, they are used to generate photon weights. Instead of a variable width and zenith angle cut, photon weights are generated by selectively scanning a range of possible pulsar spectral parameters in an attempt to maximize the pulsed signal significance. This technique was applied to 30 MeV - 1 Tev photons from within 11° of J1846, and also failed to yield a detection.

# Chapter 8

# PSR J2022+3842: A Big Softie

The following chapter is an excerpt from a paper in progress on PSR J2022+3842. All elements should be considered preliminary. A more formal introduction will follow, but given the current lack of a formal citation I wish to give credit to those who have contributed to this project since its inception, as well as provide context for the excerpt.

The first $\gamma$-ray pulsations from PSR J2022+3842 were seen by Ohuchi et al. [196] in 2015. Smith [215] extended this detection to cover MJD 55000 - 55750 using contemporaneous observations from the Robert C. Byrd Green Bank Telescope (GBT), RXTE, and XMM-Newton. He has generously provided me with his timing solution, which I use in the work below. An additional multi-wavelength interpretation of the pulse profile during this time period will be presented in an upcoming paper.

In 2018, PSR J2022+3842 was observed by NuSTAR as the result of a proposal led by P.M. Saz Parkinson. These data was analyzed by C. Hu, who is also contributing a joint re-analysis of archival Chandra and XMM-Newton data.

Using observations from NICER, I generated a timing solution for PSR J2022+3842 covering MJD 58083 - 59415. Using the LAT, I perform an all-phase analysis of PSR J2022+3842 covering MJD 54683 - 59470. I use the LAT's best fit model to generate photon *weights*, the probability that a given photon in the analysis originates from the pulsar.

Using the NICER timing solution, as well as the one provided by D.A. Smith, I perform a phased analysis of PSR J2022+3842. The final data product, spectral points, were provided to D. Torres. Combined with X-ray data from [162], he used this in his modeling software to shed light on this pulsar's emission mechanism. We hope to eventually supplement this with the aforementioned X-ray analysis by C. Hu.

Additional contributions to the above have been made by N. Kawai, L. Guillemot, S. Ransom, E.Gotthelf, and C.-Y Ng.

## 8.1 Introduction

PSR J2022+3842 was first discovered by Arzoumanian et al. [36], who believed the supernova remnant (SNR) G76.9+1.0 to be a promising candidate for housing a pulsar. Using the *Chandra* telescope, they were able to precisely locate an X-ray source in an appropriate location to be the pulsar. Follow-up observations with the Robert C. Byrd Green Bank Telescope (GBT) confirmed that this X-ray source was indeed a pulsar, with an analysis of archival RXTE data providing an X-ray pulse profile. At the time, it was believed PSR J2022+3842 was one of the most energetic pulsars discovered, second only to PSR B0531+21 in the Crab Nebula.

Follow-up observations with XMM-Newton showed that this was not the case [35]. PSR J2022+3842 has a double-peaked pulse profile with an offset of $\sim 0.48$ in phase and no emission between the peaks. This setup had caused the pulsar to be interpreted as one with a single pulse, in turn halving the pulsars true period and period derivative of 48.6 ms and $8.6 \times 10^{-14}$ s/s.

While the loss of this near record setting status was unfortunate, the updated geometry is noteworthy in its own right. This particular pulse profile implies a maximally misaligned rotation axis and magnetic moment, with each peak being emitted from opposite and isolated portions of the magnetosphere. Additionally, PSR J2022+3842 is one of only a few known soft $\gamma$-ray pulsars, which have spectral peaks in the MeV energy range[162]. These two factors make PSR J2022+3842 particularly compelling for studying the emission mechanism of soft pulsars [227, 70]. In such work, properly measuring the MeV (and GeV, if available) spectrum is essential to strongly constrain the underlying emission models. While this type of analysis would greatly benefit from the launching a Compton telescope mission, the Large Area Telescope (LAT) aboard the *Fermi* spacecraft can make headway towards this regime [41].

In this chapter I report on the detection of PSR J2022+3842 X-rays with NuSTAR (although previously published by Bachetti et al. [44], this detection was exclusively used for characterizing the timing characteristics of NuSTAR, and not for pulsar science) and NICER, and in the MeV/GeV range with the LAT. Of note, unpublished [196, 215] LAT detections of PSR J2022+3842 have already informed emission mechanism modeling of this source [227, 70]. However, by generating a timing solution with NICER and applying it to LAT data, I was able to increase the total length of the LAT timing solution by about a factor of 3, from 750 days to $\sim$ 2100 days.

Section 8.2 covers my work timing PSR J2022+3842 with NICER. Section 8.3.1 details how LAT photon weights were generated, and Section 8.3.2 details how the LAT phased analysis was carried out. Modeling of the pulsar is discussed in Section 8.4. Preliminary results are briefly covered in Section 8.5.

## 8.2 NICER Timing

NICER data are retrieved covering the time span 58083 - 59415 MJD, with a total exposure of 405 ks. PSR J2022+3842 is frequently observed by NICER as part of the Magnetars and Magnetospheres working group, and there are more recent observations available than analyzed here[1]. Data from the NICER telescope is processed using HEASoft 6.29c and NICERDAS 2021-08-31_V008c. The data are first reprocessed using `nicerl2`, and then prepared for analysis with the `psrpipe.py` script from the NICERSoft[2] software package. In addition to standard filtering, data from MPU1 is removed during the July 2019 timing anomaly. More information on the NICER analysis process is given in Chapter 4.2.

---

[1] `https://heasarc.gsfc.nasa.gov/docs/nicer/proposals/science_team_investigations/`

[2] https://github.com/paulray/NICERsoft

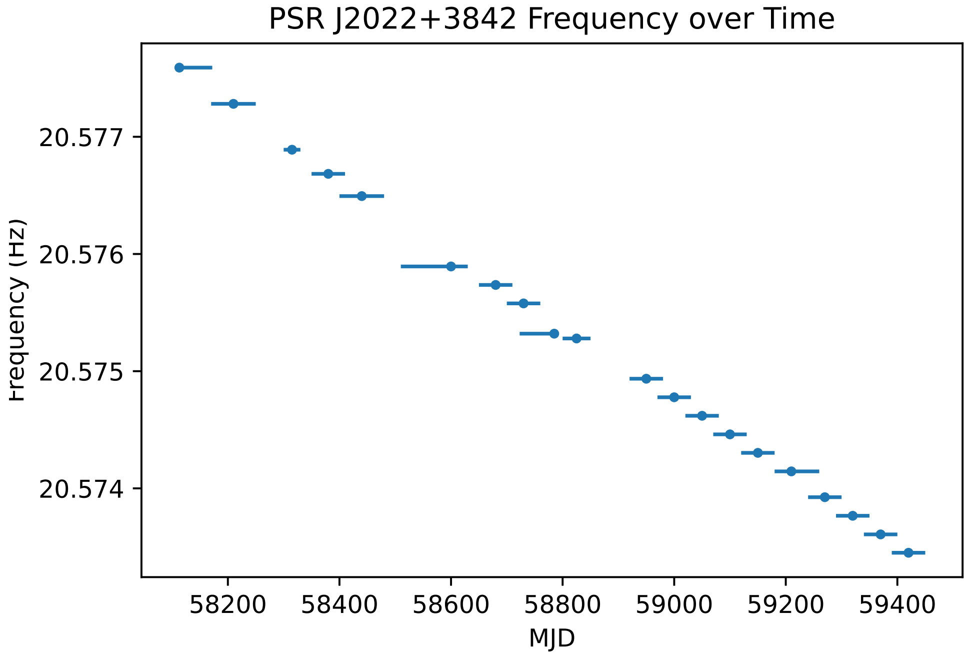

Figure 8.1: The frequency of each of the 20 individual timing solutions generated from NICER's observations of PSR J2022+3842. Horizontal bars show the time range covered by each timing solution. These often overlap slightly.

To create the timing solution for PSR J2022+3842, the NICER data are barycentered using the DE405 planetary ephemeris to the position of RA = 305.590371, DEC = 38.704117[36]. It proved challenging to generate a single timing solution covering all of the NICER time span. There is evidence for at least one glitch (a sudden discontinuity in the pulsar's rotational rate) around MJD 58850 (further discussed in Appendix D). In addition to glitches, young pulsars often exhibit timing noise (random wandering of phase), which can also contribute to timing difficulties. Because of this, the data was broken into 20 (often slightly overlapping) segments, each with its own timing solution. Frequency and frequency derivative were included. The frequency of these timing solutions is presented graphically in Fig. 8.1. When these timing solutions are appropriately stacked[3], a significance of H-Test = 5601 (73.81 $\sigma$) is achieved.

---

[3] The H-Test was maximized by fitting a phase offset to each time period.

| Energy Interval (GeV) | NBins | Width (deg) | Zmax (deg) | Pixel Size (deg) | | | | |
|---|---|---|---|---|---|---|---|---|
| | | | | PSF0 | PSF1 | PSF2 | PSF3 | All |
| 0.05 - 0.1 | 3 | 7.7345 | 80 | ... | ... | ... | 0.6 | ... |
| 0.1 - 0.3 | 5 | 7.7345 | 90 | ... | ... | 0.6 | 0.6 | ... |
| 0.3 - 1 | 6 | 5.7345 | 100 | ... | 0.4 | 0.3 | 0.2 | ... |
| 1 - 3 | 5 | 4.7345 | 105 | 0.4 | 0.15 | 0.1 | 0.1 | ... |
| 3 - 10 | 6 | 3.7345 | 105 | 0.25 | 0.1 | 0.05 | 0.04 | ... |
| 10 - 1000 | 10 | 2.7345 | 105 | ... | ... | ... | ... | 0.04 |

Table 8.1: Specifics of the 15 component model used when analyzing the RoI, with each PSF selection corresponding to a single component. Nbins refers to the number of energy bins, and Zmax refers to the maximum zenith angle. Width is the size of the total extracted region, which is composed of a 1.0287° core surrounded by a ring of various widths.

## 8.3 LAT Analysis

### 8.3.1 Non-Phased Analysis

Using `Fermipy` [247], I select a region of interest (RoI) spanning 13 years of Pass 8 data [39, 58] (specifically, P8R3_SOURCE_V3) from 2008 August 4 (MJD 54682.7) to 2021 September 13 (MJD 59470). The RoI is centered on the position of 4FGL J2022.3+3840 (RA = 305.5845, Dec = 38.6711), the counterpart to PSR J2022+3842 in the 10-year *Fermi*-LAT Fourth Source Catalog (4FGL) [13, 45]. As in the 4FGL, the RoI consists of fifteen components with varying cuts (as described in Table 8.1) based on their Point Spread Function (PSF) class. PSF class quantifies the precision which which the origin of an incoming photon can be determined. PSF4 represents best 25% of reconstructed photons, with PSF3 - PSF0 containing subsequent quartiles of decreasing reconstruction quality[4]. Across all PSF classes, precision also increases with energy[5]. The increased precision allows for wider maximum Earth zenith angles (to exclude contamination from Earth's limb) and smaller extraction regions at higher energies. Overall, the energy range of the extracted data covers 50 MeV to 1 TeV. Finally, data from all components is screened to ensure times are only included when the LAT is in normal science configuration and taking good data.

---

[4] `https://fermi.gsfc.nasa.gov/ssc/data/analysis/documentation/Cicerone/Cicerone_Data/LAT_DP.html`

[5] `https://www.slac.stanford.edu/exp/glast/groups/canda/lat_Performance.htm`

We proceed to perform a binned Likelihood analysis of the LAT data, as an unbinned of such a complicated region of sky would be computationally prohibitive. Within each of the fifteen aforementioned components, the photons are divided into spatial and energy bins as described in Table 8.1. The LAT's finite energy resolution, particularly <100 MeV, introduces the possibility that a photon's true energy lies in a different energy bin than that to which the photon has been assigned. This phenomena is referred to as "energy dispersion". Further discussion of energy dispersion, and how its negative effects can be mitigated, can be found in Chapter 4.1.6. `Fermi Tools 2.0.8` was used in this analysis, with `edisp_bins=-1` used to account for the energy dispersion[6]. The initial RoI model is seeded by including sources from the 4FGL which lie within a square 20°×20° region centered on 4FGL J2022.3+3840. J2022 is modeled as a powerlaw with super exponential cuttoff (version 3)[7], defined as:

$$\frac{dN}{dE} = N_0\left(\frac{E}{E_0}\right)^{\gamma_0+bc} \exp\left(c\left(1-\left(\frac{E}{E_0}\right)^{b}\right)\right) \tag{8.1}$$

This RoI model is iteratively fit to the data, with sources being removed if their significance, as measured by the Test Statistic (TS) falls below 9. TS is further discussed in Appendix A.1. Of particular note, the model for isotropic diffuse emission was not found to contribute enough to the region of interest to be included in the model.

The last iteration, which generates the final RoI model, is performed using Minuit [149]. The $N_0$, $\gamma_0$, and $c$ spectral parameters of J2022 are allowed to vary, along with the normalizations of sources with a significance greater than TS=100. Additionally, the normalization and index of the galactic diffuse are allowed to vary. When the RoI model has been successfully fit, the `gtsrcprob fermi tool` is used to calculate the probability that a given photon originated from PSR J2022+3842, which will hereafter be referred to as the photon *weight*. These weights are used in the generation of the pulse profile, which in turn is used to select the on and

---

[6] `https://fermi.gsfc.nasa.gov/ssc/data/analysis/documentation/Pass8_edisp_usage.html`

[7] `https://fermi.gsfc.nasa.gov/ssc/data/analysis/scitools/source_models.html`

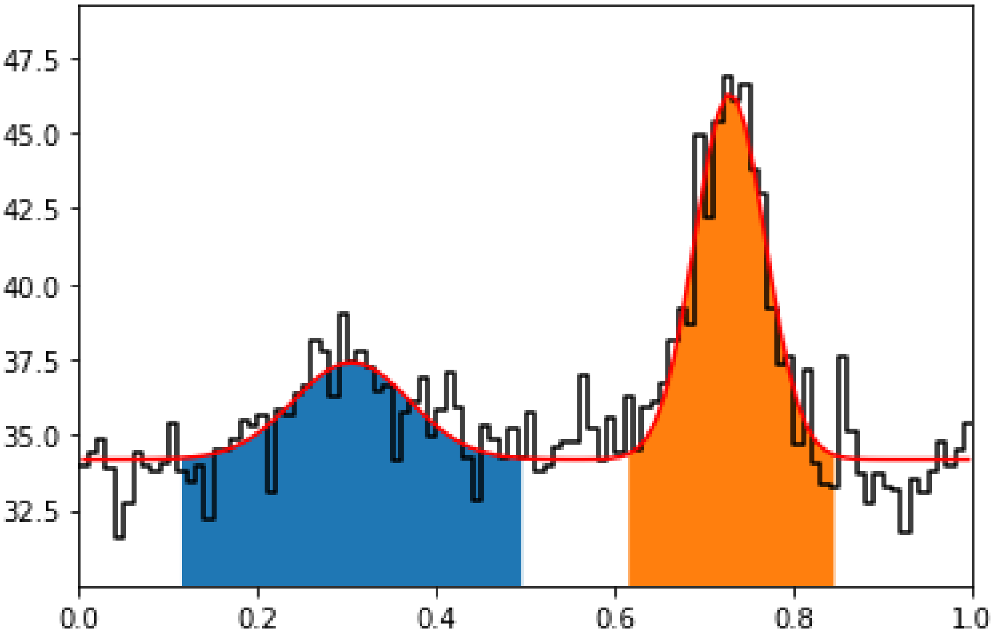

Figure 8.2: The timing solutions presented in [215] and Section 8.2 have been artificially aligned. The histogram in black shows the resultant pulse profile. A double-gaussian, shown in red, has been fit to this binned data. The blue and orange regions show the $\pm 3\sigma$ range of each gaussian, used for the phased analysis.

off time periods for the phased analysis. Further discussion on *Fermi*-LAT analyses and photon weights can be found in Chapter 4.

### 8.3.2 Phased Analysis

The work of [215] and Section 8.2 present two timing solutions for PSR J2022+3842 covering a combined total of 2082 days, but separated by 2333 days (i.e. not coherent). To perform a phased analysis, a phase-offset between the two timing solutions is calculated via maximization of the weighted H-Test. This combined pulse profile, with H-Test 587 ($\approx 13\ \sigma$), is shown in black in Fig. 8.2. It is fit with a double-gaussian pulse profile, shown in red in Fig. 8.2. The shaded regions show the $\pm 3\sigma$ (standard deviation of the fitted profile) region around the center of each selected as the on-pulse region. This width, in phase, is 0.37 for the dimmer pulse, and 0.24 for the brighter pulse.

The phased analysis proceeds similarly to the DC analysis described in Sec. 8.3.1. The same RoI and earth zenith angle cuts described Table 8.1 in are applied, with

| Parameter | Value |
|---|---|
| $N_0$ | $(4.0 \pm 0.3) \times 10^{-12}$ |
| $\gamma_0$ | $-2.57 \pm 0.08$ |
| $E_0$ | 1.159 (fixed) |
| $c$ | $2.2 \pm 0.5$ |
| $b$ | 0.5 (fixed) |

Table 8.2: Spectral parameters from the phased analysis of PSR J2022+3842.

an additional cut applied which selects only times with which a timing solution for J2022 exists. Further, only photons lying in the "on-pulse" phase are selected. The sources in the RoI, rather than being seeded from the 4FGL, are seeded from the final product of the DC analysis.

The analysis steps are likewise similar. The sources have their spectra optimized via the `fermipy` optimize routine. Sources are removed from the RoI if their TS falls below 9. To perform the final fit, the normalization of sources with a TS of at least 25 is allowed to vary. The $N_0$, $\gamma_0$, and $c$ spectral parameters of J2022 are allowed to vary. Additionally, the normalization and index of the galactic diffuse are allowed to vary.

To generate the source spectrum of J2022, normalizations of sources with a TS of at least 600 are allowed to vary, as well as the normalization and index of the galactic diffuse. J2022 is replaced by a power law source with photon index -2. Energy bins are combined to aid in convergence of the individual SED points. This produces the high energy portion of the spectrum shown in Figure 8.4, with the parameters for J2022 being displayed in Table 8.2. Further discussion on generating spectra with the LAT is presented in Chapter 4.

## 8.4 Theoretical Modeling

After extracting the $\gamma$-ray spectrum using *Fermi*-LAT, we combined the data with the X-ray spectrum extracted by Kuiper and Hermsen [162] to examine the emission model of the pulsar. We used the synchrocurvature model described in Torres [226] and Torres et al. [227], as well as Section 2.3 of this thesis. Briefly, this model parameterizes pulsar emission with three key parameters plus one normalization

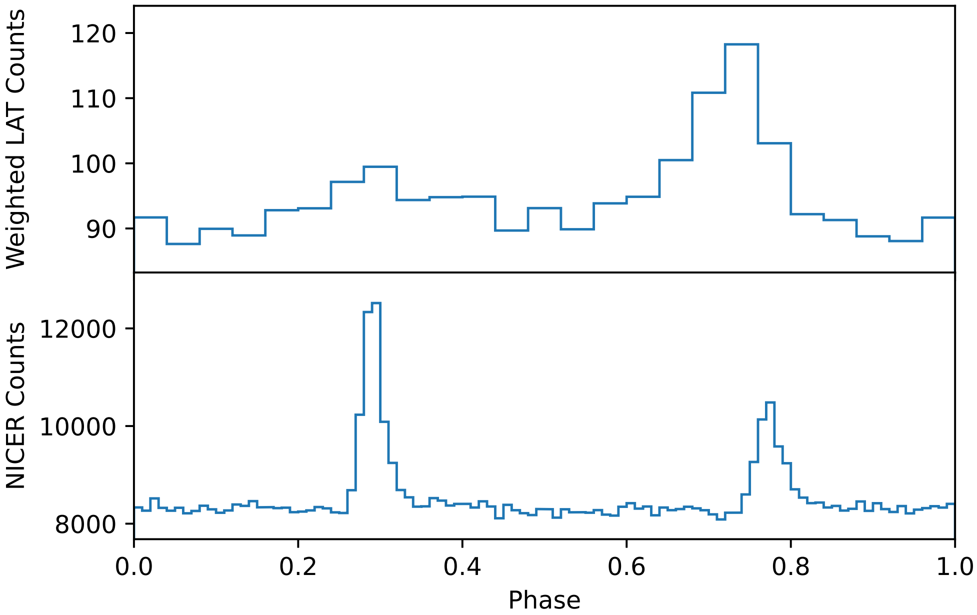

Figure 8.3: The pulse profile of PSR J2022+3842 as seen with the LAT (Top) and the NICER (bottom).

parameter. This includes the accelerating electric field ($E_{||}$), contrast ($R_{lc}/x_0$), and magnetic gradient ($b$). $E_{||}$ exists in the region around the light cylinder, where it acts on particles injected from a region closer to the star. The contrast parameterizes the distribution of the accelerated particles from the point of view of the observer. The magnetic gradient models the strength of the magnetic field as a function of distance from the pulsar.

## 8.5 Preliminary Conclusions

The preliminary results of this analysis are presented in Figure 8.4. When compared to the prior analysis, the addition of the time span covered by NICER has allowed us to add an additional spectral point below $10^8$ eV. The new best-fit modeling parameters are $\log E_{||} = 9.16$, $\log x_0/R_{lc} = -3.28$, and $b = 3.20$. This does not substantially change the previously published values [227], nor does it appear to significantly affect prospects for viewing this source with future Compton telescopes. However, as detection of $\gamma$-ray pulsations have yet to be formally published for

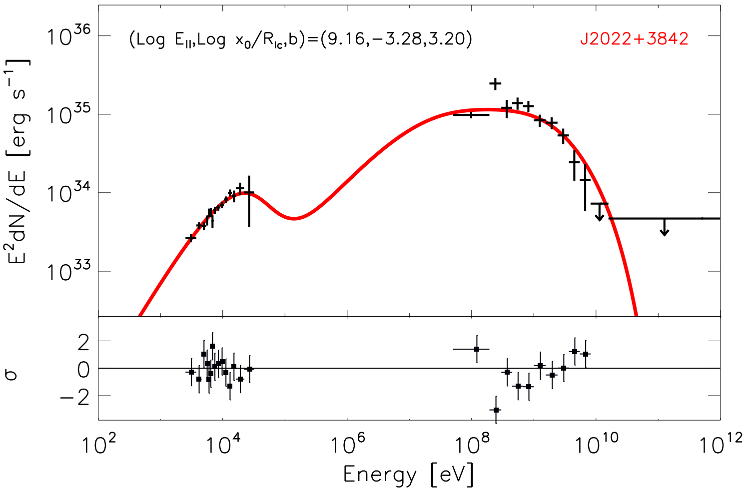

Figure 8.4: The result of fitting the LAT data described in this section (right spectral points), along with XMM data (left spectral points)from Kuiper and Hermsen [161], with the synchrocurvature modeling software.

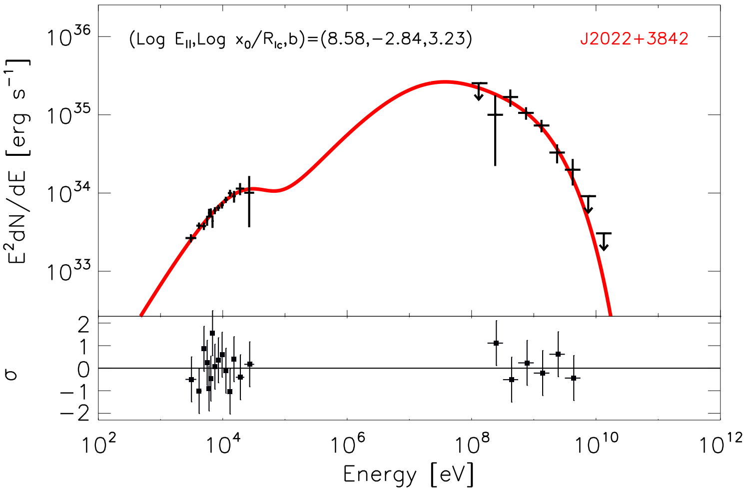

Figure 8.5: Prior results, from Torres et al. [227]. Data points on the left are from XMM, and points on the right are from the LAT.

PSR J2022+3842, confirmation of the prior values is meritorious.

Future prospects include the addition of data from Chandra and NuSTAR, extending the X-ray portion of the analysis to both lower and higher energies. Preliminary analysis shows that the spectral shapes extracted by these telescopes agree with one another, but we are still looking into the proper parameters to use in accounting for interstellar absorption, so that they agree with the XMM data from Kuiper and Hermsen [161].

Additionally, we have shown that it is possible to analyze each pulse individually with *Fermi*-LAT, although this work is not presented here. This is of particular interest, given the thoughts in Arumugasamy, Pavlov, and Kargaltsev [35] that each pulse may come from independent parts of the pulsar magnetosphere. However, it does not appear that such an analysis would currently be very constraining.

# Chapter 9

# PSR J0218+4232: Wish you were MAGIC

The following chapter has been modified from Acciari et al. [14] “Search for Very High-energy Emission from the Millisecond Pulsar PSR J0218+4232”, for which I performed the analysis described in Sec. 9.2.1 below.

PSR J0218+4232 is one of the most energetic millisecond pulsars known and has long been considered as one of the best candidates for very high energy (VHE; >100 GeV) pulsed $\gamma$-ray emission. Using 11.5 years of *Fermi* Large Area Telescope (LAT) data between 100 MeV and 870 GeV, and ∼90 hours of MAGIC observations in the 20 GeV to 20 TeV range, we have searched for the highest energy $\gamma$-ray emission from PSR J0218+4232. Based on the analysis of the LAT data, we find evidence for pulsed emission above 25 GeV, but see no evidence for emission above 100 GeV (VHE) with MAGIC. This chapter presents the results of searches for $\gamma$-ray emission, along with theoretical modeling to interpret the lack of observed VHE emission. We conclude that, based on the experimental observations and theoretical modeling, it will remain extremely challenging to detect VHE emission from PSR J0218+4232 with the current generation of Imaging Atmospheric Cherenkov Telescopes (IACTs), and maybe even with future ones, such as the Cherenkov Telescope Array (CTA).

## 9.1 Background

PSR J0218+4232 (hereafter J0218) is a millisecond pulsar (MSP) with a period of 2.3 ms in a 2-day orbit with a $\sim 0.2 M_\odot$ white dwarf companion [46]. It was serendipitously discovered as a steep spectrum, highly polarized source in a low-frequency radio study of an unrelated supernova [192]. Its broad radio peak, with a large unpulsed component ($\sim$ 50%) makes it unusual, suggesting that it may be an *aligned rotator*, a pulsar in which the magnetic field is aligned with the axis of rotation. This view is further supported by subsequent polarimetry studies [220]. With a characteristic age $\tau$ <0.5 Gyr and a spindown power of $2.4 \times 10^{35}$ erg $s^{-1}$, it is one of the youngest and most energetic MSPs known. It has an extremely strong magnetic field at the light cylinder ($B_{LC} \sim 3.2 \times 10^5$ G, and a function of its small light cylinder radius), only slightly weaker than young Crab-like pulsars, but several orders of magnitude weaker at the neutron star surface than Crab-like pulsars [207]. Like the Crab Pulsar, J0218 also displays giant radio pulses [151, 156] (an occasional pulse ~100 times the intensity of a standard pulse), something very uncommon among MSPs. Its distance, previously estimated to be greater than 6 kpc, potentially making it the most luminous MSP known [81], has since been revised downwards to ~3 kpc [233]. Table 9.1 provides a summary of the key properties of J0218.

J0218 was first detected as a steady source of X-rays and $\gamma$-rays using *ROSAT* and EGRET, respectively [234]. It was later shown to display non-thermal pulsed X-ray emission [165]. Like in radio, J0218 has a large unpulsed component in X-rays. It has been detected by most of the X-ray missions, including *BeppoSAX* [188], *Chandra* [166], *XMM-Newton* [241], *RXTE* [164], and most recently *NICER* [79]. Non-thermal hard X-ray emission was detected with *NuSTAR* up to ~70 keV [112]. The spectrum must turn over (reach a maximum) somewhere between 100 KeV and 100 MeV for consistency between X-ray and GeV $\gamma$-ray emission. However, there is no curvature in the hard X-ray data to otherwise suggest where this spectral break occurs [112].

The $\gamma$-ray emission of J0218 has often been confused with that of the blazar

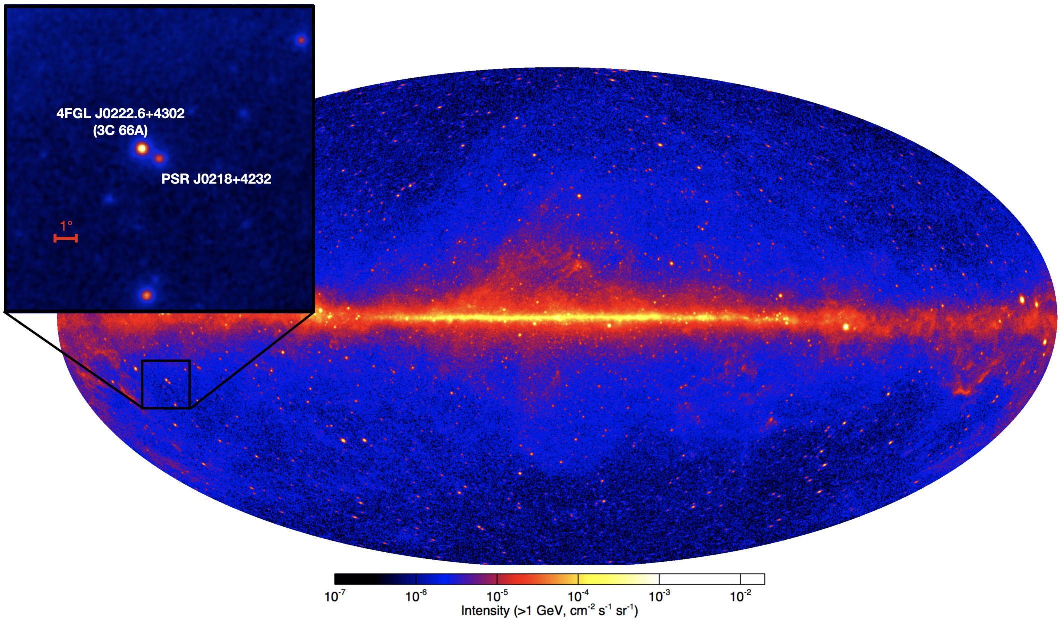

Figure 9.1: LAT All-sky map showing the location of PSR J0218+4232 (aka 4FGL J0218.1+4232). The background map shows the 12-year (August 4, 2008 - August 4, 2020) all-sky intensity map, generated using $\gamma$-ray data above 1 GeV, in Galactic coordinates (Credit: Seth Digel). The square inset region shows the $15^\circ \times 15^\circ$ counts map centered on PSR J0218+4232, generated with the 11.5 years of data analyzed in this paper (from 2008 August 4 to 2020 February 10), using all events above 1 GeV. Note the bright $\gamma$-ray blazar 3C 66A (aka 4FGL J0222.6+4302) located less than one degree away from PSR J0218+4232.

3C 66A because of their close proximity (0.97° separation, see Figure 9.1) and the poor angular resolution of many $\gamma$-ray instruments. The Second EGRET (2EG) Catalog [225] contained a source (2EG J0220+4228) that was more often associated with 3C 66A than J0218. In the third EGRET (3EG) catalog [132], the source 3EG J0222+4253 was identified with 3C 66A based on its >1 GeV emission. However, its low-energy flux (100-300 MeV) was found to be dominated by the pulsar, rather than the blazar, leading to the conclusion that both were likely contributing to the EGRET source [167, 115]. Indeed, Kuiper et al. [167] reported marginal evidence ($\sim 3.5\sigma$) for the detection of pulsed $\gamma$-ray emission by EGRET from J0218, making it potentially the first MSP detected at these energies.

Within a year of launch, *Fermi*-LAT [41] adequately resolved both sources to solve the aforementioned ambiguity. The First *Fermi*-LAT Catalog, based on 11 months of data [8], reported 1FGL J0218.1+4232 as a strong source ($> 19\sigma$) distinct from 3C 66A. A firm detection of GeV $\gamma$-ray pulsations confirmed the association with J0218 [7, 11]. The LAT detection, however, showed a broad single-peaked $\gamma$-ray light curve, bearing little similarity to the EGRET one reported in Kuiper et al. [167], or indeed the double-peaked X-ray pulse profile [166, 241]. Despite the fact that the First LAT Catalog of sources above 10 GeV (1FHL) [19] contained no source associated with J0218, this pulsar was identified as having hints of pulsed emission above 10 GeV [19]. The Third Catalog of Hard *Fermi*-LAT Sources (3FHL) [21] contained a source associated with J0218 (3FHL J0218.3+4230), which was shown to have >10 GeV (and even >25 GeV) pulsations [209]. These preliminary LAT results, despite the limited statistics due to the small effective area of the LAT at such high energies, provided a strong motivation for observing this pulsar at even higher energies using ground-based $\gamma$-ray telescopes[1].

At very high energies (VHE; >100 GeV), J0218 has been a target for the Major Atmospheric Gamma Imaging Cherenkov (MAGIC) telescope, starting in 2004, when it was observed for 13 hours during the commissioning phase (when only one of MAGIC's eventual two telescopes had been built), in large part due to it being in the same field of view as 3C 66A [197]. It was subsequently observed for 20 hours, between October 2006 and January 2007, yielding no significant detection and a $3\sigma$ flux upper limit of $< 9.4 \times 10^{-12}$ cm$^{-2}$ s$^{-1}$, above 140 GeV [30]. Since then, the performance of the MAGIC telescopes (the second telescope was constructed in 2008 [229]) has significantly improved [24].

The remainder of this chapter reports results from an analysis of 11.5 years of *Fermi*-LAT data, together with ~90 hours of data from new MAGIC stereoscopic observations of J0218, collected from November 2018 to November 2019, using the low-energy threshold Sum-Trigger-II system[2][98].

---

[1] Note that the sensitivity of ground-based $\gamma$-ray telescopes like MAGIC depends not only on their large effective areas, but also on their ability to reject the cosmic-ray background. Given the challenges of performing background rejection with MAGIC in the 10–100 GeV range, it is perhaps not surprising that MAGIC is less sensitive than *Fermi*-LAT at these energies, despite its much larger effective area.

[2] The Sum-Trigger-II system is an upgraded version of the Sum-Trigger system, which allowed for the first VHE detection of pulsations from the Crab Pulsar[98]

## 9.2 Data Analysis

### 9.2.1 *Fermi*-LAT Data Analysis

For the *Fermi*-LAT analysis, we used 11.5 years of Pass 8 data [39, 58](specifically, P8R3_SOURCE_V2), from 2008 August 4 (MJD 54682.7) to 2020 February 10 (MJD 58890).[3] We used `Fermipy` [247] to select *Source* class (evclass 128), *Front* and *Back* converting events (evtype 3) with an energy range from 100 MeV to 870 GeV, and from a square region of $15^\circ \times 15^\circ$, centered on the position of 4FGL J0218.1+4232 (RA=34.5344°, DEC=42.5459°). A maximum Earth zenith angle of 90° is imposed, helping eliminate contamination from the Earth's limb. We further ensured that the selection only included events acquired at times when the LAT was in normal science configuration and taking good data. *Fermi*-LAT data selection is described in further detail in Sec. 4.1.2.

Figure 9.1 shows the *Fermi*-LAT >1 GeV all-sky $\gamma$-ray intensity map, highlighting the region around J0218. As discussed in Section 9.1, the blazar 3C 66A, located 0.97° away, complicates the analysis of J0218. The bright $\gamma$-ray counterpart of 3C 66A (4FGL J0222.6+4302, see Figure 9.1) has a $> 1$ GeV flux of $1.6 \times 10^{-8}$ cm$^{-2}$ s$^{-1}$ ($> 160\sigma$) in 4FGL, compared to $5.2 \times 10^{-9}$ cm$^{-2}$ s$^{-1}$ ($73.5\sigma$) for J0218. Because blazars are typically variable sources, we considered excluding times when 3C 66A was particularly bright. Unfortunately, the *Fermi*-LAT light curves of J0218 and 3C 66A, over the entire time interval (11.5 years) and energy (100 MeV to 870 GeV) range (Figure 9.2) reveal that such a strategy would not be possible, as the blazar has been quite active throughout the entire 11.5-year period of our observations. Figure 9.3 shows the zoomed-in 1-year period covered by our MAGIC observations, illustrating how 3C 66A is brighter than J0218 at GeV energies. We note that there is a report of quasi-periodic variability in the optical light curve of 3C 66A with a period of ∼3 years, but these variations have not been seen in the $\gamma$-ray data [199].

---

[3] We considered the possibility of including *Calorimeter-Only* (Cal-Only) data [223, 222] in our analysis. However, after a preliminary look at 8 years of such data, covering the period 2008-2016, using three different Cal-Only event classes, we found no evidence for pulsed emission, most likely due to the large PSF and corresponding large cosmic-ray background level. Thus, we opted to limit our analysis to *standard* LAT data.

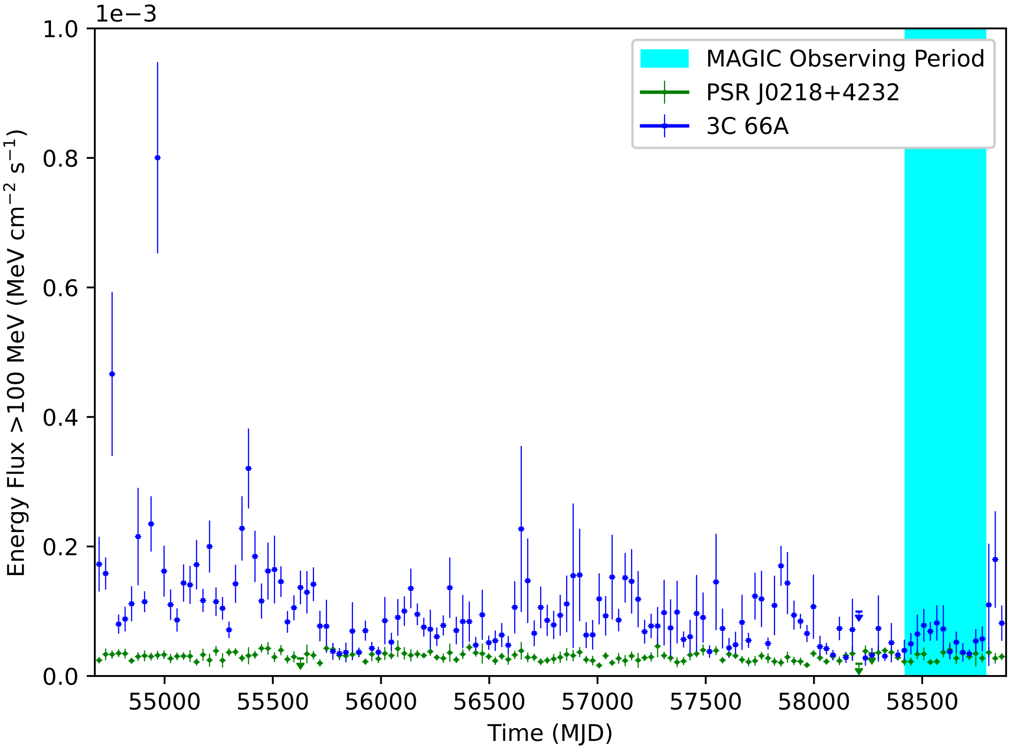

Figure 9.2: Light curve showing PSR J0218+4232 (green circles) and 3C 66A (blue squares). The LAT data ranges from 2008 August 4 (MJD 54682.7) to 2020 February 10 (MJD 58890), and covers the 100 MeV - 870 GeV energy bands. The time period of MAGIC observations (MJD 58424 – 58791) is shown in cyan. Note the larger variability and $\gamma$-ray flux of 3C 66A.To generate this plot, background sources were fixed to the value in the region model, and the normalizations of 3C 66A and J0218 were allowed to vary.

A binned likelihood analysis was performed, as described in Sec. 4.1, utilizing spatial bins of $0.1^\circ \times 0.1^\circ$ and 8 logarithmically spaced bins per decade of energy. The initial region model was seeded from the 8-year *Fermi*-LAT Fourth Source Catalog (4FGL) [13] by including sources lying within a square region of $40^\circ \times 40^\circ$ centered on 4FGL J0218.1+4232. Energy dispersion corrections were enabled for all sources except the isotropic diffuse emission (where it has already been accounted for in the underlying template) as described in Chapter 4.1.6 and Appendix A.2.

The fitting of source spectra was carried out in an iterative process, with sources being removed from the model if they fell below a test statistic (TS) of 10 (as defined in Sec. 4.1.1, Eqn. 4.5). The final iteration of the fit was performed with Minuit [149]. In addition to the spectral parameters of 4FGL J0218.1+4232, the normalization

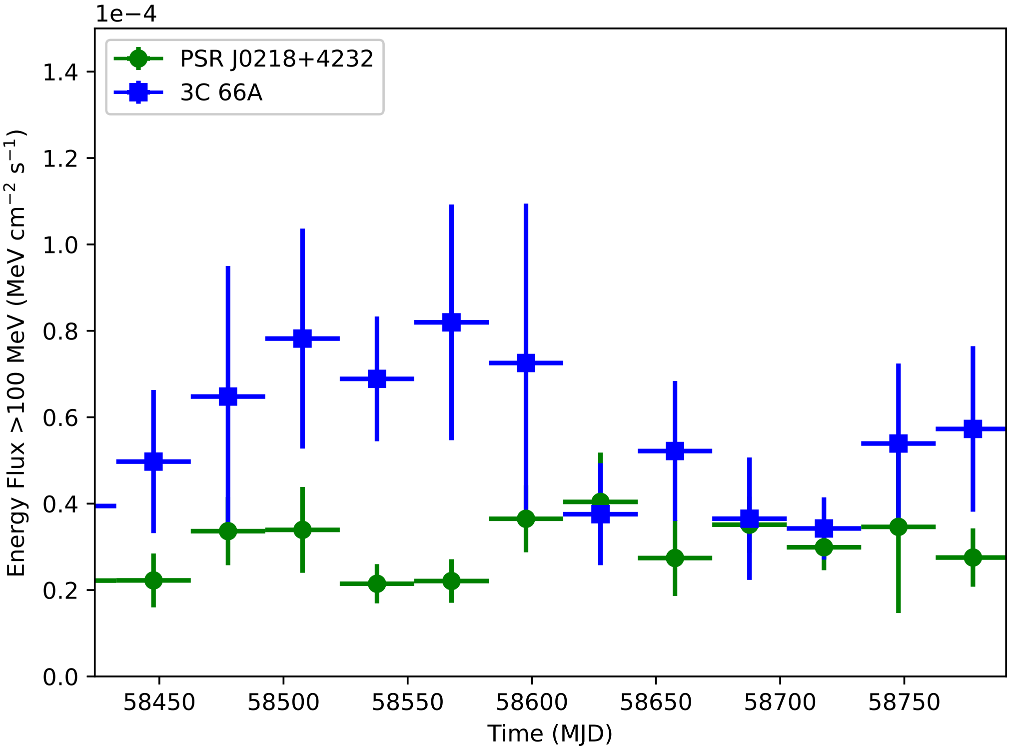

Figure 9.3: *Fermi*-LAT light curve showing PSR J0218+4232 (green circles) and 3C 66A (blue squares), zoomed in on the time period of MAGIC observations (MJD 58424 – 58791). Note that 3C 66A has a significantly larger flux than J0218 most of the time.

and index of the Galactic diffuse emission (modeled with a power-law spectrum), the normalization of the isotropic diffuse emission, and the normalizations of background sources with a TS of at least 100 were allowed to vary.

We modeled the J0218 spectrum using a power law with an exponential cutoff [4], $\frac{dN}{dE} = N_0\left(\frac{E}{E_0}\right)^{\gamma}\exp(-aE^b)$. We set the index (b) to a fixed "sub-exponential" value of 2/3, as this source is too faint for it to be determined by maximum likelihood estimation, and 2/3 approximates the values of other, brighter pulsars [13].

After obtaining our best region model, we examined events within 5° of J0218, and used the "`gtsrcprob`" `Fermitool` to assign them a probability (*weight*) of originating from either J0218 or 3C 66A relative to other sources in the model (See Sec. 4.1.11). Finally, we used TEMPO2 [145] with the `fermi` plug-in [201] to assign the pulsar rotational phases $\phi_i$, according to our pulsar ephemeris obtained with the

---

[4] See `https://fermi.gsfc.nasa.gov/ssc/data/analysis/scitools/source_models.html`

| Timing and binary parameters | |
|---|---|
| R.A., $\alpha$ (J2000.0) | $02^{\mathrm{h}}\,18^{\mathrm{m}}\,06.35863(1)^{\mathrm{s}}$ |
| Decl., $\delta$ (J2000.0) | $+42^{\circ}32'17.3722(2)''$ |
| Frequency, $F0$ (Hz) | 430.46105998103612106(6) |
| 1st frequency derivative, $F1$, (Hz $\mathrm{s}^{-1}$) | $-1.434128(1) \times 10^{-14}$ |
| PMRA ($\dot{\alpha}/cos\delta, \mathrm{mas}\, yr^{-1}$) | 5.32(3) |
| PMDEC ($\dot{\delta}, \mathrm{mas}\, yr^{-1}$) | -3.68(6) |
| PEPOCH (MJD) | 56000 |
| POSEPOCH (MJD) | 56000 |
| DMEPOCH (MJD) | 56000 |
| DM ($\mathrm{cm}^{-3}$ pc) | 61.2374(7) |
| DM1 ($\mathrm{cm}^{-3}$ pc $\mathrm{s}^{-1}$) | -0.0004(2) |
| BINARY MODEL | ELL1 |
| PB (d) | 2.0288460845(6) |
| A1 (lt-s) | 1.9844348(2) |
| TASC (MJD) | 49148.5799767(2) |
| EPS1 | $5.0(2)\times10^{-6}$ |
| EPS2 | $4.9(2)\times10^{-6}$ |
| START (MJD) | 53579.2 |
| FINISH (MJD) | 58960.5 |
| UNITS | TDB (Barycentric Dynamical Time) |
| EPHEM | DE436 |
| Derived parameters | |
| Period, $P$ (ms) | 2.32309053 |
| 1st period derivative, $\dot{P}$ (s $\mathrm{s}^{-1}$) | $7.739 \times 10^{-20}$ |
| Characteristic age, $\tau_{\mathrm{c}}$ (yr) | $4.8 \times 10^{8}$ |
| Spin-down power, $\dot{E}$ (erg $\mathrm{s}^{-1}$) | $2.4 \times 10^{35}$ |
| Surface $B$-field strength, $B_{\mathrm{S}}$ (G) | $4.3 \times 10^{8}$ |
| Light-cylinder $B$-field, $B_{\mathrm{LC}}$ (G) | $3.1 \times 10^{5}$ |
| Distance, $d$ (kpc) | $3.15^{+0.85}_{-0.60}$ |
| ON pulse region | (0.34–0.98) |
| OFF pulse region | $[0,0.34)\cup(0.98,1]$ |

Table 9.1: Timing ephemeris for PSR J0218+4232, obtained with the Nançay radio telescope. We used the DE436 Solar System ephemeris, with time units in barycentric dynamic time (TDB) and the ELL1 binary model for low eccentricity orbits, where EPS1 and EPS2 represent the first and second Laplace-Lagrange parameters [168]. We refer the reader to the TEMPO2 manual [145] for the detailed definition of all parameters included in our timing model.

| Parameter | Value |
|---|---|
| $N_0$ (ph cm$^{-2}$ s$^{-1}$ MeV$^{-1}$) | $(2.07 \pm 0.03) \times 10^{-11}$ |
| $\gamma$ | $-1.76 \pm 0.01$ |
| $E_0$ (MeV) | 821.6 (fixed) |
| $a$ | $(6.19751 \pm 0.00007) \times 10^{-3}$ |
| $b$ | 0.6667 (fixed) |
| Photon flux (photons cm$^{-2}$ s$^{-1}$) | $(7.67 \pm 0.15) \times 10^{-8}$ |
| Energy flux (MeV cm$^{-2}$ s$^{-1}$) | $(3.05 \pm 0.04) \times 10^{-5}$ |

Table 9.2: Gamma-ray spectral parameters for the total emission from PSR J0218+4232. Photon and energy flux cover the entire 100 MeV - 870 GeV energy range.

Nançay radio telescope, given in Table 9.1.

We calculated the source spectrum and flux points for the theoretical modeling described in Section **??** by utilizing the aforementioned region model. Three energy bins spanning 12.38 - 28.99 GeV were combined in order to produce a flux point instead of an upper limit. To extract the overall spectrum of J0218, the normalization of the isotropic and Galactic diffuse emission components were allowed to vary while Minuit fit the spectral parameters (summarized in Table 9.2). To generate flux points, the index of the Galactic diffuse emission was also allowed to vary, along with the normalizations of background sources with a TS of at least 500 or which lie within 5° of 4FGL J0218.1+4232. The spectrum of 4FGL J0218.1+4232 is replaced by a power law with an index of -2, and Minuit is used to fit the normalization of this modified spectrum within each energy bin. The result is interpreted as either a flux point or an upper limit, depending on the significance with which the power law source was detected (see Sec. 4.1.9 for further details on spectrum calculation).

### 9.2.2 MAGIC Observations and Data Analysis

The MAGIC collaboration used their telescopes to search for the VHE emission component of J0218. MAGIC consists of two imaging atmospheric Cherenkov telescopes (IACTs) of 17m diameter located at the Roque de Los Muchachos Observatory in La Palma, Canary Islands, Spain [24]. Data was collected in stereoscopic mode with the Sum-Trigger-II system[5] This system is designed to improve the performance of the telescopes in the sub-100 GeV energy range [73].

J0218 was observed from 2018 November 2 to 2019 November 4 (MJD 58424 – 58791) with a zenith angle range from 13 to 30 degrees, for maximum sensitivity at low energies. Wobble mode was used for robust flux and background estimation by pointing the telescopes 0.4° away from the source [91][6] Weather conditions were monitored simultaneously by measuring the atmospheric transmission with the LIDAR system operating together with the MAGIC Telescopes [92]. The Cherenkov radiation produced by the sub-100 GeV particle showers is fainter; consequently, they are more affected by the lower atmospheric transmissions. Therefore, strict requirement of excellent atmospheric conditions was set, a minimum of 0.85 atmospheric transmission at an altitude of 9km. After discarding around 20% of the total data, 87 hours of good quality data remained.

The data were analyzed using the Magic Standard Analysis Software, MARS [248]. The Sum-Trigger-II dedicated algorithm for calibration and image cleaning[7]was applied, which improved the performance and achieved an energy threshold of 20 GeV. A higher-level analysis was performed following the standard pipeline [25].

## 9.3 Results

### 9.3.1 *Fermi*-LAT results

Figure 9.4 shows the LAT spectrum obtained in our analysis. Table 9.2 reports the best-fit spectral parameters and Table 9.3 gives the spectral values, including upper limits. Note that the spectrum falls steeply at energies above 10 GeV with

---

[5] Each of the two MAGIC telescopes includes a camera containing 1039 photomultiplier tubes (PMTs) [73]. Initially, one of the criteria for recording an event was that three nearest neighbor PMTs cross a voltage threshold within a short time period. This criterion is hard to satisfy for photons below 50 GeV. Sum-Trigger-II sums the voltage of clusters of 19 PMTs for comparison to a threshold voltage, lowering MAGIC's minimum energy threshold to 25 - 30 GeV and broadly improving low energy performance.

[6] The "False Source Tracking Method" described in Fomin et al. [91] allows for the source of interest to remain in the field of view of the telescope for the entire observational period. For comparison, other methods of flux and background estimation described in Fomin et al. [91] require the target of interest to be outside the field of view for $\sim 50\%$ of the observation time.

[7] Image cleaning is the process by which relevant PMTs in the MAGIC cameras are selected. The cleaning method is called "MaTaJu cleaning". Details of this method have not yet been published.

only upper limits reported for energies above ~29 GeV. These results are consistent with previous LAT results reported in 4FGL [13] and 3FHL [21], the latter of which reported an index of $\Gamma = -4.5$, when fitting the >10 GeV data with a simple power law.

### Search for high-energy pulsation with LAT events

To test for possible pulsed emission above 10 GeV, an analysis analogous to what was carried out in the First *Fermi*-LAT Catalog of >10 GeV sources (1FHL) [19] and in Saz Parkinson et al. [209] was performed. We defined a *low-energy* probability density function (PDF), which we refer to as $\mathrm{PDF}_{LE}$, based on the best estimate fit of the 1-10 GeV events (see Figure 9.5, top panel). For the high-energy PDF, we considered the family of distributions given by $\mathrm{PDF}_{HE}(\phi) = (1-x) + x{\cdot}\mathrm{PDF}_{LE}(\phi)$, with $0 \leq x \leq 1$. We maximized the unbinned likelihood function derived from this PDF, with respect to $x$, obtaining $\mathcal{L}(\hat{x})$, and comparing it to the null hypothesis, for $x = 0$, that there is no pulsation (i.e. $\mathrm{PDF}_{HE}(\phi)$=1). By construction, $\mathcal{L}(0) = 1$, so the test statistic (TS=$-2\ln(\mathcal{L}(0)/\mathcal{L}(\hat{x}))$) can be simplified to TS = $2\ \ln\mathcal{L}(\hat{x})$. We converted the measured TS value into a tail probability (or p-value), by assuming, following Wilks' theorem [242], that for the null hypothesis the TS follows a $\chi^2$ distribution with 1 degree of freedom[8].

Using the LAT data set described in Section 9.2.1, we first selected events in the 1–10 GeV energy range (with a probability >50% of coming from the pulsar, as obtained via the method described in Sec. 4.1.11) and used this histogram to generate a 'low energy template'. We used the non-parametric SOPIE (Sequential Off-Pulse Interval Estimation) R package [210], to obtain a *smooth* kernel density estimator of our histogram (which we defined as our "low-energy template"), and also derived an estimate of the off-pulse interval of the light curve, using the median value of the results obtained from four different goodness-of-fit tests: Kolmogorov–Smirnov, Cramér–von Mises, Anderson–Darling, and Rayleigh test statistics. Figure 9.5 (top panel) shows our results, including the 1–10 GeV histogram, along with the result-

---

[8] See Sec. 4.1.1 for more detailed discussion of TS and Wilks' theorem.

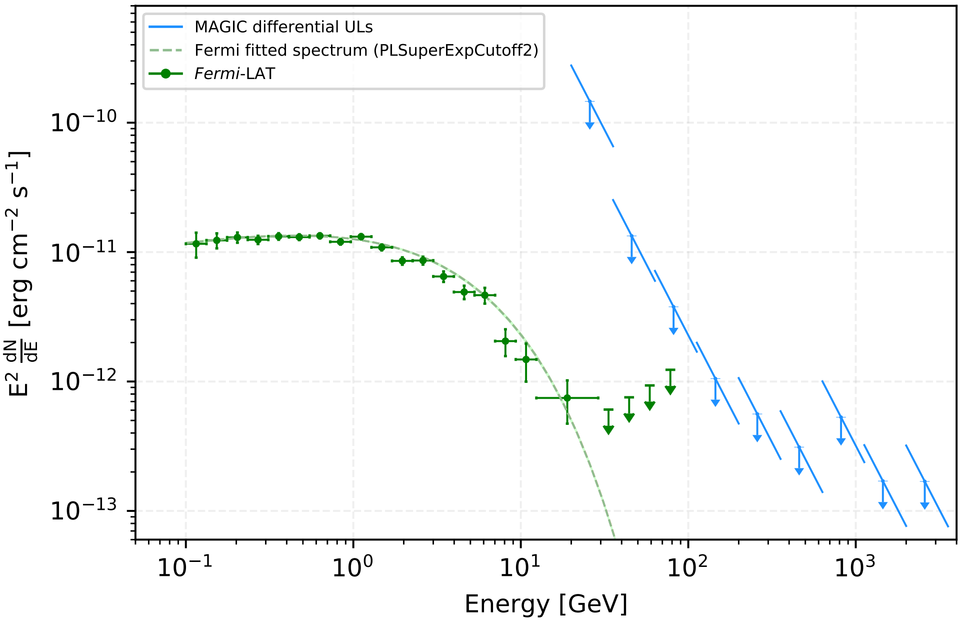

Figure 9.4: Spectrum of the total emission of millisecond pulsar J0218+4232 measured by *Fermi*-LAT (green points and upper limits) and the MAGIC telescopes (light blue upper limits). The green dashes represent the fit of the *Fermi*-LAT data with an exponentially cutoff power-law model. Note that the width of the $\pm 1\ \sigma$ error region is narrower than the dashes showing the best-fit model. Although included, it is difficult to distinguish in this plot. For the MAGIC analysis we assumed a spectral index $\Gamma = -4.5$ obtained from the spectral index of the power-law fit to the high-energy (>10 GeV) part of the *Fermi*-LAT spectrum.

ing *low-energy* template, and the estimated off-pulse interval, all calculated using SOPIE.

To test for emission at higher energies, we looked at the >10 GeV events arriving within the 95% containment radius of the point-spread function (0.5/0.8 degrees for front/back converting events, as described in Chapter. 3) and performed a likelihood test to determine whether they are likely to come from a similar distribution function, as represented by the lower energy template. We set a threshold p-value of 0.05 to claim evidence for emission at a specific energy. We carried out the same test with events of energies greater than 25 GeV. Figure 9.5 (bottom panel) shows the distribution of 58 (17) events above 10 (25) GeV, leading to a p-value of 1e-4 (0.01), thus showing evidence for emission above 10 and, marginally, above 25 GeV. We also tested for possible emission above 30 GeV but found that, despite the presence

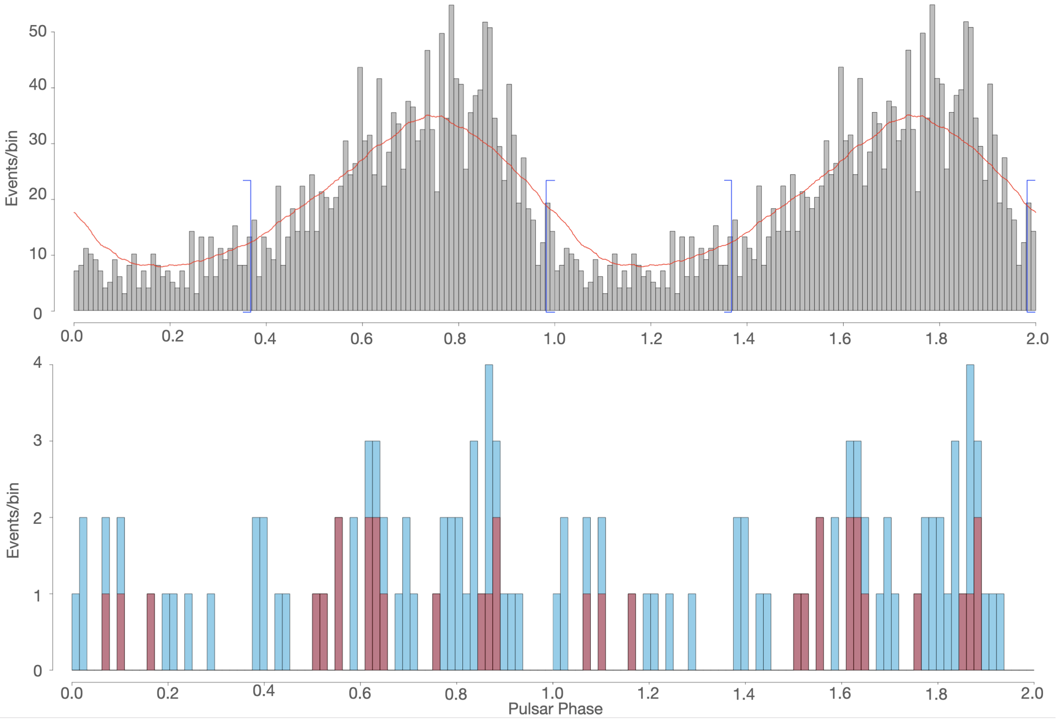

Figure 9.5: **Top panel** – Histogram of the 1–10 GeV events for PSR J0218+4232, along with the smooth circular kernel density estimator (red line) fitted to the data, which we define as the *low-energy* template in our subsequent searches for pulsed emission above 10 GeV. Two rotation cycles are shown, with 100 bins per cycle. The blue brackets indicate the estimated off-pulse interval, [0–0.34)∪(0.98,1], obtained using SOPIE [210]. **Bottom panel** – Search for high-energy pulsations using LAT standard events above 10 GeV. The blue histogram are the 58 events above 10 GeV in energy, while the pink histogram are the 17 events above 25 GeV. Two rotation cycles are shown, with 65 bins per cycle.

of 10 events above this energy, their distribution in phase yielded a p-value that was not significant ($p > 0.05$).

### 9.3.2 MAGIC Results

We analyzed our MAGIC data to search for possible pulsed and un-pulsed $\gamma$-ray emission above 20 GeV. The skymap is shown in Figure 9.6, where no emission is observed from J0218. The high emission spot observed in the image is the blazar 3C 66A, which is significantly detected as a by-product of the observations centered on J0218.

We used the TEMPO2 package [145] to assign the rotational phase to each event using the same ephemeris as in our LAT analysis described in Section 9.3.1 given in

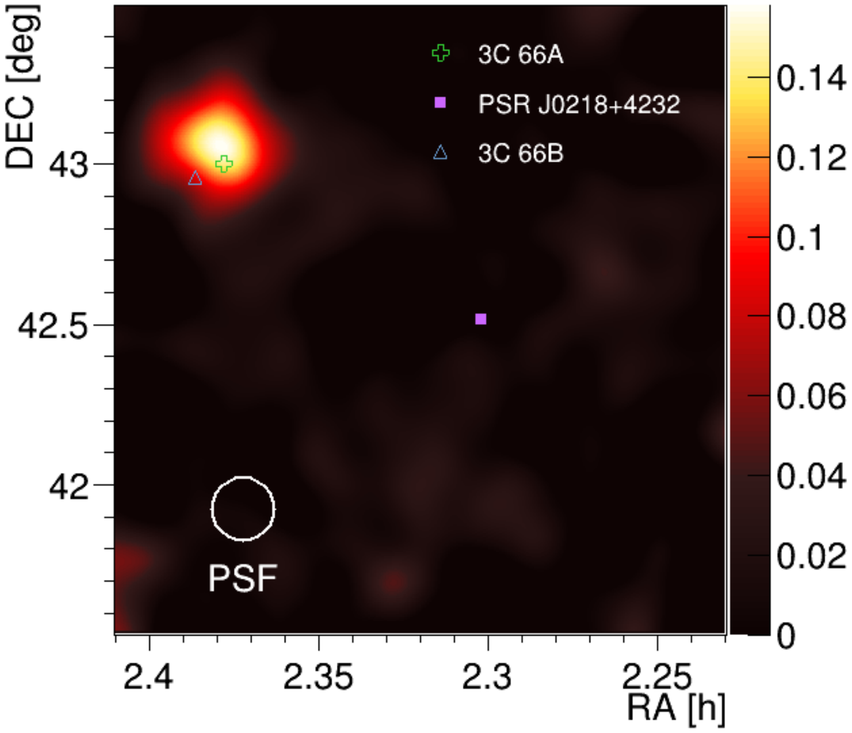

Figure 9.6: MAGIC skymap of the region around PSR J0218+4232 (indicated by a purple square) above 20 GeV. The relative flux (in arbitrary units) is calculated by the number of smeared excess events divided by the residual background flux within 0.1 degrees [248]). Although no VHE emission is detected from J0218, the blazar 3C 66A (green cross), a well-known VHE source [15, 27], is seen with high significance.

Table 9.1.

Given the broad pulse shape in the high-energy band, the use of the off-pulse region to estimate the background would lead to large uncertainties due to its smaller phase extent of 0.36 compared to the on-pulse width of 0.64. Therefore, we chose three source-free reflected-region backgrounds located at the same distance from the FoV center, which we expect to have the same acceptance as the region containing the source [51]. The upper limits (ULs) to the differential flux were obtained by following the Rolke and López [202] method under the assumption of a Gaussian systematic uncertainty in the detection efficiency, with a standard deviation of 30% systematic uncertainty in the flux level. Hereafter, the ULs will be given at 95% confidence level (CL). We assumed a spectral index $\Gamma = -4.5$ obtained from the power-law fit to the high-energy (>10 GeV) *Fermi*-LAT data, as reported in the

Third Hard Source Catalog [21].

Figure 9.4 shows our MAGIC upper limits, indicated with blue arrows, along with the green points and upper limits from the *Fermi*-LAT analysis. The numerical values are reported in Table 9.3.

Table 9.3: *Fermi*-LAT and MAGIC spectral points and Upper Limits. Centers of energy bins are reported. *Fermi*-LAT data utilizes 32 logarithmically spaced bins between 100 MeV and 870 GeV. Three bins, spanning 12.38 - 28.99 GeV, were combined in order to produce a flux point instead of an upper limit. As such, a total of 30 bins are reported for *Fermi*-LAT. MAGIC utilizes 14 logarithmically spaced bins between 20 GeV and 63 TeV. Note that we did not obtain upper limits for the last five MAGIC bins (i.e. E> 3.56 TeV) because they have zero counts and such limits would be considered too unreliable.

| **E** [GeV] | **Fermi-LAT** **$E^2$dN/(dEdAdt)** [TeV $cm^{-2}$ $s^{-1}$] | **MAGIC** **$E^2$dN/(dEdAdt)** [TeV $cm^{-2}$ $s^{-1}$] | **E** [GeV] | **Fermi-LAT** **$E^2$dN/(dEdAdt)** [TeV $cm^{-2}$ $s^{-1}$] | **MAGIC** **$E^2$dN/(dEdAdt)** [TeV $cm^{-2}$ $s^{-1}$] |
|---|---|---|---|---|---|
| 0.12 | $(7.24 \pm 1.58) \times 10^{-12}$ | $\cdots$ | 33.40 | $< 3.79 \times 10^{-13}$ | $\cdots$ |
| 0.15 | $(7.69 \pm 1.02) \times 10^{-12}$ | $\cdots$ | 44.35 | $< 4.71 \times 10^{-13}$ | $\cdots$ |
| 0.20 | $(8.11 \pm 0.73) \times 10^{-12}$ | $\cdots$ | 45.93 | $\cdots$ | $< 8.32 \times 10^{-12}$ |
| 0.27 | $(7.77 \pm 0.57) \times 10^{-12}$ | $\cdots$ | 58.88 | $< 5.82 \times 10^{-13}$ | $\cdots$ |
| 0.36 | $(8.25 \pm 0.48) \times 10^{-12}$ | $\cdots$ | 78.18 | $< 7.69 \times 10^{-13}$ | $\cdots$ |
| 0.48 | $(8.15 \pm 0.42) \times 10^{-12}$ | $\cdots$ | 81.68 | $\cdots$ | $< 2.36 \times 10^{-12}$ |
| 0.63 | $(8.34 \pm 0.38) \times 10^{-12}$ | $\cdots$ | 103.80 | $< 1.33 \times 10^{-12}$ | $\cdots$ |
| 0.84 | $(7.50 \pm 0.36) \times 10^{-12}$ | $\cdots$ | 137.80 | $< 1.38 \times 10^{-12}$ | $\cdots$ |
| 1.11 | $(8.22 \pm 0.37) \times 10^{-12}$ | $\cdots$ | 145.25 | $\cdots$ | $< 6.57 \times 10^{-13}$ |
| 1.48 | $(6.79 \pm 0.36) \times 10^{-12}$ | $\cdots$ | 183.00 | $< 1.80 \times 10^{-12}$ | $\cdots$ |
| 1.96 | $(5.34 \pm 0.35) \times 10^{-12}$ | $\cdots$ | 243.00 | $< 2.40 \times 10^{-12}$ | $\cdots$ |
| 2.61 | $(5.37 \pm 0.38) \times 10^{-12}$ | $\cdots$ | 258.30 | $\cdots$ | $< 3.50 \times 10^{-13}$ |
| 3.46 | $(4.05 \pm 0.38) \times 10^{-12}$ | $\cdots$ | 322.60 | $< 3.19 \times 10^{-12}$ | $\cdots$ |
| 4.59 | $(3.07 \pm 0.37) \times 10^{-12}$ | $\cdots$ | 428.30 | $< 4.29 \times 10^{-12}$ | $\cdots$ |
| 6.10 | $(2.90 \pm 0.40) \times 10^{-12}$ | $\cdots$ | 459.34 | $\cdots$ | $< 1.94 \times 10^{-13}$ |
| 8.10 | $(1.28 \pm 0.30) \times 10^{-12}$ | $\cdots$ | 568.70 | $< 5.83 \times 10^{-12}$ | $\cdots$ |
| 10.75 | $(9.24 \pm 3.01) \times 10^{-13}$ | $\cdots$ | 755.00 | $< 8.10 \times 10^{-12}$ | $\cdots$ |
| 18.95 | $(4.66 \pm 1.71) \times 10^{-13}$ | $\cdots$ | 816.84 | $\cdots$ | $< 3.30 \times 10^{-13}$ |
| 25.83 | $\cdots$ | $< 9.12 \times 10^{-11}$ | 1452.58 | $\cdots$ | $< 1.06 \times 10^{-13}$ |
|  |  |  | 2583.09 | $\cdots$ | $< 1.05 \times 10^{-13}$ |

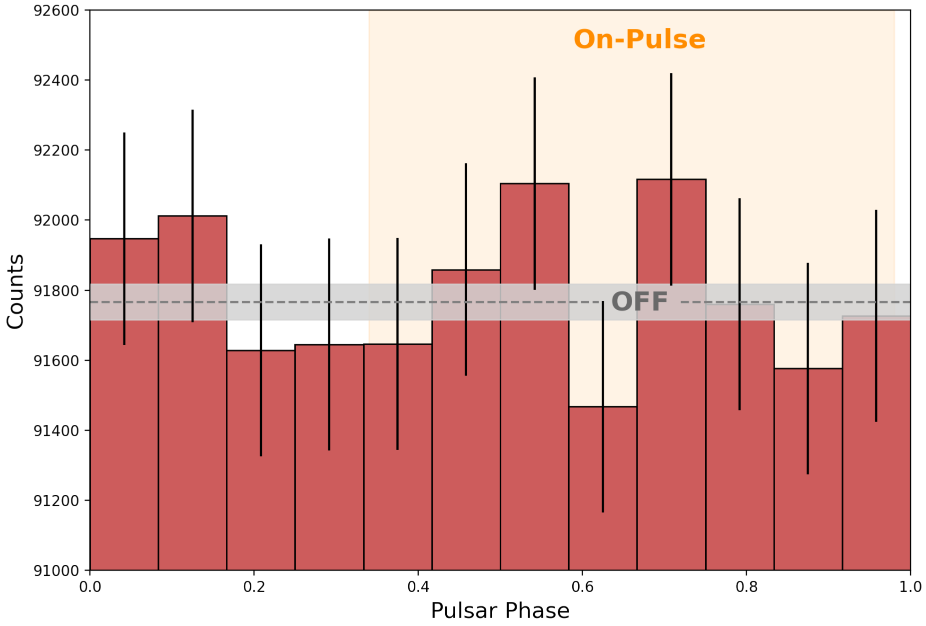

Figure 9.7: Search for VHE pulsations using MAGIC events between 20 - 200 GeV, shown with the pink histogram. We used the same on-pulse interval as LAT analysis, [0.34-0.98], presented with the gold area. The grey horizontal dashed line within the one sigma uncertainty band indicates the average number of OFF events collected from three reflected-region backgrounds in the FoV. No significant pulsation is detected.

Given the hard spectrum observed by *Fermi*-LAT, we concentrated our search for a pulsed signal in the lowest energy decade starting at threshold energy for the MAGIC observations. Hence, the phase-folded light curve of J0218 (see Figure 9.7) is computed in the energy range from 20 GeV to 200 GeV. We performed the same unbinned likelihood test described in Section 9.3.1, to determine whether the detected photons are likely to come from the distribution function represented by the lower energy template (see Figure 9.5, top panel), obtaining no evidence for pulsation (p-value $\gg 0.05$). In addition, we chose to carry out a standard pulsation search, looking at *ON* and *OFF* events. The on-pulse region was selected as the phase interval between 0.34-0.98 and shown as the gold area in Figure 9.7, as defined by our *Fermi*-LAT analysis (see the top panel of Figure 9.5 and Table 9.1). The same source-free reflected-region backgrounds, shown with the grey horizontal band in Figure 9.7, were used for calculating the significance of the excess events using Eq.17 of [169]), and no significant ($0.057\sigma$) pulsation was found. Moreover, we applied region-independent signal tests [75] ( $\chi^2$, and H-test), also with null results (5.54, for 11 degrees of freedom, and $0.05\sigma$, respectively).

## 9.4 Theoretical Modeling

We modeled the broadband spectrum of J0218 from UV to VHE $\gamma$-rays (14 orders of magnitude in energy) using a numerical force-free magnetosphere model for the global magnetic field, computing the individual trajectories of particles injected at the neutron star surface. Two populations of particles are injected: primary electrons/positrons along field lines that connect to the current sheet and are accelerated by an assumed parallel electric field distribution, and secondary electrons/positrons from polar cap pair cascades along field lines where there is no accelerating electric field. The dynamics and radiation of the particles are followed from the neutron star surface to a distance of 2 light cylinder radii ($2R_{lc}$) and radiated photons are stored in energy-dependent sky maps of observer angle vs. rotation phase [125, 130].

All particles radiate by synchro-curvature (SC) and inverse Compton (IC) emission. The pitch angles for SC are maintained through cyclotron resonant absorption of radio photons emitted above the polar cap (PC) [129]. The SC also assumes the radius of curvature of the particle trajectory in the inertial observers' frame. The IC requires that trajectories be followed twice, once to store the SC radiation emissivity and another to compute the local photon densities from the stored emissivity and radiate IC [125, 130].

The main assumptions of the model are the parallel electric field ($E_{||}$) distribution, the source of pairs, pair multiplicity (how many pairs are produced in a vacuum gap pair cascade) and their injection distribution on the PC, and the mechanism for generating pitch angle. Apart from this, the model requires the observed parameters of the pulsar ($P$ and $\dot{P}$). The magnetic and electric field distribution assumptions are based on results of Particle-In-Cell (PIC) simulations showing that pulsars producing high pair multiplicity have near-force-free magnetospheres and

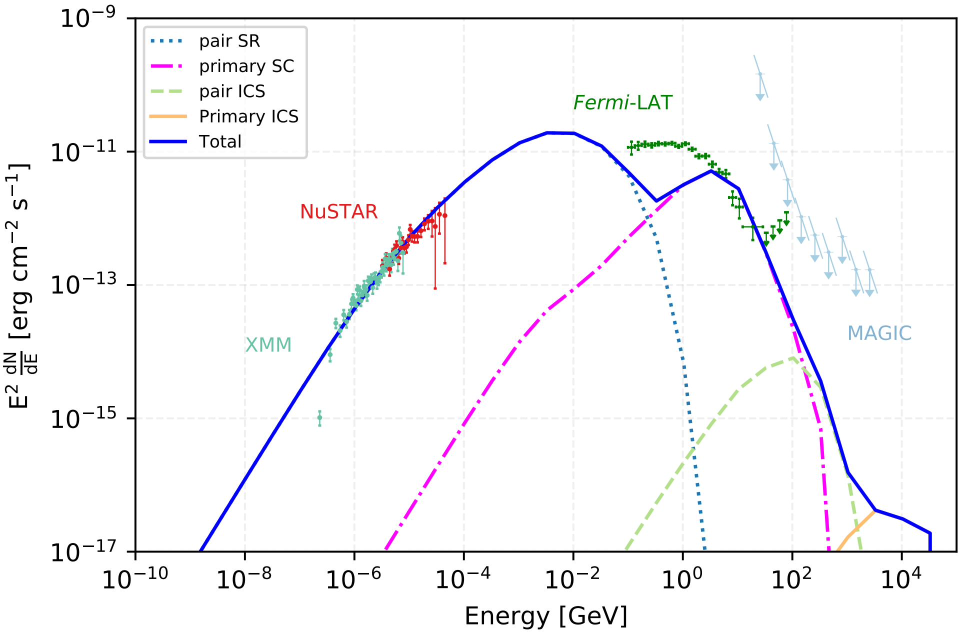

Figure 9.8: Model predictions for the spectrum of phase-averaged emission from accelerated particles and pairs in PSR J0218+4232, for an assumed magnetic inclination angle $\alpha = 45°$ and viewing angle $\zeta = 65°$. The solid orange line represents the predicted ICS component due to accelerated SC-emitting primaries scattering the pair SR component (blue dotted line). The thick blue line identifies the overall emission model. Data points show the soft (XMM) and hard (NuSTAR) X-ray emission [from 112], as well as the LAT spectral points and MAGIC upper limits obtained in this work. Note that the LAT and MAGIC spectral points and upper limits represent the total (pulsed plus unpulsed) emission, however, given the broad peak and large pulsed fraction (see Figure 9.5), the differences between this and the *pulsed* spectrum would be marginal, and would not significantly affect the model fit parameters. Note that the $\gamma$-ray data are identical to those in Figure 9.4.

that the highest parallel electric fields are in the current sheet. Increasing the pair multiplicity increases the pair SC (mostly synchrotron radiation (SR)) and the pair IC (mostly synchrotron self-Compton, SSC). Increasing the E parallel increases the SC of primaries, increases the high-energy (GeV) cutoff, and increases the IC (at 10 TeV). For J0218, we assumed a magnetic inclination angle $\alpha = 45°$, a viewing angle $\zeta = 65°$, and a pair multiplicity of $M_{+} = 1 \times 10^5$. Figure 9.8 shows the model predictions, including the various individual emission components.

We have also used a synchro-curvature model where all unknowns are reduced to just a few parameters that represent the observed spectrum (see Torres [226] and

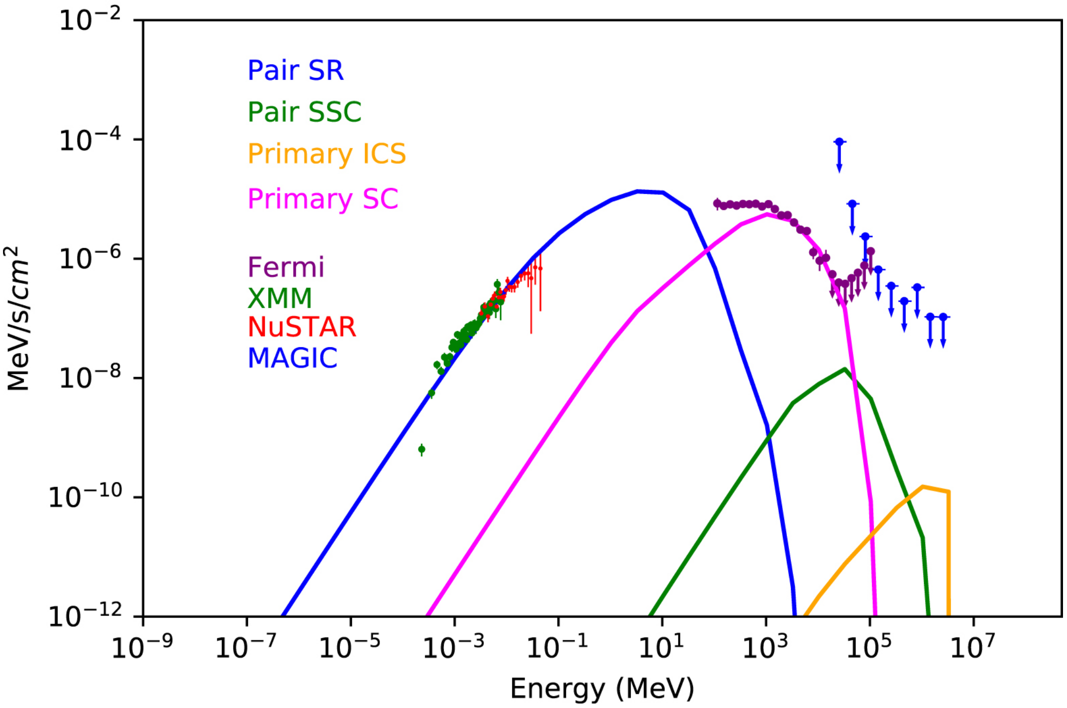

Figure 9.9: Updated modeling of PSR J0218+4232, using the same data as Figure 9.8 but with an assumed magnetic inclination angle $\alpha = 60°$ and viewing angle $\zeta = 65°$. The model and data agreement has improved above 1 GeV. Image from Harding, Venter, and Kalapotharakos [128].

Torres et al. [227] for details). The model follows particle trajectories in a generic region of a pulsar magnetosphere threaded by an accelerating parallel electric field, ($E_{||}$). The region is located around the light cylinder, and particles are assumed to enter it at position $x_{in}$ with a (sizeable) pitch angle $\alpha$. The model parameterizes the magnetic field by a power law $B(x) = B_s(R_s/x)^b$ (see the discussion in Viganò et al. [237]), where $x$ is the distance along the field line, $b$ is referred to as the magnetic gradient, $B_s$ is the surface magnetic field, and $R_s$ is the pulsar radius. Given $(E_{||}, b)$ as free parameters, and the period and period derivative $(P, \dot{P})$, the model solves the equations of motion that balance acceleration and losses by SC radiation (see Cheng and Zhang [65] and Viganò et al. [238]), computing the total emission. The model assumes that the distribution of particles emitting towards us can be parameterized as $dN_e/dx \propto e^{-(x-x_{\rm in})/x_0}$ where the inverse of $x_0/R_{lc}$ ($R_{lc}$ is the light cylinder radius and $x_0$ is a length scale) is referred to as the *contrast*.

Figure 9.10 shows the results of the model with best fit parameters,

$\log(E_{||}/V\,m^{-1})$=10.92, $\log(x_0/R_{lc})$=$-4.20$ and $b$=3.70. The agreement between the model description and the broad-band data is acceptable (the fractional residual errors are of the order ~10%), despite the significant increase in both the precision of each spectral measurement and the number of data points.

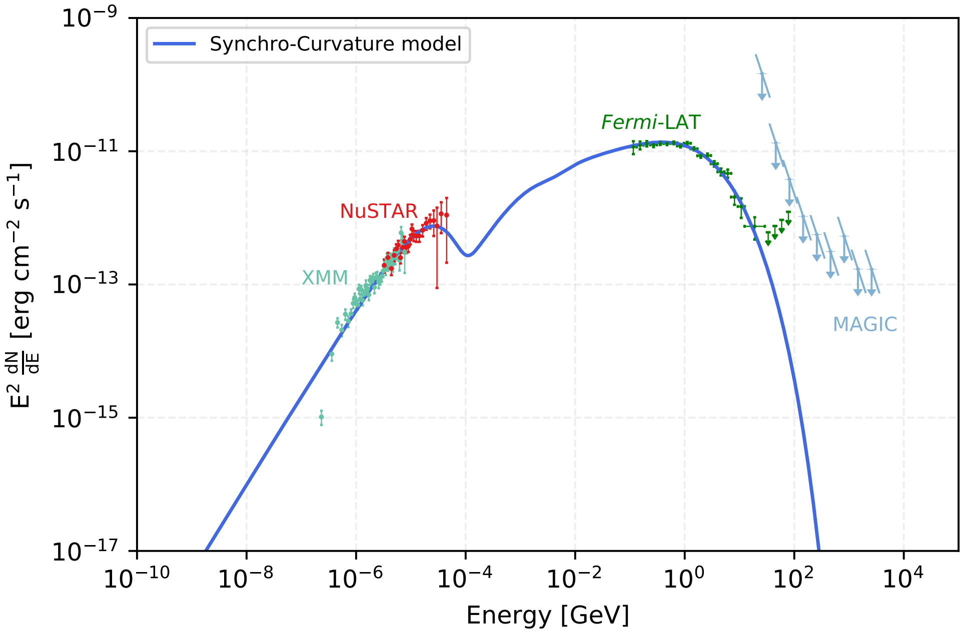

Figure 9.10: Broad-band spectrum of PSR J0218+4232, from the X-ray (XMM and NuSTAR) to the $\gamma$-ray (*Fermi*-LAT and MAGIC) range, along with the best fit to the synchro-curvature model [226]. The model is described by these parameters: *log*$(E_{||}/V\,m^{-1})$=10.92, $\log(x_0/R_{lc})$=$-4.20$, and $b$=3.70. Note that the X-ray and $\gamma$-ray data are identical to those in Figure 9.8.

## 9.5 Discussion and Conclusions

The detection by ground-based Cherenkov telescopes of pulsed emission from the Crab pulsar [28, 235], most recently detected up to TeV energies [31], followed by the detection of pulsations from Vela [116], also up to TeV energies [130], has led to a flurry of activity by pulsar experts to develop self-consistent models able to explain the detected emission over such a broad range of energies.

In addition, the development of the Sum-Trigger-II system in MAGIC has significantly improved the sensitivity of the telescopes below 100 GeV, something which has enabled the detection of pulses from Geminga between 15 GeV and 75 GeV [176], making this the third $\gamma$-ray pulsar (and first *middle-aged* one) detected with ground-based telescopes [9].

J0218 is part of a small but diverse population of MSPs with a well-characterized broad-band non-thermal energy distribution. Several of these MSPs have an 'inverted' spectrum in X-rays (where $E^2dF/dE$ decreases with energy), quite different from that of J0218 as we have reported here, see Figure 3 of Coti Zelati et al. [70].

We also note that the fitted magnetic gradient $b$ for J0218 and other MSPs within the synchro-curvature model [226] is larger than for normal pulsars. This is perhaps the result of the larger $B_{lc}$ of MSPs compared to typical pulsars, due to the smaller size of $R_{lc}$. This needs to be taken into account when making predictions for their observability at lower energies based only on the $\gamma$-ray data. Fits to the $\gamma$-ray data alone are mostly insensitive to the value of the magnetic gradient, and assuming a lower $b$ could lead to incorrect predictions that an MSP is undetectable in the X-ray band.

In accordance with previous studies, we also find here that the relevant scales for the production of the pulsar's spectrum (given by $x_0$) is small in comparison with the light cylinder radius. This is true in general for MSPs, for which the light cylinder is already orders of magnitude smaller than in normal pulsars, i.e., the $x_0/R_{lc}$-values imply a relevant region of emission $\ll 1$ km.

Instead of subtracting the background events from the off-pulse region, we applied a reflected-region background subtraction approach for the MAGIC analysis, due to the large on-pulse interval of the LAT phaseogram. No evidence of emission (either pulsed or unpulsed) is apparent in the MAGIC data, and the measured MAGIC upper limits are well above our two theoretical model predictions for VHE emission. The curvature radiation component from particles accelerated mostly in the current sheet is expected to fall to flux levels too low at VHE energies for de-

---

[9] The H.E.S.S. Collaboration has also reported at the 36th International Cosmic Ray Conference (ICRC2019) the detection of $\gamma$-ray pulsations up to $\sim$70 GeV from PSR B1706–44 [219], which, if confirmed, would bring the total number of ground-based detected $\gamma$-ray pulsars to four.

tection by MAGIC, and the ICS components from both pairs (mostly SSC) and accelerated primaries are predicted to be at even lower flux levels.

There is a notable discrepancy in the spectrum generated by the Harding model and the Fermi-LAT data. This is due to an under-prediction of SR, either from the low-energy component of the Primary SC radiation, or the high-energy component of Pair SR. In regards to the Primary SC radiation, lowering the electric field within the light cylinder would decrease the energy of SR, pushing the spectrum in the correct direction. Similarly, increasing the number of pairs at high energies would increase the energy of Pair SR. However, the current values of these quantities are set via the underlying models informing the simulation. While it would be possible to tweak the values manually, a fully consistent solution would see theoretical changes being made to the underlying models. Providing a better fit, the results from the Torres model could also inform these changes.

A more recent version of the Harding model was applied to the same data shown in Figure 9.8, and is presented in Harding, Venter, and Kalapotharakos [128] (with subsequent updates to the model also described). As seen in Figure 9.9, the updated model better matches the higher energy LAT points, but still under-predicts the spectrum below 1 GeV, and for much the same reasons.

Most models for $\gamma$-ray emission from pulsars do not predict high levels of ICS and SSC emission for MSPs. In the model we used here, described by Harding and Kalapotharakos [125] and Harding et al. [130], for example, the pairs that come from the PC cascade and MSP surface magnetic fields are so low that the photons need to have much higher energies to produce pairs by one-photon magnetic pair production than do photons from normal pulsars. The MSP pair spectra are thus shifted to much higher energies (typically $\gamma \sim 10^4 - 10^7$) [126]. This will produce higher energy SR near the light cylinder (to account for the discrepancies, the pair spectra would need to be pushed *even higher*). Since VHE emission is most likely ICS or SSC, and both particles and photons have higher energies, the VHE emission will be Klein-Nishina limited and therefore suppressed. This is also a problem for outer gap (OG) models since the latest models have pairs also produced near the PC as otherwise, MSPs cannot sustain OGs [122]. Observationally, we see that the SR spectra seem to extend to higher energy in MSPs (at least the energetic ones that have non-thermal emission). So the SR photons and the particles that produce them must be at higher energy. The Cherenkov Telescope Array (CTA) is expected to have significantly better sensitivity than MAGIC in the 10–100 GeV range, and this and other pulsars will thus be prime targets for observation [63]. On the other hand, pulsars like J0218 are also good sources for MeV telescopes, such as AMEGO [182], that can detect the predicted SR peaks around 1 - 10 MeV.

# Chapter 10

# Conclusion

In this thesis, I have attempted to further our understanding of the emission mechanism of pulsars, with particular focus on the MeV and millisecond pulsar varieties.

Chapter 6 addressed PSR J1813-1749, a soft $\gamma$-ray pulsar we hoped would be visible with *Fermi*-LAT. I timed this pulsar with NICER, contributing to Ho et al. [141]. Applying my timing solution to data from *Fermi*-LAT did not yield a detection of pulsations, limiting insights into the emission mechanism of the source. However, such a timing solution will help to inform a search for this source with future MeV missions.

Chapter 7 addressed the curious case of PSR J1846-0258. This is the only pulsar with a published $\gamma$-ray pulsation that did not reach the significance criteria to be included in the upcoming 3PC. I verified the published detection by Kuiper, Hermsen, and Dekker [163], and showed that the significance of pulsations continues to increase after the time of initial publIACTion. I also generated a timing solution for this pulsar with NICER, which I applied to data from *Fermi*-LAT. No additional pulsations were detected, although given the relatively short duration of NICER observations when compared to those presented in Kuiper, Hermsen, and Dekker [163], this does not contradict the prior published results. As this pulsar can only be detected via non-standard techniques, I did not extract a spectrum for use in modeling of the emission mechanism. Like PSR J1813-1749, this additional timing provides long-term spin-down information of the source, which can help inform future efforts to detect pulsations from this source.

PSR J2022+3842 is a soft $\gamma$-ray pulsar from which I was able to extract sufficient spectral information to inform modeling of its emission mechanism. To do this, I performed a phased analysis of the source with *Fermi*-LAT, informed by timing solutions from Ohuchi et al. [196] and Smith [215], as well as one I generated with NICER. Preliminary results of the emission modeling agree with and improve upon those previously published in Torres et al. [227]. Future work on this project involves the inclusion of additional X-ray data in the modeling analysis, particularly in the higher energies covered by NuSTAR. As with the other MeV pulsars, this is a promising source for observation with a future MeV mission.

Finally, I examined the millisecond pulsar PSR J0218+4232. We hoped that this pulsar would be the first MSP detected by IACTs. However, collaborators in the MAGIC collaboration showed this was not the case. Further, theoretical modeling of this source showed that detection by future IACTs, such as CTA, is unlikely. However, the *Fermi*-LAT spectrum I extracted was able to shed insight to this non-detection when analyzed with emission mechanism modeling programs.

# Appendix A

# Appendix

## A.1 *Fermi*-LAT's Test Statistic and $\sigma$

In this section, I will use the following notation:

- $H_0$: null hypothesis
- $H_1$: alternate hypothesis
- $\phi(\phi_0)(\phi_1)$: parameters of interest (of $H_0$)(of $H_1$)
- $\theta(\theta_0)(\theta_1)$: nuisance parameters(of $H_0$)(of $H_1$)
- $L(x)$: maximum likelihood of $x$

When attempting to quantify the detection significance of a $\gamma$-ray source, the underlying question being asked is "What is the probability that random fluctuations would produce a source-like signal that is at least as significant as the one I think I see?". In mathematical terms, this is equivalent to seeking the p-value of the signal. p-value is also convenient conceptually in that it is simply the decimal representation of a percentage, e.g. a p-value of 0.05 means that there is only a 5% probability that a random fluctuation could produce a signal at least as significant as the one observed. However, particle physicists often prefer to present significances in terms of $n\sigma$ (e.g. $3\sigma$, $5\sigma$, etc.)..

In this instance, $\sigma$ refers to the standard deviation of a normal distribution centered at position $\mu$ (i.e. the distribution's mean), and $n$ is a simple multiplicative factor. A claim of $n\sigma$ significance can be converted to a p-value by finding the fraction of a normal distribution lying above $\mu + n\sigma$. As the opposite value, the fraction of the distribution lying below $\mu + n\sigma$, is simply the cumulative density function (CDF), $n\sigma$ can be converted to p-value as:

$$\text{p-value} = 1 - \text{CDF}(n\sigma) = \frac{1}{2}\left[1 - \text{erf}\left(\frac{n}{\sqrt{2}}\right)\right] \tag{A.1}$$

where erf is the error function $\text{erf}(x) = \int_0^x e^{-t^2} dt$

Recall from Sec. 4.1 that the test statistic (TS) resulting from a *Fermi*-LAT likelihood analysis is defined as follows:

$$\text{TS} = -2\ln\left[L(H_0)/L(H_1)\right] \tag{A.2}$$

A natural next step is to convert this TS to a value of $n\sigma$. The approximation most commonly used is

$$n\sigma \approx \sqrt{\text{TS}} \tag{A.3}$$

One path towards this approximation is by way of Wilks' Theorem [242], with a procedure outlined in Ackermann et al. [19]. Wilks' Theorem states that, when testing the null hypothesis, the log-likelihood ratio will approach a $\chi^2_k$ distribution as the number of data samples goes to infinity, where $k$ is the difference in the number of degrees of freedom between the null hypothesis and alternate hypothesis. Additional conditions necessary for Wilks' Theorem to be valid are [26]:

- The parameters of interest and nuisance parameters must be far from their boundary conditions.
- The model cannot have redundant parameters.
- The null hypothesis must be a subset of the parameters in the alternate hypothesis.
- Either the null hypothesis or the alternate hypothesis must be correct.

A common application of TS is to determine the significance of a power-law source with fixed photon index. In this instance:

- $H_0$: maximum likelihood model with the normalization of the source of interest set to 0
- $H_1$: maximum likelihood model with the normalization of the source of interest set to its maximum likelihood value

In this instance, the difference in the degrees of freedom between the null and alternate hypothesis is 1 (the normalization of the target source). If Wilks' Theorem is applied, TS can be said to follow a $\chi^2_1$ distribution. The cumulative distribution function is then:

$$\mathrm{CDF}(\mathrm{TS}) = \mathrm{erf}\left(\frac{\sqrt{\mathrm{TS}}}{\sqrt{2}}\right) \tag{A.4}$$

Which can be converted to a p-value as follows:

$$\text{p-value} = 1 - \mathrm{CDF} = 1 - \mathrm{erf}\left(\frac{\sqrt{\mathrm{TS}}}{\sqrt{2}}\right) \tag{A.5}$$

However, this p-value is twice as large as the value being sought. This is because, as currently defined, TS is sensitive to both *positive* and *negative* sources simultaneously. Very rarely in astrophysics is it not known if a source should be emitting or absorbing photons. If the maximum likelihood of the alternate hypothesis indicates a source of negative brightness, it should be rejected. After accounting for this feature, the new equation for p-value becomes:

$$\text{p-value} = \frac{1}{2}\left[1 - \mathrm{erf}\left(\frac{\sqrt{\mathrm{TS}}}{\sqrt{2}}\right)\right] \tag{A.6}$$

Setting this equal to Eqn. A.1

$$\frac{1}{2}\left[1 - \mathrm{erf}\left(\frac{n}{\sqrt{2}}\right)\right] = \frac{1}{2}\left[1 - \mathrm{erf}\left(\frac{\sqrt{\mathrm{TS}}}{\sqrt{2}}\right)\right] \tag{A.7}$$

The original claim

$$n\sigma \approx \sqrt{\mathrm{TS}} \tag{A.8}$$

clearly holds if the underlying assumptions are believed.

However, in the process of adding the factor of $\frac{1}{2}$, an interesting situation has arisen. As stated previously, Wilks' Theorem requires that the parameters in the null and alternative hypothesis be far from their boundaries. By requiring that our source of interest have a positive normalization, we have imposed the boundary condition that it be greater than 0. However, in the null hypothesis, the normalization of that source is set to 0. Is it fair to ignore this condition before applying Wilks' Theorem, only to impose it afterwords?

Chernoff [66], building on the work of Wilks [242], describes the distribution of the log-likelihood ratio in a variety of constrained parameter spaces, including the scenario where "one may wish to test whether [a parameter value] is on one side of a hyperplane", e.g. the scenario described above. A review of how the techniques of Chernoff [66] can be applied to particle physics is presented in Cowan et al. [71], and summarized below.

In the scenario where the source of interest is restricted to be a positive photon emitter, the TS can be written as follows:

$$\mathrm{TS} = \begin{cases} -2\ln\left[L(\phi_0,\theta_0)/L(\phi_1,\theta_1)\right] & \text{if } \phi_1 \geq 0 \\ -2\ln\left[L(\phi_0,\theta_0)/L(0,\theta_1(0))\right] & \text{if } \phi_1 < 0 \end{cases}$$

where $H_0$ and $H_1$ have been notationally replaced by their maximum likelihood parameter values $\phi$ and $\theta$. $\theta_1(0)$ indicates that the nuisance parameters have been re-maximized for the $\phi_1 = 0$ case. It follows that, definitionally, $L(\phi_0,\theta_0) = L(0,\theta_1(0))$, and as such

$$\mathrm{TS} = \begin{cases} -2\ln\left[L(\phi_0,\theta_0)/L(\phi_1,\theta_1)\right] & \text{if } \phi_1 \geq 0 \\ 0 & \text{if } \phi_1 < 0 \end{cases} \tag{A.9}$$

This is the desired result for TS. In the event that a test source is positive, TS will default to the same value presented in Eqn. A.2. In the non-physical event that a test source is negative, TS will default to 0. The task is then to find the CDF(TS) of Eqn. A.9, from which the p-value will readily follow.

Wald [239] proved the approximation

$$-2\ln\left[L(\phi_0,\theta_0)/L(\phi_1,\theta_1)\right] = \frac{(\phi_0-\phi_1)^2}{\sigma^2} + \mathcal{O}(1/\sqrt{N}) \tag{A.10}$$

under the condition that there is only a single parameter of interest. Further, $\phi_1$ is distributed according to a Gaussian distribution of mean $\phi'$ and standard deviation $\sigma$. $\mathcal{O}$ represents the error of the approximation, which scales as $1/\sqrt{N}$, where $N$ is the number of samples. Applying this approximation to Eqn. A.9 yields

$$\mathrm{TS} = \begin{cases} \phi_1^2/\sigma^2 & \text{if } \phi_1 \geq 0 \\ 0 & \text{if } \phi_1 < 0 \end{cases} \tag{A.11}$$

where we have assumed $N$ is large enough to neglect $\mathcal{O}$, and used the fact that we are testing the null hypothesis to set $\mu_0 = 0$.

Although the following assumption is not strictly necessary at this stage, we will further assume the distribution $\phi_1$ is centered on 0 ($\phi' = 0$), as seems reasonable when testing the null hypothesis.

The probability distribution for Eqn. A.11 can now be converted into a probability density function (PDF). If $\phi_1 \geq 0$, TS is distributed as $\chi_1^2$. This follows from the definition of a $\chi_k^2$ distribution as the sum of the squares of $k$ independently-sampled normally distributed values. $\phi_1/\sigma$ is the $k = 1$ normal distribution sample which is being squared. If $\phi_1 < 0$, the TS will simply be 0, leading to the PDF $\delta(\mathrm{TS})$. Finally, note that 50% of the time $\phi_1 < 0$ and 50% of the time $\phi_1 \geq 0$, as Wald's approximation holds that $\phi_1$ is Gaussian distributed, and we made the assumption that it is centered on 0 when we test the null hypothesis. The final PDF will thus be an equally weighted sum of a delta function and a $\chi_1^2$ distribution. This gives

$$\mathrm{PDF(TS)} = \frac{1}{2}\delta(\mathrm{TS}) + \frac{1}{2}\frac{1}{\sqrt{2\pi}}\frac{1}{\sqrt{\mathrm{TS}}}e^{-\frac{1}{2}\mathrm{TS}} \tag{A.12}$$

Converting this to a PDF by integrating from $-\infty$ to TS yields:

$$\mathrm{CDF(TS)} = \frac{1}{2} + \frac{1}{2}\mathrm{erf}\left(\frac{\sqrt{\mathrm{TS}}}{\sqrt{2}}\right) = \frac{1}{2}\left[1 + \mathrm{erf}\left(\frac{\sqrt{\mathrm{TS}}}{\sqrt{2}}\right)\right] \tag{A.13}$$

Converting this to a p-value:

$$\text{p-value} = 1 - \mathrm{CDF(TS)} = \frac{1}{2}\left[1 - \mathrm{erf}\left(\frac{\sqrt{\mathrm{TS}}}{\sqrt{2}}\right)\right] \tag{A.14}$$

Comparing this to the p-value for a normal distribution:

$$\frac{1}{2}\left[1 - \mathrm{erf}\left(\frac{n}{\sqrt{2}}\right)\right] = \frac{1}{2}\left[1 - \mathrm{erf}\left(\frac{\sqrt{\mathrm{TS}}}{\sqrt{2}}\right)\right] \tag{A.15}$$

once again reproduces the approximation $n\sigma = \sqrt{\mathrm{TS}}$ under the very particular set of circumstances outlined above (notably, a sufficiently large data set and only one additional degree of freedom in the alternate hypothesis).

## A.2 Illustrative Example of Energy Dispersion

Let the vector $V_{true}$, representing the number of photons at energies $E_{true}$, be the following:

$$V_{true} = \begin{bmatrix} 10000 \\ 1000 \\ 100 \\ 10 \end{bmatrix}, \; E_{true} = \begin{bmatrix} 100MeV \\ 1GeV \\ 10GeV \\ 100GeV \end{bmatrix} \tag{A.16}$$

One energy bin is added to each end of the analysis, with the number of photons in that bin estimated via extrapolation:

$$V_{true} = \begin{bmatrix} 100000 \\ 10000 \\ 1000 \\ 100 \\ 10 \\ 1 \end{bmatrix}, E_{true} = \begin{bmatrix} 10MeV \\ 100MeV \\ 1GeV \\ 10GeV \\ 100GeV \\ 1TeV \end{bmatrix} \tag{A.17}$$

For illustrative purposes, a detector response matrix (DRM) may look like the following:

$$V_{true} = \begin{bmatrix} 0 & 0 & 0 & 0 & 0.02 & 0.99 \\ 0 & 0 & 0 & 0.04 & 0.95 & 0.01 \\ 0 & 0 & 0.04 & 0.9 & 0.03 & 0 \\ 0 & 0.08 & 0.8 & 0.05 & 0 & 0 \\ 0.3 & 0.7 & 0.1 & 0.01 & 0 & 0 \\ 0.7 & 0.2 & 0.06 & 0 & 0 & 0 \end{bmatrix} \tag{A.18}$$

The anti-diagonal nature of the DRM is a matter of convention, allowing it to be “read” in a typical manner, with the lowest energy values located in the bottom left corner. Consequently, the energy bins referenced by $V_{measured}$ are in the opposite order of those appearing in $V_{true}$. One should also note that the values in the illustrative DRM are *much* larger than those in a true DRM. For reference, the DRM used to apply energy dispersion in Ch. 9 is graphically represented in Figure A.1.

The corrected number of counts, $V_{measured}$, is calculated by matrix multiplica-

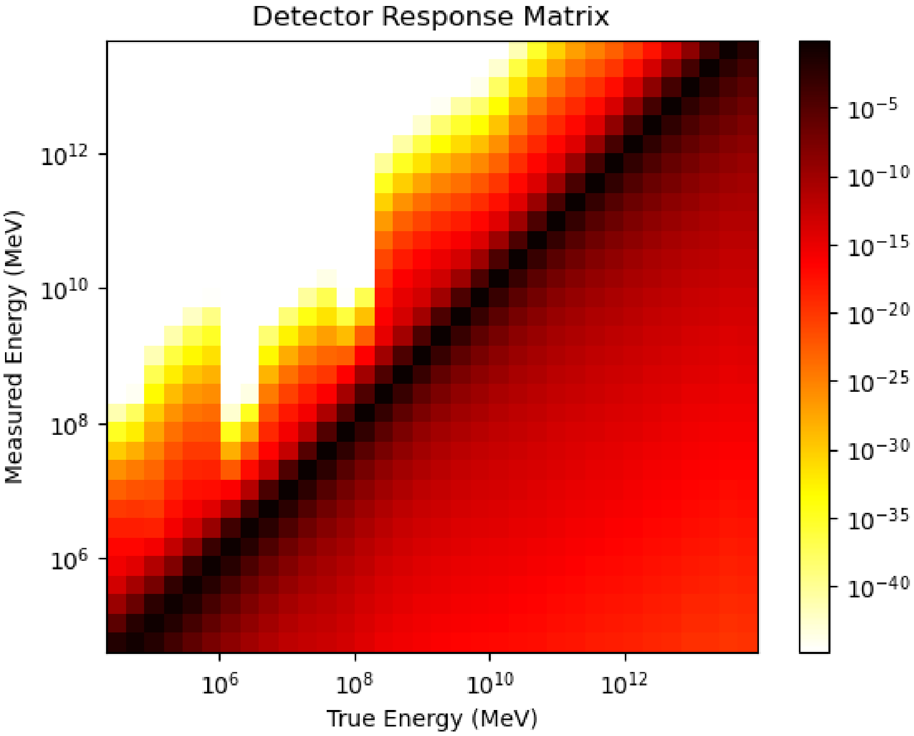

Figure A.1: The detector response matrix used in the analysis presented in Ch. 9.

tion: $V_{measured} = DRM * V_{true}$, which produces:

$$V_{true} = \begin{bmatrix} 1.2 \\ 14 \\ 130 \\ 1605 \\ 37101 \\ 72260 \end{bmatrix}, \; E_{measured} = \begin{bmatrix} 1TeV \\ 100GeV \\ 10GeV \\ 1GeV \\ 100MeV \\ 10MeV \end{bmatrix} \tag{A.19}$$

Scale factors are then computed for each corresponding energy bin $V_{scale} = V_{measured}^{E_{measured}} / V_{true}^{E_{true}}$:

$$V_{scale} = \begin{bmatrix} 1.2 \\ 1.4 \\ 1.3 \\ 1.6 \\ 3.7 \\ 7.2 \end{bmatrix}, \; E_{scale} = \begin{bmatrix} 1TeV \\ 100GeV \\ 10GeV \\ 1GeV \\ 100MeV \\ 10MeV \end{bmatrix} \tag{A.20}$$

$V_{scale}$ is used to scale all corresponding energy bins of the model (regardless of the spatial location of the bin) before it is compared to the counts cube.

# Appendix B

# Characteristic Age

As discussed in Chapter 2, characteristic age can be used to get a rough idea of the age of a rotation powered pulsar. I have encountered two primary methods of deriving the characteristic age, and present a summary here in the hope that this will illuminate underlying approximations that go into the value. Key to both derivations is the idea that $P\dot{P}$ is a constant, and the idea that the inclusion of $\dot{P}$ also makes $P\dot{P}$ a differential equation (recall that $P$ is the pulsar period).

The first path to derivation comes from Condon and Ransom [69]. Axiomatically

$$P\dot{P} = P\dot{P} \tag{B.1}$$

Treating the left hand side as a differential equation, but the right hand side as a constant (implied by examining Eqn. 2.2 and assuming constant magnetic field and inclination angle)

$$P\frac{dP}{dt} = P\dot{P} \tag{B.2}$$

$$P\,dP = P\dot{P}\,dt \tag{B.3}$$

$$\int_{P_0}^{P} P\,dP = P\dot{P}\int_0^{\tau} dt \tag{B.4}$$

$$\frac{1}{2}[P^2 - P_0^2] = P\dot{P}\,\tau \tag{B.5}$$

where $P$ is the currently measured period, and $P_0$ is some unknown initial period.

Assuming $P \gg P_0$ (that is, that the pulsar has significantly slowed down since its birth)

$$\frac{1}{2}P^2 = P\dot{P}\,\tau \tag{B.6}$$

finally leading to

$$\tau = \frac{P}{2\dot{P}} \tag{B.7}$$

where $\tau$ is the characteristic age.

The same conclusion can be reached by starting from the formula for the breaking index [171]:

$$\dot{P} = KP^{2-n} \tag{B.8}$$

$$\frac{dP}{dt} = KP^{2-n} \tag{B.9}$$

$$P^{2-n}dP = K\,dt \tag{B.10}$$

$$\int_{P_0}^{P} P^{2-n}dP = \int_0^{\tau} K\,dt \tag{B.11}$$

$$\frac{P^{n-1} - P_0^{n-1}}{n-1} = K\tau \tag{B.12}$$

inserting Eqn. B.8

$$\frac{P^{(n-1)}P^{(2-n)} - P_0^{(n-1)}P^{(2-n)}}{(n-1)\dot{P}} = \tau \tag{B.13}$$

$$\frac{P}{(n-1)\dot{P}}\left[1 - P_0^{(n-1)}P^{(1-n)}\right] = \tau \tag{B.14}$$

$$\frac{P}{(n-1)\dot{P}}\left[1 - \left(\frac{P_0}{P}\right)^{(n-1)}\right] = \tau \tag{B.15}$$

In doing this, we have assumed $n \neq 1$. In the case of a dipole, $n = 3$, although different values could be used if desired. Finally, assuming $P \gg P_0$ again yields the formula for characteristic age.

$$\tau = \frac{P}{2\dot{P}} \tag{B.16}$$

As discussed in Chapter 2, the characteristic age can at times be far from accurate [186, 158]. This inaccuracy is investigated in terms of the above mentioned $n = 3$ and $P \gg P_0$ assumptions, but broadly keeps Eqn. B.8.

# Appendix C

# PSR J1846-0258 Timing Solutions

The following are the timing solutions, in Tempo2 format [145], generated from the NICER data presented in Ch. 7. The timing solutions are the *best* parameters from an MCMC optimization using PINT [173]. The presented MCMC results are the 50th percentile values, with asymmetric $1\sigma$ errors (16th and 84th percentile values).

## C.1 MJD 58261 - 58675

```
PSR                                 J1846
RAJ                     18:46:24.94000000
DECJ                    -2:58:30.10000000
PMRA                                  0.0
PMDEC                                 0.0
PX                                    0.0
F0                   3.040309859642360557 1 5.8e-08
F1              -6.5485671718815273736e-11 1 3e-15
F2               1.2453086383760032703e-20 1 1e-22
PEPOCH             58643.6685416700000000
PLANET_SHAPIRO                          N
```

```
TZRMJD             58643.6685416700000000
TZRSITE                                 0
TZRFRQ                                inf
```

The result of the MCMC optimization is:

```
F0:         3.04030985777592 (+   4.8263e-09  / -    5.602e-09)
F1:     -6.5486006975927e-11 (+    8.995e-16  / -   7.5184e-16)
F2:     1.24309680705971e-20 (+   6.3513e-23  / -   3.9007e-23)
```

## C.2 MJD 58675 - 58900

```
PSR                                 J1846
RAJ                     18:46:24.94000000
DECJ                    -2:58:30.10000000
PMRA                                  0.0
PMDEC                                 0.0
PX                                    0.0
F0                  3.0403150854964420269 1 1e-07
F1              -6.608889419573677785e-11 1 1e-13
F2              1.4620604896331714068e-20 1 1e-22
PEPOCH             58643.6685416700000000
PLANET_SHAPIRO                          N
TZRMJD             58643.6685416700000000
TZRSITE                                 0
TZRFRQ                                inf
```

The result of the MCMC optimization is:

```
F0:         3.04031513350757 (+   7.5909e-08  / -   8.0131e-08)
F1:     -6.6096440933303e-11 (+   1.1013e-14  / -   1.2456e-14)
F2:     1.48990699873271e-20 (+   3.2598e-22  / -   3.5034e-22)
```

## C.3 MJD 58900 - 59026

```
PSR                                 J1846
RAJ                     18:46:24.94000000
DECJ                    -2:58:30.10000000
PMRA                                  0.0
PMDEC                                 0.0
PX                                    0.0
F0                  3.0403136736738005652 1 1e-07
F1              -6.609876107133421944e-11 1 1e-13
F2               9.303080994648443332e-21 1 1e-22
PEPOCH             58643.6685416700000000
PLANET_SHAPIRO                          N
TZRMJD             58643.6685416700000000
TZRSITE                                 0
TZRFRQ                                inf
```

The result of the MCMC optimization is:

```
F0:           3.040313708102 (+    6.986e-08  / -   5.2326e-08)
F1:    -6.61038636108639e-11 (+   1.2618e-14  / -   1.3845e-14)
F2:     9.59988717121591e-21 (+   7.6409e-23  / -   1.6536e-22)
```

Note that the second frequency derivative, `F2`, does not appear particularly reliable for this dataset. This is likely due to the comparably short time span which the data covers.

## C.4 MJD 58261 - 59026, Artificially Stacked

Artificial glitches are used to align the above timing solutions. The phase offset `GLPH` is fit via maximization of the H-Test.

```
PSR                                 J1846
RAJ                     18:46:24.94000000
DECJ                    -2:58:30.10000000
PMRA                                  0.0
PMDEC                                 0.0
PX                                    0.0
F0                   3.040309859642360557 0 5.8e-08
F1              -6.5485671718815273736e-11 0 3e-15
F2              1.2453086383760032703e-20 0 1e-22
PEPOCH             58643.6685416700000000
PLANET_SHAPIRO                          N
TZRMJD             58643.6685416700000000
TZRSITE                                 0
TZRFRQ                                inf
GLEP_0                            58675.0 0 0.0
GLPH_0                0.25962774290140667 1 0.001
GLF0_0              3.600849761475899e-06 0 0.0
GLF1_0             -5.973549219429154e-13 0 0.0
GLF2_0             2.1675185125716814e-21 0 0.0
GLF0D_0                               0.0
GLTD_0                                0.0
GLEP_1                            58900.0 0 0.0
GLPH_1               -0.07112847746166338 1 0.001
GLF0_1             -2.934444125024527e-06 0 0.0
GLF1_1             -1.276342795364935e-13 0 0.0
GLF2_1             -5.317523901683271e-21 0 0.0
```

```
GLF0D_1                              0.0

GLTD_1                               0.0
```

The result of fitting the phase offset is:

```
GLPH_1:      -0.0623263621679205 (+      0.14602  / -     0.021614)

GLPH_0:        0.210136141306674 (+     0.050107  / -      0.20953)
```

# Appendix D

# PSR J2022+3842: Evidence for Glitches

As the primary focus of the analysis presented in Chapter 8 was to generate spectral points for use in modeling of the pulsar emission mechanism, I opted to use less detailed timing techniques when generating a timing solution. Even though glitches and timing noise appear to be present, they are not strictly relevant on the time scales which I covered by single timing solutions. However, as they may be of interest for other work, I discuss the evidence I have for glitches present in PSR J2022+3842 over the time which it has been observed by NICER.

I repeat Figure 8.1, showing the frequency values of the 20 individual timing solutions over time. Subtracting the average frequency leaves the residuals shown in Figure D.2. While the first two points may deserve further inspection on their own (could they perhaps show another glitch and subsequent relaxation?), two distinct time periods emerge: MJD 58300 - 58850 and MJD 58920 - 59450.

Isolating these two time periods and re-fitting a frequency and frequency derivative yields the residuals shown in Figure D.3. The error bars on these plots are consistent with the case of zero residuals, suggesting the pulsar's spin properties have been sufficiently modeled. However, if the error bars are disregarded, the residuals are parabolic, suggesting the existence of a positive *second* frequency derivative.

Fitting a timing solution with two derivatives and finding the residuals is shown

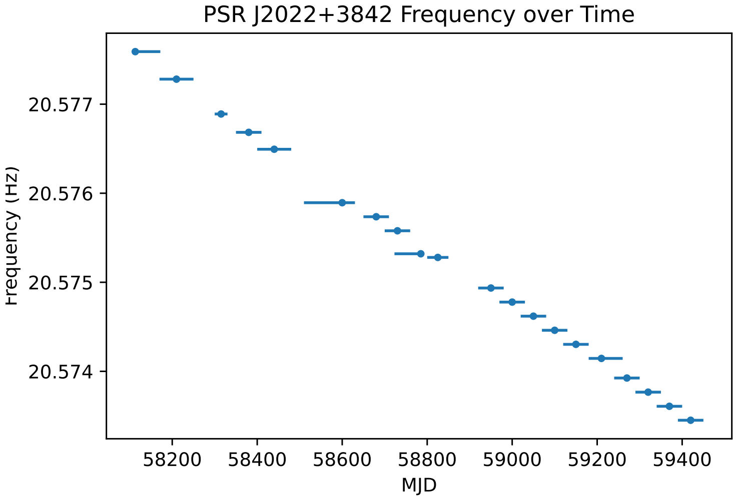

Figure D.1: Measured frequency from each of the 20 individual timing solutions presented graphically. Horizontal bars show the time range covered by each timing solution. These often overlap slightly. Note: This is the same as Figure 8.1.

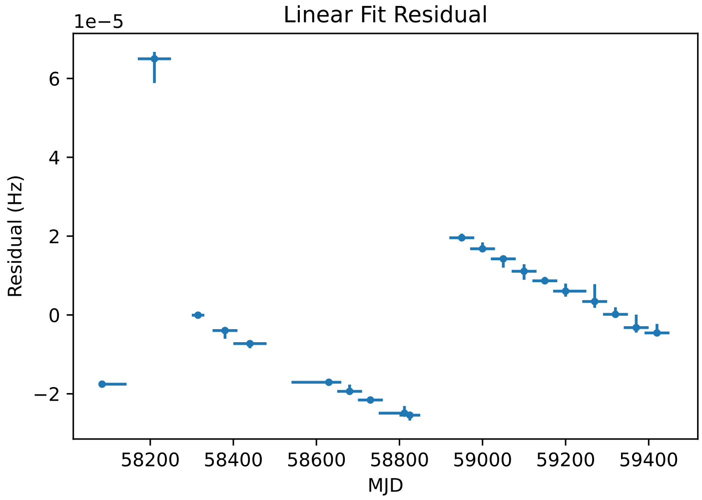

Figure D.2: The result of subtracting the average frequency from each of the individual timing solutions. Two distinct time periods are apparent, with a likely glitch occurring between them. The first two data points could indicate another timing glitch, but more analysis would be needed to confirm this.

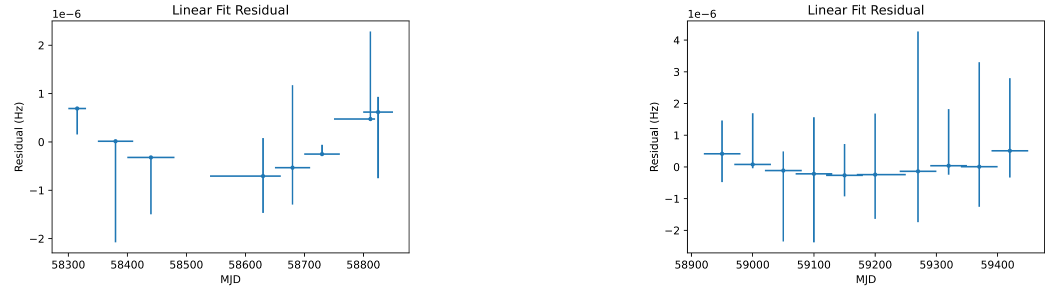

(a) The earlier time period.

(b) The later time period.

Figure D.3: The residuals from fitting a frequency and frequency derivative to the two time periods. The parabolic shape indicates a second frequency derivative may also be present.

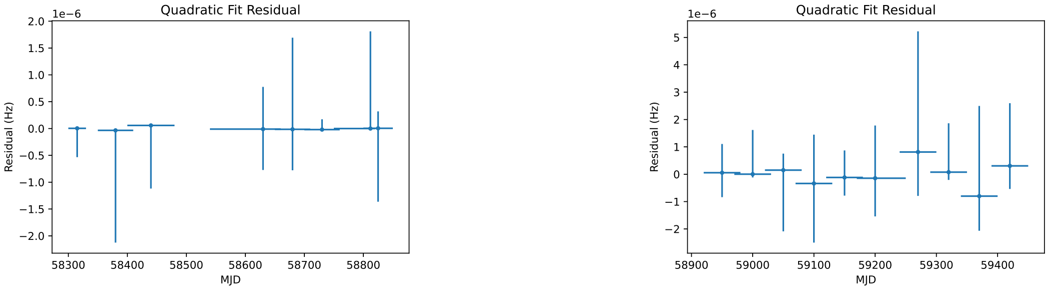

(a) The earlier time period.

(b) The later time period.

Figure D.4: The residuals from fitting a frequency and two derivatives to each of the two segments. The residuals now appear flat, suggesting the pulsar has been adequately modeled.

|  | Span 1 | Span 2 |
|---|---|---|
| Start (MJD) | 58300 | 58920 |
| Finish (MJD) | 58850 | 59450 |
| Epoch (MJD) | 58601.5 | 59183 |
| $f$ (Hz) | 20.5759835 | 20.5741988 |
| $\dot{f}$ (Hz/s) | -3.65360028e-11 | -3.65767397e-11 |
| $\ddot{f}$ (Hz/s/s) | 2.91706368e-21 | 8.96901117e-22 |

Table D.1: The resultant timing parameters from fitting a quadratic to the frequency values in Figure D.1.

in Figure D.4. One possible explanation for this trend, despite large error bars, can be found in the Markov-chain Monte Carlo analysis used to generate the timing solutions. Choosing a less than ideal step size and temperature could artificially inflate the error. Defining an ellipse in frequency and frequency derivative outside which the H-Test drops below a certain value, similar to the TS in LAT analyses, might be more illuminating. However, I leave this to future work.

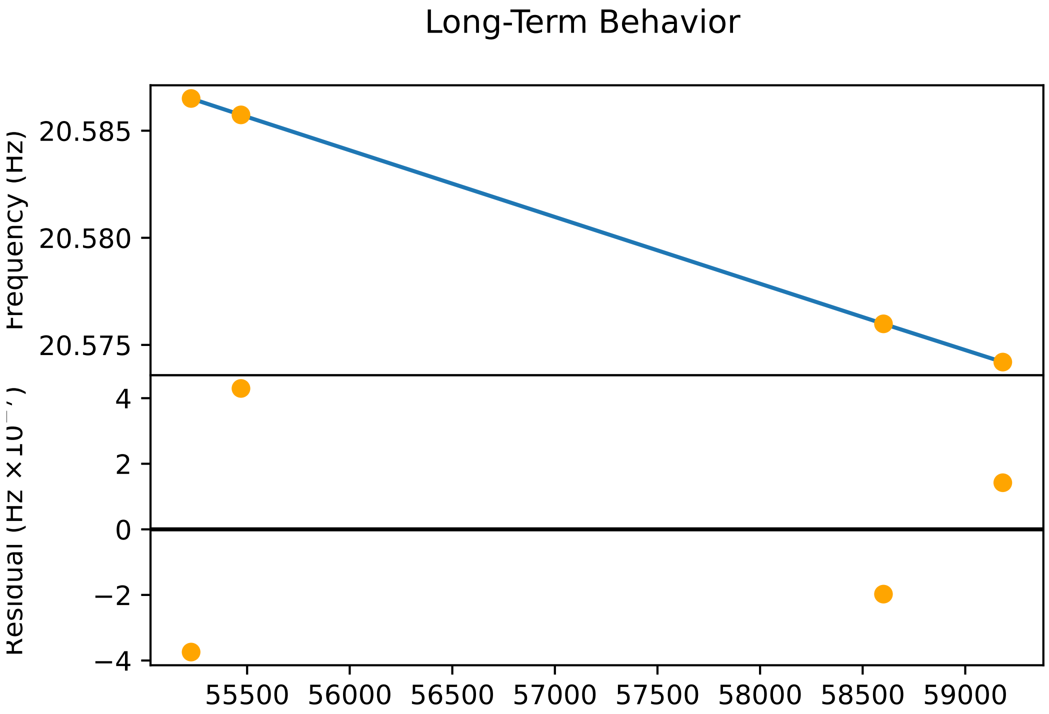

Figure D.5: The result of fitting the frequencies presented in Table D.1 with those of Smith [215] using a quadratic timing solution. The residuals show that the two time periods are consistent. However, I will leave this as a qualitative statement until the results are published.

# Appendix E

# PSR J2022+3842 Timing Solutions

## E.1 MJD 58083 - 59450

```
PSR                        PSR_J2022+3842
START              58083.0000000000000000
FINISH             58143.0000000000000000
DILATEFREQ                              N
DMDATA                                  N
NTOA                                    0
CHI2                                  0.0
RAJ                     20:22:21.68900000
DECJ                    38:42:14.82000000
PMRA                                  0.0
PMDEC                                 0.0
PX                                    0.0
F0                    20.5775902517116549 1 1.16e-05
F1              -3.6491213693739044985e-11 1 1e-10
PEPOCH             58084.0000000000000000
PLANET_SHAPIRO                          N
```

```
TZRMJD             58084.0000000000000000

TZRSITE                                  ssb

TZRFRQ                                   inf
```

The result of the MCMC optimization is:

```
F0:         20.5775902516903 (+   2.5767e-08  / -    8.341e-08)

F1:     -3.6492550008052e-11 (+   3.7315e-13  / -   5.8927e-13)
```

## E.2 MJD 58170 - 58250

```
PSR                        PSR_J2022+3842
START              58170.0000000000000000
FINISH             58250.0000000000000000
DILATEFREQ                              N
DMDATA                                  N
NTOA                                    0
CHI2                                  0.0
RAJ                     20:22:21.68900000
DECJ                    38:42:14.82000000
PMRA                                  0.0
PMDEC                                 0.0
PX                                    0.0
F0                  20.577279376439470582 1 1.16e-05
F1              -4.2898189045330489563e-11 1 1e-10
PEPOCH             58210.0000000000000000
PLANET_SHAPIRO                          N
TZRMJD             58210.0000000000000000
TZRSITE                               ssb
TZRFRQ                                inf
```

The result of the MCMC optimization is:

```
F0:         20.5772811433275 (+   1.7562e-06  / -   6.1519e-06)
F1:    -4.28463992376397e-11 (+   3.4205e-11  / -   3.8398e-12)
```

## E.3 MJD 58300 - 58330

```
PSR                          PSR_J2022+3842

START                  58300.0000000000000000

FINISH                 58330.0000000000000000

DILATEFREQ                                N

DMDATA                                    N

NTOA                                      0

CHI2                                    0.0

RAJ                         20:22:21.68900000

DECJ                        38:42:14.82000000

PMRA                                    0.0

PMDEC                                   0.0

PX                                      0.0

F0                       20.57688973668117427 1 1.16e-05

F1                 -3.6763649920553300304e-11 1 1e-12

PEPOCH                 58315.0000000000000000

PLANET_SHAPIRO                            N

TZRMJD                 58315.0000000000000000

TZRSITE                                 ssb

TZRFRQ                                  inf
```

The result of the MCMC optimization is:

```
F0:         20.5768897298714 (+   8.9629e-09  / -   5.3705e-07)

F1:    -3.67734046011694e-11 (+   1.4284e-14  / -   2.3733e-13)
```

## E.4 MJD 58350 - 58410

```
PSR                        PSR_J2022+3842
START              58350.0000000000000000
FINISH             58410.0000000000000000
DILATEFREQ                              N
DMDATA                                  N
NTOA                                    0
CHI2                                  0.0
RAJ                     20:22:21.68900000
DECJ                    38:42:14.82000000
PMRA                                  0.0
PMDEC                                 0.0
PX                                    0.0
F0                  20.576683793640498266 1 1.16e-05
F1              -3.662346327309358962e-11 1 1e-12
PEPOCH             58380.0000000000000000
PLANET_SHAPIRO                          N
TZRMJD             58380.0000000000000000
TZRSITE                               ssb
TZRFRQ                                inf
```

The result of the MCMC optimization is:

```
F0:         20.5766837930437 (+   5.2054e-09  / -   2.0915e-06)
F1:    -3.66253239805236e-11 (+   4.3178e-15  / -    1.395e-13)
```

## E.5 MJD 58400 - 58480

```
PSR                        PSR_J2022+3842
START              58400.0000000000000000
FINISH             58480.0000000000000000
DILATEFREQ                              N
DMDATA                                  N
NTOA                                    0
CHI2                                  0.0
RAJ                     20:22:21.68900000
DECJ                    38:42:14.82000000
PMRA                                  0.0
PMDEC                                 0.0
PX                                    0.0
F0                  20.576493982525242643 1 1.16e-05
F1              -3.6605352663626004905e-11 1 1e-12
PEPOCH             58440.0000000000000000
PLANET_SHAPIRO                          N
TZRMJD             58440.0000000000000000
TZRSITE                               ssb
TZRFRQ                                inf
```

The result of the MCMC optimization is:

```
F0:         20.5764939822807 (+   6.4668e-10  / -   1.1764e-06)
F1:    -3.66052322409659e-11 (+   1.4148e-13  / -   2.0064e-15)
```

## E.6 MJD 58450 - 58660

```
PSR                        PSR_J2022+3842
START              58540.0000000000000000
FINISH             58660.0000000000000000
DILATEFREQ                              N
DMDATA                                  N
NTOA                                    0
CHI2                                  0.0
RAJ                     20:22:21.68900000
DECJ                    38:42:14.82000000
PMRA                                  0.0
PMDEC                                 0.0
PX                                    0.0
F0                  20.575893588755068464 1 1.16e-05
F1               -3.65551192100554763e-11 1 1e-12
PEPOCH             58630.0000000000000000
PLANET_SHAPIRO                          N
TZRMJD             58630.0000000000000000
TZRSITE                               ssb
TZRFRQ                                inf
```

The result of the MCMC optimization is:

```
F0:         20.5758935882771 (+   7.8672e-07  / -   7.6184e-07)
F1:    -3.65552524771935e-11 (+   9.8839e-14  / -   8.5018e-14)
```

## E.7 MJD 58650 - 58710

```
PSR                        PSR_J2022+3842
START              58650.0000000000000000
FINISH             58710.0000000000000000
DILATEFREQ                              N
DMDATA                                  N
NTOA                                    0
CHI2                                  0.0
RAJ                     20:22:21.68900000
DECJ                    38:42:14.82000000
PMRA                                  0.0
PMDEC                                 0.0
PX                                    0.0
F0                  20.575735865972820449 1 1.16e-05
F1              -3.6498360090676598565e-11 1 1e-12
PEPOCH             58680.0000000000000000
PLANET_SHAPIRO                          N
TZRMJD             58680.0000000000000000
TZRSITE                               ssb
TZRFRQ                                inf
```

The result of the MCMC optimization is:

```
F0:         20.5757358702119 (+   1.7073e-06  / -   7.6361e-07)
F1:    -3.65015817797695e-11 (+   8.7166e-14  / -   2.7489e-13)
```

## E.8 MJD 58700 - 58760

```
PSR                            PSR_J2022+3842
START                  58700.0000000000000000
FINISH                 58760.0000000000000000
DILATEFREQ                                  N
DMDATA                                      N
NTOA                                        0
CHI2                                      0.0
RAJ                         20:22:21.68900000
DECJ                        38:42:14.82000000
PMRA                                      0.0
PMDEC                                     0.0
PX                                        0.0
F0                       20.57557825063091883 1 1.16e-05
F1                -3.6443327936832165952e-11 1 1e-12
PEPOCH                 58730.0000000000000000
PLANET_SHAPIRO                              N
TZRMJD                 58730.0000000000000000
TZRSITE                                   ssb
TZRFRQ                                    inf
```

The result of the MCMC optimization is:

```
F0:         20.5755782549427 (+     1.92e-07  / -    1.027e-08)
F1:     -3.6441513531925e-11 (+   4.0181e-14  / -   4.0381e-14)
```

## E.9 MJD 58750 - 58820

```
PSR                        PSR_J2022+3842
START              58750.0000000000000000
FINISH             58820.0000000000000000
DILATEFREQ                              N
DMDATA                                  N
NTOA                                    0
CHI2                                  0.0
RAJ                     20:22:21.68900000
DECJ                    38:42:14.82000000
PMRA                                  0.0
PMDEC                                 0.0
PX                                    0.0
F0                  20.575320025151242476 1 1.16e-05
F1              -3.64401104263770107 12e-11 1 1e-12
PEPOCH             58812.0000000000000000
PLANET_SHAPIRO                          N
TZRMJD             58812.0000000000000000
TZRSITE                               ssb
TZRFRQ                                inf
```

The result of the MCMC optimization is:

```
F0:         20.5753200385448 (+   1.8113e-06  / -   1.5999e-08)
F1:    -3.64404492834035e-11 (+   1.3702e-14  / -   2.7156e-13)
```

## E.10 MJD 58800 - 58850

```
PSR                        PSR_J2022+3842
START              58800.0000000000000000
FINISH             58850.0000000000000000
DILATEFREQ                              N
DMDATA                                  N
NTOA                                    0
CHI2                                  0.0
RAJ                     20:22:21.68900000
DECJ                    38:42:14.82000000
PMRA                                  0.0
PMDEC                                 0.0
PX                                    0.0
F0                  20.575279115306525313 1 1.16e-05
F1              -3.6426594496322606178e-11 1 1e-12
PEPOCH             58825.0000000000000000
PLANET_SHAPIRO                          N
TZRMJD             58825.0000000000000000
TZRSITE                               ssb
TZRFRQ                                inf
```

The result of the MCMC optimization is:

```
F0:          20.575279115399 (+   3.1526e-07  / -   1.3682e-06)
F1:    -3.64252552069949e-11 (+   1.9289e-13  / -   5.9181e-14)
```

## E.11 MJD 58920 - 58980

```
PSR                        PSR_J2022+3842
START                58920.0000000000000000
FINISH               58980.0000000000000000
DILATEFREQ                              N
DMDATA                                  N
NTOA                                    0
CHI2                                  0.0
RAJ                     20:22:21.68900000
DECJ                    38:42:14.82000000
PMRA                                  0.0
PMDEC                                 0.0
PX                                    0.0
F0                   20.57493572161175166 1 1.16e-05
F1              -3.6709188203786643805e-11 1 1e-10
PEPOCH               58950.0000000000000000
PLANET_SHAPIRO                          N
TZRMJD               58950.0000000000000000
TZRSITE                               ssb
TZRFRQ                                inf
```

The result of the MCMC optimization is:

```
F0:         20.5749355802488 (+   1.0506e-06  / -   8.9318e-07)
F1:    -3.67053962453116e-11 (+   5.2989e-12  / -   6.9992e-12)
```

## E.12 MJD 58970 - 59030

```
PSR                        PSR_J2022+3842
START              58970.0000000000000000
FINISH             59030.0000000000000000
DILATEFREQ                              N
DMDATA                                  N
NTOA                                    0
CHI2                                  0.0
RAJ                     20:22:21.68900000
DECJ                    38:42:14.82000000
PMRA                                  0.0
PMDEC                                 0.0
PX                                    0.0
F0                   20.57477737607818824 1 1.16e-05
F1              -3.6630938087461094567e-11 1 1e-10
PEPOCH             59000.0000000000000000
PLANET_SHAPIRO                          N
TZRMJD             59000.0000000000000000
TZRSITE                               ssb
TZRFRQ                                inf
```

The result of the MCMC optimization is:

```
F0:         20.5747773764476 (+   1.6152e-06  / -   1.2036e-07)
F1:    -3.53061959105945e-11 (+   1.3296e-12  / -   1.4436e-12)
```

## E.13 MJD 59020 - 59080

```
PSR                               PSR_J2022+3842
START                   59020.0000000000000000
FINISH                  59080.0000000000000000
DILATEFREQ                                   N
DMDATA                                       N
NTOA                                         0
CHI2                                       0.0
RAJ                          20:22:21.68900000
DECJ                         38:42:14.82000000
PMRA                                       0.0
PMDEC                                      0.0
PX                                         0.0
F0                       20.574619173702853203 1 1.16e-05
F1                    -3.660916977560387403e-11 1 1e-10
PEPOCH                  59050.0000000000000000
PLANET_SHAPIRO                               N
TZRMJD                  59050.0000000000000000
TZRSITE                                    ssb
TZRFRQ                                     inf
```

The result of the MCMC optimization is:

```
F0:         20.5746194067038 (+   6.0349e-07  / -    2.237e-06)
F1:    -3.81324866268409e-11 (+   1.5594e-12  / -   1.0121e-11)
```

## E.14 MJD 59070 - 59130

```
PSR                           PSR_J2022+3842
START                   59070.0000000000000000
FINISH                  59130.0000000000000000
DILATEFREQ                                 N
DMDATA                                     N
NTOA                                       0
CHI2                                     0.0
RAJ                          20:22:21.68900000
DECJ                         38:42:14.82000000
PMRA                                     0.0
PMDEC                                    0.0
PX                                       0.0
F0                       20.574461060785566247 1 1.16e-05
F1                 -3.6596523897908475315e-11 1 1e-10
PEPOCH                  59100.0000000000000000
PLANET_SHAPIRO                             N
TZRMJD                  59100.0000000000000000
TZRSITE                                  ssb
TZRFRQ                                   inf
```

The result of the MCMC optimization is:

```
F0:         20.5744608351422 (+    1.785e-06  / -    2.161e-06)
F1:    -3.68918008473094e-11 (+   5.1167e-12  / -   2.4446e-11)
```

## E.15 MJD 59120 - 59180

```
PSR                        PSR_J2022+3842
START              59120.0000000000000000
FINISH             59180.0000000000000000
DILATEFREQ                              N
DMDATA                                  N
NTOA                                    0
CHI2                                  0.0
RAJ                     20:22:21.68900000
DECJ                    38:42:14.82000000
PMRA                                  0.0
PMDEC                                 0.0
PX                                    0.0
F0                   20.57430300392576683 1 1.16e-05
F1              -3.6576675166826707982e-11 1 1e-10
PEPOCH             59150.0000000000000000
PLANET_SHAPIRO                          N
TZRMJD             59150.0000000000000000
TZRSITE                               ssb
TZRFRQ                                inf
```

The result of the MCMC optimization is:

```
F0:         20.5743030045986 (+   9.8787e-07  / -   6.6374e-07)
F1:     -3.6577350248164e-11 (+   6.4608e-13  / -   8.0175e-13)
```

## E.16 MJD 59170 - 59250

```
PSR                        PSR_J2022+3842
START              59170.0000000000000000
FINISH             59250.0000000000000000
DILATEFREQ                              N
DMDATA                                  N
NTOA                                    0
CHI2                                  0.0
RAJ                     20:22:21.68900000
DECJ                    38:42:14.82000000
PMRA                                  0.0
PMDEC                                 0.0
PX                                    0.0
F0                    20.5741450166318387 1 1.16e-05
F1              -3.656588529128389037e-11 1 1e-10
PEPOCH             59200.0000000000000000
PLANET_SHAPIRO                          N
TZRMJD             59200.0000000000000000
TZRSITE                               ssb
TZRFRQ                                inf
```

The result of the MCMC optimization is:

```
F0:         20.5741449602542 (+   1.9262e-06  / -   1.3961e-06)
F1:    -3.66063477952584e-11 (+   9.6803e-12  / -   7.0461e-12)
```

## E.17 MJD 59240 - 59300

```
PSR                        PSR_J2022+3842
START              59240.0000000000000000
FINISH             59300.0000000000000000
DILATEFREQ                              N
DMDATA                                  N
NTOA                                    0
CHI2                                  0.0
RAJ                     20:22:21.68900000
DECJ                    38:42:14.82000000
PMRA                                  0.0
PMDEC                                 0.0
PX                                    0.0
POSEPOCH           59270.0000000000000000
F0                  20.573923907714839032 1 1.16e-05
F1              -3.6532243980320815983e-11 1 1e-10
PEPOCH             59270.0000000000000000
PLANET_SHAPIRO                          N
TZRMJD             59270.0000000000000000
TZRSITE                               ssb
TZRFRQ                                inf
```

The result of the MCMC optimization is:

```
F0:          20.573924750201 (+   4.4108e-06  / -   1.6039e-06)
F1:    -3.65322439803208e-11 (+   6.0074e-11  / -   9.9902e-12)
```

## E.18 MJD 59290 - 59350

```
PSR                        PSR_J2022+3842
START                  59290.0000000000000000
FINISH                 59350.0000000000000000
DILATEFREQ                              N
DMDATA                                  N
NTOA                                    0
CHI2                                  0.0
RAJ                     20:22:21.68900000
DECJ                    38:42:14.82000000
PMRA                                  0.0
PMDEC                                 0.0
PX                                    0.0
POSEPOCH               59320.0000000000000000
F0                    20.573766074348508681 1 1.16e-05
F1                -3.6533463508436972157e-11 1 1e-10
PEPOCH                 59320.0000000000000000
PLANET_SHAPIRO                          N
TZRMJD                 59320.0000000000000000
TZRSITE                               ssb
TZRFRQ                                inf
```

The result of the MCMC optimization is:

```
F0:         20.5737660779602 (+   1.7862e-06  / -   2.8368e-07)
F1:    -3.65331573166199e-11 (+   3.1567e-12  / -   2.4276e-11)
```

## E.19 MJD 59340 - 59400

```
PSR                        PSR_J2022+3842
START              59340.0000000000000000
FINISH             59400.0000000000000000
DILATEFREQ                              N
DMDATA                                  N
NTOA                                    0
CHI2                                  0.0
RAJ                     20:22:21.68900000
DECJ                    38:42:14.82000000
PMRA                                  0.0
PMDEC                                 0.0
PX                                    0.0
POSEPOCH           59370.0000000000000000
F0                  20.573608034151057211 1 1.16e-05
F1              -3.671182253911937167e-11 1 1e-10
PEPOCH             59370.0000000000000000
PLANET_SHAPIRO                          N
TZRMJD             59370.0000000000000000
TZRSITE                               ssb
TZRFRQ                                inf
```

The result of the MCMC optimization is:

```
F0:         20.5736072984671 (+    3.296e-06  / -   1.2652e-06)
F1:    -3.79060602541483e-11 (+   1.5782e-12  / -   1.0891e-11)
```

## E.20 MJD 59390 - 59450

```
PSR                        PSR_J2022+3842
START              59390.0000000000000000
FINISH             59450.0000000000000000
DILATEFREQ                              N
DMDATA                                  N
NTOA                                    0
CHI2                                  0.0
RAJ                     20:22:21.68900000
DECJ                    38:42:14.82000000
PMRA                                  0.0
PMDEC                                 0.0
PX                                    0.0
POSEPOCH           59420.0000000000000000
F0                  20.573450526255818716 1 1.16e-05
F1              -3.6515055015677950426e-11 1 1e-10
PEPOCH             59420.0000000000000000
PLANET_SHAPIRO                          N
TZRMJD             59420.0000000000000000
TZRSITE                               ssb
TZRFRQ                                inf
```

The result of the MCMC optimization is:

```
F0:         20.5734505347505 (+   2.2908e-06  / -   8.4344e-07)
F1:    -3.65183193326984e-11 (+   1.2074e-11  / -   3.1227e-12)
```

## E.21 MJD 58083 - 59450

The following timing solution was generated by using fake glitches to artificially align the timing solutions presented above.

```
PSR                        PSR_J2022+3842
START              58083.0000000000000000
FINISH             59450.0000000000000000
DILATEFREQ                              N
DMDATA                                  N
NTOA                                    0
CHI2                                  0.0
RAJ                     20:22:21.68900000
DECJ                    38:42:14.82000000
PMRA                                  0.0
PMDEC                                 0.0
PX                                    0.0
F0                    20.5775902517116549 0 1.16e-05
F1              -3.6491213693739044985e-11 0 1e-10
PEPOCH             58084.0000000000000000
PLANET_SHAPIRO                          N
TZRMJD             58084.0000000000000000
TZRSITE                               ssb
TZRFRQ                                inf
GLEP_0             58170.0000000000000000 0 0.0
GLPH_0              0.0060277866243253105 1 0.001
GLF0_0             0.00010852518338630277 0 0.1
GLF1_0            -6.4069753515914446e-12 0 0.1
GLF2_0                                0.0
GLF0D_0                               0.0
GLTD_0                                0.0
```

```
GLEP_1             58300.0000000000000000 0 0.0
GLPH_1               -0.24397568498094643 1 0.001
GLF0_1             -8.417749982785035e-06 0 0.1
GLF1_1              6.134539124777189e-12 0 0.1
GLF2_1                                0.0
GLF0D_1                               0.0
GLTD_1                                0.0
GLEP_2             58350.0000000000000000 0 0.0
GLPH_2                  0.292028440356692 1 0.001
GLF0_2              1.582534876077644e-07 0 0.1
GLF1_2             1.4018664745971068e-13 0 0.1
GLF2_2                                0.0
GLF0D_2                               0.0
GLTD_2                                0.0
GLEP_3             58400.0000000000000000 0 0.0
GLPH_3               0.008119617894841016 1 0.001
GLF0_3            -1.7671914225804184e-08 0 0.1
GLF1_3             1.8110609467584717e-14 0 0.1
GLF2_3                                0.0
GLF0D_3                               0.0
GLTD_3                                0.0
GLEP_4             58540.0000000000000000 0 0.0
GLPH_4                -0.5419400760272471 1 0.001
GLF0_4             1.2908381694084316e-07 0 0.1
GLF1_4             5.0233453570557276e-14 0 0.1
GLF2_4                                0.0
GLF0D_4                               0.0
GLTD_4                                0.0
GLEP_5             58650.0000000000000000 0 0.0
GLPH_5                0.13789787382595356 1 0.001
```

```
GLF0_5               4.821310199455698e-08 0 0.1
GLF1_5              5.6759119378849065e-14 0 0.1
GLF2_5                                 0.0
GLF0D_5                                0.0
GLTD_5                                 0.0
GLEP_6              58700.0000000000000000 0 0.0
GLPH_6                 0.11952531752265105 1 0.001
GLF0_6              -8.506965266086354e-08 0 0.1
GLF1_6               5.503215384443261e-14 0 0.1
GLF2_6                                 0.0
GLF0D_6                                0.0
GLTD_6                                 0.0
GLEP_7              58750.0000000000000000 0 0.0
GLPH_7                -0.00558827765624101 1 0.001
GLF0_7              -4.902546949164625e-08 0 0.1
GLF1_7                3.21751045515524e-15 0 0.1
GLF2_7                                 0.0
GLF0D_7                                0.0
GLTD_7                                 0.0
GLEP_8              58800.0000000000000000 0 0.0
GLPH_8               0.0019282354641166671 1 0.001
GLF0_8              -9.507095173855361e-09 0 0.1
GLF1_8              1.3515930054404533e-14 0 0.1
GLF2_8                                 0.0
GLF0D_8                                0.0
GLTD_8                                 0.0
GLEP_9              58920.0000000000000000 0 0.0
GLPH_9                 -0.6395314585037929 1 0.001
GLF0_9               5.074600867637793e-05 0 0.1
GLF1_9             -2.8259370746403763e-13 0 0.1
```

```
GLF2_9                                0.0
GLF0D_9                               0.0
GLTD_9                                0.0
GLEP_10            58970.0000000000000000 0 0.0
GLPH_10               0.06501182862907834 1 0.001
GLF0_10             3.533517542247761e-08 0 0.1
GLF1_10             7.825011632554924e-14 0 0.1
GLF2_10                               0.0
GLF0D_10                              0.0
GLTD_10                               0.0
GLEP_11            59020.0000000000000000 0 0.0
GLPH_11              0.005576519505743242 1 0.001
GLF0_11           -1.3146261538987103e-08 0 0.1
GLF1_11            2.1768311857220536e-14 0 0.1
GLF2_11                               0.0
GLF0D_11                              0.0
GLTD_11                               0.0
GLEP_12            59070.0000000000000000 0 0.0
GLPH_12              -0.01992166402664781 1 0.001
GLF0_12             5.918028666262341e-09 0 0.1
GLF1_12            1.2645877695398715e-14 0 0.1
GLF2_12                               0.0
GLF0D_12                              0.0
GLTD_12                               0.0
GLEP_13            59120.0000000000000000 0 0.0
GLPH_13              0.008227610623956964 1 0.001
GLF0_13           -1.1324471416327567e-08 0 0.1
GLF1_13            1.9848731081767332e-14 0 0.1
GLF2_13                               0.0
GLF0D_13                              0.0
```

```
GLTD_13                               0.0
GLEP_14            59170.0000000000000000 0 0.0
GLPH_14            -0.0008482345969887053 1 0.001
GLF0_14            -4.024564845604768e-09 0 0.1
GLF1_14            1.0789875542817612e-14 0 0.1
GLF2_14                               0.0
GLF0D_14                              0.0
GLTD_14                               0.0
GLEP_15            59240.0000000000000000 0 0.0
GLPH_15               0.12954768867894723 1 0.001
GLF0_15           -4.5641035999319855e-08 0 0.1
GLF1_15            3.3641310963074386e-14 0 0.1
GLF2_15                               0.0
GLF0D_15                              0.0
GLTD_15                               0.0
GLEP_16            59290.0000000000000000 0 0.0
GLPH_16              0.008006705321797402 1 0.001
GLF0_16            -1.091131848799815e-08 0 0.1
GLF1_16            -1.219528116156174e-15 0 0.1
GLF2_16                               0.0
GLF0D_16                              0.0
GLTD_16                               0.0
GLEP_17            59340.0000000000000000 0 0.0
GLPH_17              -0.10249012164640801 1 0.001
GLF0_17            2.4667151250649924e-07 0 0.1
GLF1_17           -1.7835903068239951e-13 0 0.1
GLF2_17                               0.0
GLF0D_17                              0.0
GLTD_17                               0.0
GLEP_18            59390.0000000000000000 0 0.0
```

```
GLPH_18              -0.21597061046398666 1 0.001

GLF0_18             5.771567097405218e-07 0 0.1

GLF1_18            1.9676752344142124e-13 0 0.1

GLF2_18                               0.0

GLF0D_18                              0.0

GLTD_18                               0.0
```

# Bibliography

[1] Dec. 2021. URL: `https://www.slac.stanford.edu/exp/glast/groups/canda/lat_Performance.htm`.

[2] . `https://www.nasa.gov/mission_pages/GLAST/launch/index.html`. Accessed: 2021-02-25.

[3] B P Abbott et al. "First narrow-band search for continuous gravitational waves from known pulsars in advanced detector data". en. In: *Phys. Rev. D.* 96.12 (Dec. 2017).

[4] B P Abbott et al. "Searches for gravitational waves from known pulsars at two harmonics in 2015–2017 LIGO data". In: *Astrophys. J.* 879.1 (June 2019), p. 10.

[5] B. P. Abbott et al. "Narrow-band search for gravitational waves from known pulsars using the second LIGO observing run". In: *Phys. Rev. D* 99 (12 June 2019), p. 122002. DOI: `10.1103/PhysRevD.99.122002`. URL: `https://link.aps.org/doi/10.1103/PhysRevD.99.122002`.

[6] A A Abdo et al. "Detection of 16 gamma-ray pulsars through blind frequency searches using the Fermi LAT". en. In: *Science* 325.5942 (Aug. 2009), pp. 840–844.

[7] A. A. Abdo et al. "A Population of Gamma-Ray Millisecond Pulsars Seen with the Fermi Large Area Telescope". In: *Science* 325.5942 (Aug. 2009), p. 848. DOI: `10.1126/science.1176113`.

[8] A. A. Abdo et al. “Fermi Large Area Telescope First Source Catalog”. In: *The Astrophysical Journal Supplement Series* 188.2 (June 2010), pp. 405–436. DOI: `10.1088/0067-0049/188/2/405`. arXiv: `1002.2280 [astro-ph.HE]`.

[9] A. A. Abdo et al. “FERMI-LAT OBSERVATIONS OF THE GEMINGA PULSAR”. In: *The Astrophysical Journal* 720.1 (Aug. 2010), pp. 272–283. DOI: `10.1088/0004-637x/720/1/272`. URL: `https://doi.org/10.1088/0004-637x/720/1/272`.

[10] A. A. Abdo et al. “Measurement of the Cosmic Ray $e^{+}+e^{-}$ Spectrum from 20GeV to 1TeV with the Fermi Large Area Telescope”. In: *Physical Review Letters* 102.18, 181101 (May 2009), p. 181101. DOI: `10.1103/PhysRevLett.102.181101`. arXiv: `0905.0025 [astro-ph.HE]`.

[11] A. A. Abdo et al. “The First Fermi Large Area Telescope Catalog of Gamma-ray Pulsars”. In: *The Astrophysical Journal Supplement Series* 187.2 (Apr. 2010), pp. 460–494. DOI: `10.1088/0067-0049/187/2/460`. arXiv: `0910.1608 [astro-ph.HE]`.

[12] Abdo Abdo et al. “Fermi/LAT bright gamma-ray source list (0FGL) (Abdo+, 2009)”. In: *VizieR Online Data Catalog* 218 (Nov. 2009), p. 30046.

[13] S. Abdollahi et al. “Fermi Large Area Telescope Fourth Source Catalog”. In: *The Astrophysical Journal Supplement Series* 247.1 (Mar. 2020), p. 33. DOI: `10.3847/1538-4365/ab6bcb`. URL: `https://doi.org/10.3847/1538-4365/ab6bcb`.

[14] V. A. Acciari et al. “Search for Very High-energy Emission from the Millisecond Pulsar PSR J0218+4232”. In: *Astrophys. J.* 922.2 (2021), p. 251. DOI: `10.3847/1538-4357/ac20d7`. arXiv: `2108.11373 [astro-ph.HE]`.

[15] V. A. Acciari et al. “Veritas Observations of a Very High Energy $\gamma$-Ray Flare From the Blazar 3C 66A”. In: *The Astrophysical Journal Letters* 693.2 (Mar. 2009), pp. L104–L108. DOI: `10.1088/0004-637X/693/2/L104`. arXiv: `0901.4527 [astro-ph.HE]`.

[16] F. Acero et al. "FERMI LARGE AREA TELESCOPE THIRD SOURCE CATALOG". In: *The Astrophysical Journal Supplement Series* 218.2 (June 2015), p. 23. DOI: `10.1088/0067-0049/218/2/23`. URL: `https://doi.org/10.1088/0067-0049/218/2/23`.

[17] M. Ackermann et al. "Inferred Cosmic-Ray Spectrum from Fermi Large Area Telescope $\gamma$-Ray Observations of Earth's Limb". In: *Phys. Rev. Lett.* 112 (15 Apr. 2014), p. 151103. DOI: `10.1103/PhysRevLett.112.151103`. URL: `https://link.aps.org/doi/10.1103/PhysRevLett.112.151103`.

[18] M. Ackermann et al. "The Fermi Large Area Telescope on Orbit: Event Classification, Instrument Response Functions, and Callibration". In: *The Astrophysical Journal Supplement Series* 203.1 (Oct. 2012), p. 4. DOI: `10.1088/0067-0049/203/1/4`. URL: `https://doi.org/10.1088/0067-0049/203/1/4`.

[19] M. Ackermann et al. "The First Fermi-LAT Catalog of Sources above 10 GeV". In: *The Astrophysical Journal Supplement Series* 209.2, 34 (Dec. 2013), p. 34. DOI: `10.1088/0067-0049/209/2/34`. arXiv: `1306.6772 [astro-ph.IM]`.

[20] F Aharonian et al. "A new population of very high energy gamma-ray sources in the Milky Way". en. In: *Science* 307.5717 (Mar. 2005), pp. 1938–1942.

[21] M. Ajello et al. "3FHL: The Third Catalog of Hard Fermi-LAT Sources". In: *The Astrophysical Journal Supplement Series* 232.2, 18 (Oct. 2017), p. 18. DOI: `10.3847/1538-4365/aa8221`. arXiv: `1702.00664 [astro-ph.HE]`.

[22] M. Ajello et al. "A gamma-ray pulsar timing array constrains the nanohertz gravitational wave background". In: *Science* 376.6592 (2022), pp. 521–523. DOI: `10.1126/science.abm3231`. eprint: `https://www.science.org/doi/pdf/10.1126/science.abm3231`. URL: `https://www.science.org/doi/abs/10.1126/science.abm3231`.

[23] M. Ajello et al. "Fermi Large Area Telescope Performance after 10 Years of Operation". In: *The Astrophysical Journal Supplement Series* 256.1 (Sept.

2021), p. 12. DOI: 10.3847/1538-4365/ac0ceb. URL: https://doi.org/10.3847/1538-4365/ac0ceb.

[24] J. Aleksić et al. “The major upgrade of the MAGIC telescopes, Part I: The hardware improvements and the commissioning of the system”. In: *Astroparticle Physics* 72 (Jan. 2016), pp. 61–75. DOI: 10.1016/j.astropartphys.2015.04.004. arXiv: 1409.6073 [astro-ph.IM].

[25] J. Aleksić et al. “The major upgrade of the MAGIC telescopes, Part II: A performance study using observations of the Crab Nebula”. In: *Astroparticle Physics* 72 (Jan. 2016), pp. 76–94. DOI: 10.1016/j.astropartphys.2015.02.005. arXiv: 1409.5594 [astro-ph.IM].

[26] Sara Algeri et al. “Searching for new physics with profile likelihoods: Wilks and beyond”. In: (Nov. 2019). arXiv: 1911.10237 [physics.data-an].

[27] E. Aliu et al. “Discovery of a Very High Energy Gamma-Ray Signal from the 3C 66A/B Region”. In: *The Astrophysical Journal Letters* 692.1 (Feb. 2009), pp. L29–L33. DOI: 10.1088/0004-637X/692/1/L29. arXiv: 0810.4712 [astro-ph].

[28] E. Aliu et al. “Observation of Pulsed $\gamma$-Rays Above 25 GeV from the Crab Pulsar with MAGIC”. In: *Science* 322.5905 (Nov. 2008), p. 1221. DOI: 10.1126/science.1164718. arXiv: 0809.2998 [astro-ph].

[29] M. A. Alpar et al. “A new class of radio pulsars”. In: *Nature* 300.5894 (Dec. 1982), pp. 728–730. ISSN: 1476-4687. DOI: 10.1038/300728a0. URL: https://doi.org/10.1038/300728a0.

[30] H. Anderhub et al. “Search for Very High Energy Gamma-ray Emission from Pulsar-Pulsar Wind Nebula Systems with the MAGIC Telescope”. In: *The Astrophysical Journal* 710.1 (Feb. 2010), pp. 828–835. DOI: 10.1088/0004-637X/710/1/828.

[31] S. Ansoldi et al. “Teraelectronvolt pulsed emission from the Crab Pulsar detected by MAGIC”. In: *Astronomy and Astrophysics* 585, A133 (Jan. 2016), A133. DOI: 10.1051/0004-6361/201526853. arXiv: 1510.07048 [astro-ph.HE].

[32] Anne M. Archibald et al. "No Detectable Radio Emission from the Magnetar-Like Pulsar in Kes 75". In: *The Astrophysical Journal* 688.1 (Nov. 2008), pp. 550–554. DOI: `10.1086/591661`. arXiv: `0805.1448 [astro-ph]`.

[33] K. A. Arnaud. "XSPEC: The First Ten Years". In: *Astronomical Data Analysis Software and Systems V*. Ed. by George H. Jacoby and Jeannette Barnes. Vol. 101. Astronomical Society of the Pacific Conference Series. Jan. 1996, p. 17.

[34] J. Arons and E. T. Scharlemann. "Pair formation above pulsar polar caps: structure of the low altitude acceleration zone." In: *The Astrophysical Journal* 231 (Aug. 1979), pp. 854–879. DOI: `10.1086/157250`.

[35] P. Arumugasamy, G. G. Pavlov, and O. Kargaltsev. "XMM-Newton Observations of Young and Energetic Pulsar J2022+3842". In: *The Astrophysical Journal* 790, 103 (Aug. 2014), p. 103. DOI: `10.1088/0004-637X/790/2/103`. arXiv: `1406.2349 [astro-ph.HE]`.

[36] Z. Arzoumanian et al. "Discovery of an Energetic Pulsar Associated with SNR G76.9+1.0". In: *The Astrophysical Journal* 739, 39 (Sept. 2011), p. 39. DOI: `10.1088/0004-637X/739/1/39`. arXiv: `1105.3185 [astro-ph.HE]`.

[37] Zaven Arzoumanian et al. "The NANOGrav 12.5 yr Data Set: Search for an Isotropic Stochastic Gravitational-wave Background". In: *The Astrophysical Journal Letters* 905.2, L34 (Dec. 2020), p. L34. DOI: `10.3847/2041-8213/abd401`. arXiv: `2009.04496 [astro-ph.HE]`.

[38] W B Atwood et al. "A time-differencing technique for detecting radio-quiet gamma-ray pulsars". en. In: *Astrophys. J.* 652.1 (Nov. 2006), pp. L49–L52.

[39] W. Atwood et al. "Pass 8: Toward the Full Realization of the Fermi-LAT Scientific Potential". In: *Proceedings of the 4th Fermi Symposium* (Monterey, California, USA). Mar. 2013. arXiv: `1303.3514 [astro-ph.IM]`.

[40] W. B. Atwood et al. "A Time-differencing Technique for Detecting Radio-quiet Gamma-Ray Pulsars". In: *The Astrophysical Journal* 652.1 (Nov. 2006),

pp. L49–L52. DOI: 10.1086/510018. URL: https://doi.org/10.1086/510018.

[41] W. B. Atwood et al. "The Large Area Telescope on the Fermi Gamma-Ray Space Telescope Mission". In: *The Astrophysical Journal* 697 (June 2009). (LAT Instrument Paper), pp. 1071–1102. DOI: 10.1088/0004-637X/697/2/1071. arXiv: 0902.1089.

[42] W.B Atwood. "Gamma Large Area Silicon Telescope (GLAST) applying silicon strip detector technology to the detection of gamma rays in space". In: *Nuclear Instruments and Methods in Physics Research Section A: Accelerators, Spectrometers, Detectors and Associated Equipment* 342.1 (1994), pp. 302–307. ISSN: 0168-9002. DOI: https://doi.org/10.1016/0168-9002(94)91444-3. URL: https://www.sciencedirect.com/science/article/pii/0168900294914443.

[43] W.B. Atwood et al. "Design and initial tests of the Tracker-converter of the Gamma-ray Large Area Space Telescope". In: *Astroparticle Physics* 28.4 (2007), pp. 422–434. ISSN: 0927-6505. DOI: https://doi.org/10.1016/j.astropartphys.2007.08.010. URL: https://www.sciencedirect.com/science/article/pii/S0927650507001302.

[44] Matteo Bachetti et al. "Timing Calibration of the NuSTAR X-Ray Telescope". In: *The Astrophysical Journal* 908.2 (Feb. 2021), p. 184. DOI: 10.3847/1538-4357/abd1d6. URL: https://doi.org/10.3847/1538-4357/abd1d6.

[45] J. Ballet et al. *Fermi Large Area Telescope Fourth Source Catalog Data Release 2*. 2020. arXiv: 2005.11208 [astro-ph.HE].

[46] C. G. Bassa, M. H. van Kerkwijk, and S. R. Kulkarni. "Temperature and cooling age of the white dwarf companion of PSR J0218+4232". In: *Astronomy and Astrophysics* 403 (June 2003), pp. 1067–1075. DOI: 10.1051/0004-6361:20030384. arXiv: astro-ph/0303439 [astro-ph].

[47] W. Becker and J. Truemper. “The X-ray luminosity of rotation-powered neutron stars.” In: *Astronomy and Astrophysics* 326 (Oct. 1997), pp. 682–691. arXiv: `astro-ph/9708169 [astro-ph]`.

[48] Werner Becker. “X-ray emission from pulsars and neutron stars”. In: *Neutron Stars and Pulsars*. Berlin, Heidelberg: Springer Berlin Heidelberg, 2009, pp. 91–140.

[49] Julius S. Bendat and Allan G. Piersol. *Random Data*. John Wiley & Sons, Inc., Jan. 2010. DOI: `10.1002/9781118032428`. URL: `https://doi.org/10.1002/9781118032428`.

[50] Gregory Benford and Robert Buschauer. “Coherent pulsar radio radiation by antenna mechanisms: general theory”. In: *Monthly Notices of the Royal Astronomical Society* 179.2 (June 1977), pp. 189–207. ISSN: 0035-8711. DOI: `10.1093/mnras/179.2.189`. eprint: `https://academic.oup.com/mnras/article-pdf/179/2/189/9333538/mnras179-0189.pdf`. URL: `https://doi.org/10.1093/mnras/179.2.189`.

[51] D. Berge, S. Funk, and J. Hinton. “Background modelling in very-high-energy $\gamma$-ray astronomy”. In: *Astronomy and Astrophysics* 466.3 (May 2007), pp. 1219–1229. DOI: `10.1051/0004-6361:20066674`. arXiv: `astro-ph/0610959 [astro-ph]`.

[52] Peter Bickel, Bas Kleijn, and John Rice. “Event-Weighted Tests for Detecting Periodicity in Photon Arrival Times”. In: *The Astrophysical Journal* 685.1 (Sept. 2008), pp. 384–389. DOI: `10.1086/590399`. URL: `https://doi.org/10.1086/590399`.

[53] Harsha Blumer et al. “Reactivation of the High Magnetic Field Pulsar PSR J1846–0258 with Magnetar-like Bursts”. In: *The Astrophysical Journal Letters* 911.1 (Apr. 2021), p. L6. DOI: `10.3847/2041-8213/abf11d`. URL: `https://doi.org/10.3847/2041-8213/abf11d`.

[54] Slavko Bogdanov et al. “Constraining the Neutron Star Mass–Radius Relation and Dense Matter Equation of State with NICER. I. The Millisecond Pul-

sar X-Ray Data Set". In: *The Astrophysical Journal* 887.1 (Dec. 2019), p. L25. DOI: `10.3847/2041-8213/ab53eb`. URL: `https://doi.org/10.3847/2041-8213/ab53eb`.

[55] K. T. S. Brazier. "Confidence intervals from the Rayleigh test". In: *Monthly Notices of the Royal Astronomical Society* 268.3 (June 1994), pp. 709–712. ISSN: 0035-8711. DOI: `10.1093/mnras/268.3.709`. eprint: `https://academic.oup.com/mnras/article-pdf/268/3/709/3667184/mnras268-0709.pdf`. URL: `https://doi.org/10.1093/mnras/268.3.709`.

[56] C L Brogan et al. "Discovery of a radio supernova remnant and nonthermal X-rays coincident with the TeV source HESS J1813-178". en. In: *Astrophys. J.* 629.2 (Aug. 2005), pp. L105–L108.

[57] P. Bruel. "Extending the event-weighted pulsation search to very faint gamma-ray sources". In: *Astronomy and Astrophysics* 622, A108 (Feb. 2019), A108. DOI: `10.1051/0004-6361/201834555`. arXiv: `1812.06681 [astro-ph.IM]`.

[58] P. Bruel et al. "Fermi-LAT improved Pass~8 event selection". In: *Proceedings of the 8th Fermi Symposium* (Baltimore, Maryland, USA). Oct. 2018. arXiv: `1810.11394 [astro-ph.IM]`.

[59] R. Buccheri, B. Sacco, and M. E. Ozel. "The feasibility of periodicity searches in gamma-ray astronomy". In: *Astronomy and Astrophysics* 175.1-2 (Mar. 1987), p. 353.

[60] R. Buccheri et al. "Search for pulsed gamma-ray emission from radio pulsars in the COS-B data". In: *Astronomy and Astrophysics* 128 (Nov. 1983), pp. 245–251.

[61] D. A. H. Buckley et al. "Polarimetric evidence of a white dwarf pulsar in the binary system AR Scorpii". In: *Nature Astronomy* 1.2 (Jan. 2017), p. 0029. ISSN: 2397-3366. DOI: `10.1038/s41550-016-0029`. URL: `https://doi.org/10.1038/s41550-016-0029`.

[62] Adam S. Burrows. “Baade and Zwicky: “Super-novae,” neutron stars, and cosmic rays”. In: *Proceedings of the National Academy of Sciences* 112.5 (2015), pp. 1241–1242. ISSN: 0027-8424. DOI: `10.1073/pnas.1422666112`. eprint: `https://www.pnas.org/content/112/5/1241.full.pdf`. URL: `https://www.pnas.org/content/112/5/1241`.

[63] A. Burtovoi et al. “Prospects for the detection of high-energy (E ¿ 25 GeV) Fermi pulsars with the Cherenkov Telescope Array”. In: *Monthly Notices of the Royal Astronomical Society* 471.1 (Oct. 2017), pp. 431–446. DOI: `10.1093/mnras/stx1582`. arXiv: `1706.07228 [astro-ph.HE]`.

[64] K. S. Cheng, C. Ho, and M. Ruderman. “Energetic Radiation from Rapidly Spinning Pulsars. I. Outer Magnetosphere Gaps”. In: *The Astrophysical Journal* 300 (Jan. 1986), p. 500. DOI: `10.1086/163829`.

[65] K. S. Cheng and J. L. Zhang. “General Radiation Formulae for a Relativistic Charged Particle Moving in Curved Magnetic Field Lines: The Synchrocurvature Radiation Mechanism”. In: *The Astrophysical Journal* 463 (May 1996), p. 271. DOI: `10.1086/177239`.

[66] Herman Chernoff. “On the Distribution of the Likelihood Ratio”. In: *The Annals of Mathematical Statistics* 25.3 (1954), pp. 573–578. DOI: `10.1214/aoms/1177728725`. URL: `https://doi.org/10.1214/aoms/1177728725`.

[67] LAT collaboration et al. *Incremental Fermi Large Area Telescope Fourth Source Catalog*. 2022. arXiv: `2201.11184 [astro-ph.HE]`.

[68] George W. Collins II, William P. Claspy, and John C. Martin. “A Reinterpretation of Historical References to the Supernova of AD 1054”. In: *Publications of the Astronomical Society of the Pacific* 111.761 (July 1999), pp. 871–880. DOI: `10.1086/316401`. URL: `https://doi.org/10.1086/316401`.

[69] James J. Condon and Scott M. Ransom. *Essential Radio Astronomy*. 2016.

[70] Francesco Coti Zelati et al. “Spectral characterization of the non-thermal X-ray emission of gamma-ray pulsars”. In: *Monthly Notices of the Royal As-*

*tronomical Society* 492.1 (Feb. 2020), pp. 1025–1043. DOI: `10.1093/mnras/stz3485`. arXiv: `1912.03953 [astro-ph.HE]`.

[71] Glen Cowan et al. “Asymptotic formulae for likelihood-based tests of new physics (vol 71, pg 1554, 2011)”. In: *European Physical Journal C* 73 (July 2013). DOI: `10.1140/epjc/s10052-013-2501-z`.

[72] S J Dang et al. “Results of 12 yr of Pulsar Timing at Nanshan. I”. In: *Astrophys. J.* 896.2 (June 2020), p. 140.

[73] F. Dazzi et al. “The Stereoscopic Analog Trigger of the MAGIC Telescopes”. In: *IEEE Transactions on Nuclear Science* (2021), pp. 1–1. DOI: `10.1109/TNS.2021.3079262`.

[74] A. De Angelis et al. “The e-ASTROGAM mission”. In: *Experimental Astronomy* 44.1 (Oct. 2017), pp. 25–82. ISSN: 1572-9508. DOI: `10.1007/s10686-017-9533-6`. URL: `https://doi.org/10.1007/s10686-017-9533-6`.

[75] O. C. de Jager, B. C. Raubenheimer, and J. W. H. Swanepoel. “A powerful test for weak periodic signals with unknown light curve shape in sparse data.” In: *Astronomy and Astrophysics* 221 (Aug. 1989), pp. 180–190.

[76] de Jager, O. C. and Büsching, I. “The H-test probability distribution revisited: improved sensitivity”. In: *A&A* 517 (2010), p. L9. DOI: `10.1051/0004-6361/201014362`. URL: `https://doi.org/10.1051/0004-6361/201014362`.

[77] Morris H DeGroot and Mark J Schervish. *Probability and Statistics*. 4th ed. Upper Saddle River, NJ: Pearson, Dec. 2010.

[78] A T Deller et al. “Microarcsecond VLBI Pulsar Astrometry with PSR$\pi$ II. Parallax Distances for 57 Pulsars”. In: *Astrophys. J.* 875.2 (Apr. 2019), p. 100.

[79] J. S. Deneva et al. “High-precision X-Ray Timing of Three Millisecond Pulsars with NICER: Stability Estimates and Comparison with Radio”. In: *The Astrophysical Journal* 874.2, 160 (Apr. 2019), p. 160. DOI: `10.3847/1538-4357/ab0966`. arXiv: `1902.07130 [astro-ph.HE]`.

[80] A Djannati-Atai et al. “Probing Vela pulsar down to 20 GeV with HESS II observations”. In: *AIP Conference Proceedings*. Vol. 1792. 1. AIP Publishing LLC. 2017, p. 040028.

[81] Yuanjie Du et al. “Very Long Baseline Interferometry Measured Proper Motion and Parallax of the $\gamma$-Ray Millisecond Pulsar PSR J0218+4232”. In: *The Astrophysical Journal Letters* 782.2, L38 (Feb. 2014), p. L38. DOI: `10.1088/2041-8205/782/2/L38`. arXiv: `1402.2380 [astro-ph.SR]`.

[82] M. Duer et al. “Probing high-momentum protons and neutrons in neutron-rich nuclei”. In: *Nature* 560.7720 (Aug. 2018), pp. 617–621. ISSN: 1476-4687. DOI: `10.1038/s41586-018-0400-z`. URL: `https://doi.org/10.1038/s41586-018-0400-z`.

[83] Robert C. Duncan and Christopher Thompson. “Formation of Very Strongly Magnetized Neutron Stars: Implications for Gamma-Ray Bursts”. In: *The Astrophysical Journal Letters* 392 (June 1992), p. L9. DOI: `10.1086/186413`.

[84] S. Dzib, L. Loinard, and L. F. Rodríguez. “A Compact Radio Counterpart to the Energetic X-ray Pulsar Associated with the TeV Gamma-Ray Source J1813-178”. In: *Revista Mexicana de Astronomia y Astrofisica* 46 (Apr. 2010), pp. 153–157.

[85] Sergio A Dzib et al. “The enigmatic compact radio source coincident with the energetic X-ray pulsar PSR J1813–1749 and HESS J1813–178”. In: *Astrophys. J.* 866.2 (Oct. 2018), p. 100.

[86] R. T. Edwards, G. B. Hobbs, and R. N. Manchester. “tempo2, a new pulsar timing package – II. The timing model and precision estimates”. In: *Monthly Notices of the Royal Astronomical Society* 372.4 (Oct. 2006), pp. 1549–1574. ISSN: 0035-8711. DOI: `10.1111/j.1365-2966.2006.10870.x`. eprint: `https://academic.oup.com/mnras/article-pdf/372/4/1549/4012423/mnras0372-1549.pdf`. URL: `https://doi.org/10.1111/j.1365-2966.2006.10870.x`.

[87] Teruaki Enoto, Shota Kisaka, and Shinpei Shibata. “Observational diversity of magnetized neutron stars”. en. In: *Rep. Prog. Phys.* 82.10 (Oct. 2019), p. 106901.

[88] C M Espinoza, A G Lyne, and B W Stappers. “New long-term braking index measurements for glitching pulsars using a glitch-template method”. In: *Mon. Not. R. Astron. Soc.* 466.1 (Apr. 2017), pp. 147–162.

[89] Lord Rayleigh O.M. F.R.S. “XXXI. On the problem of random vibrations, and of random flights in one, two, or three dimensions”. In: *The London, Edinburgh, and Dublin Philosophical Magazine and Journal of Science* 37.220 (1919), pp. 321–347. DOI: `10.1080/14786440408635894`. eprint: `https://doi.org/10.1080/14786440408635894`. URL: `https://doi.org/10.1080/14786440408635894`.

[90] R. D. Ferdman, R. F. Archibald, and V. M. Kaspi. “Long-Term Timing and Emission Behavior of the Young Crab-Like Pulsar PSR B0540-69”. In: *The Astrophysical Journal* 812.2 (Oct. 2015), p. 95. DOI: `10.1088/0004-637x/812/2/95`. URL: `https://doi.org/10.1088/0004-637x/812/2/95`.

[91] V. P. Fomin et al. “New methods of atmospheric Cherenkov imaging for gamma-ray astronomy. I. The false source method”. In: *Astroparticle Physics* 2.2 (May 1994), pp. 137–150. DOI: `10.1016/0927-6505(94)90036-1`.

[92] Christian Fruck et al. “A novel LIDAR-based Atmospheric Calibration Method for Improving the Data Analysis of MAGIC”. In: *33rd International Cosmic Ray Conference (ICRC), Rio de janerio 2013*, arXiv:1403.3591 (Mar. 2014), arXiv:1403.3591. arXiv: `1403.3591 [astro-ph.IM]`.

[93] Antonella Fruscione et al. “CIAO: Chandra’s data analysis system”. In: *Observatory Operations: Strategies, Processes, and Systems.* Ed. by David R Silva and Rodger E Doxsey. Orlando, Florida , USA: SPIE, June 2006.

[94] Chris L. Fryer. “Mass Limits For Black Hole Formation”. In: *The Astrophysical Journal* 522.1 (Sept. 1999), pp. 413–418. DOI: `10.1086/307647`. URL: `https://doi.org/10.1086/307647`.

[95] J R Fuentes, C M Espinoza, and A Reisenegger. “Glitch time series and size distributions in eight prolific pulsars”. In: *Astron. Astrophys.* 630 (Oct. 2019), A115.

[96] J R Fuentes et al. “The glitch activity of neutron stars”. In: *Astron. Astrophys.* 608 (Dec. 2017), A131.

[97] S. Funk et al. “XMM-Newton observations of HESS J1813-178 reveal a composite Supernova remnant”. In: *Astronomy and Astrophysics* 470.1 (July 2007), pp. 249–257. DOI: `10.1051/0004-6361:20066779`. arXiv: `astro-ph/0611646 [astro-ph]`.

[98] J. R. Garcia et al. “Status of the New Sum-Trigger System for the MAGIC Telescopes”. In: *International Cosmic Ray Conference*. Vol. 33. International Cosmic Ray Conference. Jan. 2013, p. 3008.

[99] Rob Garner. *About nicer*. Oct. 2017. URL: `https://www.nasa.gov/content/about-nicer`.

[100] F. P. Gavriil et al. “Magnetar-Like Emission from the Young Pulsar in Kes 75”. In: *Science* 319.5871 (2008), pp. 1802–1805. DOI: `10.1126/science.1153465`. URL: `https://www.science.org/doi/abs/10.1126/science.1153465`.

[101] Keith C. Gendreau, Zaven Arzoumanian, and Takashi Okajima. “The Neutron star Interior Composition ExploreR (NICER): an Explorer mission of opportunity for soft x-ray timing spectroscopy”. In: *Space Telescopes and Instrumentation 2012: Ultraviolet to Gamma Ray.* Ed. by Tadayuki Takahashi, Stephen S. Murray, and Jan-Willem A. den Herder. Vol. 8443. Society of Photo-Optical Instrumentation Engineers (SPIE) Conference Series. Sept. 2012, 844313, p. 844313. DOI: `10.1117/12.926396`.

[102] Keith C. Gendreau et al. “The Neutron star Interior Composition Explorer (NICER): design and development”. In: *Space Telescopes and Instrumentation 2016: Ultraviolet to Gamma Ray.* Ed. by Jan-Willem A. den Herder, Tadayuki Takahashi, and Marshall Bautz. Vol. 9905. International Society for

Optics and Photonics. SPIE, 2016, pp. 420–435. DOI: `10.1117/12.2231304`. URL: `https://doi.org/10.1117/12.2231304`.

[103] Gabriele Ghisellini. “Synchrotron Self-Compton”. In: *Radiative Processes in High Energy Astrophysics*. Heidelberg: Springer International Publishing, 2013, pp. 89–93. ISBN: 978-3-319-00612-3. DOI: `10.1007/978-3-319-00612-3_6`. URL: `https://doi.org/10.1007/978-3-319-00612-3_6`.

[104] P. Ghosh. *Rotation and Accretion Powered Pulsars*. 2007.

[105] Olivia C. Ginn. “Quantitative Estimation of Eteric Pathogens and Antibioic Resistance Genes in Aerosols Near Urban Waste Flows”. PhD thesis. 2021. URL: `http://hdl.handle.net/1853/66495`.

[106] Norman K. Glendenning. *Compact Stars: Nuclear Physics, Particle Physics and General Relativity*. 2012.

[107] T. Gold. “Rotating Neutron Stars as the Origin of the Pulsating Radio Sources”. In: *Nature* 218.5143 (May 1968), pp. 731–732. ISSN: 1476-4687. DOI: `10.1038/218731a0`. URL: `https://doi.org/10.1038/218731a0`.

[108] Thomas Gold. “Rotating Neutron Stars and the Nature of Pulsars”. In: *Nature* 221.5175 (Jan. 1969), pp. 25–27. ISSN: 1476-4687. DOI: `10.1038/221025a0`. URL: `https://doi.org/10.1038/221025a0`.

[109] Peter Goldreich and William H. Julian. “Pulsar Electrodynamics”. In: *The Astrophysical Journal* 157 (Aug. 1969), p. 869. DOI: `10.1086/150119`.

[110] Peter L. Gonthier et al. “Galactic Populations of Radio and Gamma-Ray Pulsars in the Polar Cap Model”. In: *The Astrophysical Journal* 565.1 (Jan. 2002), pp. 482–499. DOI: `10.1086/324535`. URL: `https://doi.org/10.1086/324535`.

[111] E V Gotthelf and J P Halpern. “Discovery of a highly energetic x-ray pulsar powering Hess j1813–178 in the young supernova remnant g12.82–0.02”. In: *Astrophys. J.* 700.2 (Aug. 2009), pp. L158–L161.

[112] E. V. Gotthelf and S. Bogdanov. “NuSTAR Hard X-Ray Observations of the Energetic Millisecond Pulsars PSR B1821-24, PSR B1937+21, and PSR J0218+4232”. In: *The Astrophysical Journal* 845.2, 159 (Aug. 2017), p. 159. DOI: `10.3847/1538-4357/aa813c`. arXiv: `1704.02964 [astro-ph.HE]`.

[113] E. V. Gotthelf et al. “A 700 Year-old Pulsar in the Supernova Remnant Kesteven 75”. In: *The Astrophysical Journal Letters* 542.1 (Oct. 2000), pp. L37–L40. DOI: `10.1086/312923`. arXiv: `astro-ph/0008097 [astro-ph]`.

[114] David J Griffiths. *Introduction to electrodynamics; 4th ed.* Re-published by Cambridge University Press in 2017. Boston, MA: Pearson, 2013. DOI: `1108420419`. URL: `https://cds.cern.ch/record/1492149`.

[115] L. Guillemot et al. “Preparing GLAST LAT studies of the millisecond pulsar PSR J0218+4232 and the blazar 3C 66A”. In: *The First GLAST Symposium.* Ed. by Steven Ritz, Peter Michelson, and Charles A. Meegan. Vol. 921. American Institute of Physics Conference Series. July 2007, pp. 395–396. DOI: `10.1063/1.2757369`.

[116] H. E. S. S. Collaboration et al. “First ground-based measurement of sub-20 GeV to 100 GeV $\gamma$-Rays from the Vela pulsar with H.E.S.S. II”. In: *Astronomy and Astrophysics* 620, A66 (Dec. 2018), A66. DOI: `10.1051/0004-6361/201732153`. arXiv: `1807.01302 [astro-ph.HE]`.

[117] J P Halpern, E V Gotthelf, and F Camilo. “Spin-down measurement of psr j1813–1749: The energetic pulsar powering Hess j1813–178”. In: *Astrophys. J. Lett.* 753.1 (July 2012), p. L14.

[118] A Harding et al. “Prospects for Pulsar Studies at MeV Energies”. In: *Bulletin of the American Astronomical Society* 51 (May 2019).

[119] Alice Harding. “Pulsar Polar Cap and Slot Gap Models: Confronting Fermi Data”. In: *Journal of Astronomy and Space Sciences* 30 (Sept. 2013), pp. 145–152. DOI: `10.5140/JASS.2013.30.3.145`.

[120] Alice K. Harding. “Gamma-ray pulsars: Models and predictions”. In: *AIP Conf. Proc.* 558.1 (2001). Ed. by F. A. Aharonian and H. J. Volk, pp. 115–126. DOI: `10.1063/1.1370785`. arXiv: `astro-ph/0012268`.

[121] Alice K. Harding. “Pulsar Emission Physics: The First Fifty Years”. In: *Pulsar Astrophysics the Next Fifty Years*. Ed. by P. Weltevrede et al. Vol. 337. Aug. 2018, pp. 52–57. DOI: `10.1017/S1743921318000509`. arXiv: `1712.02409 [astro-ph.HE]`.

[122] Alice K. Harding. “The Emission Physics of Millisecond Pulsars”. In: *arXiv e-prints*, arXiv:2101.05751 (Jan. 2021), arXiv:2101.05751. arXiv: `2101.05751 [astro-ph.HE]`.

[123] Alice K. Harding. “The neutron star zoo”. In: *Frontiers of Physics* 8.6 (Dec. 2013), pp. 679–692. ISSN: 2095-0470. DOI: `10.1007/s11467-013-0285-0`. URL: `https://doi.org/10.1007/s11467-013-0285-0`.

[124] Alice K. Harding, Isabelle A. Grenier, and Peter L. Gonthier. “The Geminga fraction”. In: *Astrophysics and Space Science* 309.1 (June 2007), pp. 221–230. ISSN: 1572-946X. DOI: `10.1007/s10509-007-9435-6`. URL: `https://doi.org/10.1007/s10509-007-9435-6`.

[125] Alice K. Harding and Constantinos Kalapotharakos. “Synchrotron Self-Compton Emission from the Crab and Other Pulsars”. In: *The Astrophysical Journal* 811.1, 63 (Sept. 2015), p. 63. DOI: `10.1088/0004-637X/811/1/63`. arXiv: `1508.06251 [astro-ph.HE]`.

[126] Alice K. Harding and Alex G. Muslimov. “Pulsar Pair Cascades in Magnetic Fields with Offset Polar Caps”. In: *The Astrophysical Journal* 743.2, 181 (Dec. 2011), p. 181. DOI: `10.1088/0004-637X/743/2/181`. arXiv: `1111.1668 [astro-ph.HE]`.

[127] Alice K. Harding and Alexander G. Muslimov. “Particle Acceleration Zones above Pulsar Polar Caps: Electron and Positron Pair Formation Fronts”. In: *The Astrophysical Journal* 508.1 (Nov. 1998), pp. 328–346. DOI: `10.1086/306394`. arXiv: `astro-ph/9805132 [astro-ph]`.

[128] Alice K. Harding, Christo Venter, and Constantinos Kalapotharakos. “Very-high-energy Emission from Pulsars”. In: *The Astrophysical Journal* 923.2 (Dec. 2021), p. 194. DOI: `10.3847/1538-4357/ac3084`. URL: `https://doi.org/10.3847/1538-4357/ac3084`.

[129] Alice K. Harding et al. “High-Altitude Emission from Pulsar Slot Gaps: The Crab Pulsar”. In: *The Astrophysical Journal* 680.2 (June 2008), pp. 1378–1393. DOI: `10.1086/588037`. arXiv: `0803.0699 [astro-ph]`.

[130] Alice K. Harding et al. “Multi-TeV Emission from the Vela Pulsar”. In: *The Astrophysical Journal Letters* 869.1, L18 (Dec. 2018), p. L18. DOI: `10.3847/2041-8213/aaf3b2`. arXiv: `1811.11157 [astro-ph.HE]`.

[131] Jeffrey D. Hart. “On the choice of a truncation point in fourier series density estimation”. In: *Journal of Statistical Computation and Simulation* 21.2 (1985), pp. 95–116. DOI: `10.1080/00949658508810808`. eprint: `https://doi.org/10.1080/00949658508810808`. URL: `https://doi.org/10.1080/00949658508810808`.

[132] R. C. Hartman et al. “The Third EGRET Catalog of High-Energy Gamma-Ray Sources”. In: *The Astrophysical Journal Supplement Series* 123.1 (July 1999), pp. 79–202. DOI: `10.1086/313231`.

[133] B Haskell, P M Pizzochero, and T Sidery. “Modelling pulsar glitches with realistic pinning forces: a hydrodynamical approach”. en. In: *Mon. Not. R. Astron. Soc.* 420.1 (Feb. 2012), pp. 658–671.

[134] A. Heger et al. “How Massive Single Stars End Their Life”. In: *The Astrophysical Journal* 591.1 (July 2003), pp. 288–300. DOI: `10.1086/375341`. URL: `https://doi.org/10.1086/375341`.

[135] D J Helfand et al. “Discovery of the putative pulsar and wind nebula associated with the TeV gamma-ray source HESS J1813-178”. en. In: *Astrophys. J.* 665.2 (Aug. 2007), pp. 1297–1303.

[136] David J. Helfand, Benjamin F. Collins, and E. V. Gotthelf. "ChandraX-Ray Imaging Spectroscopy of the Young Supernova Remnant Kesteven 75". In: *The Astrophysical Journal* 582.2 (Jan. 2003), pp. 783–792. DOI: `10.1086/344725`. URL: `https://doi.org/10.1086/344725`.

[137] W Hermsen et al. "Simultaneous X-ray and radio observations of the radio-mode-switching pulsar PSR B1822-09". en. In: *Mon. Not. R. Astron. Soc.* 466.2 (Apr. 2017), pp. 1688–1708.

[138] Jason W. T. Hessels et al. "A Radio Pulsar Spinning at 716 Hz". In: *Science* 311.5769 (2006), pp. 1901–1904. DOI: `10.1126/science.1123430`. eprint: `https://www.science.org/doi/pdf/10.1126/science.1123430`. URL: `https://www.science.org/doi/abs/10.1126/science.1123430`.

[139] A. Hewish et al. "Observation of a Rapidly Pulsating Radio Source". In: *Nature* 217.5130 (Feb. 1968), pp. 709–713. ISSN: 1476-4687. DOI: `10.1038/217709a0`. URL: `https://doi.org/10.1038/217709a0`.

[140] HI4PI Collaboration: et al. "HI4PI: a full-sky H i survey based on EBHIS and GASS". In: *Astron. Astrophys.* 594 (Oct. 2016), A116.

[141] Wynn C G Ho et al. "Proper motion, spectra, and timing of PSR J1813–1749 using Chandra and NICER". In: *Monthly Notices of the Royal Astronomical Society* 498.3 (Sept. 2020), pp. 4396–4403. ISSN: 0035-8711. DOI: `10.1093/mnras/staa2653`. eprint: `https://academic.oup.com/mnras/article-pdf/498/3/4396/33791552/staa2653.pdf`. URL: `https://doi.org/10.1093/mnras/staa2653`.

[142] G Hobbs, A G Lyne, and M Kramer. "An analysis of the timing irregularities for 366 pulsars". en. In: *Mon. Not. R. Astron. Soc.* 402.2 (Feb. 2010), pp. 1027–1048.

[143] G B Hobbs, R T Edwards, and R N Manchester. "tempo2, a new pulsar-timing package - I. An overview". In: *Mon. Not. R. Astron. Soc.* 369.2 (June 2006), pp. 655–672.

[144] G. Hobbs et al. “Development of a pulsar-based time-scale”. In: *Monthly Notices of the Royal Astronomical Society* 427.4 (Dec. 2012), pp. 2780–2787. DOI: `10.1111/j.1365-2966.2012.21946.x`. arXiv: `1208.3560 [astro-ph.IM]`.

[145] G. B. Hobbs, R. T. Edwards, and R. N. Manchester. “TEMPO2, a new pulsar-timing package - I. An overview”. In: *Monthly Notices of the Royal Astronomical Society* 369.2 (June 2006), pp. 655–672. DOI: `10.1111/j.1365-2966.2006.10302.x`. arXiv: `astro-ph/0603381 [astro-ph]`.

[146] N. J. Holloway. “P-N Junctions in Pulsar Magnetospheres ?” In: *Nature Physical Science* 246.149 (Nov. 1973), pp. 6–9. ISSN: 2058-1106. DOI: `10.1038/physci246006a0`. URL: `https://doi.org/10.1038/physci246006a0`.

[147] Oxford Instruments. *Silicon Drift Detectors Explained.* URL: `https://www.exvil.lt/wp-content/uploads/2012/04/SDD_Explained.pdf`.

[148] O C de Jager and I Büsching. “The H-test probability distribution revisited: improved sensitivity”. In: *Astron. Astrophys.* 517 (July 2010), p. L9.

[149] F. James. “MINUIT Function Minimization and Error Analysis: Reference Manual Version 94.1”. In: *CERN Report* CERN-D-506 (1994).

[150] Fredrick A. Jenet et al. “Detecting the stochastic gravitational wave background using pulsar timing”. In: *Astrophys. J. Lett.* 625 (2005), pp. L123–L126. DOI: `10.1086/431220`. arXiv: `astro-ph/0504458`.

[151] B. C. Joshi et al. “Giant Pulses in Millisecond Pulsars”. In: *Young Neutron Stars and Their Environments.* Ed. by Fernando Camilo and Bryan M. Gaensler. Vol. 218. IAU Symposium. Jan. 2004, p. 319. arXiv: `astro-ph/0310285 [astro-ph]`.

[152] Vassiliki Kalogera and Gordon Baym. “The Maximum Mass of a Neutron Star”. In: *The Astrophysical Journal* 470.1 (Oct. 1996), pp. L61–L64. DOI: `10.1086/310296`. URL: `https://doi.org/10.1086/310296`.

[153] O Kargaltsev et al. “Pulsar wind nebulae created by fast-moving pulsars”. en. In: *J. Plasma Phys.* 83.5 (Oct. 2017).

[154] S. R. Kelner, A. Yu. Prosekin, and F. A. Aharonian. "SYNCHRO-CURVATURE RADIATION OF CHARGED PARTICLES IN THE STRONG CURVED MAGNETIC FIELDS". In: *The Astronomical Journal* 149.1 (Jan. 2015), p. 33. DOI: `10.1088/0004-6256/149/1/33`. URL: `https://doi.org/10.1088/0004-6256/149/1/33`.

[155] M. Kerr. "Improving Sensitivity to Weak Pulsations with Photon Probability Weighting". In: *The Astrophysical Journal* 732.1 (Apr. 2011), p. 38. DOI: `10.1088/0004-637x/732/1/38`. URL: `https://doi.org/10.1088/0004-637x/732/1/38`.

[156] H. S. Knight et al. "Green Bank Telescope Studies of Giant Pulses from Millisecond Pulsars". In: *The Astrophysical Journal* 640.2 (Apr. 2006), pp. 941–949. DOI: `10.1086/500292`. arXiv: `astro-ph/0512341 [astro-ph]`.

[157] M Kramer et al. "A periodically active pulsar giving insight into magnetospheric physics". en. In: *Science* 312.5773 (Apr. 2006), pp. 549–551.

[158] M. Kramer et al. "The Proper Motion, Age, and Initial Spin Period of PSR J0538+2817 in S147". In: *The Astrophysical Journal* 593.1 (July 2003), pp. L31–L34. DOI: `10.1086/378082`. URL: `https://doi.org/10.1086/378082`.

[159] E. C. Krupp. "Star Trek: The Search for the First Alleged Crab Supernova Rock Art". In: *American Astronomical Society Meeting Abstracts #223*. Vol. 223. American Astronomical Society Meeting Abstracts. Jan. 2014, 437.01, p. 437.01.

[160] L Kuiper, W Hermsen, and A Dekker. "The Fermi-LAT detection of magnetar-like pulsar PSR J1846-0258 at high-energy gamma-rays". In: *Monthly Notices of the Royal Astronomical Society* 1 (Dec. 2017), pp. 1238–1250. ISSN: 0035-8711. DOI: `10.1093/mnras/stx3128`. eprint: `https://academic.oup.com/mnras/article-pdf/475/1/1238/23585129/stx3128.pdf`. URL: `https://doi.org/10.1093/mnras/stx3128`.

[161] L. Kuiper and W. Hermsen. “The soft $\gamma$-ray pulsar population: a high-energy overview”. In: *Monthly Notices of the Royal Astronomical Society* 449 (June 2015), pp. 3827–3866. DOI: `10.1093/mnras/stv426`. arXiv: `1502.06769 [astro-ph.HE]`.

[162] L. Kuiper and W. Hermsen. “The soft gamma-ray pulsar population: a high-energy overview”. In: *Monthly Notices of the Royal Astronomical Society* 449.4 (Apr. 2015), pp. 3827–3866. ISSN: 0035-8711. DOI: `10.1093/mnras/stv426`. eprint: `http://oup.prod.sis.lan/mnras/article-pdf/449/4/3827/18503444/stv426.pdf`. URL: `https://dx.doi.org/10.1093/mnras/stv426`.

[163] L. Kuiper, W. Hermsen, and A. Dekker. “The Fermi-LAT detection of magnetar-like pulsar PSR J1846-0258 at high-energy gamma-rays”. In: *Monthly Notices of the Royal Astronomical Society* 475.1 (Mar. 2018), pp. 1238–1250. DOI: `10.1093/mnras/stx3128`. arXiv: `1709.00899 [astro-ph.HE]`.

[164] L. Kuiper, W. Hermsen, and B. Stappers. “Chandra and RXTE studies of the X-ray/$\gamma$-ray millisecond pulsar PSR J0218+4232”. In: *Advances in Space Research* 33.4 (Jan. 2004), pp. 507–512. DOI: `10.1016/j.asr.2003.08.019`. arXiv: `astro-ph/0306622 [astro-ph]`.

[165] L. Kuiper et al. “Detection of pulsed X-ray emission from the binary millisecond pulsar PSR J0218+4232”. In: *Astronomy and Astrophysics* 336 (Aug. 1998), pp. 545–552.

[166] L. Kuiper et al. “High-Resolution Spatial and Timing Observations of Millisecond Pulsar PSR J0218+4232 with Chandra”. In: *The Astrophysical Journal* 577.2 (Oct. 2002), pp. 917–922. DOI: `10.1086/342220`. arXiv: `astro-ph/0206081 [astro-ph]`.

[167] L. Kuiper et al. “The likely detection of pulsed high-energy gamma -ray emission from millisecond pulsar PSR J0218+4232”. In: *Astronomy and Astrophysics* 359 (July 2000), pp. 615–626. arXiv: `astro-ph/0005338 [astro-ph]`.

[168] Ch. Lange et al. "Precision timing measurements of PSR J1012+5307". In: *Monthly Notices of the Royal Astronomical Society* 326.1 (Sept. 2001), pp. 274–282. DOI: `10.1046/j.1365-8711.2001.04606.x`. arXiv: `astro-ph/0102309 [astro-ph]`.

[169] T. -P. Li and Y. -Q. Ma. "Analysis methods for results in gamma-ray astronomy." In: *The Astrophysical Journal* 272 (Sept. 1983), pp. 317–324. DOI: `10.1086/161295`.

[170] Brent Limyansky. "The Third Fermi Pulsar Catalog". In: *AAS/High Energy Astrophysics Division*. Vol. 17. AAS/High Energy Astrophysics Division. Mar. 2019, 109.32, p. 109.32.

[171] D. R. Lorimer et al. "Age constraints in the double pulsar system J0737–3039". In: *Monthly Notices of the Royal Astronomical Society* 379.3 (July 2007), pp. 1217–1221. ISSN: 0035-8711. DOI: `10.1111/j.1365-2966.2007.12013.x`. eprint: `https://academic.oup.com/mnras/article-pdf/379/3/1217/3526365/mnras0379-1217.pdf`. URL: `https://doi.org/10.1111/j.1365-2966.2007.12013.x`.

[172] Jing Luo et al. "PINT: A Modern Software Package for Pulsar Timing". In: *The Astrophysical Journal* 911.1 (Apr. 2021), p. 45. DOI: `10.3847/1538-4357/abe62f`. URL: `https://doi.org/10.3847/1538-4357/abe62f`.

[173] Jing Luo et al. *PINT: High-precision pulsar timing analysis package*. Astrophysics Source Code Library, record ascl:1902.007. Feb. 2019. ascl: `1902.007`.

[174] Andrew Lyne et al. "Switched magnetospheric regulation of pulsar spin-down". en. In: *Science* 329.5990 (July 2010), pp. 408–412.

[175] Y. E. Lyubarskii and S. A. Petrova. "Synchrotron absorption in pulsar magnetospheres". In: *Astronomy and Astrophysics* 337 (Sept. 1998), pp. 433–440.

[176] MAGIC Collaboration et al. "Detection of the Geminga pulsar with MAGIC hints at a power-law tail emission beyond 15 GeV". In: *Astronomy and Astrophysics* 643, L14 (Nov. 2020), p. L14. DOI: `10.1051/0004-6361/202039131`. arXiv: `2011.10412 [astro-ph.HE]`.

[177] R N Manchester et al. “The Australia telescope national facility pulsar catalogue”. en. In: *Astron. J.* 129.4 (Apr. 2005), pp. 1993–2006.

[178] Martino Marelli, Andrea De Luca, and Patrizia A Caraveo. “A multiwavelength study on the high-energy behavior of thefermi/lat pulsars”. In: *Astrophys. J.* 733.2 (June 2011), p. 82.

[179] F E Marshall et al. “A new, low braking index for the lmc pulsar b0540–69”. In: *Astrophys. J. Lett.* 827.2 (Aug. 2016), p. L39.

[180] F. E. Marshall et al. “Discovery of a Spin-down State Change in the LMC Pulsar B0540-69”. In: *The Astrophysical Journal Letters* 807.2, L27 (July 2015), p. L27. DOI: `10.1088/2041-8205/807/2/L27`. arXiv: `1506.05765 [astro-ph.HE]`.

[181] Massaro, E. et al. “Log-parabolic spectra and particle acceleration in the BL Lac object Mkn 421: Spectral analysis of the complete BeppoSAX wide band X-ray data set”. In: *A&A* 413.2 (2004), pp. 489–503. DOI: `10.1051/0004-6361:20031558`. URL: `https://doi.org/10.1051/0004-6361:20031558`.

[182] Julie McEnery et al. “All-sky Medium Energy Gamma-ray Observatory: Exploring the Extreme Multimessenger Universe”. In: *Bulletin of the American Astronomical Society*. Vol. 51. Sept. 2019, 245, p. 245. arXiv: `1907.07558 [astro-ph.IM]`.

[183] Charles Meegan et al. “The Fermi Gamma-ray Burst Monitor”. In: *The Astrophysical Journal* 702.1 (Sept. 2009), pp. 791–804. DOI: `10.1088/0004-637X/702/1/791`. arXiv: `0908.0450 [astro-ph.IM]`.

[184] Maria Messineo et al. “Massive Stars in the cl 1813-178 Cluster: An Episode of Massive Star Formation in the W33 Complex”. In: *Astrophys. J.* 733.1 (May 2011), p. 41.

[185] P Mészáros. “Gamma-ray bursts”. In: *Reports on Progress in Physics* 69.8 (July 2006), pp. 2259–2321. DOI: `10.1088/0034-4885/69/8/r01`. URL: `https://doi.org/10.1088/0034-4885/69/8/r01`.

[186] J. M. Migliazzo et al. "Proper-Motion Measurements of Pulsar B1951+32 in the Supernova Remnant CTB 80". In: *The Astrophysical Journal* 567.2 (Feb. 2002), pp. L141–L144. DOI: `10.1086/340002`. URL: `https://doi.org/10.1086/340002`.

[187] William C. Miller. "Two Prehistoric Drawings of Possible Astronomical Significance". In: *Leaflet of the Astronomical Society of the Pacific* 7.314 (Jan. 1955), p. 105.

[188] T. Mineo et al. "The pulse shape and spectrum of the millisecond pulsar PSR J0218+4232 in the energy band 1-10 keV observed with BeppoSAX". In: *Astronomy and Astrophysics* 355 (Mar. 2000), pp. 1053–1059.

[189] Alex G. Muslimov and Alice K. Harding. "Extended Acceleration in Slot Gaps and Pulsar High-Energy Emission". In: *The Astrophysical Journal* 588.1 (May 2003), pp. 430–440. DOI: `10.1086/368162`. URL: `https://doi.org/10.1086/368162`.

[190] *NASA - NSSDCA - Spacecraft - Telemtry Details*. `https://nssdc.gsfc.nasa.gov/nmc/spacecraft/displayTrajectory.action?id=2008-029A`. Accessed: 2021-02-24.

[191] *NASA Renames Observatory For Fermi, Reveals Entire Gamma-Ray Sky.*

[192] Jose Navarro et al. "A Very Luminous Binary Millisecond Pulsar". In: *The Astrophysical Journal Letters* 455 (Dec. 1995), p. L55. DOI: `10.1086/309816`.

[193] *NICER Payload*. NASA. Oct. 2018. URL: `https://images.nasa.gov/details-iss057e055490`.

[194] P. L. Nolan et al. "FERMI LARGE AREA TELESCOPE SECOND SOURCE CATALOG". In: *The Astrophysical Journal Supplement Series* 199.2 (Mar. 2012), p. 31. DOI: `10.1088/0067-0049/199/2/31`. URL: `https://doi.org/10.1088/0067-0049/199/2/31`.

[195] A. Noutsos et al. "Pulsar spin–velocity alignment: kinematic ages, birth periods and braking indices". In: *Monthly Notices of the Royal Astronomical Society* 430.3 (Feb. 2013), pp. 2281–2301. ISSN: 0035-8711. DOI: `10.1093/`

mnras/stt047. eprint: https://academic.oup.com/mnras/article-pdf/430/3/2281/4930626/stt047.pdf. URL: https://doi.org/10.1093/mnras/stt047.

[196] H. Ohuchi et al. "Does PSR J2022+3842 emit gamma-rays?" Sixth international Fermi Symposium. 2015.

[197] E. Oña-Wilhemi et al. "First pulsar observations with the MAGIC telescope". In: *29th International Cosmic Ray Conference (ICRC29), Volume 4*. Vol. 4. International Cosmic Ray Conference. Jan. 2005, p. 247.

[198] J. R. Oppenheimer and G. M. Volkoff. "On Massive Neutron Cores". In: *Phys. Rev.* 55 (4 Feb. 1939), pp. 374–381. DOI: 10.1103/PhysRev.55.374. URL: https://link.aps.org/doi/10.1103/PhysRev.55.374.

[199] J. Otero-Santos et al. "Quasi-periodic behaviour in the optical and $\gamma$-ray light curves of blazars 3C 66A and B2 1633+38". In: *Monthly Notices of the Royal Astronomical Society* 492.4 (Mar. 2020), pp. 5524–5539. DOI: 10.1093/mnras/staa134. arXiv: 2001.06014 [astro-ph.HE].

[200] David W. Pankenier. "Notes on translations of the East Asian records relating to the supernova of AD 1054". In: *Journal of Astronomical History and Heritage* 9.1 (June 2006), pp. 77–82.

[201] P. S. Ray et al. "Precise $\gamma$-ray Timing and Radio Observations of 17 Fermi $\gamma$-ray Pulsars". In: *The Astrophysical Journal Supplement Series* 194.2, 17 (June 2011), p. 17. DOI: 10.1088/0067-0049/194/2/17. arXiv: 1011.2468 [astro-ph.HE].

[202] Wolfgang A. Rolke and Angel M. López. "Confidence intervals and upper bounds for small signals in the presence of background noise". In: *Nuclear Instruments and Methods in Physics Research A* 458.3 (Feb. 2001), pp. 745–758. DOI: 10.1016/S0168-9002(00)00935-9. arXiv: hep-ph/0005187 [hep-ph].

[203] Wolfgang A. Rolke, Angel M. López, and Jan Conrad. “Limits and confidence intervals in the presence of nuisance parameters”. In: *Nuclear Instruments and Methods in Physics Research A* 551.2-3 (Oct. 2005), pp. 493–503. DOI: `10.1016/j.nima.2005.05.068`. arXiv: `physics/0403059 [physics.data-an]`.

[204] Bronisław Rudak and Jarosław Dyks. “The modeling of the Vela pulsar pulses - from optical to hard gamma-ray energy”. In: *PoS* ICRC2017 (2018), p. 680. DOI: `10.22323/1.301.0680`. arXiv: `1708.01556 [astro-ph.HE]`.

[205] M. Ruderman. “Matter in Superstrong Magnetic Fields”. In: *Symposium - International Astronomical Union* 53 (1974), pp. 117–131. DOI: `10.1017/S0074180900099964`.

[206] M. A. Ruderman and P. G. Sutherland. “Theory of pulsars: polar gaps, sparks, and coherent microwave radiation.” In: *The Astrophysical Journal* 196 (Feb. 1975), pp. 51–72. DOI: `10.1086/153393`.

[207] Y. Saito et al. “Detection of Magnetospheric X-Ray Pulsation from Millisecond Pulsar PSR B1821-24”. In: *The Astrophysical Journal Letters* 477.1 (Mar. 1997), pp. L37–L40. DOI: `10.1086/310512`.

[208] P M Saz Parkinson et al. “Eight $\gamma$-ray pulsars discovered in blind frequency searches offermilat data”. In: *Astrophys. J.* 725.1 (Dec. 2010), pp. 571–584.

[209] P. Saz Parkinson et al. “On the highest energy emission from millisecond pulsars”. In: *Proceedings of the 7th International Fermi Symposium.* Oct. 2017, 8, p. 8. arXiv: `1712.06808 [astro-ph.HE]`.

[210] Willem D. Schutte and Jan W. H. Swanepoel. “SOPIE: an R package for the non-parametric estimation of the off-pulse interval of a pulsar light curve”. In: *Monthly Notices of the Royal Astronomical Society* 461.1 (Sept. 2016), pp. 627–640. DOI: `10.1093/mnras/stw1335`.

[211] Ryan M. Shannon and James M. Cordes. “Assessing the Role of Spin Noise in the Precision Timing of Millisecond Pulsars”. In: *The Astrophysical Journal* 725.2 (Nov. 2010), pp. 1607–1619. DOI: `10.1088/0004-637x/725/2/1607`. URL: `https://doi.org/10.1088/0004-637x/725/2/1607`.

[212] Masaru Shibata et al. "Constraint on the maximum mass of neutron stars using GW170817 event". In: *Phys. Rev. D* 100 (2 July 2019), p. 023015. DOI: `10.1103/PhysRevD.100.023015`. URL: `https://link.aps.org/doi/10.1103/PhysRevD.100.023015`.

[213] K P Singh. "Grazing incidence optics for X-ray astronomy: X-ray optics". In: *Journal of Optics* 40 (Sept. 2011). DOI: `10.1007/s12596-011-0040-2`.

[214] Claire E. Smith. "Too tired to escape tiredness: Work stress undermines healthy leisure decision-making". PhD thesis. 2021. URL: `http://rave.ohiolink.edu/etdc/view?acc_num=bgsu1620131359548271`.

[215] D. Smith. *Presented at the MODE Meeting.* 2016.

[216] D. A. Smith et al. "Pulsar timing for the Fermi gamma-ray space telescope". In: *Astronomy and Astrophysics* 492.3 (Dec. 2008), pp. 923–931. DOI: `10.1051/0004-6361:200810285`. arXiv: `0810.1637 [astro-ph]`.

[217] D. A. Smith et al. "Searching a Thousand Radio Pulsars for Gamma-Ray Emission". In: *The Astrophysical Journal* 871, 78 (Jan. 2019), p. 78. DOI: `10.3847/1538-4357/aaf57d`. arXiv: `1812.00719 [astro-ph.HE]`.

[218] Boris V. Somov. "Single-Fluid Models for Astrophysical Plasma". In: *Plasma Astrophysics, Part I: Fundamentals and Practice*. New York, NY: Springer New York, 2012. ISBN: 978-1-4614-4283-7. DOI: `10.1007/978-1-4614-4283-7_12`. URL: `https://doi.org/10.1007/978-1-4614-4283-7_12`.

[219] Marion Spir-Jacob et al. "Detection of sub-100 GeV gamma-ray pulsations from PSR B1706-44 with H.E.S.S". In: *arXiv e-prints*, arXiv:1908.06464 (Aug. 2019), arXiv:1908.06464. arXiv: `1908.06464 [astro-ph.HE]`.

[220] I. H. Stairs, S. E. Thorsett, and F. Camilo. "Coherently Dedispersed Polarimetry of Millisecond Pulsars". In: *The Astrophysical Journal Supplement Series* 123.2 (Aug. 1999), pp. 627–638. DOI: `10.1086/313245`. arXiv: `astro-ph/9810399 [astro-ph]`.

[221] F. Richard Stephenson and David A. Green. “Was the supernova of AD 1054 reported in European history?” In: *Journal of Astronomical History and Heritage* 6.1 (June 2003), pp. 46–52.

[222] M. Takahashi. “Very-high-energy GRB events in novel Fermi-LAT photon data and their emission mechanism”. In: *36th International Cosmic Ray Conference (ICRC2019).* Vol. 36. International Cosmic Ray Conference. July 2019, 606, p. 606.

[223] M. Takahashi et al. “Calorimeter-only analysis of the Fermi Large Area Telescope”. In: *5th Fermi Symposium, Nagoya, Japan, 20-24 Oct 2014*, arXiv:1503.01364 (Mar. 2015), arXiv:1503.01364. arXiv: `1503.01364 [astro-ph.HE]`.

[224] D. J. Thompson, D. L. Bertsch, and Jr. R. H. O’Neal. “The Highest-Energy Photons Seen by the Energetic Gamma Ray Experiment Telescope (EGRET) on the Compton Gamma Ray Observatory”. In: *The Astrophysical Journal Supplement Series* 157.2 (Apr. 2005), pp. 324–334. DOI: `10.1086/427981`. URL: `https://doi.org/10.1086/427981`.

[225] D. J. Thompson et al. “The Second EGRET Catalog of High-Energy Gamma-Ray Sources”. In: *The Astrophysical Journal Supplement Series* 101 (Dec. 1995), p. 259. DOI: `10.1086/192240`.

[226] Diego F. Torres. “Order parameters for the high-energy spectra of pulsars”. In: *Nature Astronomy* 2 (Feb. 2018), pp. 247–256. DOI: `10.1038/s41550-018-0384-5`. arXiv: `1802.04177 [astro-ph.HE]`.

[227] Diego F. Torres et al. “Synchrocurvature modelling of the multifrequency non-thermal emission of pulsars”. In: *Monthly Notices of the Royal Astronomical Society* 489.4 (Nov. 2019), pp. 5494–5512. DOI: `10.1093/mnras/stz2403`. arXiv: `1908.11574 [astro-ph.HE]`.

[228] Leisa K Townsley et al. “The massive star-forming regions omnibus X-ray catalog, second installment”. In: *Astrophys. J. Suppl. Ser.* 235.2 (Apr. 2018), p. 43.

[229] D. Borla Tridon et al. “The MAGIC-II gamma-ray stereoscopic telescope system”. In: *Nuclear Instruments and Methods in Physics Research Section A: Accelerators, Spectrometers, Detectors and Associated Equipment* 623.1 (2010). 1st International Conference on Technology and Instrumentation in Particle Physics, pp. 437–439. ISSN: 0168-9002. DOI: `https://doi.org/10.1016/j.nima.2010.03.028`. URL: `https://www.sciencedirect.com/science/article/pii/S0168900210005929`.

[230] P Ubertini et al. “INTEGRAL IGR J18135-1751 = HESS J1813-178: A new cosmic high-energy accelerator from keV to TeV energies”. en. In: *Astrophys. J.* 629.2 (Aug. 2005), pp. L109–L112.

[231] Dmitri A. Uzdensky and Anatoly Spitkovsky. “PHYSICAL CONDITIONS IN THE RECONNECTION LAYER IN PULSAR MAGNETOSPHERES”. In: *The Astrophysical Journal* 780.1 (Dec. 2013), p. 3. DOI: `10.1088/0004-637x/780/1/3`. URL: `https://doi.org/10.1088/0004-637x/780/1/3`.

[232] C. Venter, A. K. Harding, and L. Guillemot. “Probing Millisecond Pulsar Emission Geometry Using Light Curves from the Fermi Large Area Telescope”. In: *The Astrophysical Journal* 707.1 (Nov. 2009), pp. 800–822. DOI: `10.1088/0004-637x/707/1/800`. URL: `https://doi.org/10.1088/0004-637x/707/1/800`.

[233] J. P. W. Verbiest and D. R. Lorimer. “Why the distance of PSR J0218+4232 does not challenge pulsar emission theories”. In: *Monthly Notices of the Royal Astronomical Society* 444.2 (Oct. 2014), pp. 1859–1861. DOI: `10.1093/mnras/stu1560`. arXiv: `1408.0281 [astro-ph.HE]`.

[234] F. Verbunt et al. “High-energy observations of the millisecond pulsar PSR J0218+4232”. In: *Astronomy and Astrophysics* 311 (July 1996), pp. L9–L12.

[235] VERITAS Collaboration et al. “Detection of Pulsed Gamma Rays Above 100 GeV from the Crab Pulsar”. In: *Science* 334.6052 (Oct. 2011), p. 69. DOI: `10.1126/science.1208192`. arXiv: `1108.3797 [astro-ph.HE]`.

[236] D A Verner et al. “Atomic data for astrophysics. II. New analytic FITS for photoionization cross sections of atoms and ions”. en. In: *Astrophys. J.* 465 (July 1996), p. 487.

[237] D. Viganò et al. “An assessment of the pulsar outer gap model - II. Implications for the predicted $\gamma$-ray spectra”. In: *Monthly Notices of the Royal Astronomical Society* 447 (Mar. 2015), pp. 2649–2657. DOI: `10.1093/mnras/stu2565`. arXiv: `1412.1290 [astro-ph.HE]`.

[238] D. Viganò et al. “Compact formulae, dynamics and radiation of charged particles under synchro-curvature losses”. In: *Monthly Notices of the Royal Astronomical Society* 447 (Feb. 2015), pp. 1164–1172. DOI: `10.1093/mnras/stu2456`. arXiv: `1411.5836 [astro-ph.HE]`.

[239] Abraham Wald. “Tests of statistical hypotheses concerning several parameters when the number of observations is large”. In: *Transactions of the American Mathematical Society* 54 (1943), pp. 426–482. DOI: `10.1090/S0002-9947-1943-0012401-3`.

[240] Kyle P. Watters et al. “AN ATLAS FOR INTERPRETING gamma-RAY PULSAR LIGHT CURVES”. In: *The Astrophysical Journal* 695.2 (Apr. 2009), pp. 1289–1301. DOI: `10.1088/0004-637x/695/2/1289`. URL: `https://doi.org/10.1088/0004-637x/695/2/1289`.

[241] N. A. Webb, J. -F. Olive, and D. Barret. “XMM-Newton spectral and timing observations of the millisecond pulsar ¡ASTROBJ¿PSR J0218+4232¡/ASTROBJ¿”. In: *Astronomy and Astrophysics* 417 (Apr. 2004), pp. 181–188. DOI: `10.1051/0004-6361:20040032`. arXiv: `astro-ph/0312609 [astro-ph]`.

[242] S. S. Wilks. “The Large-Sample Distribution of the Likelihood Ratio for Testing Composite Hypotheses”. In: *Ann. Math. Statist.* 9.1 (Mar. 1938), pp. 60–62. DOI: `10.1214/aoms/1177732360`. URL: `https://doi.org/10.1214/aoms/1177732360`.

[243] J Wilms, A Allen, and R McCray. “On the absorption of X-rays in the interstellar medium”. en. In: *Astrophys. J.* 542.2 (Oct. 2000), pp. 914–924.

[244] Luke B. Winternitz et al. "SEXTANT X-ray Pulsar Navigation Demonstration: Additional On-Orbit Results". In: *2018 SpaceOps Conference*. DOI: `10.2514/6.2018-2538`. eprint: `https://arc.aiaa.org/doi/pdf/10.2514/6.2018-2538`. URL: `https://arc.aiaa.org/doi/abs/10.2514/6.2018-2538`.

[245] Hans Wolter. "Spiegelsysteme streifenden Einfalls als abbildende Optiken für Röntgenstrahlen". In: *Annalen der Physik* 445.1-2 (1952), pp. 94–114. DOI: `https://doi.org/10.1002/andp.19524450108`. eprint: `https://onlinelibrary.wiley.com/doi/pdf/10.1002/andp.19524450108`. URL: `https://onlinelibrary.wiley.com/doi/abs/10.1002/andp.19524450108`.

[246] L. Woltjer. "X-Rays and Type I Supernova Remnants." In: *The Astrophysical Journal* 140 (Oct. 1964), pp. 1309–1313. DOI: `10.1086/148028`.

[247] M. Wood et al. "Fermipy: An open-source Python package for analysis of Fermi-LAT Data". In: *35th International Cosmic Ray Conference (ICRC2017)*. Vol. 301. International Cosmic Ray Conference. Jan. 2017, 824, p. 824. arXiv: `1707.09551 [astro-ph.IM]`.

[248] Roberta Zanin et al. "MARS, The MAGIC Analysis and Reconstruction Software". In: *International Cosmic Ray Conference*. Vol. 33. International Cosmic Ray Conference. Jan. 2013, p. 2937.

[249] Jerrold H. Zar. *Biostatistical analysis*. eng. Fifth edition. Upper Saddle River, New Jersey: Prentice Hall, 2010 - 2010. ISBN: 0131008463.

[250] Bing Zhang and Alice K. Harding. "Full Polar Cap Cascade Scenario: Gamma-Ray and X-Ray Luminosities from Spin-powered Pulsars". In: *The Astrophysical Journal* 532.2 (Apr. 2000), pp. 1150–1171. DOI: `10.1086/308598`. URL: `https://doi.org/10.1086/308598`.